This is to certify that the

thesis entitled

ELASTIC-PLASTIC STRAIN AND EFFECT OF NON-SINGULAR STRESS AT THE CRACK TIP IN FINITE THICKNESS PLATE USING VARIOUS EXPERIMENTAL AND ANALYTICAL METHODS

presented by

Subrato Dhar

has been accepted towards fulfillment
of the requirements for

M.S. degree in MECHANICS

Major professor

Date 21 July 1992

ELASTIC-PLASTIC STRAIN AND THE EFFECT OF NON-SINGULAR STRESS AT THE CRACK TIP IN FINITE THICKNESS PLATE USING VARIOUS EXPERIMENTAL AND ANALYTICAL METHODS

By

SUBRATO DHAR
B.Eng.(Metallurgical Engineering),
Regional Engineering College,
Suratkal, INDIA
(1985)

A THESIS

Submitted to the Department of
Materials Science and Mechanics
In Partial Fulfillment of
the Requirements for the Degree of

Master of Science in Mechanics

MICHIGAN STATE UNIVERSITY

February, 1992

ELASTIC-PLASTIC STRAIN AND EFFECT OF NON-SINGULAR STRESS AT THE CRACK TIP IN FINITE THICKNESS PLATE USING VARIOUS EXPERIMENTAL AND ANALYTICAL METHODS

by

Subrato Dhar

ABSTRACT

It is well known that for most two-dimensional problems, the stress-intensity factor K_I can be obtained by analytic techniques or by finite-element analysis. In many instances, the crack length may be of the same order of magnitude as the thickness of the specimen, and the in-plane stress can no longer be assumed to remain constant across the thickness direction since the free surface of the specimen can exert appreciable influence on the stress distribution. As a result, the crack driving force will vary along the crack front and the problem becomes three-dimensional. The generalized plane stress solution will not be a limit of the three-dimensional solution. Furthermore, it is incorrect to refer to the stress distribution on the surface layer of a plate with or without a crack as being in a state of generalized plane stress. This problem is rather complicated and may be answered by experimental techniques.

Static strain distribution and crack opening displacement near the crack tip in thick compact tension specimens obtained from multiple embedded grid moire and strain gages were reported by Paleebut and Cloud. Their results are used to calculate the variation in the apparent Mode-1 stress intensity for various interior planes and on the surface of the specimen. The stress intensity factor was found to be higher in the midplane than in the surface.

The strain energy density concept is then utilized for calculating elastic-plastic strains and stresses near the crack tip. The availability of linear or non-linear elastic notch or crack stress-strain solutions enables calculation of strain energy density distribution at and ahead of a notch and crack tip. Subsequently, the strain energy density can be translated into elastic-plastic strains and stresses which actually exist at the notch and crack tip. The stress redistribution caused by the plastic yielding around the crack tip is taken into account so that the value of the strain is improved.

The estimated values of crack tip strain based on strain energy density approach are compared with experimental results obtained from embedded grid moire technique and embedded strain gages, and the results are encouraging.

From the moire photographs it seems that large scale yielding dominates near the crack tip. In fact, the measured strain is very near the elastic solution, which means, in reality, only small-scale yielding is taking place near the crack tip. The small scale yielding approximation then incorporates the notion that, even though stresses derived from a linear elastic solution are inaccurate within and near a small crack tip yield zone, its dominant singular term governs the deformation state within that zone. This deformation state, well within the yield zone, is expressed solely in terms of J-integral. Besides this singularity term, there is a nonsingular term acting parallel to the crack tip. There is no non-singular effect on the dominant singularity, although there will, of course, be an effect on the overall shape of the yielded zone. A detailed study using finite element analysis was carried out in the estimation of distribution of stresses and assessing the effects of the non-singular term on plastic zone sizes near the crack tip of a CT specimen. The results are quite comparable with the above two experimental techniques.

In the three-dimensional photoelastic investigation, an observation near the crack tip showed that crack blunting is taking place on the surface plane, and the crack tip remained sharp in the interface after a small rupture. In a thick specimen, triaxiality near the crack tip is high and higher crack front singularity increases with distance along the thickness from the surface plane. This causes stress distribution at the midplane near the crack tip to be higher than on the surface plane, and plastic zone size on the surface to be smaller than on the mid-plane. Strain energy density in the surface plane remains elastic and almost flat, whereas strain energy density in the midplane remains fully plastic.

TABLE OF CONTENTS

LIST OF TABLES

LIST OF FIGURES

CHAPTER 1

BACKGROUND

1.1 Purpose and Motivation

This research was started by Paleebut [1] and Cloud [2] in 1980 to develop a new three-dimensional moire method using multiple embedded and surface gratings to measure strain around a coldworked hole through the thickness of a polymeric specimen and to measure the strain components near a crack tip on the surface and in the interior of a thick specimen.

One purpose of the present investigation is to further highlight the importance of the above technique in terms of measurement of the strain components near a crack tip on the surface and in the interior of a thick CT specimen. The strain energy density criterion has been adopted to give physical insight in explaining the experimental results. Stress intensity factor was calculated along the crack front by using the moire results previously obtained by Cloud and Paleebut [2]. Apparent Mode-1 SIF was then compared with the stress freezing technique of photoelasticity, the results of which are additionally encouraging. Crack opening displacement techniques are used to further explain the degree of strain near a crack tip in the interior and on the surface. The results are compared for amorphous and crystalline polycarbonate to understand the fracture behavior. Measurement of plastic zone size and shape and predictions for any thickness are developed. Numerical analysis was than carried

out using finite element packages like NISA [3] and ABAQUS [4]. Elastic analysis was done using NISA, and elastic-plastic analysis was done using ABAQUS. The estimated non-singular stresses from FEM are comparable to those obtained from photoelasticity. The effect of the non-singular stress for a power hardening material is more pronounced than for the materials which show softening. The results of all these approaches leads to understanding of fracture behavior in polycarbonate and, more or less, in any thick finite geometries.

1.2 Linear Elastic Fracture Mechanics

In order to predict against failures of engineering structures it is necessary to understand fundamental processes causing fracture in solids, and, more important, is the engineering requirement in providing calculable and measureable parameters which can characterize unambiguously such fracture events as the initiation of crack growth at different load levels. This is made possible by testing some suitable specimen in a laboratory. Near the notch and crack tip there exists stress or strain concentration. The local notch strain can be estimated from the product of nominal stress (strain) and the theoretical stress concentration factor (K_T) only when the material at the notch root remains elastic. Several methods and solutions concerning the calculation of elastic stress and strain near notches were given by Howland [5], Peterson [6] and Neuber [7]. The stress and strain field at a crack tip was first found using elastic mechanics by Irwin [8] also then [9] extended stress and strain analysis under narrow-range yield. In the near crack tip, four distinct regions can be identified, as shown in Figure 1.1a. The following comments can be made about stresses in each of the four zones:

1.2.1 Inelastic region

In practice, the region at the crack-tip may not be in the elastic state; and the crack-tip may become blunt due to local plastic yielding. The elastic stress field near the tip of a blunt crack is given by Creger and Paris [10] in the form:

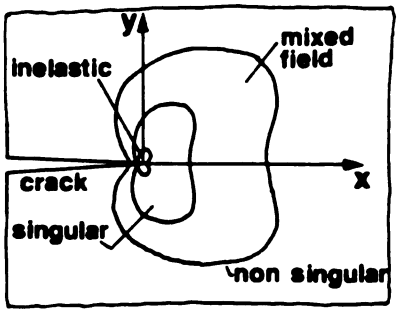

(a)

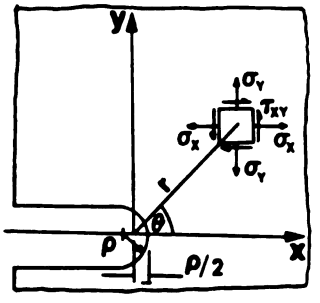

(b)

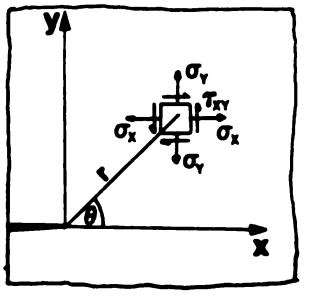

(c)

Figure 1.1. Deformed regions in front of the crack tip, (a) Four distinct regions, (b) Inelastic region and (c) Singular region.

$$\sigma_{ij} = \frac{K_I}{\sqrt{2\pi r}} f_{ij}(\theta) + \frac{K_I}{\sqrt{2\pi r}} \frac{\rho}{2r} g_{ij}(\theta) \tag{1.1}$$

where $f_{ij}(\theta)$ and $g_{ij}(\theta)$ (for i,j = 1,2) are given by (1.2,1.3).

$$f_{ij} = cos\frac{\theta}{2} \begin{bmatrix} 1 - sin\frac{\theta}{2} sin\frac{3\theta}{2} \\ 1 + sin\frac{\theta}{2} sin\frac{3\theta}{2} \\ sin\frac{\theta}{2} cos\frac{3\theta}{2} \end{bmatrix} \tag{1.2}$$

$$g_{ij} = cos\frac{\theta}{2} \begin{bmatrix} -cos\frac{3\theta}{2} \\ cos\frac{3\theta}{2} \\ -sin\frac{3\theta}{2} \end{bmatrix} \tag{1.3}$$

where (r, θ) are the coordinates of the point of interest, and ρ is the root radius of the notch as shown in Figure 1.1b. In (1.1), if notch radius $\rho = 0$, it turns into (1.4). The result is valid for ρ less than or equal to 0.18 inch as reported by Zhang and Venugopal [11]. The above equations are independent of material constants and do not differ between plane stress and plane strain in a two dimensional problem.

1.2.2 Singular region

In this region, the elastic stress components are given by (1.4 - 1.6), strain components in plane strain and plane stress are given by (1.7 - 1.8) and displacement components in plane strain and plane stress are given by (1.9 - 1.10), in the near vicinity of a sharp crack tip. These components always have a singularity $\sqrt{r}$ and are given in tensorial form (for i,j = 1,2,3) by Paris and Sih [12] in the form:

$$\sigma_{ij} = \frac{K_I}{\sqrt{2\pi r}} cos\frac{\theta}{2} \begin{bmatrix} 1 - sin\frac{\theta}{2} sin\frac{3\theta}{2} \\ 1 + sin\frac{\theta}{2} sin\frac{3\theta}{2} \\ sin\frac{\theta}{2} cos\frac{3\theta}{2} \end{bmatrix} \tag{1.4}$$

$$\sigma_{13} = \sigma_{23} = 0 \tag{1.5}$$

$$\sigma_{33} = \begin{cases} 0 & \text{for plane stress} \\ \frac{2\nu cos\left(\frac{\theta}{2}\right) K_I}{\sqrt{2\pi r}} & \text{for plane strain} \end{cases} \tag{1.6}$$

$$\epsilon_{ij} = \frac{K_I}{\sqrt{2\pi r}} cos\frac{\theta}{2} \begin{bmatrix} (1-\nu) - (1+\nu) sin\frac{\theta}{2} sin\frac{3\theta}{2} \\ (1-\nu) + (1+\nu) sin\frac{\theta}{2} sin\frac{3\theta}{2} \\ \frac{2\nu}{E} cos\frac{\theta}{2} \end{bmatrix} \tag{1.7}$$

$$\epsilon_{ij} = \frac{K_I}{\sqrt{2\pi r}} cos\frac{\theta}{2} \begin{bmatrix} (1-\nu-2\nu^2) - (1+\nu) sin\frac{\theta}{2} sin\frac{3\theta}{2} \\ (1-\nu-2\nu^2) + (1+\nu) sin\frac{\theta}{2} sin\frac{3\theta}{2} \\ 0 \end{bmatrix} \tag{1.8}$$

$$\begin{bmatrix} u_1 \\ u_2 \end{bmatrix} = 2(1+\nu)\frac{K_I}{E}\sqrt{\frac{r}{2\pi}} \begin{bmatrix} cos\frac{\theta}{2}(1-2\nu+cos^2\frac{\theta}{2}) \\ sin\frac{\theta}{2}(2-2\nu-cos^2\frac{\theta}{2}) \end{bmatrix} \tag{1.9}$$

$$\begin{bmatrix} u_1 \\ u_2 \end{bmatrix} = 2(1+\nu)\frac{K_I}{E}\sqrt{\frac{r}{2\pi}} \begin{bmatrix} cos\frac{\theta}{2}(1-2\nu+cos^2\frac{\theta}{2}) \\ sin\frac{\theta}{2}(2-2\nu-cos^2\frac{\theta}{2}) \end{bmatrix} - \epsilon_{33} \begin{bmatrix} \nu cos\theta \\ \nu sin\theta \end{bmatrix} \tag{1.10}$$

In all the above equations (r, θ) are the polar coordinates of a point measured from the crack tip and crack plane as shown in Figure 1.1c. The amplitude of the singularity is called the stress intensity factor K. Fields that are symmetric with respect to the plane of crack $x_2 = 0$ are termed mode I, while antisymmetric fields are termed mode II. For a given mode, the θ variation, σ and ϵ are fixed. The θ variations of the in-plane stress components are the same for plane stress and plane strain, but the strains depend on the condition which is in effect. The stress intensity factor K depends linearly on the applied load and is a function of crack length and other geometric parameters characterizing the body. The stress intensity factor provides a measure

of the level of deformation in the vicinity of the crack tip. It is used to characterize the onset or continuation of crack growth in a real material, which may undergo creep or other inelastic deformation in the most highly stressed region at the tip. It relies on satisfaction of a condition known as small-scale yielding. In other words, this condition requires that the zone of inelasticity, whatever its source, be contained well within the region over which the singularity fields given by (1.4) provide a good approximation to the full linear elasticity solution. Small-scale yielding assures that all the pertinent information related to the geometry and loads applied to the cracked body are communicated to the crack tip through K for a given mode of loading. As the value of r increases, the stresses due to a general stress field become more dominant. Based on the 2D elastic solution (1.1) or (1.4), the crack opening strain for nominal stress S_N = 4.1375, 17.927 and 31.717 MPa are shown in Figures 1.2, 1.3 and 1.4. These figures represent the strain distribution for $\rho = 0$ (sharp crack), 0.18, 0.72 and 1.65 mm for plane stress and plane strain. The calculated strain in plane stress is higher than in plane strain. With increasing crack tip radius, the values of strain increase due to the second term in (1.1) being dominant. All the load levels are chosen such that the crack tip deformation may be considered undergoing small scale yielding. For this reason an understanding of plastic zones and sizes are important. A Fortran code was developed (refer to Appendix A) to generate Figures 1.5 to 1.10, which show plastic zone contours for several different situations. The plastic zone shape and sizes are non-dimensionalized with $\frac{J}{E\epsilon_o}$, where J is the value of the path independent J-integral, E is the modulus of elasticity and ϵ_o is the yield strain. The yield surface is based on the Mises yield criterion.

A comparison of the plastic zone size and shape between plane stress and plane strain is made for $\frac{\epsilon_{ys}}{\epsilon_o}$ = 1.0, 1.1, 1.2 and 1.3. In general the plastic zone size in plane strain is three times smaller than its size in plane stress. The shape of the plastic zone in plane strain is like an ellipse and in plane stress it is like a kidney. Figures 1.5 and 1.6 are for $\rho = 0$. With increasing load, the shape will remain the same, but the magnitude would increase if scales are properly normalized. Since the scales are normalized with $\frac{J}{E\epsilon_o}$, for all load levels the plastic zone sizes will overlap on each other, except for the shape. Figure 1.7 and 1.8 are for ρ = 0.18 mm at a load level of 4.137 MPa. A comparison of plastic zone size and shape for three different load levels $\frac{S_N}{\sigma_o}$ = 0.1478, 0.6408 and 1.1338 are made. Finally, it is to be noted that all these Figures are valid in the range of application of the 2D elastic equations (1.1) and (1.4).

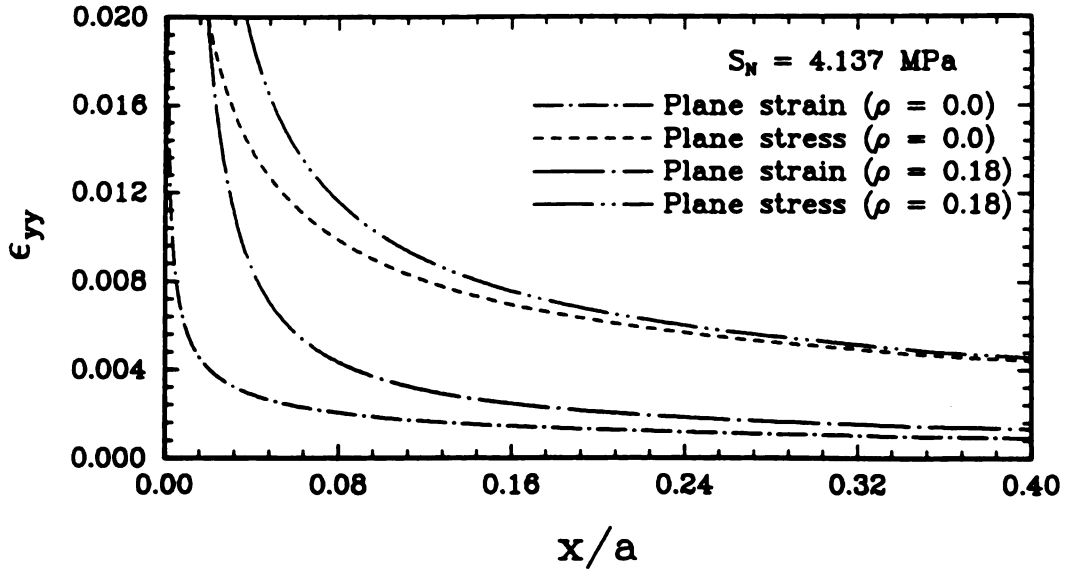

Figure 1.2: Crack opening strain distribution in a CT specimen for a/W = 0.4966 and $\theta = 0°$ based on equation (1.1) and (1.4) for S_N = 4.137 MPa.

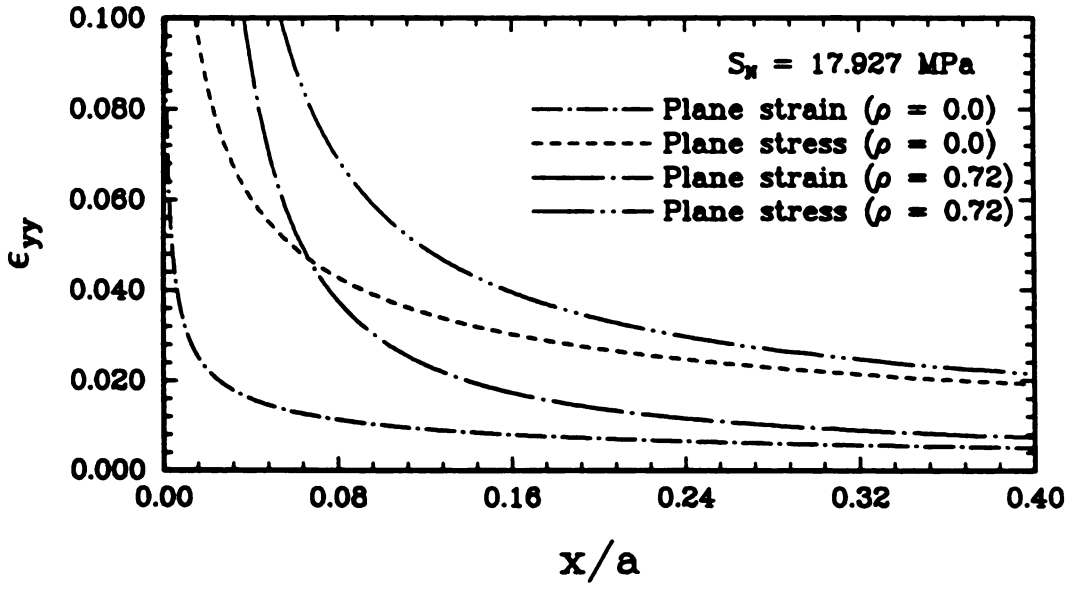

Figure 1.3: Crack opening strain distribution in a CT specimen for a/W = 0.4966 and $\theta = 0°$ based on equation (1.1) and (1.4) for S_N = 17.927 MPa.

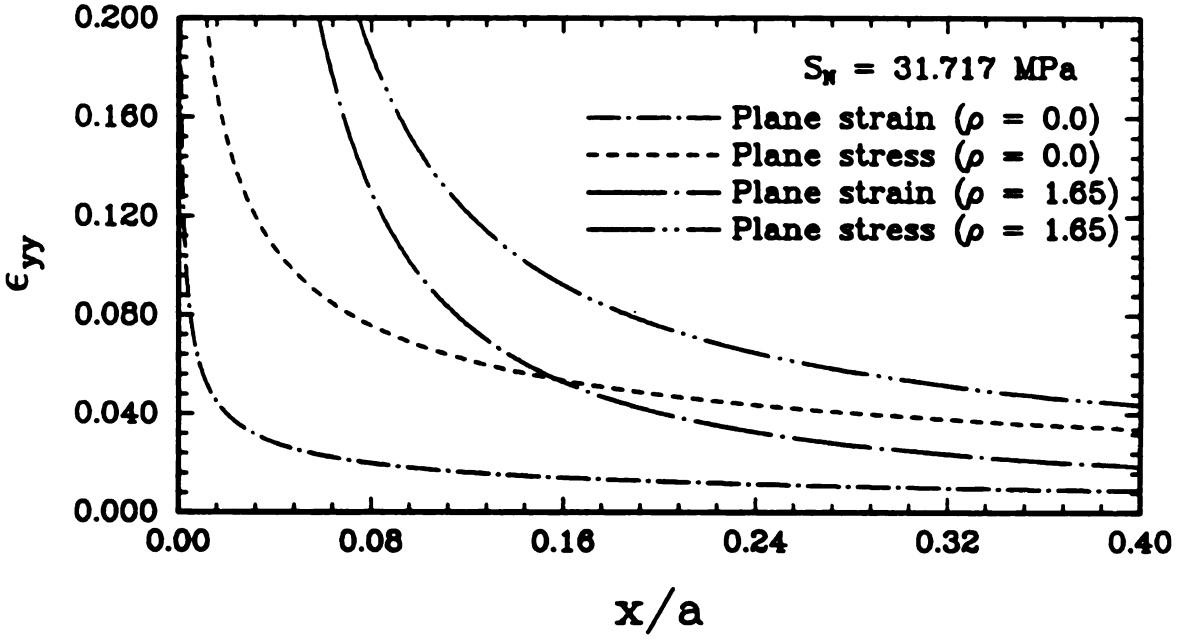

Figure 1.4: Crack opening strain distribution in a CT specimen for a/W = 0.4966 and $\theta = 0°$ based on equation (1.1) and (1.4) for S_N = 31.717 MPa.

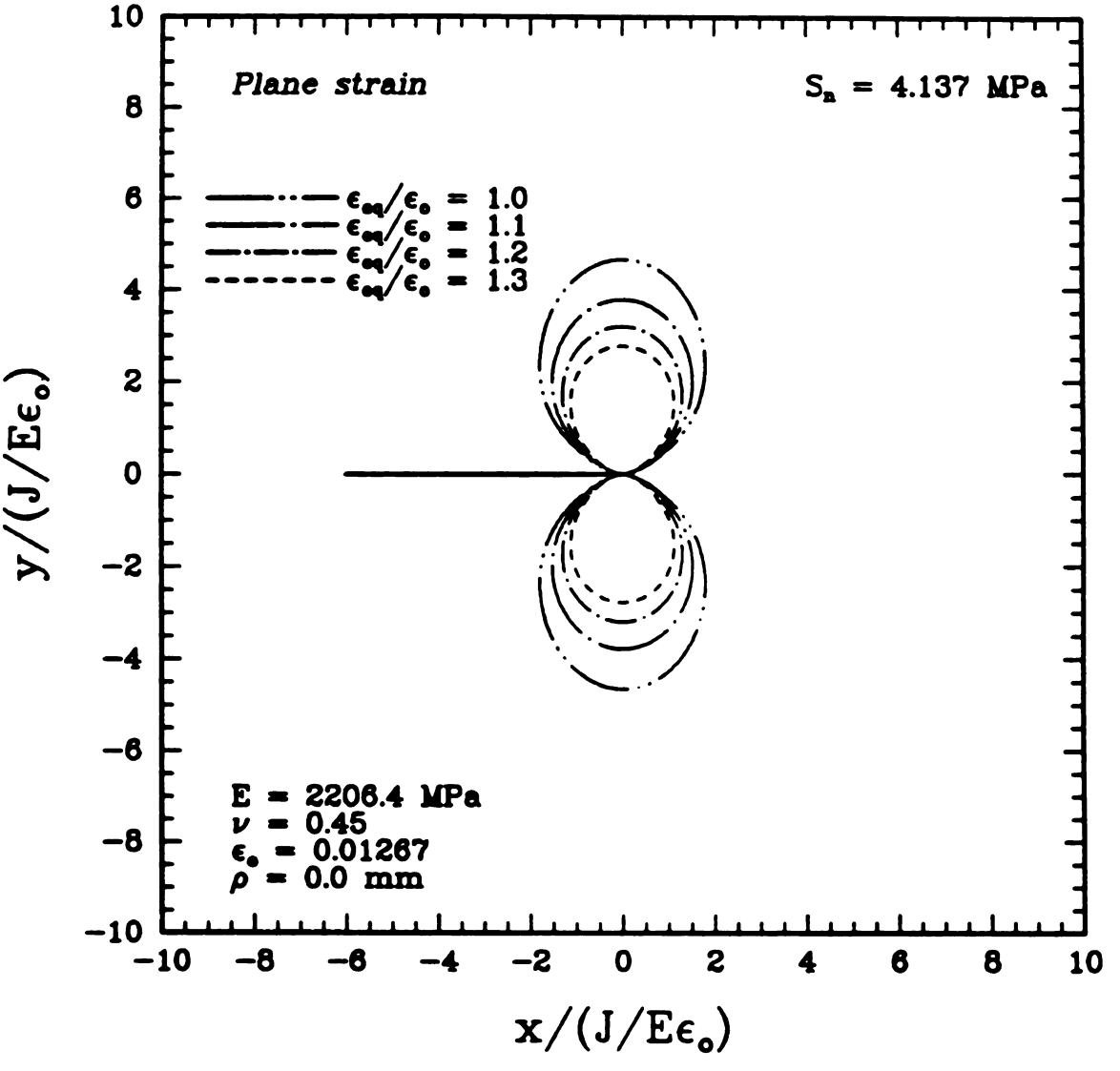

Figure 1.5: Plastic zones in coordinate system, non-dimensionalized with respect to the characteristic length parameter (J/E ϵ_o), based on equation (1.1) and (1.4) for S_N = 4.137 MPa and $\rho = 0$ in plane strain.

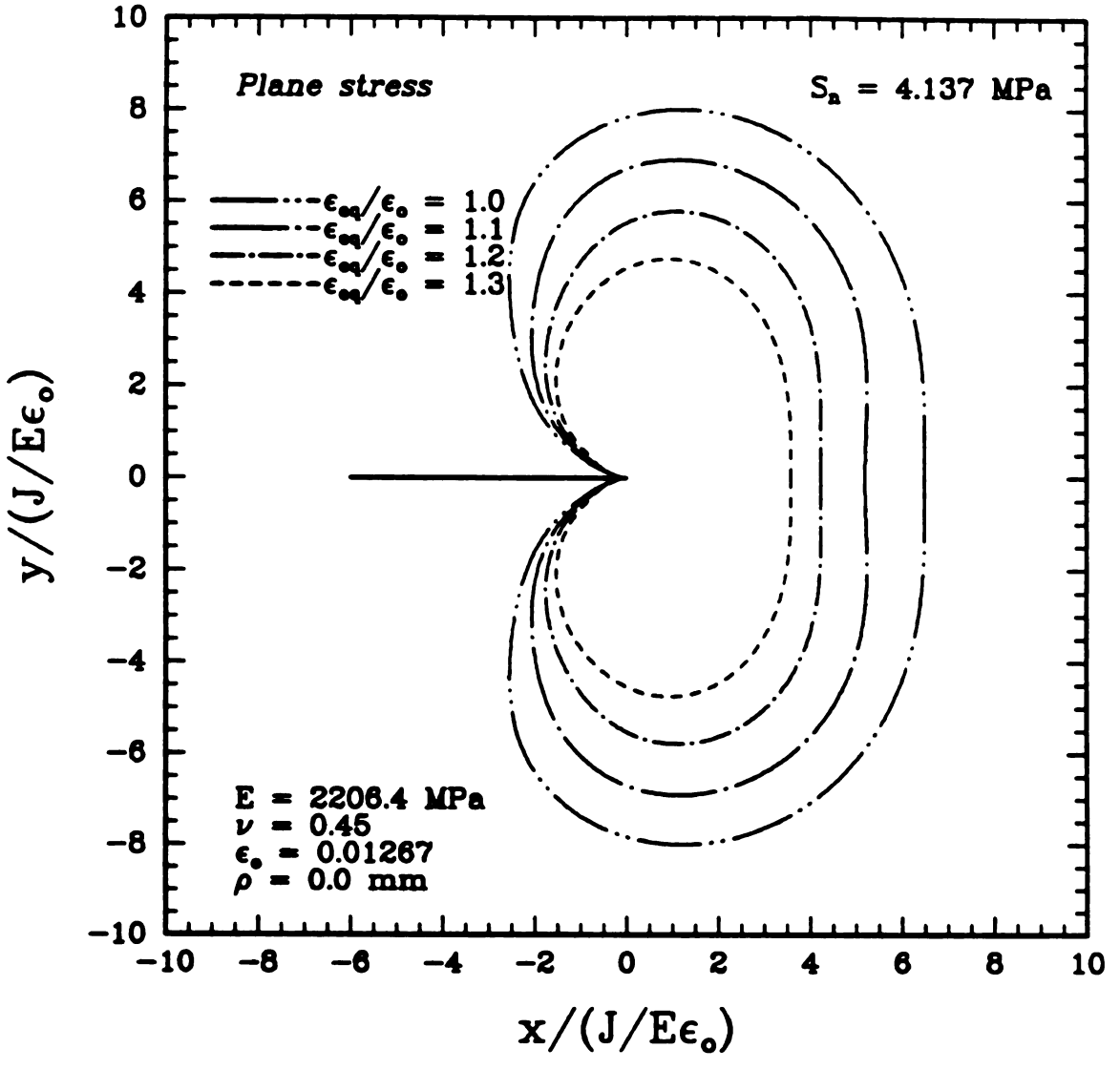

Figure 1.6: Plastic zones in coordinate system, non-dimensionalized with respect to the characteristic length parameter (J/E ϵ_o), based on equation (1.1) and (1.4) for S_N = 4.1371 MPa and $\rho = 0$ in plane stress.

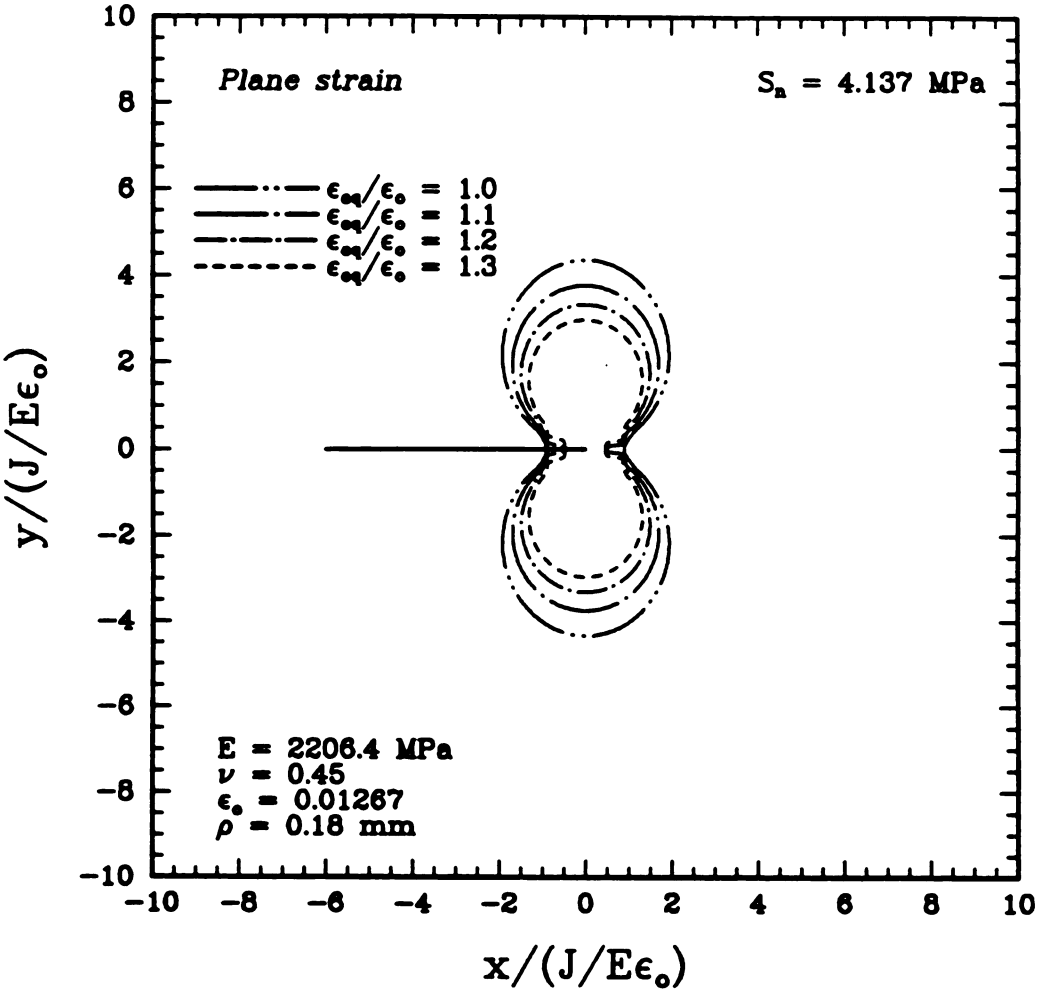

Figure 1.7: Plastic zones in coordinate system, non-dimensionalized with respect to the characteristic length parameter (J/E ϵ_o), based on equation (1.1) and (1.4) for S_N = 4.1371 MPa and ρ = 0.18 mm in plane strain.

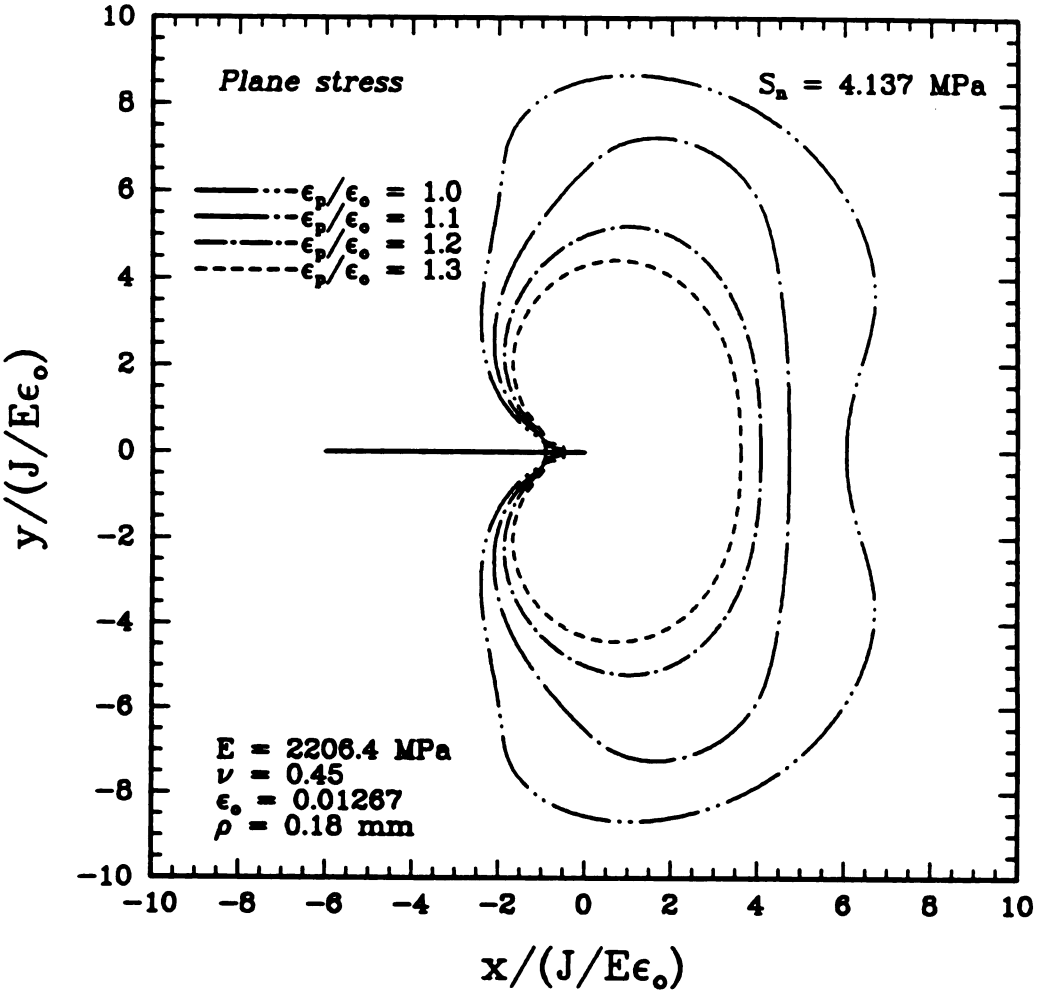

Figure 1.8: Plastic zones in coordinate system, non-dimensionalized with respect to the characteristic length parameter (J/E ϵ_o), based on equation (1.1) and (1.4) for S_N = 4.1371 MPa and ρ = 0.18 mm in plane stress.

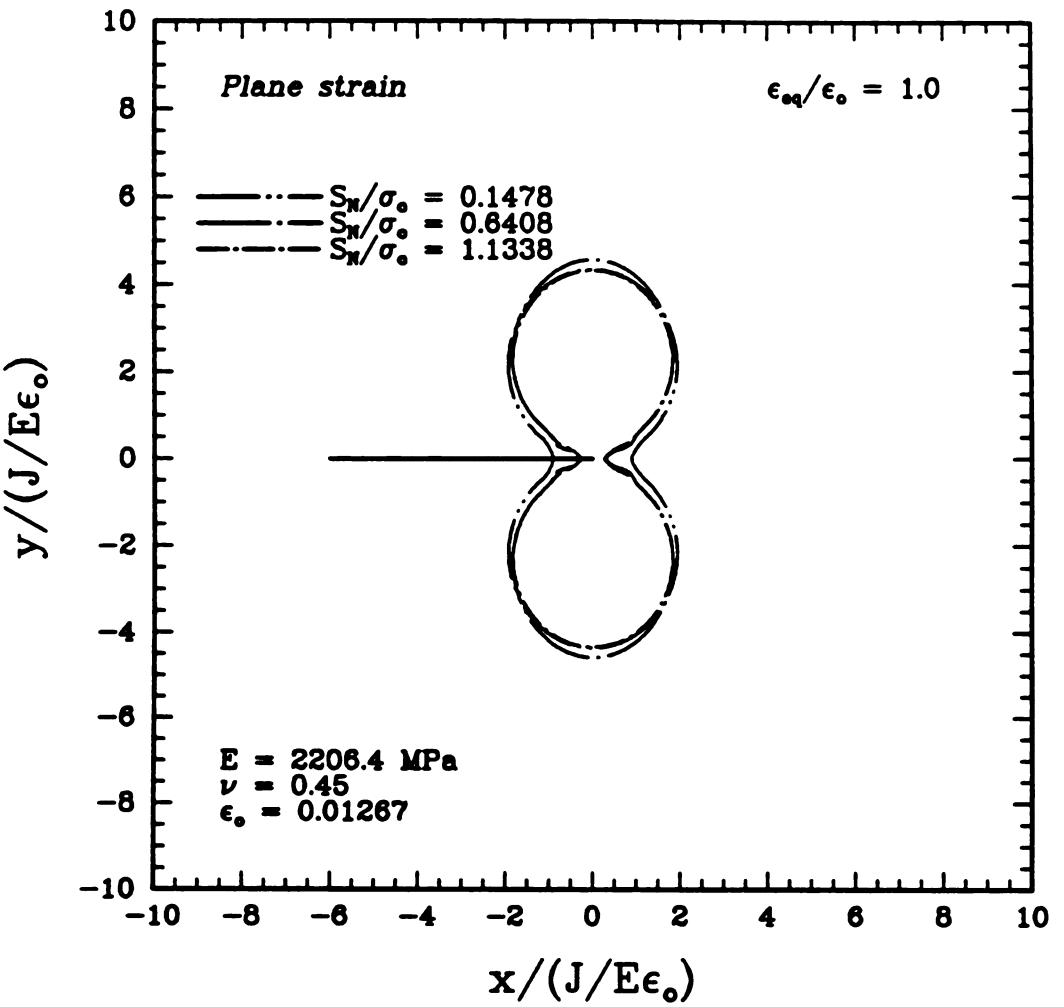

Figure 1.9: Plastic zones in coordinate system, non-dimensionalized with respect to the characteristic length parameter (J/E ϵ_o), based on equation (1.1) and (1.4) for $\frac{S_N}{\sigma_o}$ = 0.1478, 0.6408 and 1.1338 in plane strain.

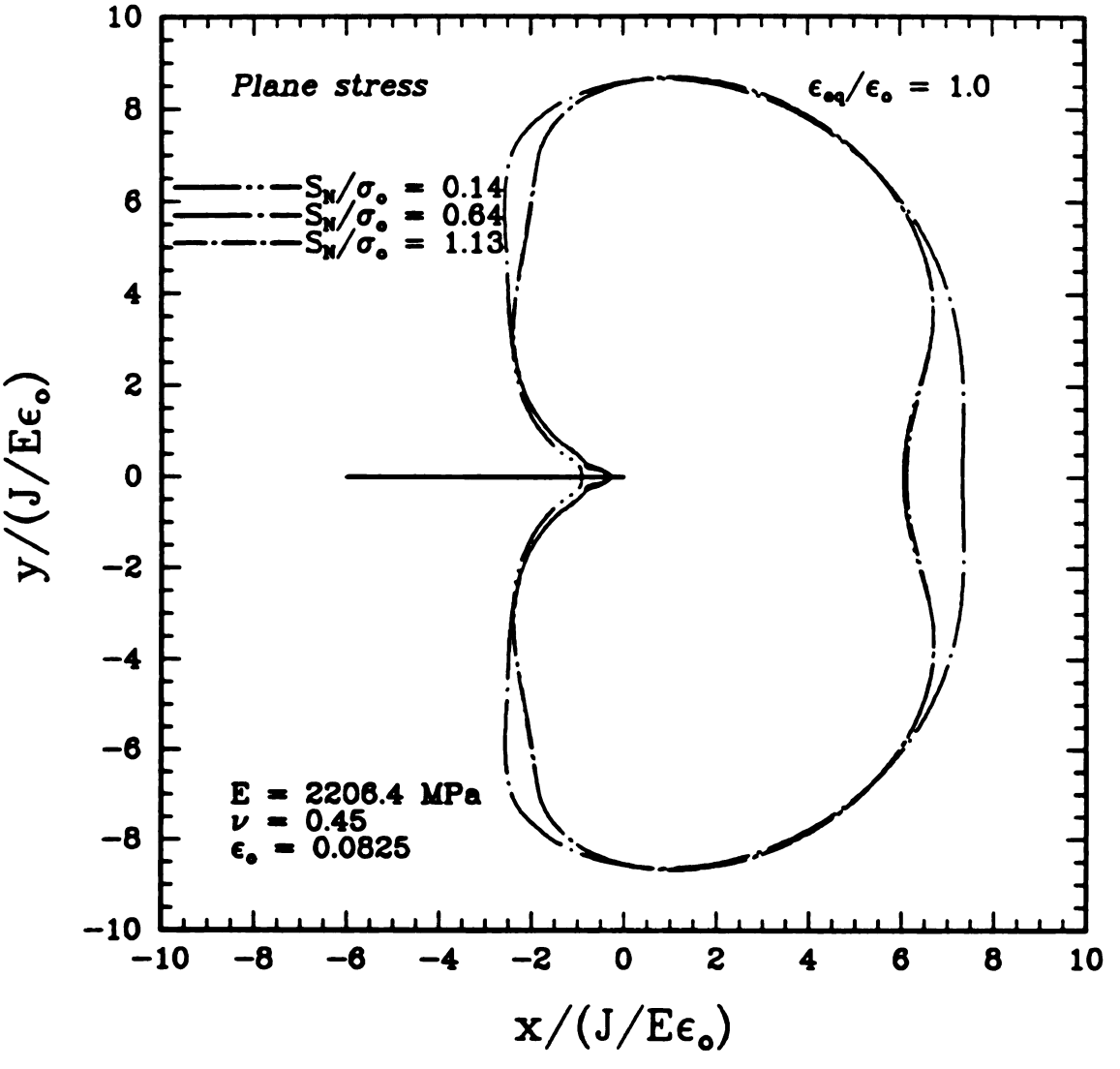

Figure 1.10: Plastic zones in coordinate system, non-dimensionalized with respect to the characteristic length parameter (J/E ϵ_o), based on equation (1.1) and (1.4) for $\frac{S_N}{\sigma_o}$ = 0.1478, 0.6408 and 1.1338 in plane stress.

1.2.3 Non-singular region

The general or far-field stress dominates in this region, and the importance of the stress intensity factor in describing singular or non-singular domains was observed by expanding the stress field around a straight, mathematical sharp crack tip by an infinite series given by William [13].

$$\sigma_{ij} = \frac{A_{ij}}{\sqrt{r}} + B_{ij}(\theta) + C_{ij}(\theta)\sqrt{r} + \cdots \tag{1.11}$$

Equation (1.11) applies for a crack in a symmetrically-loaded plane, and crack faces are assumed to be traction free, such that uniform perpendicular and shear components do not exist. The first term A_{ij} in the expansion is singular and dominates very near to the crack tip where linear elastic fracture mechanics is valid. The asymptotic elastic stress field of a symmetrically loaded mode-1 crack is expressed in the form given by (1.12 - 1.14)* and the corresponding displacement fields in cartesian coordinates for plane strain and plane stress are given by (1.15) and (1.16) respectively.

$$\sigma_{ij} = \frac{K_I}{\sqrt{2\pi r}} cos\frac{\theta}{2} \begin{bmatrix} 1 - sin\frac{\theta}{2}sin\frac{3\theta}{2} \\ 1 + sin\frac{\theta}{2}sin\frac{3\theta}{2} \\ sin\frac{\theta}{2}cos\frac{3\theta}{2} \end{bmatrix} + \begin{bmatrix} \sigma_{ox} \\ 0 \\ 0 \end{bmatrix} \tag{1.12}$$

$$\sigma_{13} = \sigma_{23} = 0 \tag{1.13}$$

$$\sigma_{33} = \begin{cases} 0 & \text{for plane stress} \\ \frac{2\nu cos\left(\frac{\theta}{2}\right)K_I}{\sqrt{2\pi r}} & \text{for plane strain} \end{cases} \tag{1.14}$$

$$\begin{bmatrix} u_1 \\ u_2 \end{bmatrix} = 2(1+\nu)\frac{K_I}{E}\sqrt{\frac{r}{2\pi}} \begin{bmatrix} cos\frac{\theta}{2}(1 - 2\nu + cos^2\frac{\theta}{2}) \\ sin\frac{\theta}{2}(2 - 2\nu - cos^2\frac{\theta}{2}) \end{bmatrix}$$

*same as Irwin [9]

$$+\frac{\sigma_{ox}}{E}r\begin{bmatrix}(1-\nu^2)cos\theta\\-\nu(1+\nu)sin\theta\end{bmatrix} \tag{1.15}$$

$$\begin{bmatrix}u_1\\u_2\end{bmatrix} = 2(1+\nu)\frac{K_I}{E}\sqrt{\frac{r}{2\pi}}\begin{bmatrix}cos\frac{\theta}{2}(1-2\nu+cos^2\frac{\theta}{2})\\sin\frac{\theta}{2}(2-2\nu-cos^2\frac{\theta}{2})\end{bmatrix}$$
$$-\epsilon_{33}\begin{bmatrix}\nu cos\theta\\\nu sin\theta\end{bmatrix}+\frac{\sigma_{ox}}{E}r\begin{bmatrix}(1-\nu^2)cos\theta\\-\nu(1+\nu)sin\theta\end{bmatrix} \tag{1.16}$$

Equation (1.11) gives the exact solution for the region r→0 and can also be used in the area where r is small compared to other geometric dimensions of the problem, such as, for example, crack length "a". A requirement of a maximum allowable K_I such that $K_I < 0.632\sigma_Y\sqrt{a}$ as in ASTM Standard [14], guarantees that the plastic zone size is much smaller than the crack length. The second term B_{ij} in the expansion denotes the transverse, nonsingular T or σ_{ox} stress† The third and other higher terms in (1.11) are zero near the crack tip, but are significant at large r. Finally terms A_{ij} and B_{ij} are the ones which dominate the crack tip process zone. If we know the value of σ_{ox} for a given geometry, than we can perform the same analysis as was done for (1.1) and (1.4). A numerical estimation of the non-singular terms was obtained using FEM and later compared with the photoelastic investigation.

1.2.4 Mixed field region

In this region, the stress distribution is affected by the singularity effect of the crack-tip and also by the effect of far-field stress. The use of (1.11) is justified only if a few more higher order terms are taken into consideration along with the first singular terms.

---

†σ_{ox} was proposed earlier by Irwin [8] and this is measured in stress freezing and in moire technique at 90° to calculate the apparent stress intensity factor. Numerically, T stress is measured at 180°. The T stress acts parallel to the crack flanks, as was later proposed by Rice [15].

1.3 Non-Linear Fracture Mechanics

Nonlinear fracture mechanics is largely concerned with inelastic effects. Some inelasticity is almost always present in the vicinity of a stressed crack tip. Depending on material and conditions, the inelasticity can take various forms, including rate-independent plasticity, creep, and phase change. When the zone of inelasticity is small enough, the solution from linear elasticity can be used to analyze, or, more precisely, to correlate, data from test spcimens. Linear-elastic fracture mechanics has found extensive applications to high-strength, relatively brittle materials. For certain fracture phenomena, such as fatigue crack growth and corrosion cracking, the zone of inelasticity is often small enough to use linear-elastic fracture mechanics. However, the more ductile a material, the more likely it is that the inelastic zone will not be small enough at the point of fracture to justify the use of solutions based on linear elasticity. Under this situation it is essential to use solutions to crack problems based on the theory of plasticity. Nonlinear fracture mechanics encompasses a semiempirical approach, which for the most part is an extension of linear-elastic fracture mechanics. The unifying theoretical idea behind non-linear fracture mechanics, for rate independent materials under monotonic loading, is the J-integral by Rice [16]. A small-strain deformation theory of plasticity (i.e., small-strain, nonlinearly elastic material) is assumed as the material model. The strain energy density of the material is $W(\epsilon)$ with stress given by (1.17), and the path-independent line integral expression for J is given by (1.18).

$$\sigma_{ij} = \frac{\partial W}{\partial \epsilon_{ij}} \tag{1.17}$$

$$J = \int_s (W n_1 - \sigma_{ij} n_j u_{i,1})\, ds \tag{1.18}$$

where u is the displacement vector, s is the arc length along the contour, and n is the outward unit normal to any counter Γ encircling the tip of the crack in a contour clockwise direction. The important role of J is in the measurement of the intensity of the near-tip deformation which has $\frac{1}{r}$ singularity. This suggests an intimate relation between J and the near-tip deformation. A more explicit connection is revealed if a power-law relation between the stress and strain is assumed. A widely used uniaxial

stress-strain relation is the Ramberg-Osgood form:

$$\frac{\epsilon}{\epsilon_o} = \frac{\sigma}{\sigma_o} + \alpha \left(\frac{\sigma}{\sigma_o}\right)^n \text{for } \sigma \geq \sigma_o \tag{1.19}$$

where σ_o is an effective yield stress, ϵ_o is the associated elastic strain with E as the Young's modulus, and α and n are the parameters chosen to fit the data. Asymptotically, as the crack tip is approached, the contribution to the strain components that depend linearly on stress components are negligible compared to the power-law terms. The power law relation from (1.19) is

$$\frac{\epsilon}{\epsilon_o} = \alpha \left(\frac{\sigma}{\sigma_o}\right)^n \text{for } \sigma \geq \sigma_o \tag{1.20}$$

If J_2 deformation theory [17] is used to extend (1.20) to multiaxial states, then

$$\frac{\epsilon}{\epsilon_o} = 1.5\alpha \left(\frac{\sigma}{\sigma_o}\right)^{n-1} \frac{S_{ij}}{\sigma_{ij}} \text{for } \sigma \geq \sigma_o \tag{1.21}$$

$$\epsilon_e = \sqrt{1.5 S_{ij} S_{ij}} \tag{1.22}$$

where S_{ij} is the stress deviator. For a power-law material, the $\frac{1}{r}$ singularity in W implies a $r^{\frac{-1}{n+1}}$ singularity in the stresses, a $r^{\frac{-n}{n+1}}$ singularity in the strain, and $r^{\frac{1}{n+1}}$ variations in the displacements. In the vicinity of the crack tip the elastic strain components are negligible as compared with the plastic strains. The plastic part of the strain dominates the asymptotic solution. The asymptotic crack tip stress, strain and displacement fields are given by (1.23 - 1.25), which were derived by Hutchinson [17], Rice [16] and Rice and Rosengreen [18].

$$\sigma_{ij} = \sigma_o \left[\frac{J}{\alpha \sigma_o \epsilon_o I_n r}\right]^n \tilde{\sigma_{ij}}(\theta, n) \tag{1.23}$$

$$\epsilon_{ij} = \alpha \epsilon_o \left[\frac{J}{\alpha \sigma_o \epsilon_o I_n r}\right]^{\frac{n}{n+1}} \tilde{\epsilon_{ij}}(\theta, n) \tag{1.24}$$

$$u_i = \alpha\epsilon_o r \left[\frac{J}{\alpha\sigma_o\epsilon_o I_n r}\right]^{\frac{n}{n+1}} \tilde{u}_i(\theta, n) \tag{1.25}$$

Here the dimensionless constant I_n and θ-variation of the dimensionless function $\tilde{\sigma_{ij}}$, $\tilde{\epsilon_{ij}}$ and $\tilde{u_i}$ depend not only on n, but also on the symmetry of the fields with respect to the crack plane, and whether plane strain or plane stress conditions prevail in the vicinity of the crack tip. These variations are normalized by setting the maximum value of the θ variations of the effective stress, $\tilde{\sigma_e} = [\frac{3}{2}\tilde{S_{ij}}\tilde{S_{ij}}]^{\frac{1}{2}}$, to unity where $\tilde{S_{ij}} = \tilde{\sigma_{ij}} - (\frac{\tilde{\sigma_{kk}}}{3})\delta_{ij}$. With this normalization, the numerical quantities I_n assume definite values. All the quantities in (1.23 - 1.25) have been defined by Shih [19] and are listed in Table 1.1 for plane strain only. The contribution of u allows for a possible translation of the crack itself. There are two conditions to be met in problems where the J-integral can be used. First, the deformation theory of plasticity must be an adequate model of the small-strain behavior of real elastic-plastic materials under the monotonic loads being considered. Second, the regions in which finite strain effects are important and in which the microscopic processes occur must each be contained well within the region of the small-strain solution dominated by the singularity fields. This latter condition is sometimes called J-dominance and is analogous to the small-scale yielding for the yielding requirements in linear fracture mechanics‡

It was shown by Hutchinson [17], Walker [20] and Schijve [21] for sharp cracks that, in the case of localized plastic yielding, the energy density distribution in the plastic zone is almost the same as in a linear elastic material. This means that, in the presence of localized small-scale plastic yielding, the gross linear elastic behavior of the material surrounding the notch also controls the deformations in the plastic zone. It follows that the complementary energy density in the plastic zone is equal to that calculated on the basis of the elastic solution. Some investigators, including Molski and Glinka [22] and Glinka [23], have assumed that this conclusion was true for notches and materials exhibiting non-linear stress-strain behavior. The first step involves finding local stress and strain at the notch root, from which the crack initiation can be predicted. The most popular and frequently used formulae in notch analysis are Neuber's rule [7]; the modified version of Hardrath and Ohman [24]; and Stowell's [25] approximate formula. Based on energy considerations, elastic-plastic notch strain (stress) analysis

‡ $J = \frac{(1-\nu^2)}{E} K_I^2$ in plane strain and $J = \frac{K_I^2}{E}$ in plane stress

Table 1.1. Table of Hutchinson, Rosengreen and Rice as presented by Shih [19].

n	I_n	$\tilde{\sigma}_{e(\theta=0°)}$	$\tilde{\sigma}_{rr(\theta=0°)}$	$\tilde{\sigma}_{\theta\theta(\theta=0°)}$	$\tilde{\epsilon}_{rr(\theta=0°)}$	$\tilde{\epsilon}_{\theta\theta(\theta=0°)}$
5	5.02	0.4621	1.6836	2.2172	-0.0183	0.0183
10	4.54	0.6691	1.7243	2.4969	-0.0156	0.0156

has been developed [22,23]. It has been shown by Hult and McClintock [26] that the elastic stress distribution near different notches are similar to each other and can be satisfactorily characterized by two parameters: the notch radius and the stress concentration factor K_T. The stress state at the crack tip is reduced to uniaxial stress in the case of plane stress and to biaxial stress in the case of plane strain. The avilability of linear or non-linear elastic notch stress-strain solutions enables us to calculate the energy distribution ahead of a sharp or blunted crack tip. Subsequently, the energy density can be translated into the elastic-plastic strains and stresses which actually exist at the crack tip. Hence it is necessary to know the non-linear stress-strain curve of the analyzed material. The way in which the non-linear stresses and strains are computed is very important.

1.4 Experimental Techniques

Experiment methods are available for studing elasto-plastic problems in three dimensional cracked structures. Hybrid methods are well known for studying such problems. Three-dimensional photoelasticity data was used by Barispolsky [27] in solving the elasticity problem. Balas, Sladek and Drzik [28] have used holography with the boundary element method. Laser speckle photography was combined with the finite element method to study stresses in a compressed disk by Weathers, Foster, Swinson and Turner [29]. Kannien et.al. [30] and Shih et.al. [31] have used experimentally obtained load-time-displacement data [30] in a finite element model, and then they simulated the field parameters ahead of a growing crack in a hardening material. The applicabilty of a hybrid scheme for differentiating experimental data for determining full field strain distributions has been demonstrated by Segalman [32]. A review on

the progress of the above techniques useful in dynamic fracture study was prepared by Kobayashi [33]. Recently Hareesh and Chiang [34] have demonstrated a hybrid method for studying elastic-plastic displacement and strain fields around a crack tip using moire technique in conjuction with the finite element method. There are many other references in this area which will be mentioned in chapter 5.

CHAPTER 2

MATERIALS SPECIFICATION

2.1 Application and General Properties

Polycarbonate has been used for the past two decades where reliability and higher performance is needed in adverse conditions. Some critical applications are: aircraft wind shields, pipe lines, pump impellers, cams and gears, truck wheel oil seals, football helmets etc. The combination of high strength and rigidy with toughness under impact loading or in low temperature environment is important, because this is obtained without the addition of toughening constituents or impact modifiers. Owing to increased usage of polymers in structural components, a great deal of attention in recent years has been focused towards modern adhesives. Bonded joints tend to be damage-tolerant because of the high damping behavior of the adhesive layer. Polycarbonate has time dependent properties and it suffers delayed failure. It shows an elastic-plastic tensile instability point or Luders band formation studied by Brinson [35,36]. For a constant stress input, a variety of stress distributions and interactions will be developed in the adherend and adhesive layer. A simple delayed failure, delamination, or rupture at an isolated point will not cause the joint or structure to cease transmitting load from one adherand to the other. But a failure at one point will cause a step increase in stress at the next point with a corresponding change in failure or rupture time.

2.1.1 Material stress and strain curve

Mechanical testing was conducted at room temperature, 25°C, and relative humidity 65 % in a 100kN closed loop servo hydraulic materials testing system. An MTS 1.0 inch extensometer capable of measuring strains up to 15 % was calibrated to 0.1 inch full scale deformation. The sensitivity was better than $\pm 10\ \mu\ \frac{inch}{inch}$. Load was measured with an accuracy of 0.3 % and with a precision of 0.01 lbs. Strain-time and load-time data were digitized and stored on an IBM PC. Data were sampled and stored in the hard disc. Analog signals proportional to load and displacement were recorded using X-Y recorders. The uniaxial tensile tests were conducted in displacement control mode as opposed to strain control because of the high elongation expected. Displacement rate was kept at 5 % per minute. Figure 2.1 represents the true stress-strain curves belonging to polycarbonate. The polycarbonate true stress-strain reponses are in agreement with those reported by an Engineering Handbook [37]. The experimental true stress and strain data are listed in Table 2.1, which will be used later for elastic-plastic analysis at the crack tip using incremental plasticity theory.

The fracture behavior can be explained as follows. During the elastic loading, molecular bonds along the polymer chain are stretched and secondary bonds may be broken to accomodate the imposed elastic strains. At yielding, however, large scale molecular motion takes place, resulting in permanent deformation. Amorphous polycarbonate (LEXAN) is more suceptible to large scale molecular motion in the form of cavitation because there are a high number of heterogeneous nucleation sites provided by the particles. Crystalline polycarbonate, on the other hand, has no preferred sites for the nucleation of cavities. Thus, for large scale molecular motion to take place, molecular entanglement must be broken, requiring a higher stress for initiating the yield stress. In Figure 2.1 the Lexan showed nonlinear behavior, indicating that it does not obey the power law commonly observed for metals. After the yield, there is a sudden drop in the stress, which is then followed by its steady rise with further straining until failure occurs. Such materials behavior is classified as linear or nonlinear elastic regions followed by strain-softening, yielding and neck formation, propagation and further deformation to failure. The yielded region is represented by a plateau.

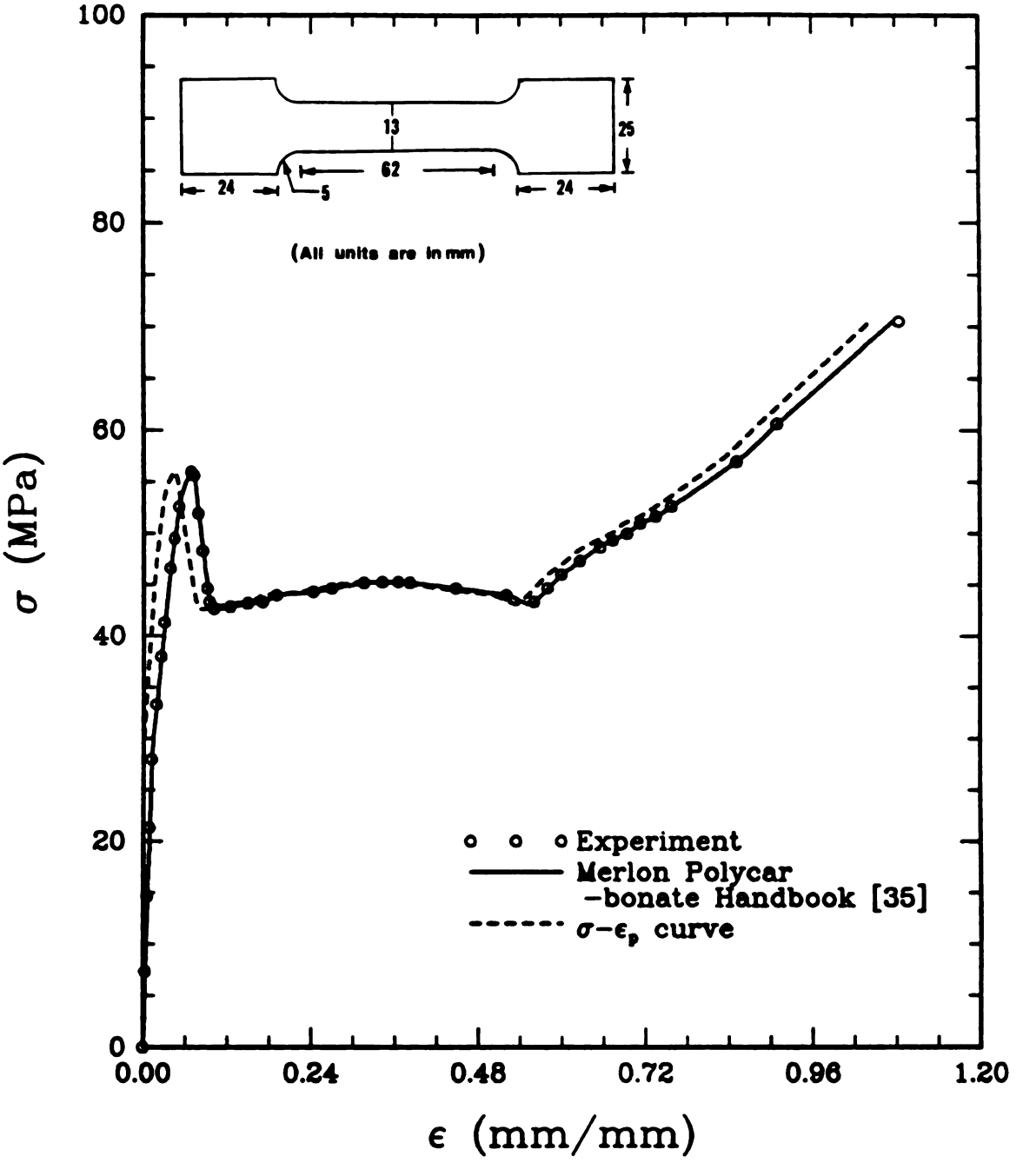

Figure 2.1: True stress-strain curve for polycarbonate.

Table 2.1: Polycarbonate true stress and strain experimental data.

strain(mm/mm)	stress (MPa)	strain(mm/mm)	stress (MPa)
0.0000000E+00	0.0000000E+00	3.4267700E-01	4.5221000E+01
3.3203400E-03	7.3260000E+00	3.1627700E-01	4.5154000E+01
6.6406000E-03	1.4652000E+01	2.7007700E-01	4.4622000E+01
9.6590000E-03	2.1312000E+01	2.4367700E-01	4.4289000E+01
1.2677000E-02	2.7972000E+01	3.6247700E-01	4.5223000E+01
1.9277000E-02	3.3300000E+01	3.8227700E-01	4.5154000E+01
2.5877000E-02	3.7962000E+01	4.4827700E-01	4.4622000E+01
3.0777000E-02	4.1292000E+01	5.2087700E-01	4.3956000E+01
3.9077000E-02	4.6620000E+01	5.6047700E-01	4.3290000E+01
4.4677000E-02	4.9483000E+01	5.8027700E-01	4.4622000E+01
5.1577000E-02	5.2614000E+01	6.0007700E-01	4.5954000E+01
6.8777000E-02	5.5944000E+01	6.2647700E-01	4.7286000E+01
7.3077000E-02	5.5611000E+01	6.5287700E-01	4.8618000E+01
7.8677000E-02	5.1948000E+01	6.7267700E-01	4.9284000E+01
8.5277000E-02	4.8285000E+01	6.9247700E-01	4.9950000E+01
9.1877000E-02	4.4622000E+01	7.1227700E-01	5.0949000E+01
9.5177000E-02	4.3290000E+01	7.3537700E-01	5.1615000E+01
1.0177700E-01	4.2624000E+01	7.5847700E-01	5.2614000E+01
1.2487700E-01	4.2823000E+01	8.5087700E-01	5.6943000E+01
1.4987700E-01	4.3156000E+01	9.1027700E-01	6.0606000E+01
1.7107700E-01	4.3290000E+01	1.0752770E+00	7.0509000E+01
1.9087700E-01	4.3956000E+01		

2.1.2 Tensile load-elongation curves for CT specimen

Strain gages were used to measure local strain in CT specimen. Strain gages were bonded very near to the notch tip of each specimen. Two such specimens were then bonded using epoxy resin in such a way that local strain could be measured in the mid-plane as well as in the surface plane. Local stress and strain plots at the notch tip are shown in Figure 2.2. Material true stress -strain curve obtained from tensile testing up to 2 % strain is superimposed. Under slow tensile loading, a sharply notched specimen fails in a brittle manner, and a bluntly notched specimen fails in a ductile manner. Amorphous polycarbonate, therefore, affects the ductile-brittle transition of the fracture mode by varying the notch geometry and also the thickness. More experimental evidence of fracture in amorphous polycarbonate and the limiting condition for the transition of fracture mode from ductile to brittle is shown in Figures 2.3 and 2.4, which were taken from Nisitani [38]. In Figure 2.3 at point A, the shear bands are visible inside the specimen; and the plastic zone is made up of many fine individual shear bands as shown in Figure 2.4 (a).

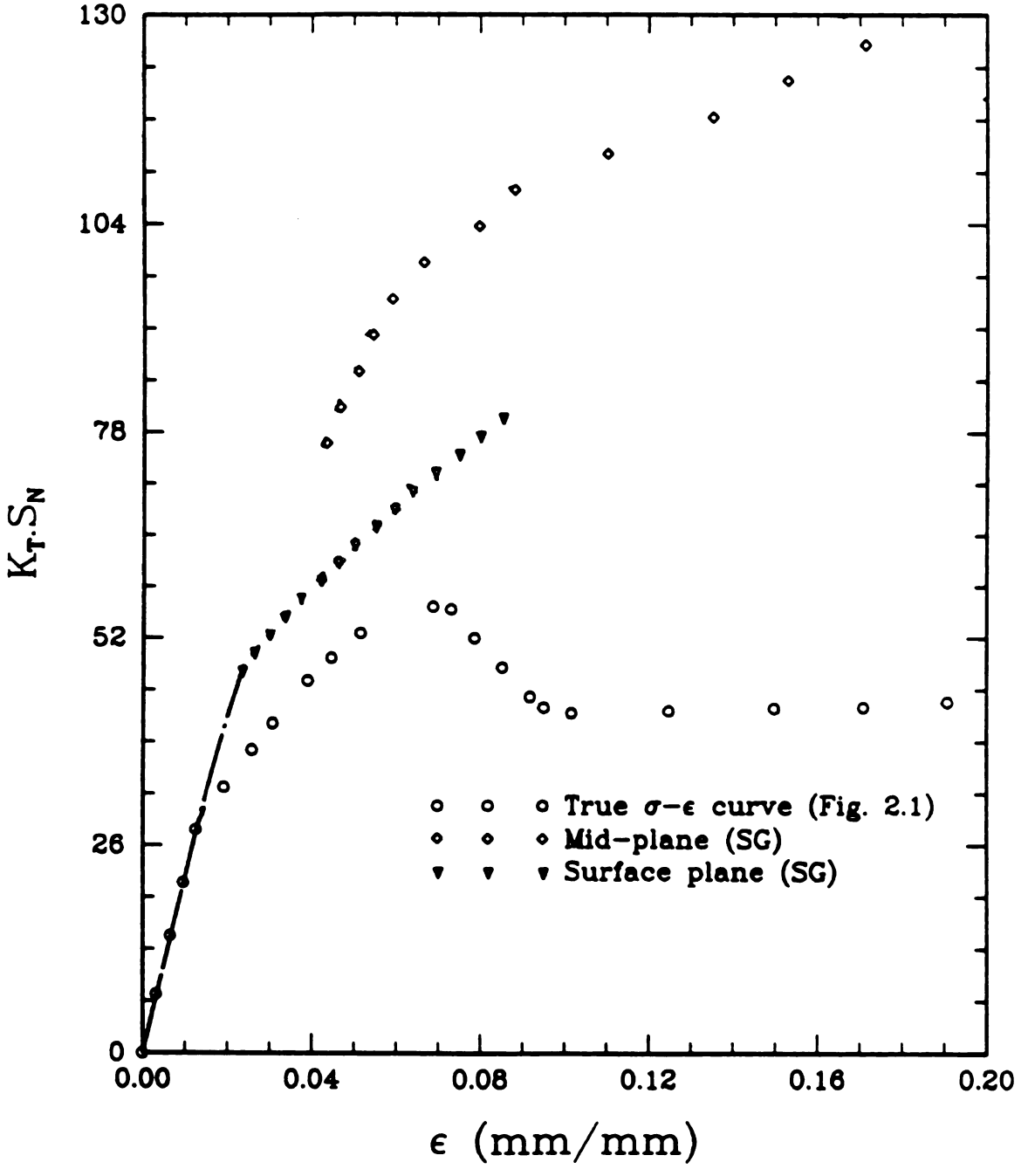

Figure 2.2. Experimental notch strains in a sharp notched compact tension specimen made out of polycarbonate.

At point B, the plastic zone size expands to about the size of the notch root radius of the specimen, and then a small crack is nucleated at the tip of the plastic zone as shown in Figure 2.4 (b). However, for B, the crack nucleated inside the specimen and shear bands are formed on the surface as shown in Figure 2.4 (c). A bluntly notched specimen failed in a ductile manner with large shear bands. The plastic zone at point D in Figure 2.3 is shown in Figure 2.4 (d). At E in Figure 2.3, the plastic zone is as large as the size of the notch root radius of the specimen. The process in which the plastic zone expands to the size of the notch root radius is similar to that of the sharply notched specimen. It was also reported by Nisitani [38] that with a notch root radius $\rho = 0.2$ mm, all the specimens of 1 mm thickness failed in a ductile manner and all specimens of 2 mm thickness failed in a brittle manner. With $\rho = 0.5$ mm, all the specimens of 5 mm thickness failed in a brittle manner, independent of notch depth, c. The general conclusion is that the mode of failure depends on the notch root radius and the thickness in amorphous polycarbonate.

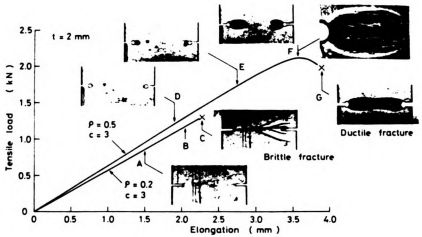

Figure 2.3. Tensile load-elongation curve for two different specimens of 2mm thickness. The sharply notched fails in a brittle manner and bluntly notched specimen fails in a ductile manner [38].

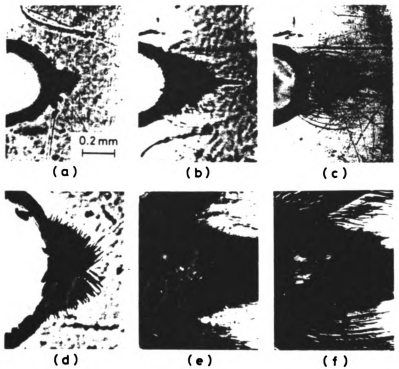

Figure 2.4. Optical micrograph near root of the specimen in Figure 2.2: (a) internal plastic zone at point A; (b) internal small crack at the tip of plastic zone at B; (c) surface shear bands at point B; (d) internal plastic zone at point D; (e) internal plastic zone at point E; (f) surface shear bands at point E [38].

CHAPTER 3

STRAIN ENERGY DENSITY APPROACH

3.1 The Continuum Mechanics Model

The continuum mechanics model for a notched body is based on only equilibrium equations, strain displacement relations and boundary conditions, without using any constitutive equation, as mentioned in the introduction.

Consider a notched body of linear or nonlinear elastic material such as in Figure 3.1a, free of body force, but subjected to a slowly increasing surface force on the portion Ω_T of the boundary. Suppose that the maximum applied force on the boundary Ω_T is denoted by traction T_i, the stresses denoted by σ_{ij} are in equilibrium within the body, i.e., $\sigma_{ij} = 0$; $\sigma_{ij} = \sigma_{ji}$ (i, j = 1,2,3), and thus satisfy boundary conditions on Ω_T and on the notch surface Γ_T. On the boundary surface Ω_T, $\sigma_{ij}n_j = T_i$, and on the notch surface Γ_T, $\sigma_{ij}n_j = 0$, where n_j is the unit vector normal to the surface boundary and directed towards the exterior of the body. The infinitesimal strain tensor is defined by $\epsilon_{ij} = u_{ij,j}$. Once the stress and strain tensors σ_{ij} and ϵ_{ij} are known, the strain energy density per unit volume is given by;

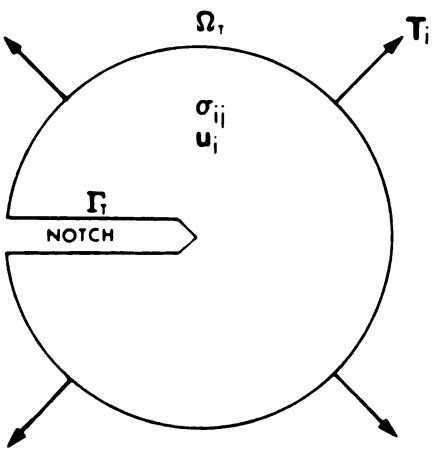

(a)

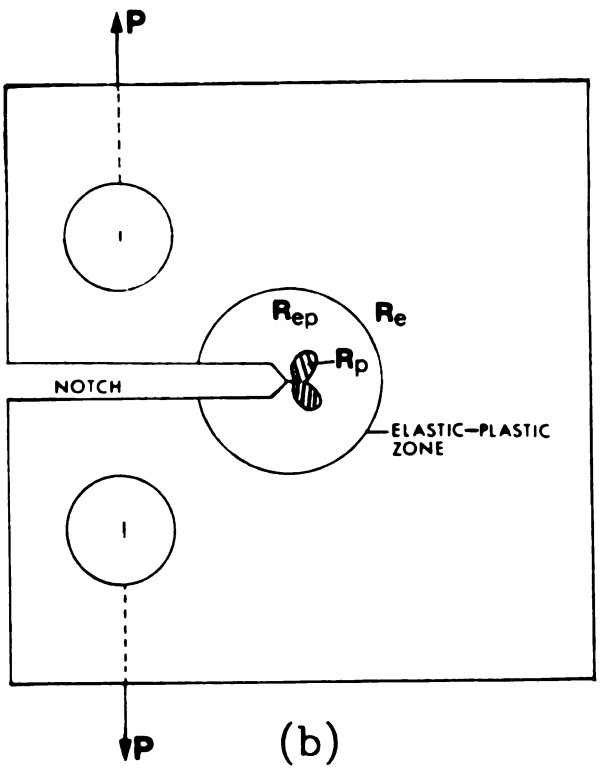

(b)

Figure 3.1: Schematics of notched body extending to a cracked geometry; (a) A smooth sharp notched body and (b) A sharp pre-cracked compact tension specimen.

$$\int_V (\sigma_{ij}\epsilon_{ij})\,dV = \int_V (\sigma_{ij}u_i)_{,j}\,dV \tag{3.1}$$

$$\int_V (\sigma_{ij}\epsilon_{ij})\,dV = \int_V (\sigma_{ij,j}u_i + \sigma_{ij}u_{i,j})\,dV \tag{3.2}$$

$$\int_V (\sigma_{ij}\epsilon_{ij})\,dV = \int_V (\sigma_{ij}u_{i,j})\,dV \tag{3.3}$$

$$\int_V (\sigma_{ij}\epsilon_{ij})\,dV = \int_S (T_i u_i)\,dS \tag{3.4}$$

The term $\sigma_{ij,j}u_{ij}$ is zero from the equilibrium condition. Consider now a compact tension specimen of elastic-plastic material with a notch as shown in Figure 3.1b loaded remotely by load P, which causes yielding of the material in a zone defined by R_p near the crack tip. Near the crack tip, we have an inelastic region, a singular region, a mixed-mode region, and a non-singular region. In the singular region, stress distribution is best described by (1.4). In the mixed-mode region, stress distribution is affected by both the singularity of the crack tip and the far field stress. In the inelastic region, the crack tip may not be in the elastic state and the tip may become blunt due to local plastic yielding, which invalidates (1.4). In small scale yielding, when the plastic region dimensions R_p are negligible compared with specimen geometric dimensions, the surrounding elastic singularities set the boundary conditions on the elastic-plastic boundary value problem. That is to say, the plastically yielding material can be described by the surrounding stress field through the inverse square root term in the elastic solution. This stress field is approached by the elastic-plastic solution at a distance which is large compared with the plastic zone size but still small compared with the other geometric dimensions. Thus, the stress field under the small-scale yielding solution for any loading may be obtained by considering a semi-infinite crack, with the assymptotic boundary conditions given by (1.12). If $R_e \geq R_p$ is satisfied, then from (3.4) traction, $T_i = \sigma_{ij}n_j = \sigma_{ij(ne)}n_j$; and displacement vector, $u_i = u_{i(ne)}$. In small scale yielding the total strain energy is the sum of strain energy caused by elastic-plastic strain $W(\epsilon)_{ep}$ and complementary strain energy density caused by elastic-plastic stresses $W(\sigma)_{ep}$. It is given as;

$$\int_V (\sigma_{ij}\epsilon_{ij}dV) = \int_V [d(\sigma_{ij}\epsilon_{ij})]\, dV \tag{3.5}$$

$$\int_V (\sigma_{ij}\epsilon_{ij})\, dV = \int_V (\sigma_{ij}d\epsilon_{ij})\, dV + \int_V (\epsilon_{ij}d\sigma_{ij})\, dV \tag{3.6}$$

$$\int_V (\sigma_{ij}\epsilon_{ij})\, dV = W(\epsilon)_{ep} + W(\sigma)_{ep} \tag{3.7}$$

Equation (3.7) holds good for proportional loading, where it can be assumed that the plastic flow occurs in the direction of the deviatoric stress minus the back stress for forward loading. Now taking,

$$\sigma_{ne} = \sqrt{1.5 D_{ij} D_{ij}} \tag{3.8}$$

$$D_{ij} = \sigma_{ij} - \frac{\sigma_{kk}\delta_{ij}}{3} \tag{3.9}$$

$$\epsilon_{ne} = \sqrt{\frac{2\epsilon_{ij}\epsilon_{ij}}{3}} \tag{3.10}$$

3.1.1 Elastic-plastic stress and strain at the notch tip

The elastic strain energy density at the blunt notch tip $W(\epsilon)_{ne}$ can be calculated;

$$W(\epsilon)_{ne} = \int_0^{\epsilon_{ij}} \sigma_{ij}d\epsilon_{ij} = \frac{1}{2}(\sigma_{ne}\epsilon_{ne}) = \frac{\sigma_{ne}^2}{2E} \tag{3.11}$$

In the case of elastic material behavior, the local stress at the notch tip in plane stress is given by (3.12 - 3.13).

$$\sigma_{yy} = \sigma_{ne} = S_n K_T \tag{3.12}$$

$$\sigma_{xx} = \sigma_{zz} = 0 \tag{3.13}$$

For plane strain the stress is given by (3.14 - 3.16). From (3.11),(3.12) and (3.14) we obtain (3.17).

$$\sigma_{yy} = \sigma_{ne} = S_n K_T \tag{3.14}$$

$$\sigma_{xx} = 0 \tag{3.15}$$

$$\sigma_{zz} = \nu \sigma_{ne} \tag{3.16}$$

$$W(\epsilon)_{ne} = \frac{(S_n K_T)^2}{2E} \tag{3.17}$$

The strain energy density at the notch tip created by nominal stress S_n is $W_n = S_n^2/2E$. Finally, the relation between the strain energy density at the notch tip caused by σ_{ne} and strain energy density caused by the nominal stress S_n is $W(\epsilon)_{ne} = W_n K_T$. It was shown for cracks by Hutchinson [17] and Hult and McClintock [26] that, in the case of localized plastic yielding, the energy density distribution in the plastic zone is almost the same as in the linear elastic material. This means that in the presence of localized small scale plastic yielding, the gross linear elastic behavior of the material surrounding the notch also controls the deformation in the plastic zone. The strain energy in the plastic zone $W(\epsilon)_{np}$ is given as;

$$W(\epsilon)_{np} = W(\epsilon)_{ne} = W_n K_T^2 \tag{3.18}$$

It is known from Glinka [23] that the stress state in the plane stress condition is reduced to uniaxial stress, and that in the plane strain condition the stress state is reduced to biaxial. It is apparent that in the plane stress condition a uniaxial stress state exists at the notch tip, and therefore uniaxial stress-strain relations can be used. A basic assumption made in the development of stress-strain relations for elastic-

plastic material is that, for each load increment, the corresponding strain increment can be decomposed into elastic and plastic components. The strain energy density $W(\epsilon)_{ep}$ is simply given by;

$$W(\epsilon)_{ep} = \int \sigma_{ij} \left(d\epsilon_{ij(ne)} + d\epsilon_{ij(np)} \right) \tag{3.19}$$

$$W(\epsilon)_{ep} = W(\epsilon)_{ne} + W(\epsilon)_{np} \tag{3.20}$$

Now, if the material shows elastic behavior at the crack tip, the elastic strain at the notch tip ϵ_{ne} is given by (3.21).

$$\epsilon_{ne} = \sigma_{ne} E \tag{3.21}$$

In actuality, at the crack tip the material shows elastic-plastic behavior inside region R_{ep}, and the corrsponding elastic-plastic strain ϵ_{ep} is given by Raske and Morrow Dean Jo [39] and ASTM Standard [40] as the exponential rule in (3.22).

$$\epsilon_{ep} = \frac{\sigma_{ep}}{E} + \left(\frac{\sigma_{ep}}{K} \right)^{\frac{1}{n}} \tag{3.22}$$

Energy density at the notch tip may be calculated on the basis of a non-linear stress-strain curve by the Ramberg-Osgood relationship.

$$W(\epsilon)_{ep} = \int_0^{\epsilon_{ij}} \sigma_{ij} d\epsilon_{ij} = \frac{\sigma_{ep}^2}{E} + \left(\frac{\sigma_{ep}}{n+1} \right) \left(\frac{\sigma_{ep}}{K} \right)^{\frac{1}{n}} \tag{3.23}$$

The first term in the right hand side of the above equation shows the elasticity behavior, and the second term shows the plasticity behavior. In fact, when dealing with the plastic zone, assuming small scale yielding such that $R_e >> R_p$, it is possible to write from (3.23);

$$W(\epsilon)_{ep} = \left(\frac{1}{n+1} \right) \sigma_{ep} \epsilon_{ep} \tag{3.24}$$

$$W(\sigma_{ep}) = nW(\epsilon)_{ep} \tag{3.25}$$

On the boundary of the elastic-plastic regime shown in Figure 3.1b, when $R_e >> R_p$

$$\int_V \sigma_{ij}\epsilon_{ij}dV = \int_V \sigma_{ne}\epsilon_{ne}dV \tag{3.26}$$

From (3.20), (3.24) and (3.26) on the boundary R_e for small scale yielding,

$$\int_V [qW(\epsilon)_{ep} - W(\epsilon)_{ne}]\, dV = 0 \tag{3.27}$$

Since the strain hardening exponent n varies from 0 to 1, then $q = \frac{(1+N)}{2}$ for $\frac{1}{2} < q < 1$. Equation (3.27) is written as;

$$[qW(\epsilon)_{ep} - W(\epsilon)_{ne}]\, dV = 0 \tag{3.28}$$

In other words, from (3.28);

$$\sigma_{ij}\epsilon_{ij} = \sigma_{ne}\epsilon_{ne} \tag{3.29}$$

Equation (3.29) means that the strain energy density for a plastic regime is the same as that of the purely elastic solution under mode-1 loading for a piece-wise linear element, i.e. $W(\epsilon)_{ep} = W(\epsilon)_{ne}$. Substituting (3.23) into (3.18) and using (3.17);

$$\left(\frac{S_n^2}{2E}\right) K_T^2 = \frac{\sigma_{ep}^2}{E} + \left(\frac{\sigma_{ep}}{n+1}\right)\left(\frac{\sigma_{ep}}{K}\right)^{\frac{1}{n}} \tag{3.30}$$

where n is the strain hardening exponent, K is the strength coefficient factor, and E is Young's modulus. The material stress-strain curve showed non-linear behavior below the yield limit, and so the modified energy density due to nominal stress is given by (3.31). It is also assumed that the plastic strain increment is proportional to deviatoric stress at any instant of loading. If the nominal stress S_n is beyond the proportional limit, then;

$$W_n = \frac{S_n^2}{2E} + \left(\frac{S_n}{n+1}\right)\left(\frac{S_n}{K}\right)^{\frac{1}{n}} \tag{3.31}$$

substituting (3.31) into (3.30) and using (3.17)

$$\left[\frac{S_n^2}{2E} + \left(\frac{S_n}{n+1}\right)\left(\frac{S_n}{K}\right)^{\frac{1}{n}}\right] K_T^2 = \frac{\sigma_{ep}^2}{E} + \left(\frac{\sigma_{ep}}{n+1}\right)\left(\frac{\sigma_{ep}}{K}\right)^{\frac{1}{n}} \tag{3.32}$$

Therefore, inelastic stress and strain at the blunt notch tip in plane stress can be calculated from (3.33) and (3.34).

$$W(\epsilon)_{ep} = W_n K_T^2 \tag{3.33}$$

$$\epsilon_{ep} = \frac{\sigma_{ep}}{E} + \left(\frac{\sigma_{ep}}{K}\right)^{\frac{1}{n}} \tag{3.34}$$

In the plane strain condition, a biaxial state of stress exists and hence the relationships given by Dowling et.al [41] for the translation of the uiaxial stress-strain curve $\sigma_{ep} - \epsilon_{ep}$ into the biaxial plane strain relation $\sigma_{ep(b)} - \epsilon_{ep(b)}$ have been used.

$$\epsilon_{ep(b)} = \epsilon_{ep}\frac{(1-\mu^2)}{\sqrt{1-\mu-\mu^2}} \tag{3.35}$$

$$\sigma_{ep(b)} = \frac{\sigma_{ep}}{\sqrt{1-\mu-\mu^2}} \tag{3.36}$$

$$\mu = \left[\frac{\nu + \frac{E\epsilon_{pp}}{2\sigma_{ep}}}{1 + \frac{E\epsilon_{pp}}{\sigma_{ep}}}\right] \tag{3.37}$$

Substituting (3.35) and (3.36) into (3.34) gives the results for plane strain condition.

$$W(\epsilon)_{ep(b)} = W_n K_T^2 \tag{3.38}$$

$$\epsilon_{ep(b)} = \frac{\sigma_{ep(b)}}{E} + \left(\frac{\sigma_{ep(b)}}{K}\right)^{\frac{1}{n}} \tag{3.39}$$

and from equation (3.34)

$$\epsilon_{ep} = \frac{\sigma_{ep}}{E} + \epsilon_{pp} = \epsilon_{ee} + \epsilon_{pp} \tag{3.40}$$

where ϵ_{ee} is the elastic part of total strain and ϵ_{pp} is the plastic part of total strain. The inelastic stress and strain at the blunt notch tip are calculated from (3.33) and (3.34) for plane stress or else from (3.38) and (3.39) for plane strain, for a given nominal stress S_n and stress concentration factor K_T. It is necessary to know first the variation of stress concentration factor K_T ahead of a blunt notch tip ($\frac{x}{\rho}$). A 3D elastic finite element analysis was done using coarse mesh for this geometry using NISA. The radius of this notch is given as 0.1 mm, which yet may be considered as a crack with finite radius. The results are given in Table 3.1. The variation of theoretical stress concentration factor K_T in the mid-plane, quarter-plane and surface plane is shown in Figure 3.2.

Table 3.1: Stress concentration factor variation with normalized distance from the crack tip.

X/a	KT (MPL)	KT (QPL)	KT (SPL)
0.0000000E+00	4.1400928E+00	3.2450964E+00	2.0300081E+00
6.0016010E-04	3.9702675E+00	3.1119838E+00	1.9467379E+00
1.2003198E-03	3.8197594E+00	2.9940121E+00	1.8729393E+00
1.8004799E-03	3.6851673E+00	2.8885159E+00	1.8069450E+00
2.4006400E-03	3.5638659E+00	2.7934372E+00	1.7474674E+00
3.0007991E-03	3.4538043E+00	2.7071683E+00	1.6935010E+00
3.6009601E-03	3.3533514E+00	2.6284311E+00	1.6442459E+00
4.2011201E-03	3.2611802E+00	2.5561852E+00	1.5990517E+00
4.8012791E-03	3.1762137E+00	2.4895868E+00	1.5573902E+00
5.4014391E-03	3.0975595E+00	2.4279358E+00	1.5188237E+00
6.0016001E-03	3.0244751E+00	2.3706505E+00	1.4829882E+00
6.6017601E-03	2.9563282E+00	2.3172355E+00	1.4495739E+00
7.2019201E-03	2.8925931E+00	2.2672787E+00	1.4183228E+00
7.8020811E-03	2.8328097E+00	2.2204192E+00	1.3890092E+00
8.4022401E-03	2.7765844E+00	2.1763484E+00	1.3614403E+00
9.0023991E-03	2.7235801E+00	2.1348023E+00	1.3354506E+00
9.6025601E-03	2.6735013E+00	2.0955496E+00	1.3108956E+00
1.0202719E-02	2.6260834E+00	2.0583823E+00	1.2876452E+00
1.0802880E-02	2.5811071E+00	2.0231290E+00	1.2655921E+00
1.1403039E-02	2.5383613E+00	1.9896238E+00	1.2446325E+00
1.2003201E-02	2.4976728E+00	1.9577312E+00	1.2246817E+00
1.2603362E-02	2.4588802E+00	1.9273248E+00	1.2056606E+00
1.3203521E-02	2.4218395E+00	1.8982915E+00	1.1874985E+00
1.3803680E-02	2.3864248E+00	1.8705326E+00	1.1701336E+00
1.4403841E-02	2.3525181E+00	1.8439558E+00	1.1535082E+00
1.5004000E-02	2.3200188E+00	1.8184822E+00	1.1375729E+00
1.5604159E-02	2.2888300E+00	1.7940358E+00	1.1222801E+00
1.6204320E-02	2.2588668E+00	1.7705499E+00	1.1075883E+00
1.6804479E-02	2.2300491E+00	1.7479619E+00	1.0934581E+00
1.7404639E-02	2.2023079E+00	1.7262179E+00	1.0798558E+00
1.8004800E-02	2.1755764E+00	1.7052650E+00	1.0667486E+00
1.8604961E-02	2.1497958E+00	1.6850576E+00	1.0541075E+00
1.9205120E-02	2.1249087E+00	1.6655505E+00	1.0419047E+00
1.9805281E-02	2.1008680E+00	1.6467069E+00	1.0301168E+00
2.5806880E-02	1.8981512E+00	1.4878130E+00	9.3071884E-01
3.1808483E-02	1.7446766E+00	1.3675162E+00	8.5546583E-01
3.4451014E-02	1.6216028E+00	1.2710482E+00	7.9511911E-01
4.1224705E-02	1.5159901E+00	1.1882668E+00	7.4333417E-01
4.7998393E-02	1.4174399E+00	1.1110209E+00	6.9501215E-01
5.4772085E-02	1.3254796E+00	1.0389403E+00	6.4992130E-01
6.1545773E-02	1.2396688E+00	9.7167993E-01	6.0784578E-01
6.8319461E-02	1.1595961E+00	9.0891719E-01	5.6858379E-01
7.5093149E-02	1.0848778E+00	8.5035133E-01	5.3194726E-01
8.1866844E-02	1.0151561E+00	7.9570198E-01	4.9776068E-01
8.8640539E-02	9.5009661E-01	7.4470681E-01	4.6586007E-01
9.5414232E-02	8.8938767E-01	6.9712180E-01	4.3609273E-01
1.0218792E-01	8.3273834E-01	6.5271878E-01	4.0831590E-01
1.0896162E-01	7.7987707E-01	6.1128497E-01	3.8239646E-01
1.1573531E-01	7.3055065E-01	5.7262176E-01	3.5821027E-01

1.2250901E-01	6.8452281E-01	5.3654414E-01	3.3564150E-01
1.2928271E-01	6.4157271E-01	5.0287896E-01	3.1458181E-01
1.3605639E-01	6.0149485E-01	4.7146499E-01	2.9493046E-01
1.4283009E-01	5.6409693E-01	4.4215167E-01	2.7659315E-01
1.4960378E-01	5.2919978E-01	4.1479856E-01	2.5948209E-01
1.5637748E-01	4.9663621E-01	3.8927448E-01	2.4351522E-01
1.6315117E-01	4.6625018E-01	3.6545724E-01	2.2861606E-01
1.6992487E-01	4.3789616E-01	3.4323272E-01	2.1471326E-01
1.7669855E-01	4.1143814E-01	3.2249433E-01	2.0174012E-01
1.8347223E-01	3.8674933E-01	3.0314270E-01	1.8963447E-01
1.9024591E-01	3.6371154E-01	2.8508517E-01	1.7833836E-01
1.9701960E-01	3.4221417E-01	2.6823506E-01	1.6779760E-01
2.0379328E-01	3.2215443E-01	2.5251180E-01	1.5796171E-01
2.1056696E-01	3.0343607E-01	2.3783994E-01	1.4878356E-01
2.1734064E-01	2.8596941E-01	2.2414917E-01	1.4021914E-01
2.2411434E-01	2.6967075E-01	2.1137393E-01	1.3222744E-01
2.3088802E-01	2.5446191E-01	1.9945289E-01	1.2477010E-01
2.3766170E-01	2.4027018E-01	1.8832910E-01	1.1781148E-01
2.4443538E-01	2.2702742E-01	1.7794913E-01	1.1131816E-01
2.5120906E-01	2.1467023E-01	1.6826329E-01	1.0525907E-01
2.5798277E-01	2.0313933E-01	1.5922512E-01	9.9605143E-02
2.6475645E-01	1.9237947E-01	1.5079130E-01	9.4329268E-02
2.7153013E-01	1.8233918E-01	1.4292149E-01	8.9406215E-02
2.7830381E-01	1.7297028E-01	1.3557795E-01	8.4812373E-02
2.8507749E-01	1.6422787E-01	1.2872545E-01	8.0525719E-02
2.9185117E-01	1.5607007E-01	1.2233119E-01	7.6525711E-02
2.9862485E-01	1.4845775E-01	1.1636448E-01	7.2793163E-02
3.0539854E-01	1.4135450E-01	1.1079679E-01	6.9310233E-02
3.1217225E-01	1.3472624E-01	1.0560142E-01	6.6060208E-02
3.1894593E-01	1.2854122E-01	1.0075346E-01	6.3027509E-02
3.2571961E-01	1.2276977E-01	9.6229672E-02	6.0197599E-02

(*) crack tip is assumed to have a radius (r) of 0.1 mm.
and a is the length of the notch.

Note: The data depends on the thickness of the specimen used in 3D finite element analysis. There could be a numerical error in data extrapolation, which should be verfied before use for a given problem.

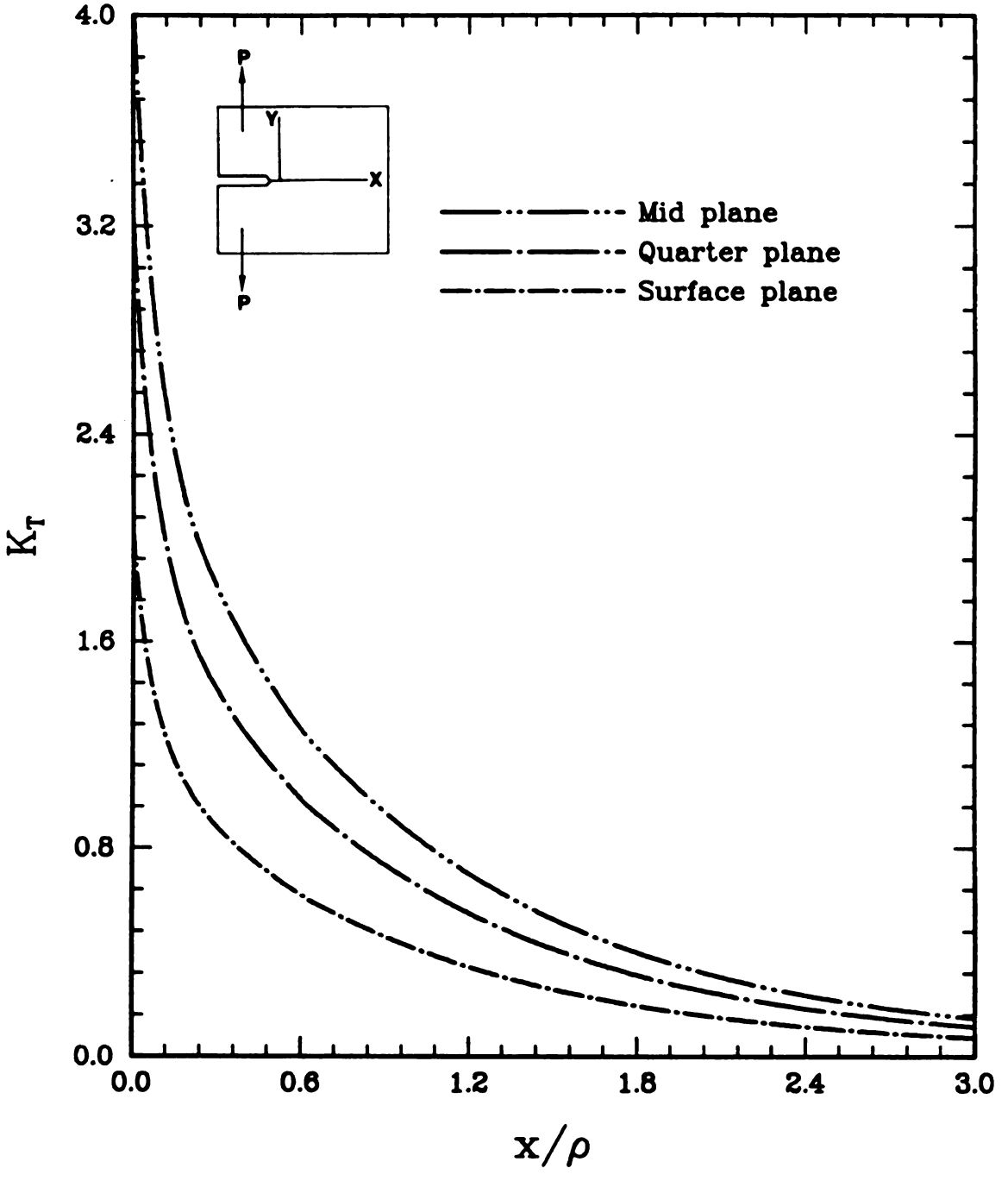

Figure 3.2: Stress concentration factor (K_T) variation in a CT specimen for a/W = 0.4966, a/t = 0.9372 and $\theta = 0°$ based on 3D elastic finite element analysis.

Monotonically increasing the nominal stress S_n for a fixed value of K_T defined by the normalized distance results in the local stress and strain curve for both plane stress and plane strain as shown in Figure 3.3. Superimposed is the Nueber's flow rule for comparison sake only. Similarly, varying K_T with respect to the normalized distance at a fixed nominal stress S_n results in the local strain or stress distribution ahead of a notch tip, which will be discussed in the next paragraph.

3.1.2 Plastic zone size and shape at the notch tip

In (1.1) it should be noted that the origin of polar coordinates is at a distance of $\frac{\rho}{2}$ behind the notch tip. For $r = \frac{\rho}{2}$ the stress intensity factor can be calculated in terms of the stress concentration factor for deep notches,

$$K_I = K_T S_n \sqrt{\frac{\rho\pi}{2}} \tag{3.41}$$

Substituting (3.41) in (1.1) for the stress intensity factor K_I, we get

$$\sigma_{ij} = K_T S_n \sqrt{\frac{\rho}{4r_p}} f_{ij}(\theta) + \frac{K_T S_n}{\sqrt{32}} \left(\frac{\rho}{r_p}\right)^{\frac{3}{2}} g_{ij}(\theta) \tag{3.42}$$

where f_{ij} and g_{ij} are given in (1.2) and (1.3). The strain distribution obtained from a 2D analytical elastic solution*for $S_N = 4.137$ MPa, $S_N = 17.927$ MPa and $S_N = 31.717$ MPa were illustrated in Figures 1.3 to 1.5. The effect of finite notch radius increases the strain distribution far from zero notch radius, also strains in plane stress are larger than in plane strain condition. The 2D analytical solution assumes that on the free surface σ_{zz} is zero in plane stress; and also in 2D, K_T is constant. This limitation causes discrepencies in experimental measurements of strain in finite notch or cracked thick geometries†

*converting (3.42) using stress-strain relation for plane stress and plane strain.

†A comparison of three dimensional normalized stress variation with distance between 3D analytical elastic solution given by Sih[49] and a finite element solution is given in Figure 5.1. The results are quite comparable.

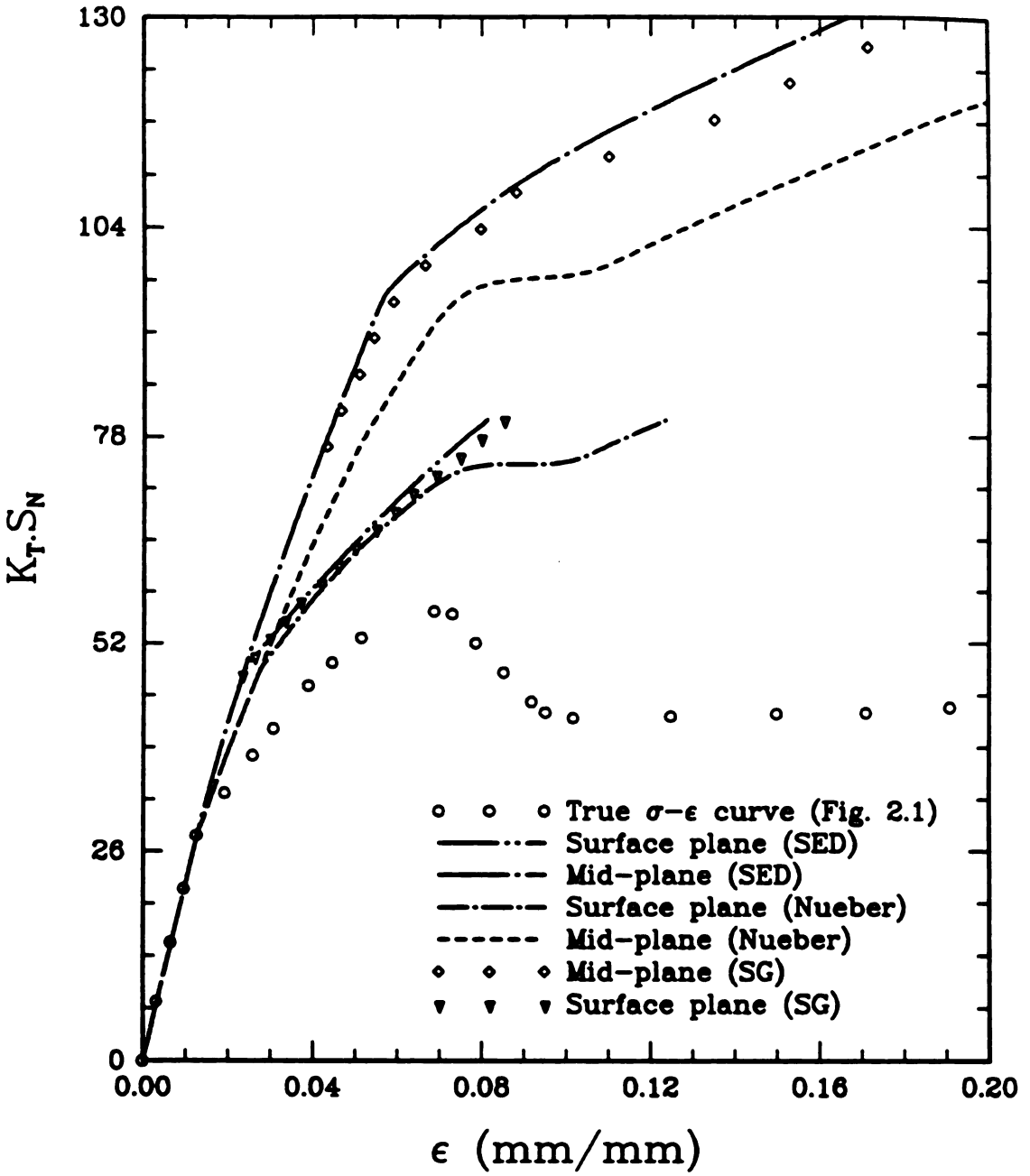

Figure 3.3: Theoretical and experimental notch strains in a sharp notched compact tension specimen made out of polycarbonate.

The first approximation of plastic zone size r_p at the notch tip was derived from the Von-Mises yield criterion on the basis of elastic stress distribution.

$$\sigma_{ys} = \frac{K_T S_n}{2\sqrt{2}} \sqrt{\alpha \left(\frac{\rho}{r_p}\right) + \beta \left(\frac{\rho}{r_p}\right)^3} \tag{3.43}$$

for plane stress;

$$\alpha = 6\left[cos\frac{\theta}{2} sin\frac{\theta}{2} sin\frac{3\theta}{2}\right]^2 + 2cos\frac{\theta}{2} + 6\left[sin\frac{\theta}{2} cos\frac{\theta}{2} cos\frac{3\theta}{2}\right]^2 \tag{3.44}$$

$$\beta = \frac{3}{2}\left[cos^2\left(\frac{3\theta}{2}\right) + \frac{3}{2} sin^2\left(\frac{3\theta}{2}\right)\right] \tag{3.45}$$

for $\theta = 0°$, $\alpha = 2$ and $\beta = \frac{3}{2}$

$$\sigma_{ys} = \frac{K_T S_n}{2\sqrt{2}} \sqrt{\left(\frac{\rho}{r_p}\right) + \frac{3}{4}\left(\frac{\rho}{r_p}\right)^3} \tag{3.46}$$

for plane strain;

$$\begin{aligned} \alpha \;=\; & 12\left[cos^2\left(\frac{\theta}{2}\right) sin^2\left(\frac{\theta}{2}\right) sin^2\left(\frac{3\theta}{2}\right)\right] + 2cos\left(\frac{\theta}{2}\right) + \\ & 2\left[sin\left(\frac{\theta}{2}\right) sin\left(\frac{3\theta}{2}\right) cos^2\left(\frac{3\theta}{2}\right)\right] + 8\nu^2 cos^2\left(\frac{\theta}{2}\right) - 8\nu cos^2\left(\frac{\theta}{2}\right) \end{aligned} \tag{3.47}$$

for $\theta = 0°$, $\alpha = (2 + 8\nu^2 - 8\nu)$ and $\beta = \frac{3}{2}$

$$\sigma_{ys} = \frac{K_T S_n}{2\sqrt{2}} \sqrt{\left(\frac{\rho}{r_p}\right)(2 + 8\nu^2 - 8\nu) + \frac{3}{4}\left(\frac{\rho}{r_p}\right)^3} \tag{3.48}$$

In the above equation $\sigma_{ys}, K_T, S_n and \rho$ are known and so r_p can be found. By 2D elastic solution, the stress distribution is known for θ varying from 0° to 180° for a given S_N and constant K_T from which plastic zone sizes are calculated (refer to

Figures 1.5 to 1.10. However in 3D case, the situations are different and will be explained in the coming paragraphs.

3.1.3 Increment in the plastic zone size at the notch tip

Since the value of r_p is known the force can be calculated; (refer to Figures 3.4 to 3.6)

$$F_1 = \int_{\frac{\rho}{2}}^{r} \sigma_y dr - \sigma_y(r_p)(r_p - 0.5\rho) \tag{3.49}$$

$$F_1 = \frac{K_T S_n}{2\sqrt{2}} \rho \left\{ 2\sqrt{\frac{r_p}{\rho}} - \sqrt{\frac{\rho}{r_p}} \right\} - \sigma_y(r_p)(r_p - 0.5\rho) \tag{3.50}$$

where;

$$\sigma_y(r_p) = \frac{K_T S_n}{2\sqrt{2}} \left\{ \sqrt{\frac{\rho}{r_p}} + \frac{1}{2} \left(\frac{\rho}{r_p} \right)^{\frac{3}{2}} \right\} \tag{3.51}$$

Because of the plastic yielding at the notch tip, the force E_1 cannot be carried through by the material in the plastic zone r_p; but, in order to satisfy the equilibrium conditions of the notched body, the force has to be carried through by the material beyond the plastic zone Δr_p. As a result, stress redistribution occurs and the plastic zone r_p is increased by an increment Δr_p. In reality $E_1 \neq F_1, E_2 \neq F_2$ and $E_3 \neq F_3$, but it is assumed that $E_1 = F_1, E_2 = F_2$ and $E_3 = F_3$ and $F_1 > F_2 > F_3$. Thus the plastic zone increment Δr_p can be calculated, if $E_1 = F_1 = \sigma_y(r_p)\Delta r_p$. Hence

$$\Delta r_p = \left\{ \frac{\rho \left[2\sqrt{\frac{r_p}{\rho}} - \sqrt{\frac{\rho}{r_p}} \right]}{\left[\sqrt{\frac{\rho}{r_p}} - \frac{1}{2} \left(\frac{\rho}{r_p} \right)^{\frac{3}{2}} \right]} - (r_p - 0.5\rho) \right\} \tag{3.52}$$

An interpretation of plastic zone size increment is shown in Figure 3.7, and a better explanation will be given in Chapter 5.

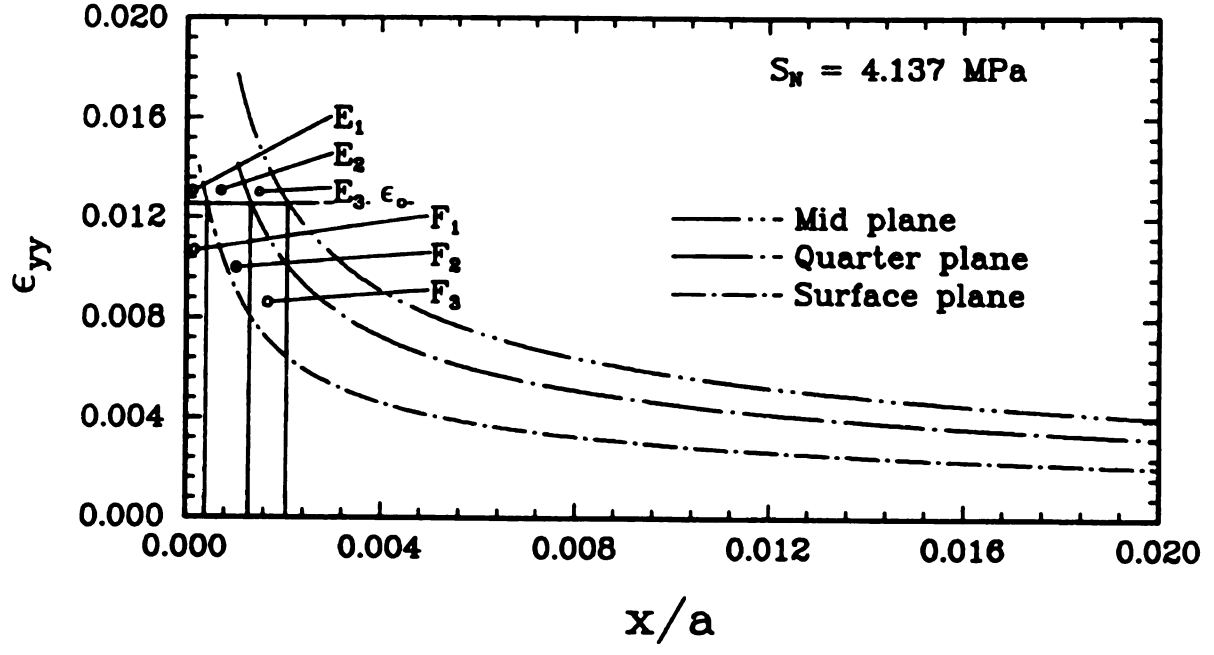

Figure 3.4. Crack opening strain re-distribution in a CT specimen throughout the specimen thickness a/W = 0.4966 and θ = 0° based on energy density apptoach, loaded to 4.137 MPa.

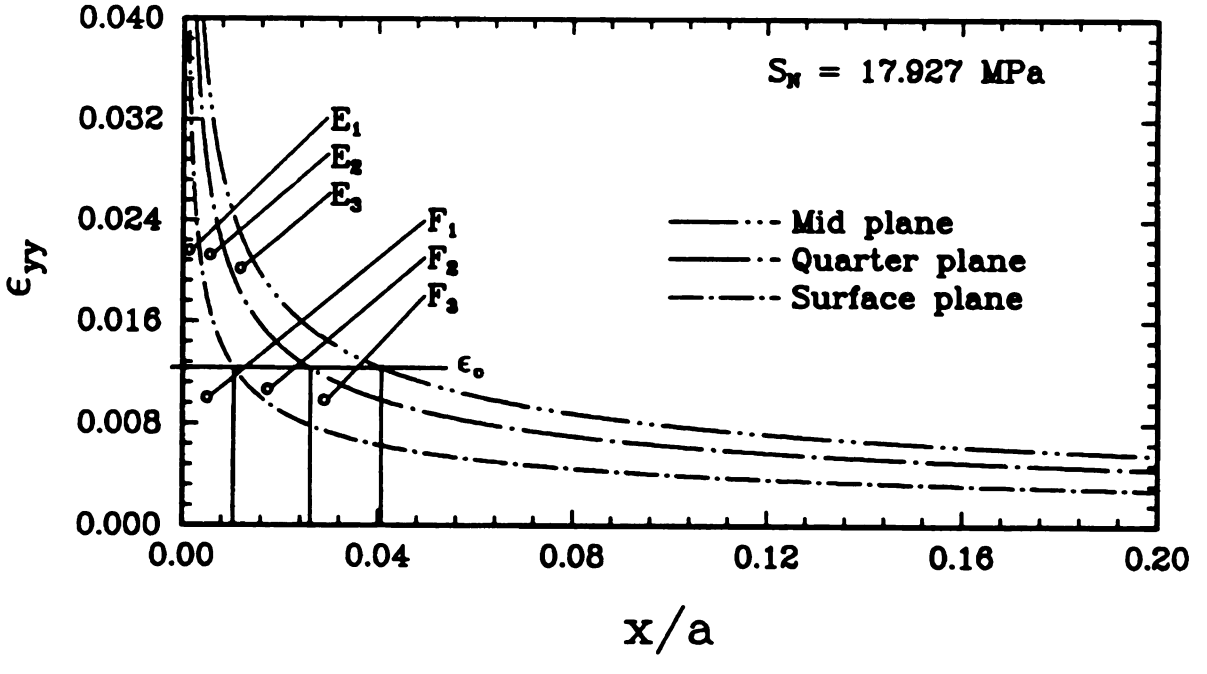

Figure 3.5. Crack opening strain re-distribution in a CT specimen throughout the specimen thickness a/W = 0.4966 and θ = 0° based on energy density approach, loaded to 17.927 MPa.

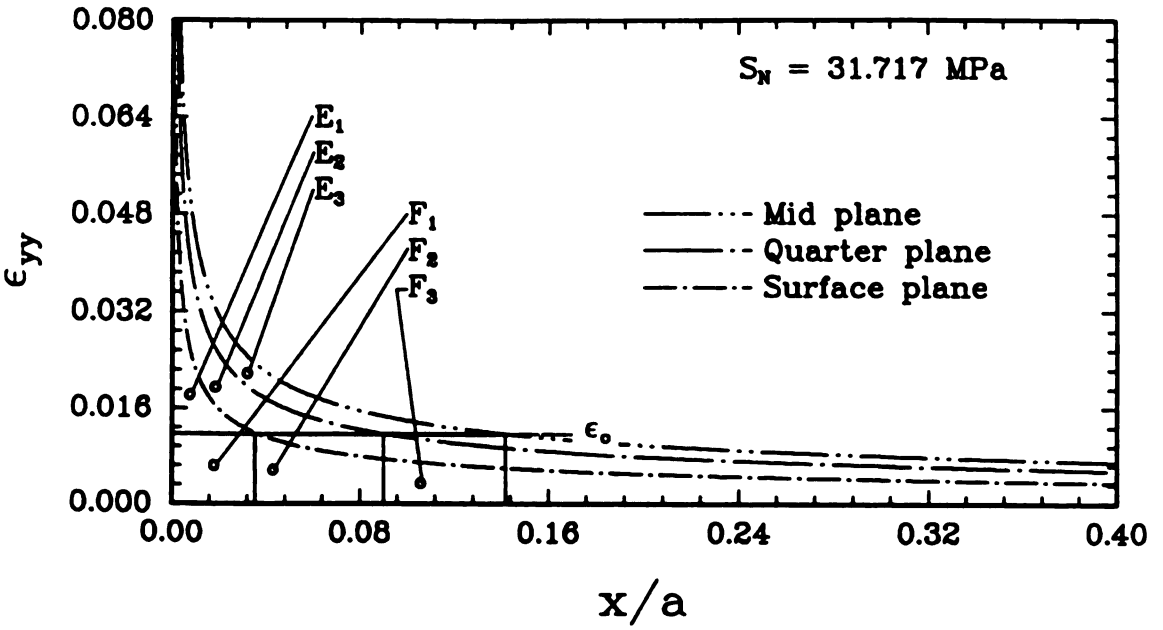

Figure 3.6. Crack opening strain re-distribution in a CT specimen throughout the specimen thickness a/W = 0.4966 and θ = 0° based on energy density approach, loaded to 31.716 MPa.

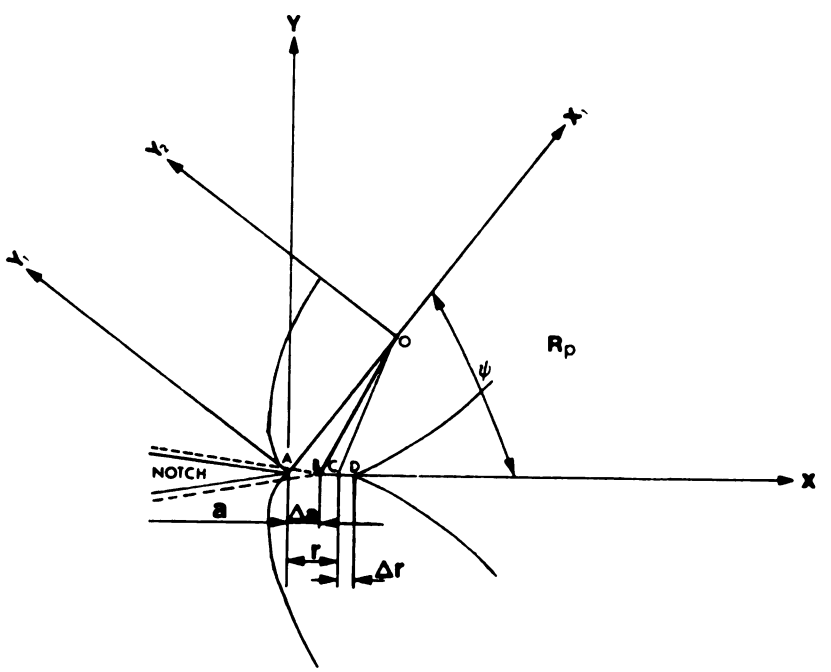

Figure 3.7: Interpretation of plastic zone size increment.

3.1.4 Elastic-plastic stress and strain at the crack tip

The elastic strain energy W_{ne} in the case of a mathematical sharp notch or crack tip is calculated from the stress intensity factor solution K_I, given in an ASTM Standard [42]. The ordinary stress concentration factor is no longer useful. For a CT specimen;

$$K_I = \frac{P}{B\sqrt{W}} f\left(\frac{a}{W}\right) \tag{3.53}$$

$$f\left(\frac{a}{W}\right) = \left[2 + \frac{\frac{a}{W}}{1-\frac{a}{W}}\right]\left[0.886 + 4.64\left(\frac{a}{W}\right) - 13.32\left(\frac{a}{W}\right)^2\right] \tag{3.54}$$

where B is the thickness, W is the width, a is the crack length, $\frac{a}{W}$ is the geometric constant and P is the applied load. The elastic stresses in x and y directions are equal for $\theta = 0$, and, subsequently at r = a;

$$W_{ne} = \frac{K_I}{\sqrt{2\pi r}}\left(\frac{1-\nu}{E}\right) \tag{3.55}$$

The stress components ahead of the crack tip are relatively high, and none of them can be neglected. The strain energy density in the plastic zone $W_{(np)}$ is the summation of x and y components.

$$W^*_{np} = \frac{\sigma_y^2}{E}\alpha + \left(\frac{\sigma_y}{n+1}\right)\left(\frac{\sigma_y}{K}\right)^{\frac{1}{n}}\beta \tag{3.56}$$

In (3.56) * indicates x and y components; for x components $\alpha = (p-\nu)p$ and $\beta = (1-p+p^2)^{\frac{1-n}{2n}}(p-\frac{1}{2})$; for y components $\alpha = (1-\nu p)$ and $\beta = (1-p+p^2)^{\frac{1-n}{2n}}(1-\frac{p}{2})$; p is the ratio between the stress component in the x direction and that of the y direction and ν is the Poisson's ratio. According to the analysis given by Knott [43], the plastic zone ahead of a crack tip is about 2 times larger than estimated on the basis of elastic stress distribution, which means that the elastic strain energy density should be multiplied by about 2 to give strain energy density in the plastic zone.

$$\frac{K_I}{\sqrt{2\pi r}}\left(\frac{1-\nu}{E}\right) = \frac{\sigma_y^2}{E}\alpha + \left(\frac{\sigma_y}{n+1}\right)\left(\frac{\sigma_y}{K}\right)^{\frac{1}{n}}\beta \tag{3.57}$$

Equation (3.57) enables to calculate elastic-plastic stress and strain at the sharp crack tip. Ahead of the sharp crack tip the stress and strain σ_x and σ_z are relatively higher than for blunt notches. The above equation also enables us to calculate strain distribution ahead of a sharp notch or crack tip. As for local elastic-plastic stress at the blunt notch tip, in plane stress $\sigma_x = \sigma_z = 0$; and in plane strain $\sigma_x = 0$ and $\sigma_z = \nu\sigma_{np}$. Ahead of a crack tip $\sigma_x \neq 0$, and in the plane strain condition $\sigma_z = \nu(\sigma_x + \sigma_y)$.

3.1.5 Plastic zone size and shape at the crack tip

The approach is the same as calculated for a blunted notch tip. Equation (1.4) is substituted in the Von-Mises criterion to obtain the yield stress.

$$\sigma_{ys} = \frac{K_I}{\sqrt{2\pi}}\sqrt{\left[\left(\frac{1}{r_p}\right)\alpha + \rho^2\left(\frac{1}{r_p}\right)^3\beta\right]} \tag{3.58}$$

for plane stress;

$$\begin{aligned}\alpha &= 3\left[cos^2\left(\frac{\theta}{2}\right)sin^2\left(\frac{\theta}{2}\right)sin^2\left(\frac{3\theta}{2}\right)\right] + 2cos\left(\frac{\theta}{2}\right) + \\ &\quad 3\left[sin^2\left(\frac{\theta}{2}\right)cos^2\left(\frac{3\theta}{2}\right)\right]\end{aligned} \tag{3.59}$$

$$\beta = 3\left[cos^2\left(\frac{3\theta}{2}\right) + \frac{3}{2}sin^2\left(\frac{3\theta}{2}\right)\right] \tag{3.60}$$

for $\theta = 0°$, $\alpha = 1$ and $\beta = 3$

$$\sigma_{ys} = \frac{K_T S_n}{2\sqrt{2}}\sqrt{\left(\frac{1}{r_p}\right) + 3\rho^2\left(\frac{1}{r_p}\right)^3} \tag{3.61}$$

If $\rho = 0$, that means the crack tip is mathematically sharp.

$$\sigma_{ys} = \frac{K_I}{\sqrt{2\pi r}} \tag{3.62}$$

for plane strain;

$$\begin{aligned}\alpha &= 3\left[cos^2\left(\frac{\theta}{2}\right)sin^2\left(\frac{\theta}{2}\right)sin^2\left(\frac{3\theta}{2}\right)\right]+cos^2\left(\frac{\theta}{2}\right)\cdot \\ &+3\left[sin\left(\frac{\theta}{2}\right)cos^2\left(\frac{\theta}{2}\right)cos^2\left(\frac{3\theta}{2}\right)\right]+4\nu^2cos^2\left(\frac{\theta}{2}\right) \\ &-4\nu cos^2\left(\frac{\theta}{2}\right)\end{aligned} \tag{3.63}$$

$$\beta = 3\left[cos^2\left(\frac{3\theta}{2}\right)+\frac{3}{2}sin^2\left(\frac{3\theta}{2}\right)\right] \tag{3.64}$$

for $\theta = 0°$, $\alpha = (1+4\nu^2-4\nu)$ and $\beta = 3$

$$\sigma_{ys} = \frac{K_T S_n}{2\sqrt{2}}\sqrt{\left(\frac{1}{r_p}\right)(1+4\nu^2-4\nu)+3\rho^2\left(\frac{1}{r_p}\right)^3} \tag{3.65}$$

In the above equation σ_{ys}, K_T, S_n and ρ are known and so r_p can be found.

3.1.6 Increment in the plastic zone size at the crack tip

In a similar way for the blunted notch tip, the increment in the plastic zone size is given by;

$$\triangle r_p = \left\{\frac{(r_p-\rho)+\left(\frac{\rho^2}{4r_p}\right)}{1+\left(\frac{\rho}{2r_p}\right)}\right\} \tag{3.66}$$

Due to stress redistribution there is an increase in the plastic zone size r_p, and the increment is given by $\triangle r_p$. The stress redistribution is relatively higher in a sharp notch or crack tip than in a blunt notch. Because of this, the elastic strain energy density is multiplied by a correction factor $C = 1+\frac{\triangle r_p}{r_p}$.

$$W(\epsilon)_c = W_{ne}\left[\left(1+\frac{\triangle r_p}{r_p}\right)\right] = W_n K_T^2\left[\left(1+\frac{\triangle r_p}{r_p}\right)\right] \tag{3.67}$$

Now, to find corrected elastic-plastic stress and strain at and ahead of a blunt notch tip and a sharp notch or crack tip, (3.18) must be replaced by (3.67). Plastic zone size r_p and the increment Δr_p were derived assuming constant stress $\sigma_y(r_p)$ throughout the plastic zone. The analytical procedures are repeated.

Analytical calculation of elastic-plastic stress and strain referring to (3.33) and (3.34) for plane stress and (3.38) and (3.39) for plane strain and corresponding plastic zone sizes are rather difficult because of the polynomial nature of the equations‡ These equations can best be solved using numerical method. A Fortran code is written to solve them in general for all classes of material provided the true stress-strain curve is known.

3.2 Numerical Method

3.2.1 Estimation of local stress and strain

The numerical method is based on calculation of areas under the piece-wise linear stress-strain curve. The experimental stress and strain curve is approximated by a series of linear elements characterized by corresponding ranges of stress $\Delta\sigma_i$ and strain $\Delta\epsilon_i$. Any material flow curve can be so characterized without limiting the calculation to the Ramberg-Osgood type only.

The procedure is based on the analysis of three matrices $(\Delta\sigma_i)$, $(\Delta\epsilon_i)$ and Γ_i. The value of coefficient Γ_i reflects the direction of loading and the degree of utilization of each linear element (N). The coefficient of Γ_i can change within a range -1 to +1. The required degree of accuracy has been achieved if the quantity in the left hand side of (3.68) is less than PTOL (tolerance).

$$\left|\frac{K_I^2 W_n - W_{ne}}{K_I^2 W_n}\right| \leq PTOL \tag{3.68}$$

The energy density W_n caused by S_n can be calculated from (3.69). The results of

‡Also due to strain softening materials like polycarbonate

this algorithm are shown in Figure 3.3 based on generalized polycarbonate true stress-strain curve. For plane strain the true stress-strain curve is converted by using (3.35) and (3.36). The notch strain in plane stress is much lower than in plane strain. This is because the three dimensional K_T variation with distance was used as the input. The state of strain after yield is higher in the mid plane than in the surface plane with increasing nominal stress. Also superimposed is Nueber's flow curve, which predicts notch strain much lower than the energy-based criterion.

$$W_n = \left(\frac{1}{2}\Delta\sigma_i.\Delta\epsilon_i.\Gamma_i^2 + \sum_{j=2}^{N}\left\{\left[\sum_{i=1}^{j-1}\Delta\sigma_i.\Gamma_i + \left(\frac{\Delta\sigma_i}{2}\right)\right](\Delta\epsilon_j.\Gamma_j)\right\}\right) K_T^2 \qquad (3.69)$$

The number of linear elements N which have to be used in relation (3.69) and the corresponding values of coefficient Γ_i can be found from (3.70).

$$S_n = \sum_{i=1}^{N}\Delta\sigma_i\Gamma_i \qquad (3.70)$$

The local energy density is calculated on the same principle as above, but now W_n is already known and, from (3.18), for a blunt notch;

$$W_{ne} = \left(\frac{1}{2}\Delta\sigma_i.\Delta\epsilon_i.\Gamma_i^2 + \sum_{j=2}^{N}\left\{\left[\sum_{i=1}^{j-1}\Delta\sigma_i.\Gamma_i + \left(\frac{\Delta\sigma_i}{2}\right)\right](\Delta\epsilon_j.\Gamma_j)\right\}\right) K_T^2 \qquad (3.71)$$

For sharp notch or crack, from (3.55);

$$W_{ne} = \left(\frac{1}{2}\Delta\sigma_i.\Delta\epsilon_i.\Gamma_i^2 + \sum_{j=2}^{N}\left\{\left[\sum_{i=1}^{j-1}\Delta\sigma_i.\Gamma_i + \left(\frac{\Delta\sigma_i}{2}\right)\right](\Delta\epsilon_j.\Gamma_j)\right\}\right) \qquad (3.72)$$

The energy density in the plastic zone is calculated in a similar way by replacing and equating W_{ne} by W_{np}. From this procedure, local stress and strain is estimated to be;

$$\sigma_{ep} = \sum_{i=1}^{N}\Delta\sigma_i\Gamma_i \qquad (3.73)$$

$$\epsilon_{ep} = \sum_{i=1}^{N} \Delta\epsilon_i \Gamma_i \tag{3.74}$$

The total number of linear elements which should be used for approximation of the σ-ϵ curve depends on the shape of the curve and required accuracy. The material stress-strain values are given in Table 2.1. The PTOL used is 0.00001. For further detail refer to Appendix A. The elastic plastic crack opening strain distribution based on strain energy density criterion are shown in Figures 3.8, 3.9 and 3.10 for S_N = 4.137 MPa, S_N = 17.927 MPa and S_N = 31.716 MPa respectively. For comparison, the strain in plane strain obtained from the 2D elastic solution is superimposed. With increasing nominal stress, the 2D analytical elastic strain doesn't match the elastic-plastic strain corresponding to the energy-based result. At the threshold the 2D elastic strain remains straight, but the elastic-plastic strain drops to zero at large distance from the crack tip. This happens because the area inside the material stress-strain curve is analyzed and not just because the material properties in the 2D elastic analytical solution are taken. The final plastic zone and size estimated for three different loads as mentioned earlier are given in Figures 3.11 to 3.13.

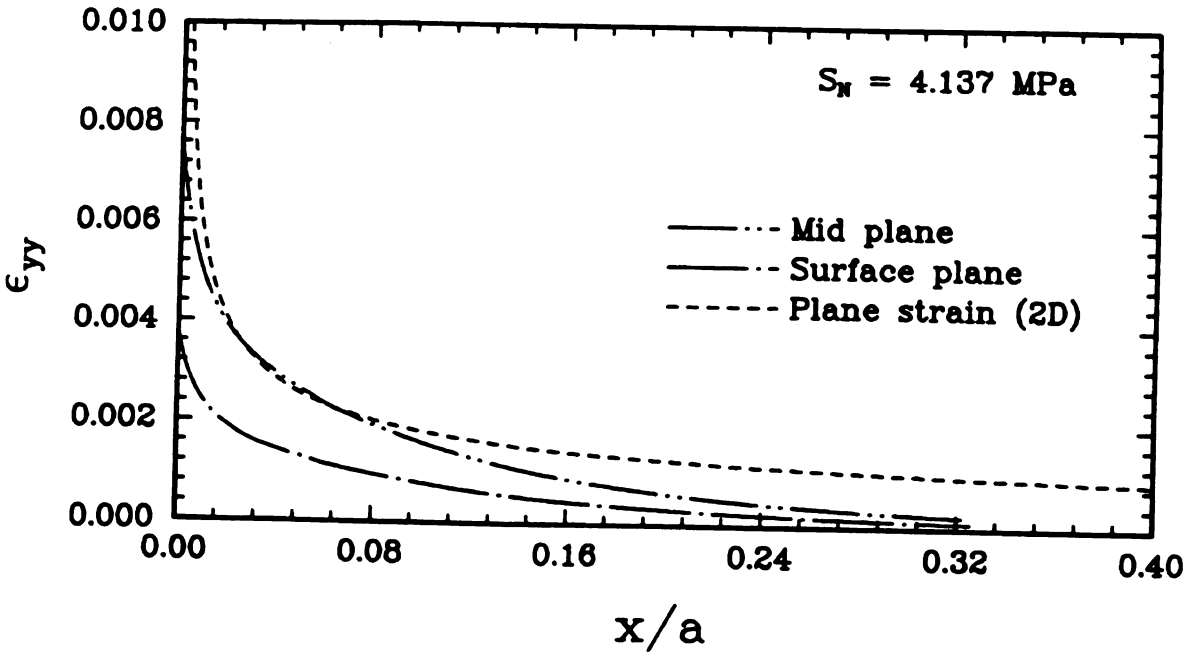

Figure 3.8: Crack opening strain distribution in a CT specimen throughout the specimen thickness a/W = 0.4966 and θ = 0° based on energy density approach, loaded to 4.137 MPa.

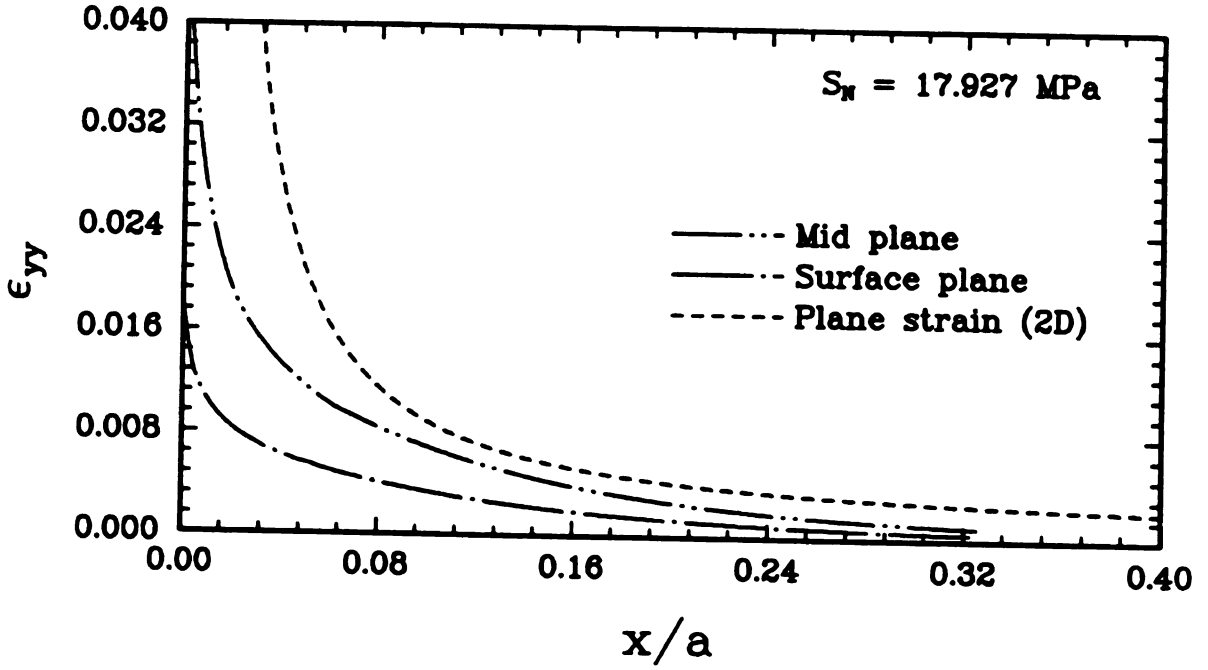

Figure 3.9. Crack opening strain distribution in a CT specimen throughout the specimen thickness a/W = 0.4966 and θ = 0° based on energy density approach, loaded to 17.927 MPa.

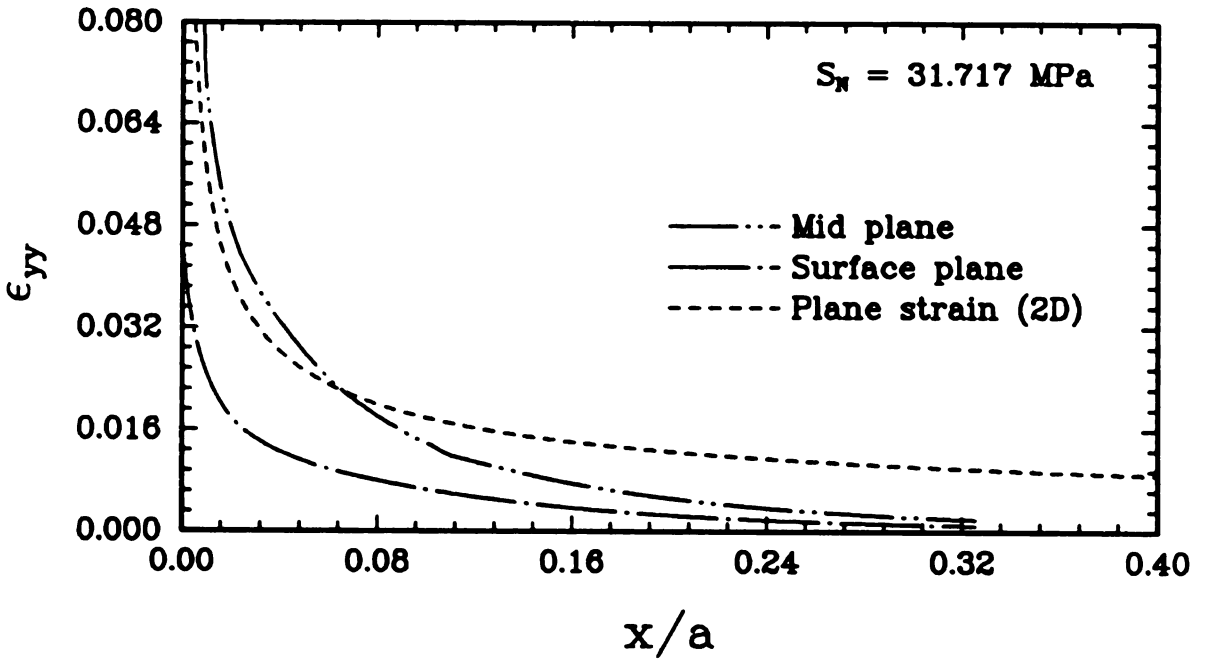

Figure 3.10. Crack opening strain distribution in a CT specimen throughout the specimen thickness a/W = 0.4966 and θ = 0° based on energy density approach, loaded to 31.717 MPa.

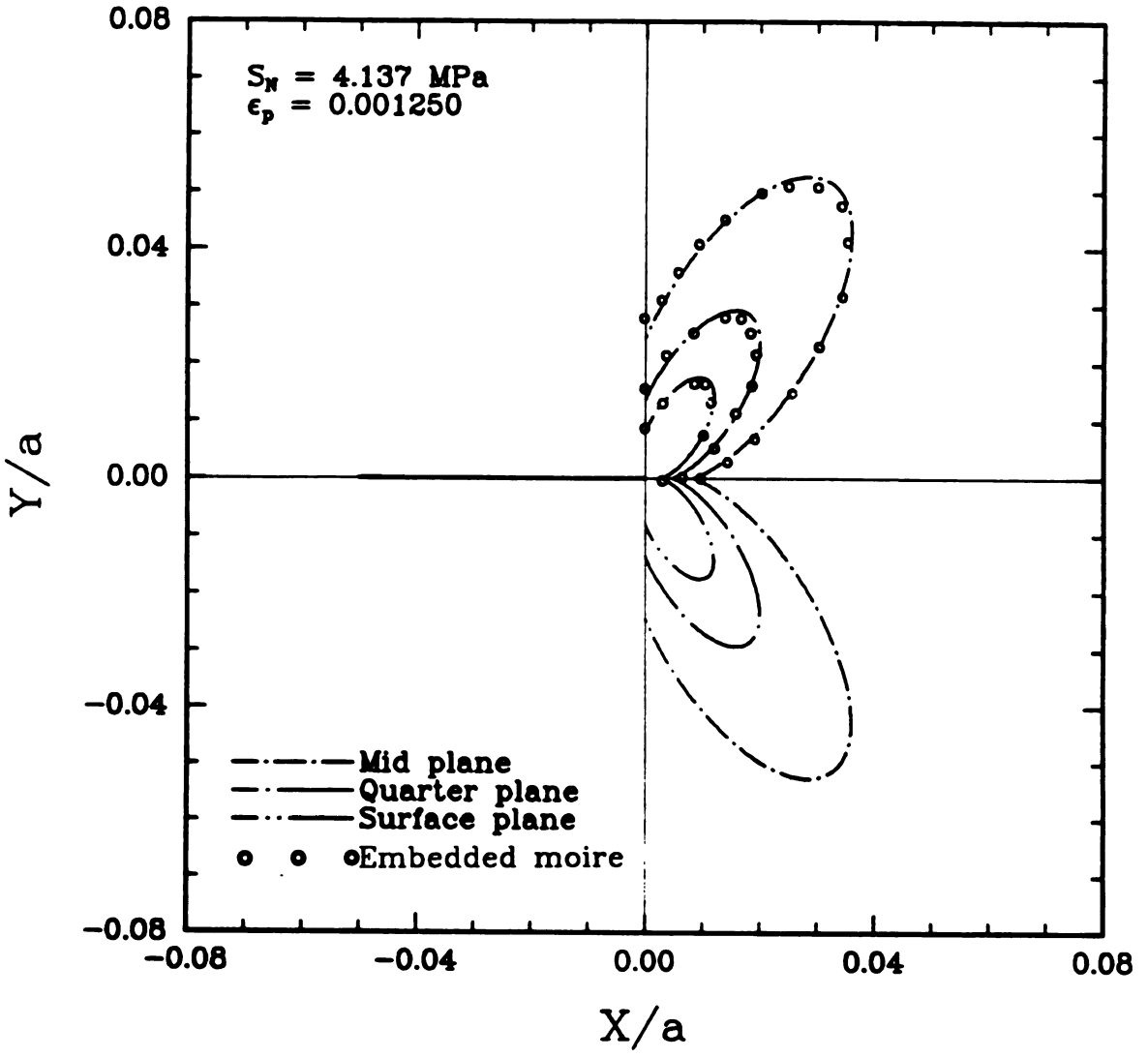

Figure 3.11: Estimation of plastic zone size based on energy density criterion for mid-plane and surface plane loaded to 4.137 MPa.

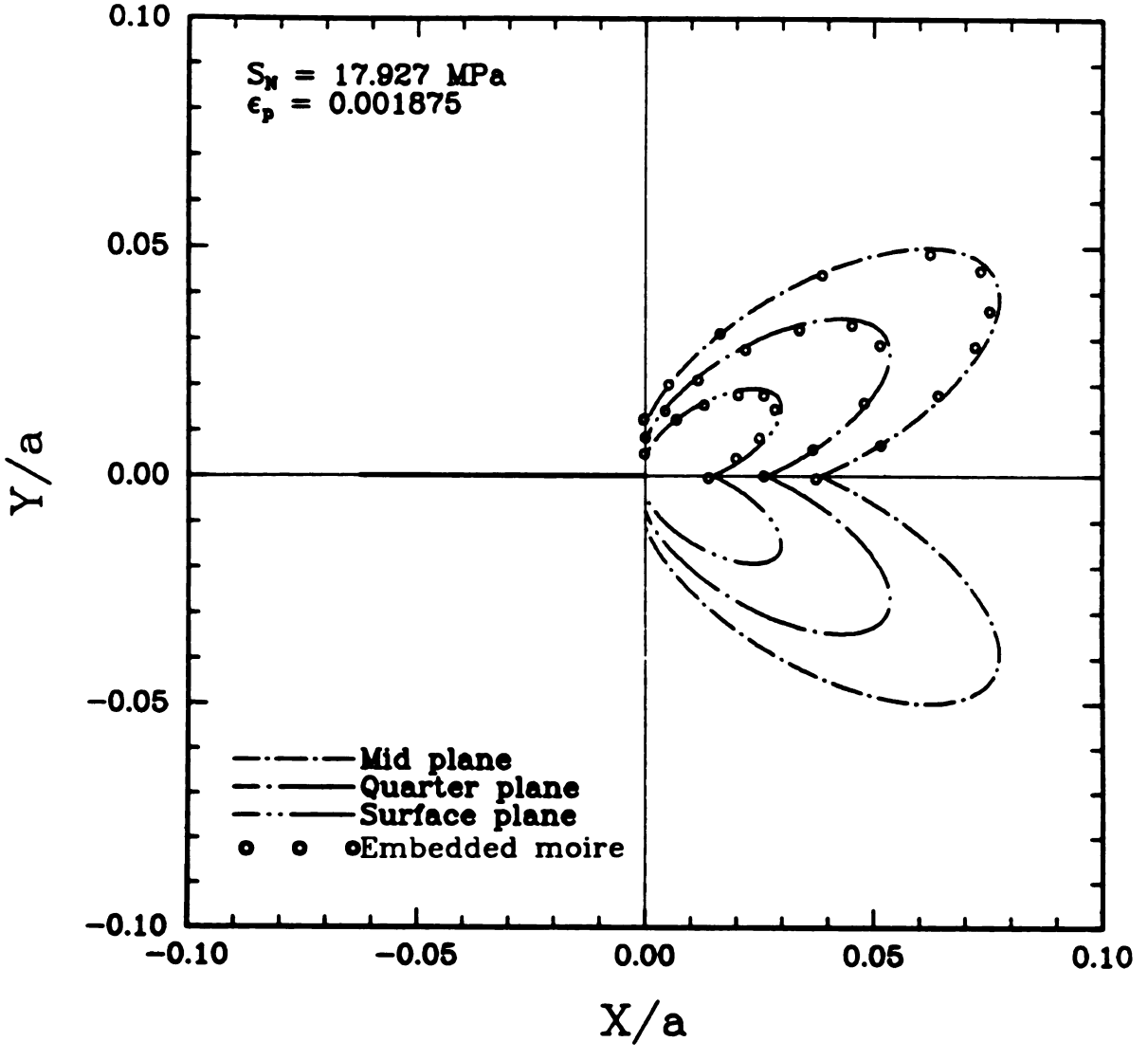

Figure 3.12: Estimation of plastic zone size based on energy density criterion for mid-plane and surface plane loaded to 17.927 MPa.

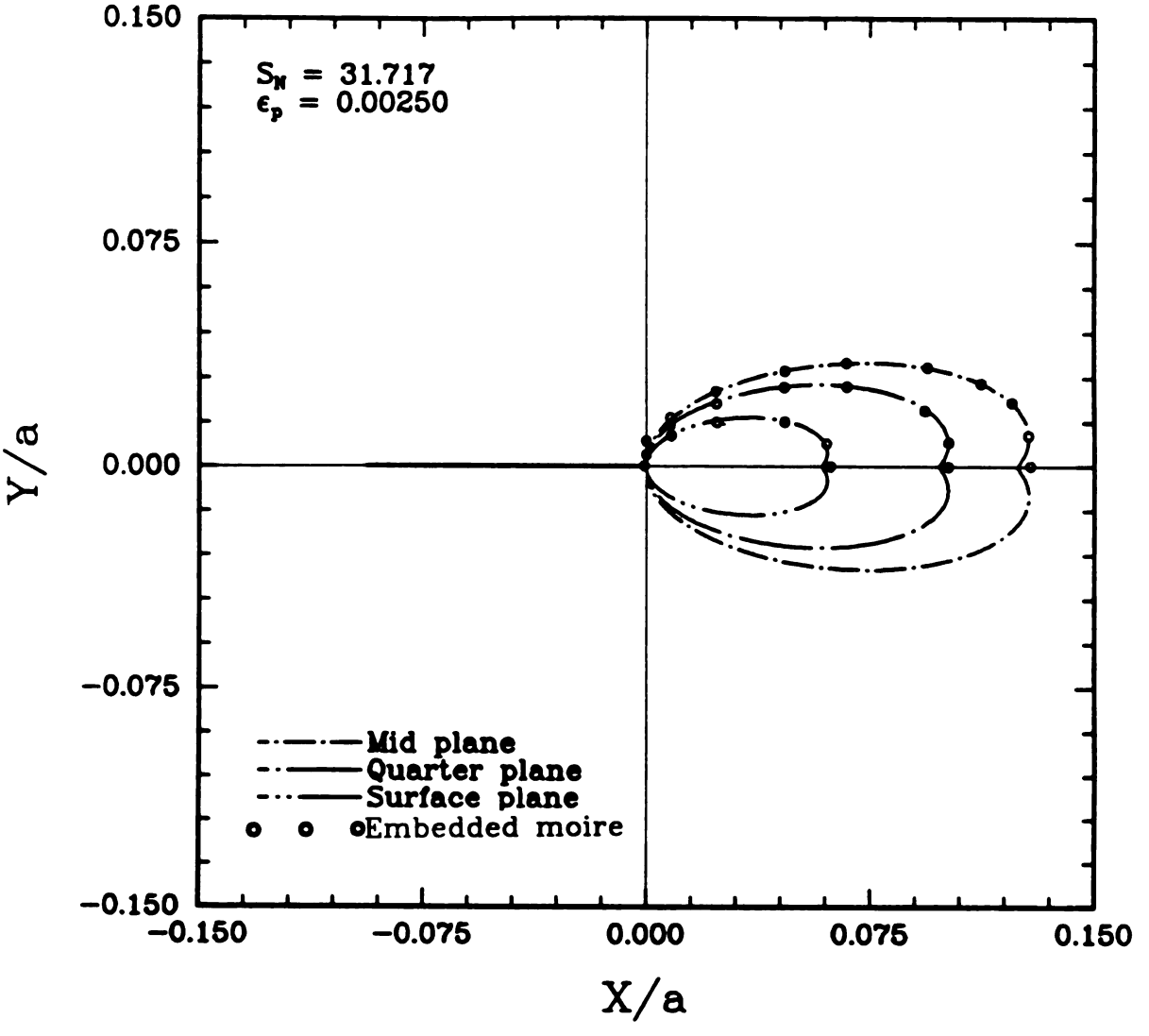

Figure 3.13: Estimation of plastic zone size based on energy density criterion for mid-plane and surface plane loaded to 31.717 MPa.

CHAPTER 4

NUMERICAL ESTIMATION OF NON-SINGULAR STRESS

4.1 Introduction

The purpose of calculating the non-singular stress σ_{ox} numerically using finite elements is to compare with the experimental stress freezing technique. Experimentally it is difficult to find the effect of the non-singular stress in elastic-plastic stress analysis of the deformed crack tip unless a hybrid technique is employed. The second-term in (1.12) is a constant elastic term and is geometry dependent. Once we know the non-singular constant term, there is no need to carry out real experiments in full scale rather than depend on numerically obtained results* At the same time, computational methods are playing an increasing role in fracture mechanics, but often they lack detailed experimental evidence supporting the inevitable modeling assumptions. Here, the two approaches will be conglomerated to see the best way to understand the effects of non-singular stress.

The effect of this non-singular term for different materials will give different results. Three different materials have been analyzed; materials that obey the Ramberg-

*The analysis for CT specimen was done at MIT by the author using ABAQUS [4].

Osgood law, the modified[†]Ramberg-Osgood power law, and, finally the experimental stress-strain curve for polycarbonate. The first two are solved based on deformation plasticity, and for polycarbonate the incremental plasticity has been used in plane strain only.

There are many methods for evaluating T or σ_{ox} stress but only the technique shown by Larsson and Carlson [47] will be used. The total x-direction stress σ_x is determined from the solutions obtained by the elastic finite element method for a given specimen and for the boundary layer problem for elements with one side on the crack surface. T stress for a CT specimen with different crack depths was analyzed by imposing a distributed load around the plane of the loading pins, the results of which are then compared with that of point loading at the pin center and of shear traction applied in the plane of pin center (Leevers and Radon [44]; Cotterell [45]; Kfouri [46] and Larsson and Carlsson [47]).

4.1.1 Modeling of CT Specimen and Boundary Conditions

The CT specimen with dimensions from ASTM E-399 [42] is shown in Figure 4.1a. Each of the CT specimens are characterized by dimensionless parameters $\frac{a}{w}$, $\frac{E}{\sigma_Y}$, and ν; where a is crack length, W is the width, ν is poissons ratio, E is young's modulus and σ_Y is yield strength. In the finite element formulation exact notch dimensions are not specified but a simpler one is shown in Figure 4.1b. Because of symmetry only meshes for the upper half of the model are shown. The crack tip was modeled by a semicircular domain on the plane y = 0. There are 32 fans of elements circumferentially, and 32 rings radially. In the plane strain case, a second-order-reduced integration, eight node quadrilateral element-type GPE8R was used. The ratio of radius of the outer boundary to the radius of the first ring elements was of the order of 2.775E+07. The first ring elements were degenerated, so as to collapse a side into a single point at the crack tip. The mesh definition for the remaining part of the geometry is self explanatory, except in the pin loading region. The mesh is sufficiently fine to minimize load distribution irregularities. However, they cannot be completely removed. The semicircular domain has 1040 elements. The mesh is sufficiently fine here.

[†]The UMAT to be used in ABAQUS was given by Dr. Y. Wang [48].

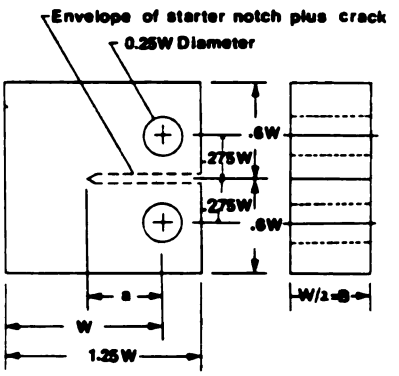

(a)

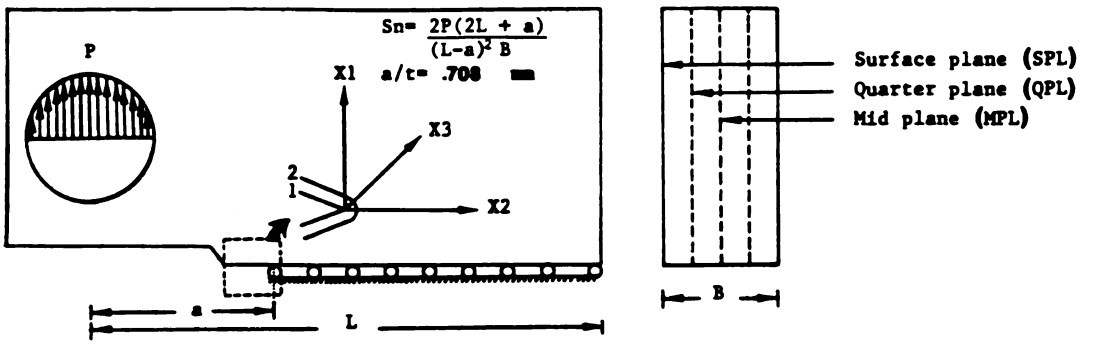

(b)

Figure 4.1. CT specimen used in energy based formulation, elastic and elastic-plastic finite element analysis, 3D photoelasticity and multiple embedded moire technique, (a) Dimensions according to ASTM E-399 [42] and (b) Loading and boundary conditions applied in FEM analysis.

In Figure 4.2 (a - e) all the nodes starting from 1 to 12801 at an increments of 400 are given $u_y = 0$ and at node 12801 both u_x and u_y are zero, to constrain the rigid body motion. Since degenerated collapsible elements have been used at the crack tip, these nodes are given displacement boundary conditions to match with node 1, using "equation [4]". This applies only for the elastic solution. A numerical error was encountered by not imposing this additional boundary condition. The specimen was loaded at the plane of the pin by giving a distributed nodal force obtained by using the shape function of elements. Loading on these types of specimens are complex in nature; but, by Saint-Venants principle, the effect of loading would not be felt near the crack tip. Constraining nodes 3 to 129 similar to node 1 (Bias=$\frac{1}{4}$) would result $\frac{1}{4}$ point concept. A sharp crack tip, and second order isoparametric elements can have such a strain singularity if they are focused at the crack tip. The only advantage obtained is that one can adjust the position of mid nodes by "Bias [4]" rather than by "Singular [4]". In the elastic solution it does not matter whether a quarter point or collapsible technique is used, but additional boundary conditions should be applied for the collapsible technique. For elastic-plastic analysis where blunting takes place, these additional boundary conditions do not apply.

4.1.2 Modeling of Boundary Layer Problem and Boundary Conditions

Plane-strain crack-tip deformation was modeled by boundary layer formulations using focused meshes of the type shown in Figure 4.3. The mesh typically involved 2048 eight node second order, reduced integration type GPE8R elements. It consists of 64 fans of elements circumfrentially, and 32 rings radially at equal angular intervals θ=5.45°. The radius of the first ring of elements was less than one-hundred thousandth of the radius of the outer ring. However the semicircular domain of radius = 100 in the boundary layer model has the same number of elements, nodes and coordinates as compared with the semicircular domain present in the CT specimen for T stress analysis. Near the crack-tip, degenerated collapsible elements have been used and nodes corresponding to these elements were given displacement boundary conditions to match with node 1. Displacement boundary conditions were imposed on the outer boundary corresponding to displacements associated with the K field.

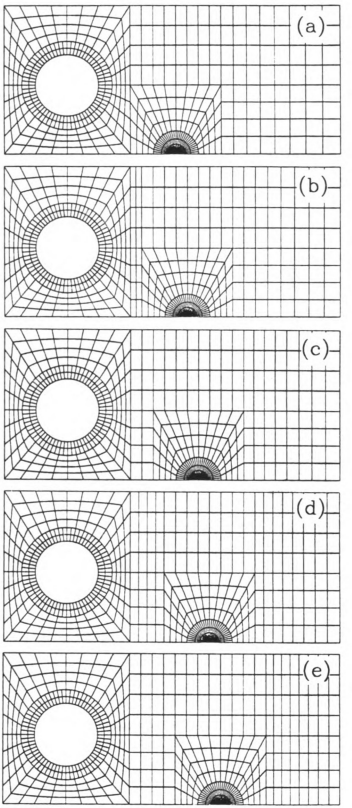

Figure 4.2: Finite element modelling of CT specimen with a/W = (a) 0.3958, (b) 0.4375, (c) 0.4790, (d) 0.5208 and (e) 0.5625.

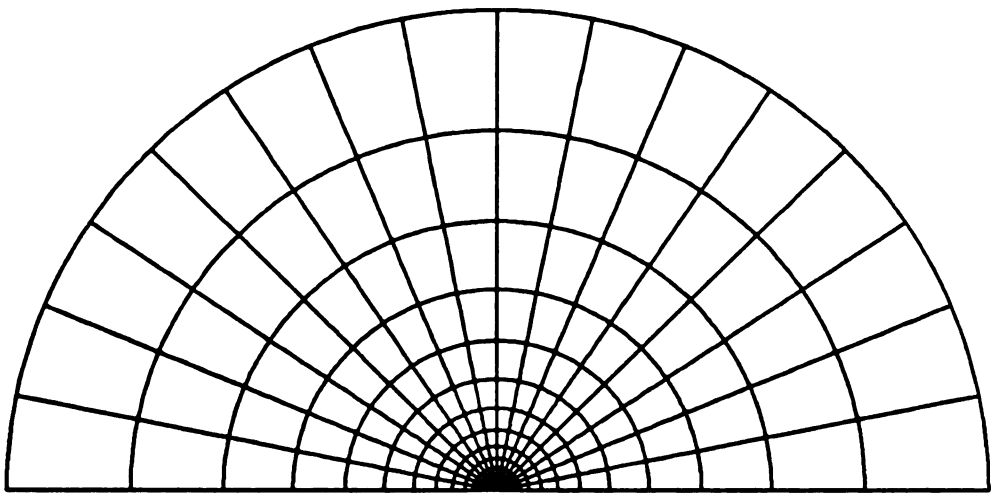

Figure 4.3: Circular domain inside the CT specimen used for boundary layer and modified boundary layer problem.

4.2 Estimation of Elastic Non-Singular Stress

In the present analysis, the total x-direction stress σ_x is determined from the solutions obtained by the elastic finite element method for the specimen with a given $\frac{a}{w}$ ratio and for the boundary layer problem for elements with one side on the crack surface. Load levels are chosen in such a way that $K_I < 0.15\sigma_Y\sqrt{a}$ for all $\frac{a}{w}$. In the first set of experiments, K_I was kept constant for all $\frac{a}{w}$ by lowering the appropriate far field load. The J value, except for the first two rings, are to be constant and should be nearly the same for both the boundary layer problem and the CT specimen. The sensivity of measuring T-stress is extremely delicate. In Larsson and Carlson [47], T stress is measured for a distance 0.02 - 0.24 times the crack length behind the crack tip‡ Before any further discussion, it is to be noted that T stress is defined by (4.1).

$$T_x = \underbrace{\sigma_x(r,\theta)_{\theta=\pi}}_{specimen} - \underbrace{\sigma_x(r,\theta)_{\theta=\pi}}_{blp} \tag{4.1}$$

The magnitude of T-stress is defined by Leevers and Radon [44] and is given in (4.2).

$$B = T_x\sqrt{\frac{\pi a}{K_I}} \tag{4.2}$$

In the above equation, B stands for biaxiality ratio. The primary reason for introducing B is as an instrument for mapping the conditions in any of the specimens analysed onto a reproducible condition of crack length and load biaxiality ratio. The crack tip stress field parameter can be regarded as a geometry-independent relative of the load biaxiality ratio. In Appendix D, as an example, the first row indicates the normalized distance $\frac{r_i}{r_o}$ where r_i represents the radius of the rings varying from inside to the outside boundary at an increment of 1.53, and $r_o = 100$ is the outer radius of the semicircular domain. The second row shows the absolute value of transverse stress σ_x behind the crack tip of a CT specimen. The third row shows the absolute value of transverse stress behind the crack tip of a boundary layer problem. The fourth row shows the difference in transverse stress between specimen and boundary layer problem. The fifth row shows the biaxiality parameter, and, finally, the last

‡they [47] stated: "The T-stress would have been exact had the average T_x been determined from element stresses over a more narrow range close to the crack tip".

row indicates all the above numerical values corresponding to the node numbers and their position radially in ascending order at an increment of 200. A comparison in the values of T-stress and biaxiality parameter B are also shown for angles varying from $\theta = 151°$ to 180°, for each $\frac{a}{w}$. The results are more consistent for 180°, even though some negative values appear at the nodes near the crack tip, which can be neglected. The numerical values of T-stress corresponding to nodes in each circumferential line are averaged as given by (4.3) and then each of these are again averaged radially to give the net T-stress.

$$T_{xc} = \sum_{i=1}^{n} \frac{T_i}{n} \tag{4.3}$$

$$T_{net} = \sum_{j=1}^{m} \frac{T_{xc}}{m} \tag{4.4}$$

In Figures 4.4 to 4.8 the biaxiality ratio for $\theta = 151°$ to 180° in the range $\frac{r_i}{r_o}$ from 0.01 to 0.2 are compared. The results are quite consistent because of the fine mesh employed in the analysis. The net T_{xc} variation with $\frac{r_i}{r_o}$ is shown in Figure 4.9. The final result in the T stress calculation is shown in Figure 4.10, in which biaxiality ratio B is compared with $\frac{a}{w}$. The results are in agreement with Leevers and Radon [44], Cotterell [45], Kfouri [46] and Larsson and Carlson [47]. The value of B depends on the ratio $\frac{\ell}{H}$ and value used in this analysis is 0.5. Kfouri [46] had used 0.833 and Larsson and Carlson [45] had used 0.4583. The values of B for $\nu = 0.3$ are listed in Table 4.1. For comparison with the photoelastic investigation the values of B for $\nu = 0.45$ are listed in Table 4.2.

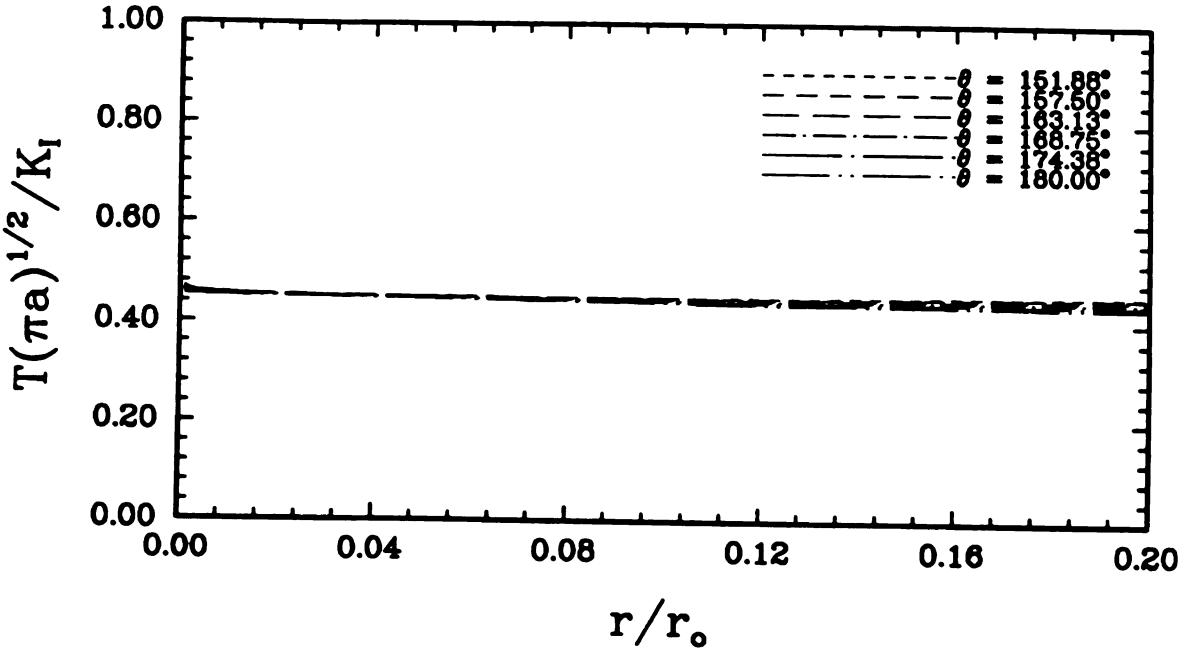

Figure 4.4: Variation of non-dimensional biaxiality parameter B for CT specimen as a function of r/r_o at a/W = 0.3958.

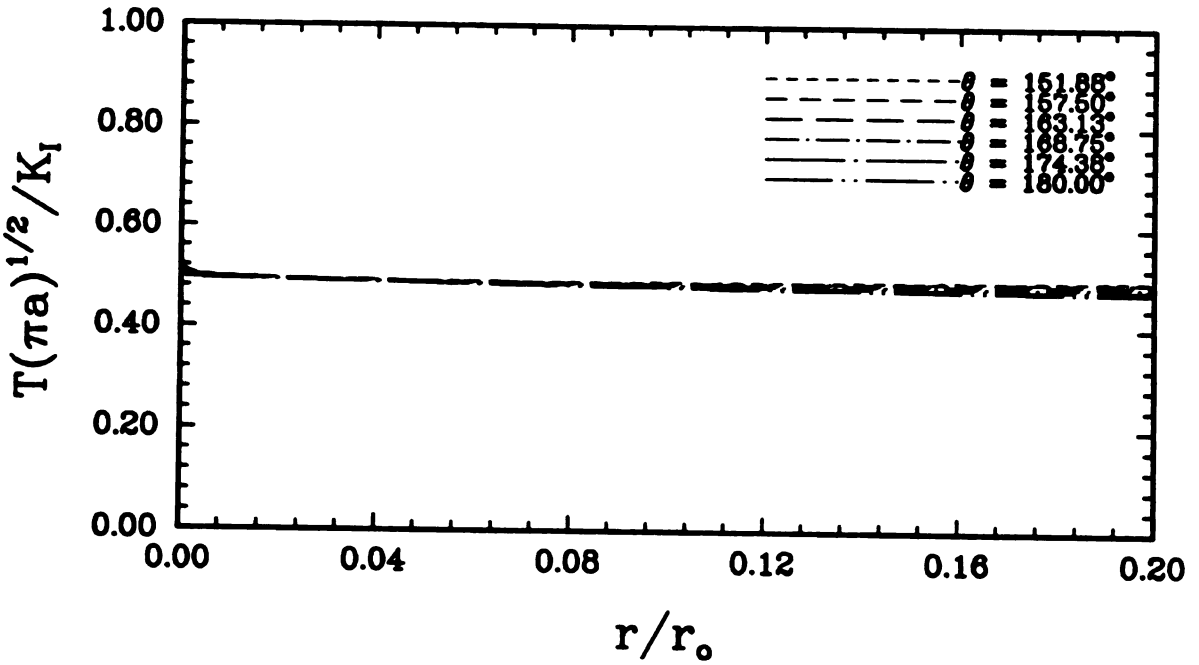

Figure 4.5: Variation of non-dimensional biaxiality parameter B for CT specimen as a function of r/r_o at a/W = 0.4375.

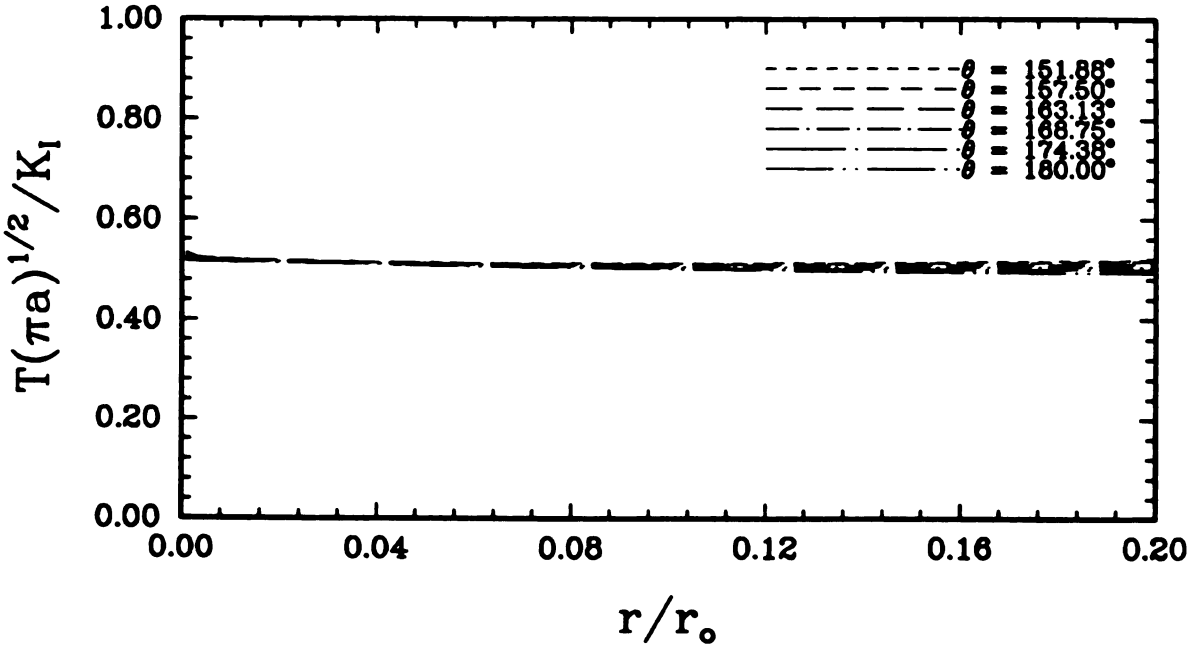

Figure 4.6: Variation of non-dimensional biaxiality parameter B for CT specimen as a function of r/r_o at a/W = 0.479.

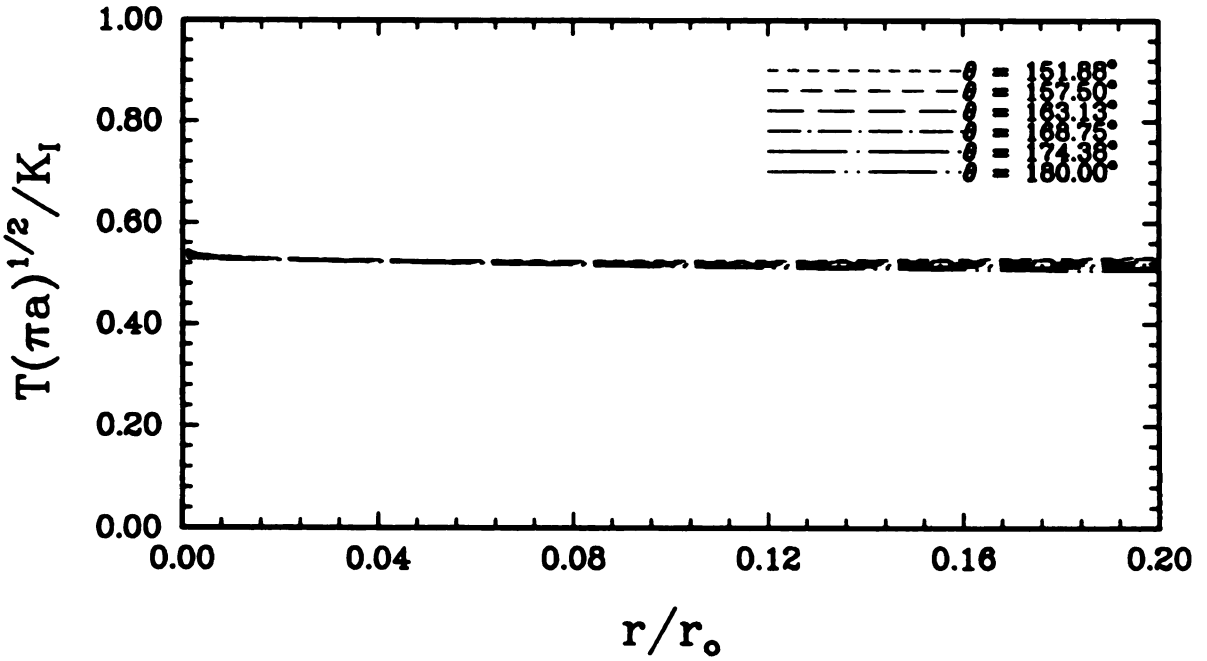

Figure 4.7: Variation of non-dimensional biaxiality parameter B for CT specimen as a function of r/r_o at a/W = 0.5208.

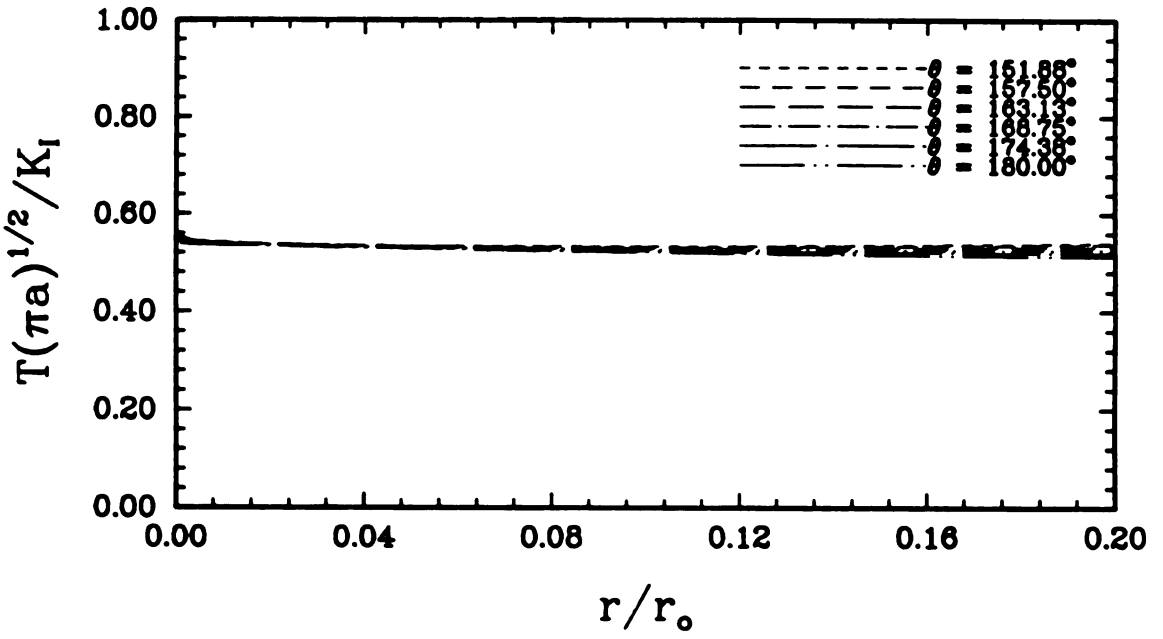

Figure 4.8: Variation of non-dimensional biaxiality parameter B for CT specimen as a function of r/r_o at a/W = 0.5625.

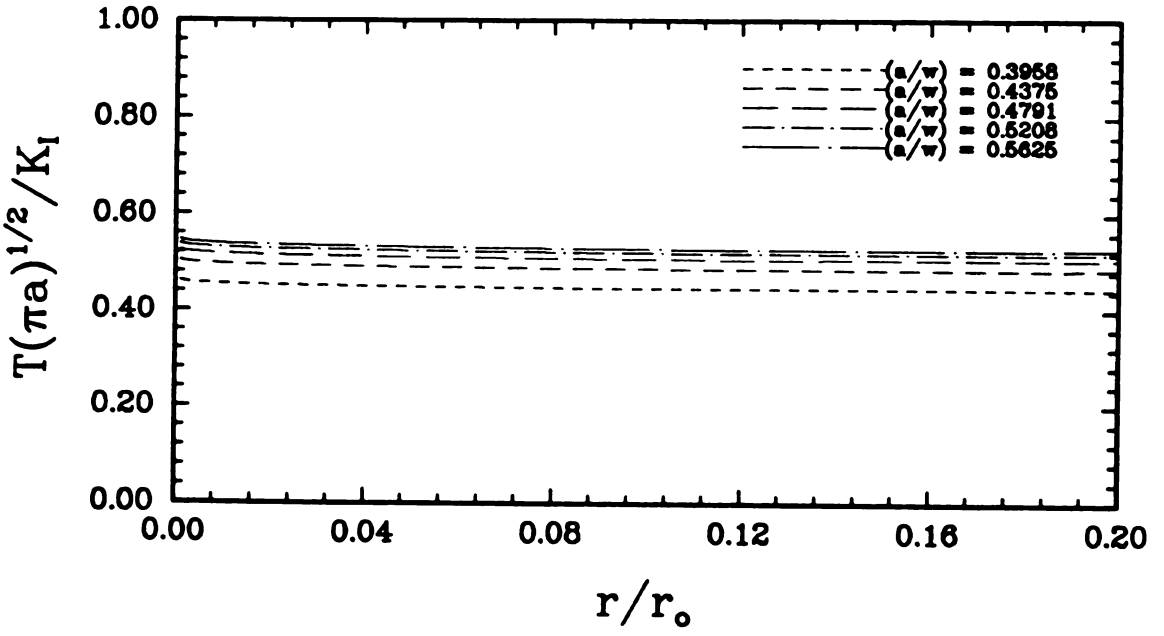

Figure 4.9: Average values of the non-dimensional biaxiality parameter B for CT specimen as a function of r/r_o.

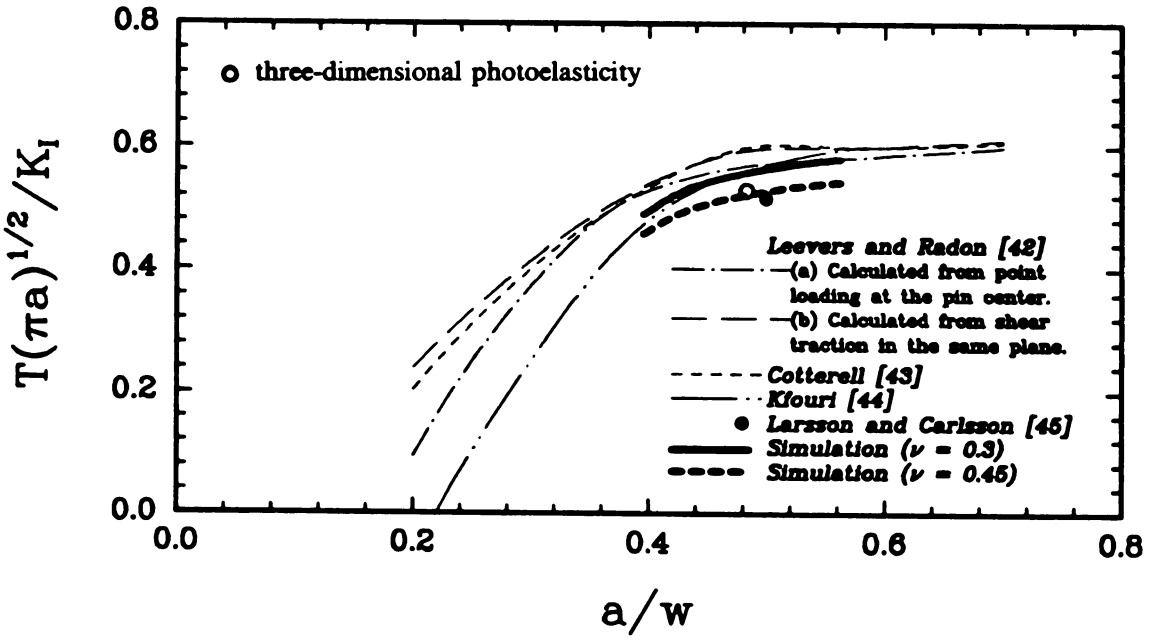

Figure 4.10. Comparision of biaxiality values for CT specimen obtained from distributed load at pin center with Leever and Radon[44], Cotterell[45], Kfouri[46] and Larsson and Carlsson [47], with simulation $\nu = 0.3$ and 0.45, 3D photoelasticity.

Table 4.1: Average biaxiality ratio (Poisson's ratio = 0.3).

B = T*Sqrt(pi*a)/K

r*	a/w = 0.3958	a/w = 0.4375	a/w = 0.4791	a/w = 0.5208	a/w = 0.5625
1.1677878E-04	5.1189304E-01	5.5882619E-01	5.8248893E-01	5.9704624E-01	6.0631162E-01
1.4849671E-04	5.0920592E-01	5.5589269E-01	5.7943122E-01	5.9391211E-01	6.0312886E-01
1.8021473E-04	5.0652948E-01	5.5297086E-01	5.7638566E-01	5.9079044E-01	5.9995874E-01
2.2901159E-04	5.0436536E-01	5.5060833E-01	5.7392309E-01	5.8826633E-01	5.9739546E-01
2.7780847E-04	5.0221072E-01	5.4825614E-01	5.7147130E-01	5.8575327E-01	5.9484339E-01
3.5288070E-04	5.0046076E-01	5.4634573E-01	5.6948000E-01	5.8371220E-01	5.9277065E-01
4.2795284E-04	4.9871985E-01	5.4444521E-01	5.6749900E-01	5.8168169E-01	5.9070863E-01
5.4344849E-04	4.9729933E-01	5.4289445E-01	5.6588258E-01	5.8002487E-01	5.8902610E-01
6.5894409E-04	4.9588613E-01	5.4135168E-01	5.6427448E-01	5.7837659E-01	5.8735224E-01
8.3662967E-04	4.9472412E-01	5.4008312E-01	5.6295221E-01	5.7702127E-01	5.8597588E-01
1.0143153E-03	4.9356892E-01	5.3882202E-01	5.6163770E-01	5.7567391E-01	5.8460762E-01
1.2876774E-03	4.9260634E-01	5.3777118E-01	5.6054236E-01	5.7455120E-01	5.8346748E-01
1.5610362E-03	4.9165088E-01	5.3672812E-01	5.5945514E-01	5.7343680E-01	5.8233579E-01
1.9815949E-03	4.9083763E-01	5.3584030E-01	5.5852973E-01	5.7248827E-01	5.8137254E-01
2.4021545E-03	4.9003130E-01	5.3496005E-01	5.5761220E-01	5.7154781E-01	5.8041748E-01
3.0491725E-03	4.8932183E-01	5.3418553E-01	5.5680489E-01	5.7072032E-01	5.7957715E-01
3.6961816E-03	4.8861897E-01	5.3341823E-01	5.5600510E-01	5.6990054E-01	5.7874465E-01
4.6915873E-03	4.8796918E-01	5.3270887E-01	5.5526570E-01	5.6914266E-01	5.7797501E-01
5.6869842E-03	4.8732573E-01	5.3200641E-01	5.5453350E-01	5.6839216E-01	5.7721287E-01
7.2183772E-03	4.8669085E-01	5.3131333E-01	5.5381107E-01	5.6765167E-01	5.7646089E-01
8.7497613E-03	4.8606171E-01	5.3062650E-01	5.5309517E-01	5.6691788E-01	5.7571571E-01
1.1105742E-02	4.8539380E-01	5.2989735E-01	5.5233514E-01	5.6613886E-01	5.7492460E-01
1.3461740E-02	4.8473078E-01	5.2917355E-01	5.5158069E-01	5.6536555E-01	5.7413929E-01
1.7086327E-02	4.8397923E-01	5.2835309E-01	5.5072548E-01	5.6448897E-01	5.7324911E-01
2.0710915E-02	4.8323079E-01	5.2753603E-01	5.4987383E-01	5.6361604E-01	5.7236262E-01
2.6287164E-02	4.8234790E-01	5.2657218E-01	5.4886917E-01	5.6258628E-01	5.7131688E-01
3.1863478E-02	4.8146545E-01	5.2560883E-01	5.4786503E-01	5.6155703E-01	5.7027167E-01
4.0442382E-02	4.8043082E-01	5.2447934E-01	5.4668770E-01	5.6035029E-01	5.6904619E-01
4.9021285E-02	4.7938911E-01	5.2334212E-01	5.4550233E-01	5.5913529E-01	5.6781234E-01
6.2219603E-02	4.7826500E-01	5.2211494E-01	5.4422319E-01	5.5782418E-01	5.6648089E-01
7.5417967E-02	4.7712220E-01	5.2086736E-01	5.4292279E-01	5.5649128E-01	5.6512729E-01
9.5723040E-02	4.7621583E-01	5.1987790E-01	5.4189142E-01	5.5543414E-01	5.6405376E-01
1.1602843E-01	4.7525305E-01	5.1882685E-01	5.4079587E-01	5.5431121E-01	5.6291340E-01
1.4726705E-01	4.7546739E-01	5.1906084E-01	5.4103976E-01	5.5456119E-01	5.6316726E-01
1.7850567E-01	4.7555641E-01	5.1915801E-01	5.4114105E-01	5.5466502E-01	5.6327270E-01
2.2656457E-01	4.7929764E-01	5.2324227E-01	5.4539825E-01	5.5902861E-01	5.6770400E-01
	4.8900342E-01	5.3383793E-01	5.5564425E-01	5.7037391E-01	5.7923414E-01

** a - crack length, W - width, r* - distance behind the crack tip, K - stress intensity factor, T - T-stress

Table 4.2: Average biaxiality ratio (Poisson's ratio = 0.45).

B = T*Sqrt(pi*a)/K

r*	a/w = 0.3958	a/w = 0.4375	a/w = 0.4791	a/w = 0.5208	a/w = 0.5625
1.1677878E-04	4.7887594E-01	5.2278190E-01	5.4491839E-01	5.5853676E-01	5.3710731E-01
1.4849671E-04	4.7636214E-01	5.2003761E-01	5.4205791E-01	5.5560478E-01	5.3544523E-01
1.8021473E-04	4.7385833E-01	5.1730424E-01	5.3920878E-01	5.5268446E-01	5.3348915E-01
2.2901159E-04	4.7183379E-01	5.1509409E-01	5.3690505E-01	5.5032315E-01	5.3118844E-01
2.7780847E-04	4.6981813E-01	5.1289362E-01	5.3461140E-01	5.4797218E-01	5.2867658E-01
3.5288070E-04	4.6818104E-01	5.1110643E-01	5.3274854E-01	5.4606276E-01	5.2660549E-01
4.2795284E-04	4.6655242E-01	5.0932849E-01	5.3089531E-01	5.4416322E-01	5.2694161E-01
5.4344849E-04	4.6522352E-01	5.0787776E-01	5.2938315E-01	5.4261327E-01	5.3483728E-01
6.5894409E-04	4.6390147E-01	5.0643450E-01	5.2787878E-01	5.4107130E-01	5.6324341E-01
8.3662967E-04	4.6281441E-01	5.0524776E-01	5.2664179E-01	5.3980340E-01	6.4337907E-01
1.0143153E-03	4.6173372E-01	5.0406800E-01	5.2541207E-01	5.3854294E-01	8.6365247E-01
1.2876774E-03	4.6083323E-01	5.0308494E-01	5.2438738E-01	5.3749265E-01	5.4583383E-01
1.5610362E-03	4.5993940E-01	5.0210916E-01	5.2337028E-01	5.3645013E-01	5.4477513E-01
1.9815949E-03	4.5917860E-01	5.0127860E-01	5.2250456E-01	5.3556278E-01	5.4387401E-01
2.4021545E-03	4.5842428E-01	5.0045513E-01	5.2164621E-01	5.3468298E-01	5.4298055E-01
3.0491725E-03	4.5776057E-01	4.9973056E-01	5.2089097E-01	5.3390886E-01	5.4219442E-01
3.6961816E-03	4.5710305E-01	4.9901275E-01	5.2014277E-01	5.3314196E-01	5.4141562E-01
4.6915873E-03	4.5649517E-01	4.9834915E-01	5.1945106E-01	5.3243296E-01	5.4069562E-01
5.6869842E-03	4.5589322E-01	4.9769200E-01	5.1876609E-01	5.3173087E-01	5.3998264E-01
7.2183772E-03	4.5529929E-01	4.9704362E-01	5.1809026E-01	5.3103814E-01	5.3927916E-01
8.7497613E-03	4.5471073E-01	4.9640109E-01	5.1742053E-01	5.3035168E-01	5.3858205E-01
1.1105742E-02	4.5408590E-01	4.9571897E-01	5.1670952E-01	5.2962290E-01	5.3784196E-01
1.3461740E-02	4.5346564E-01	4.9504186E-01	5.1600374E-01	5.2889947E-01	5.3710731E-01
1.7086327E-02	4.5276257E-01	4.9427432E-01	5.1520369E-01	5.2807943E-01	5.3627454E-01
2.0710915E-02	4.5206240E-01	4.9350996E-01	5.1440697E-01	5.2726281E-01	5.3544523E-01
2.6287164E-02	4.5123646E-01	4.9260827E-01	5.1346711E-01	5.2629946E-01	5.3446694E-01
3.1863478E-02	4.5041093E-01	4.9170706E-01	5.1252774E-01	5.2533660E-01	5.3348915E-01
4.0442382E-02	4.4944303E-01	4.9065042E-01	5.1142634E-01	5.2420770E-01	5.3234271E-01
4.9021285E-02	4.4846851E-01	4.8958655E-01	5.1031743E-01	5.2307106E-01	5.3118844E-01
6.2219603E-02	4.4741691E-01	4.8843853E-01	5.0912079E-01	5.2184452E-01	5.2994287E-01
7.5417967E-02	4.4634782E-01	4.8727142E-01	5.0790427E-01	5.2059759E-01	5.2867658E-01
9.5723040E-02	4.4549991E-01	4.8634578E-01	5.0693942E-01	5.1960864E-01	5.2767229E-01
1.1602843E-01	4.4459923E-01	4.8536252E-01	5.0591454E-01	5.1855814E-01	5.2660549E-01
1.4726705E-01	4.4479974E-01	4.8558142E-01	5.0614270E-01	5.1879199E-01	5.2684297E-01
1.7850567E-01	4.4488302E-01	4.8567232E-01	5.0623745E-01	5.1888913E-01	5.2694161E-01
2.2656457E-01	4.4838294E-01	4.8949314E-01	5.1022006E-01	5.2297126E-01	5.3108709E-01
	4.5746269E-01	4.9940534E-01	5.1980519E-01	5.3358479E-01	5.4187353E-01

** a - crack length, W - width, r* - distance behind the crack tip, K - stress intensity factor, T - T-stress

4.3 Modified Boundary Layer Formulation

The modified boundary layer was modeled using focused meshes of the type shown in Figure 4.3. The semicircular domain has an outer radius of the order 10^6. The mesh typically involved 2048 eight-noded hybrid isoparametric elements consisting of 64 rings radially and 64 fans of elements circumferentially. The ratio of radius of the outer boundary to the radius of the first ring element was on the order of 10^7. The first ring elements were degenerated so one side collapsed into a single point at the crack tip. The boundary conditions given are the same as for the boundary layer formulation, except for the nodes of the first rings, where blunting is allowed. Displacement boundary conditions were imposed on the outer boundary corresponding to the displacements associated with the K field plus the displacements due to the T or σ_{ox} stress given by (1.15).

The crack-tip fields of the modified boundary layer solution far from the outer boundary and outside the crack-tip blunting zone should represent those of any crack with the same values of K_I and T. The formulation does not involve an explicit crack or ligament length, and so a dimensional scale is introduced by the radius at which displacements appropriate to a given K and T field could be applied. The K and T terms were increased in a proportional way by an imposed biaxiality parameter B for all $\frac{a}{w}$ of the CT specimen. The T-stress is essentially based on an elastic concept, and it is calculated from the remote K field using the biaxiality paramer B.

4.3.1 Ramberg-Osgood Materials

The elastic-plastic finite element analysis was done for all $\frac{a\sigma_o}{J}$ based on deformation plasticity. In deformation plasticity the material response was described by a Ramberg-Osgood power law of the form given in (1.19), with the exponent n = 5 and 10. Poisson's ratio was set as 0.3, and $\alpha = 1$, while the ratio of the yield stress σ_o to the elastic modulus was 0.0025.

A second kind of material response was described by a Modified Ramberg-Osgood power law of the form given in (1.20), with the same material properties as above, except that material constant α is absent. This equation was made use of by Wang [48] to obtain consistent J_{local} as compared to J_{far} for $\frac{T}{\sigma_o} \leq 1.0$.

$$\frac{\epsilon}{\epsilon_o} = \begin{cases} \frac{\sigma}{\sigma_o} & \text{for } \sigma \leq \sigma_o \\ \left(\frac{\sigma}{\sigma_o}^n\right) & \text{for } \sigma > \sigma_o \end{cases} \tag{4.5}$$

A comparison between (1.19) and (4.5) is shown in Figure 4.11. The power law part of the modified Ramberg-Osgood for both n = 5 and 10 lie above the Ramberg-Osgood material. This difference is due to the material constant α. If α is sufficiently large, the power law part of the Ramberg-Osgood will lie above the modified one.

4.3.2 Effect of Non-singular Stress

For elastic-plastic solution with B = 0, the two power laws gave identical results. The presence of T stress in the elastic-plastic calculations introduced a difference larger by 0.2 % to 0.38 % of K component of the far field.

The small-scale yielding solutions are than compared with the HRR singular field. In the vicinity of the crack tip, elastic strains are negligible as compared to plastic strains. The plastic part of the strain dominates the asymptotic solution. The asymptotic crack tip stress, strain and displacement fields were given in (1.23 - 1.25).

In the present analysis, the value of $\frac{r\sigma_o}{J}$ obtained from finite element analysis of modified boundary layer problem and with the given parameters in Table 1.1 are substituted in (1.23 - 1.25) to give the stress distribution ahead of a crack tip.

The stress distribution in z and y directions for B = 0 ($\theta = 0$) for the two different material responses and for n = 5,10 are shown in Figures 4.12 and 4.13. In order to reduce the singularity near the sharp crack tip a circular hole was made. The results for this case are superimposed with the HRR solution. The stresses are normalized by the initial yield stress σ_o, while the radial distances of a point from the crack tip, r, are nondimensionalized by $\frac{J}{\sigma_o}$. The data will be self similar in the sense that data obtained for a given applied K field falls on the same curve as that for a higher K. The x component stress falls below the HRR field for a distance greater than $\frac{2r\sigma_o}{J}$ for n = 5 and $\frac{1r\sigma_o}{J}$ for n = 10. The y component stress falls below the HRR field for a distance approximately greater than $\frac{1.5r\sigma_o}{J}$ for n = 5 and 10.

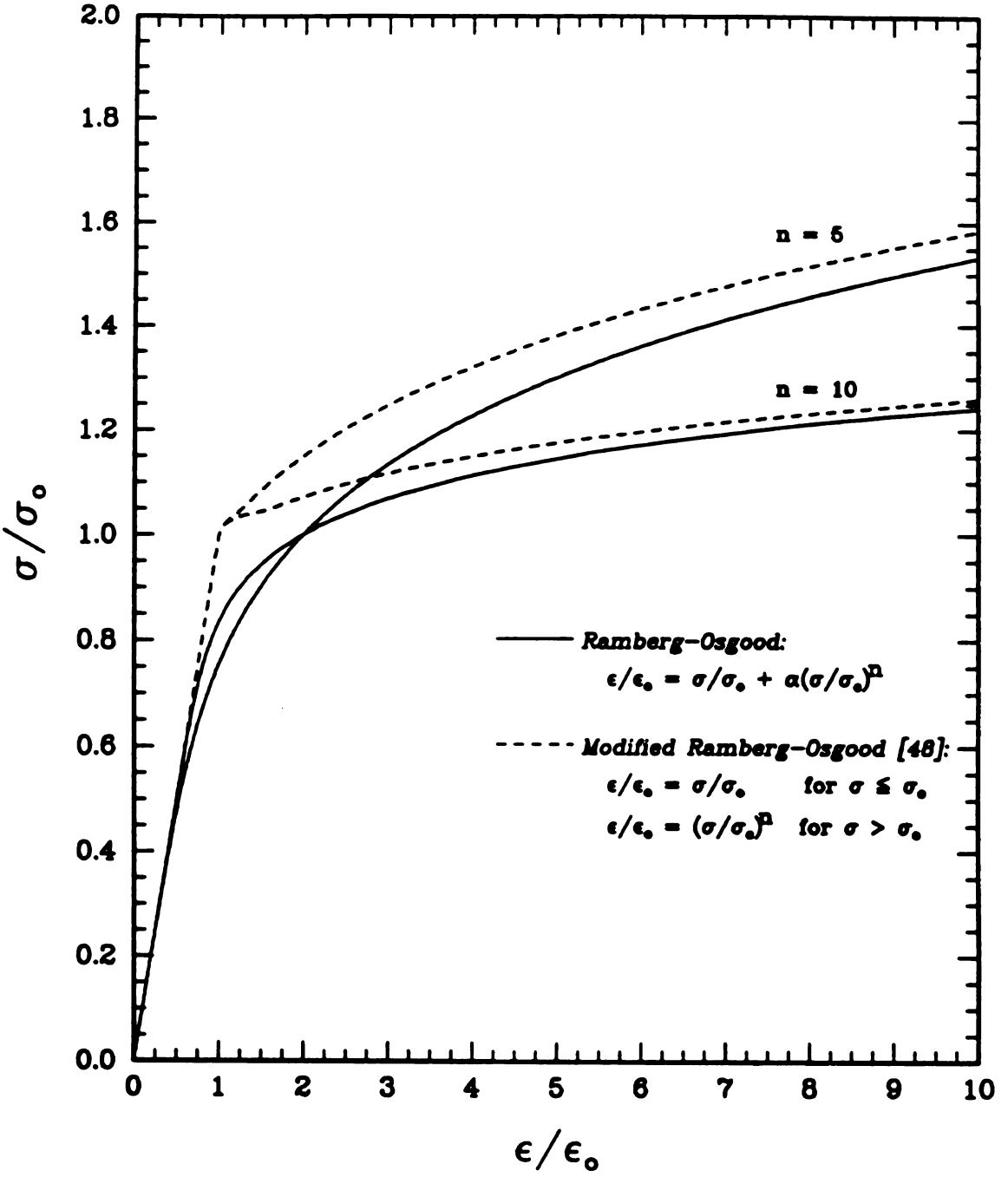

Figure 4.11: Normalized true stress-strain curve based on empirical equation.

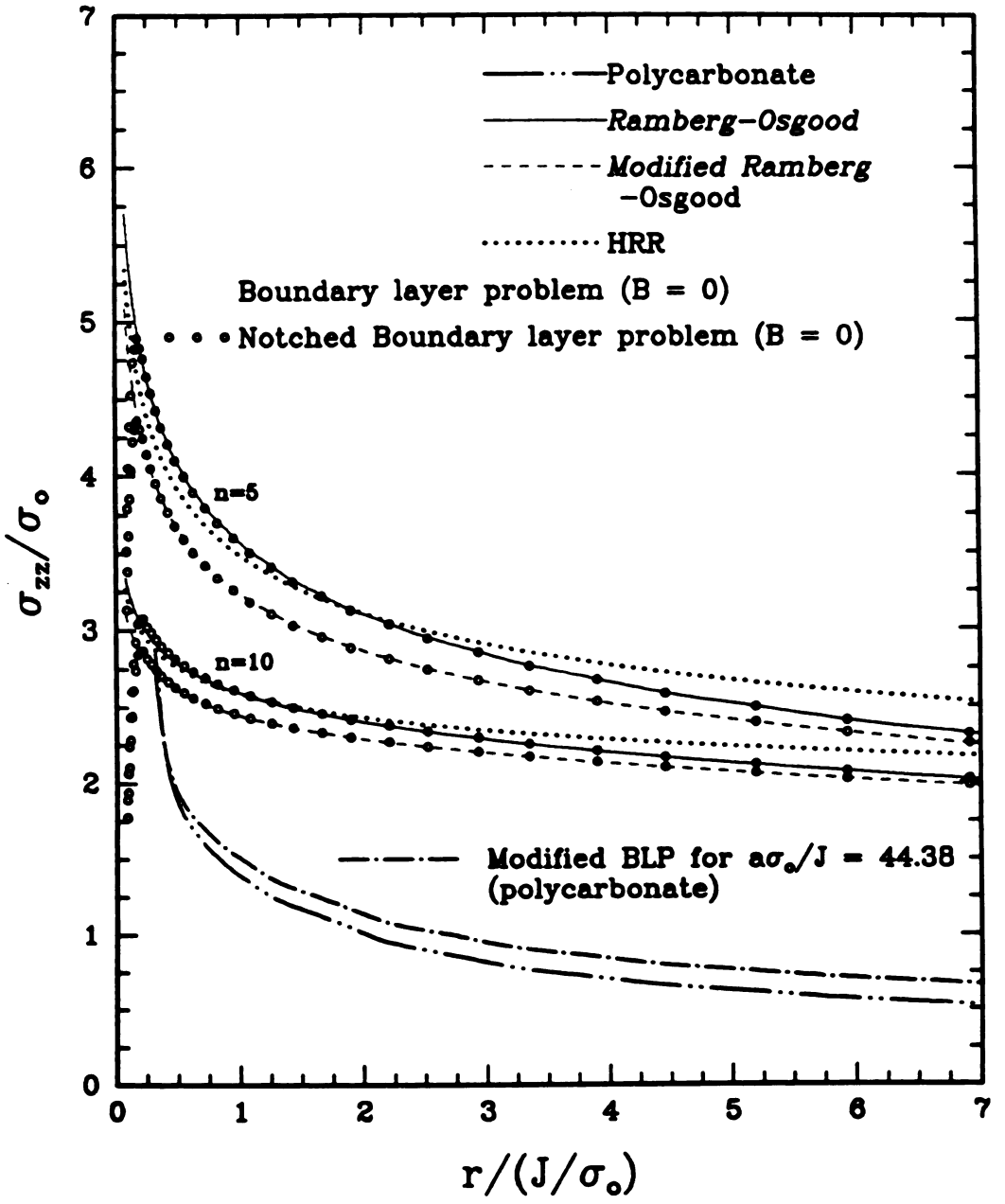

Figure 4.12: Normalized normal stress distribution for $\theta = 0°$.

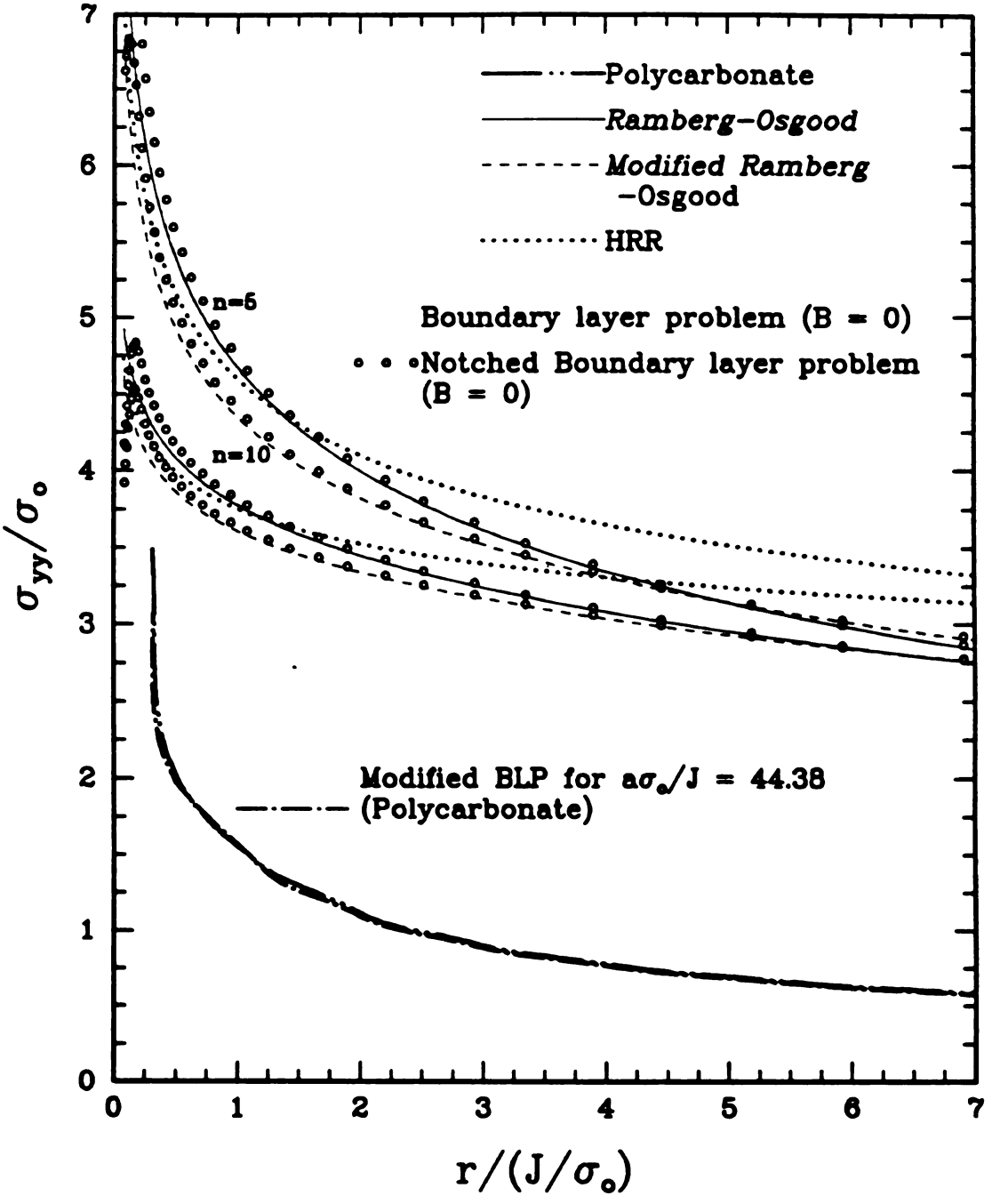

Figure 4.13: Normalized crack opening stress distribution in plane strain for $\theta = 0°$.

Figures 4.14 to 4.17 illustrates the behavior of the normal stresses on the same plane with positive biaxiality parameters B = 0.4890, 0.5338, 0.5564, and 0.5703, each of which produces tensile T stresses increasing with deformation. The data are again compared with the HRR and B = 0 fields. In this case the data are not quite self similar. Early in the deformation, the stresses are comparable to the B = 0 field, but with increased loading the stresses rise slightly, until the data closely approximate the HRR field. For the case of negative T stress, however, the data fall and depart significantly from the HRR field [48].

A consequence of equation (1) is that the plastic zone dimensions r_p and the crack tip opening displacement δ_t, when definable, are given by (4.6) and (4.7).

$$r_p = \alpha \frac{K^2}{\sigma_o} \tag{4.6}$$

$$\delta_t = \beta \frac{K^2}{E\sigma_o} \tag{4.7}$$

Here α and β are dimensionless factors which may, for example, depend on Poisson's ratio, strain-hardening exponent, etc.; but they are independent of the applied load and specimen geometry. When these equations generated by the boundary layer formulation were compared with the elastic-plastic formulation, the approximation was valid up to substantial fractions of the loads corresponding to general yielding. The plane strain elastic-plastic calculation based on the finite element method showed a significant difference from the boundary layer formulation, even within the rather small range of yield zone sizes allowed by the ASTM limits on fracture test correlation in terms of K-values. The maximum value of the plastic zone extent is at 71° with a numerical coefficent 0.152 for r_p. The results of boundary layer formulation are illustrated in Figures 4.18 and 4.19 for strain-hardening coefficients equal to 5 nd 10, and for B = 0.

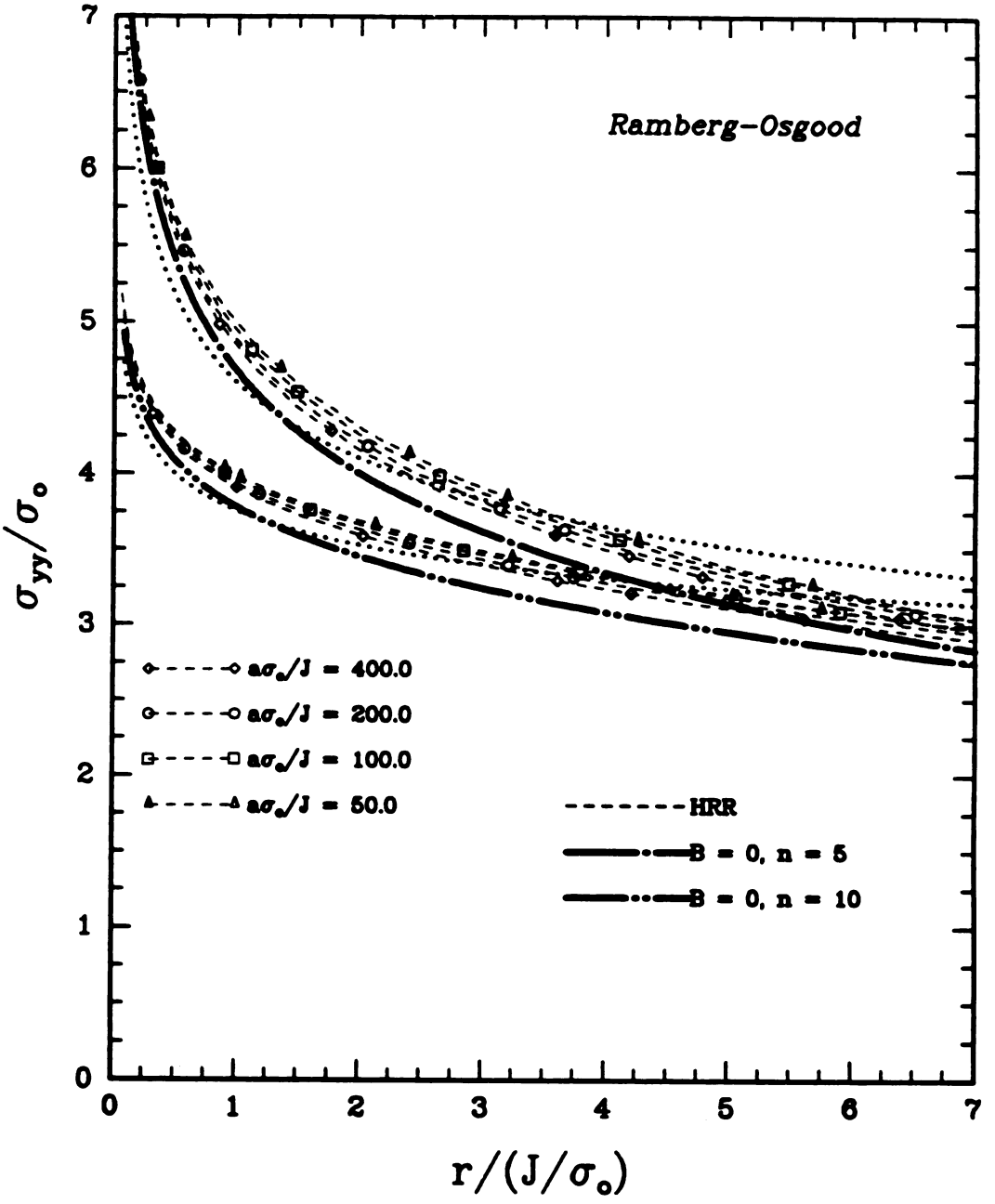

Figure 4.14: Normalized crack opening stress distribution in plane strain for biaxiality ratio B = 0.4890 and for $\theta = 0°$ for modified boundary layer problem.

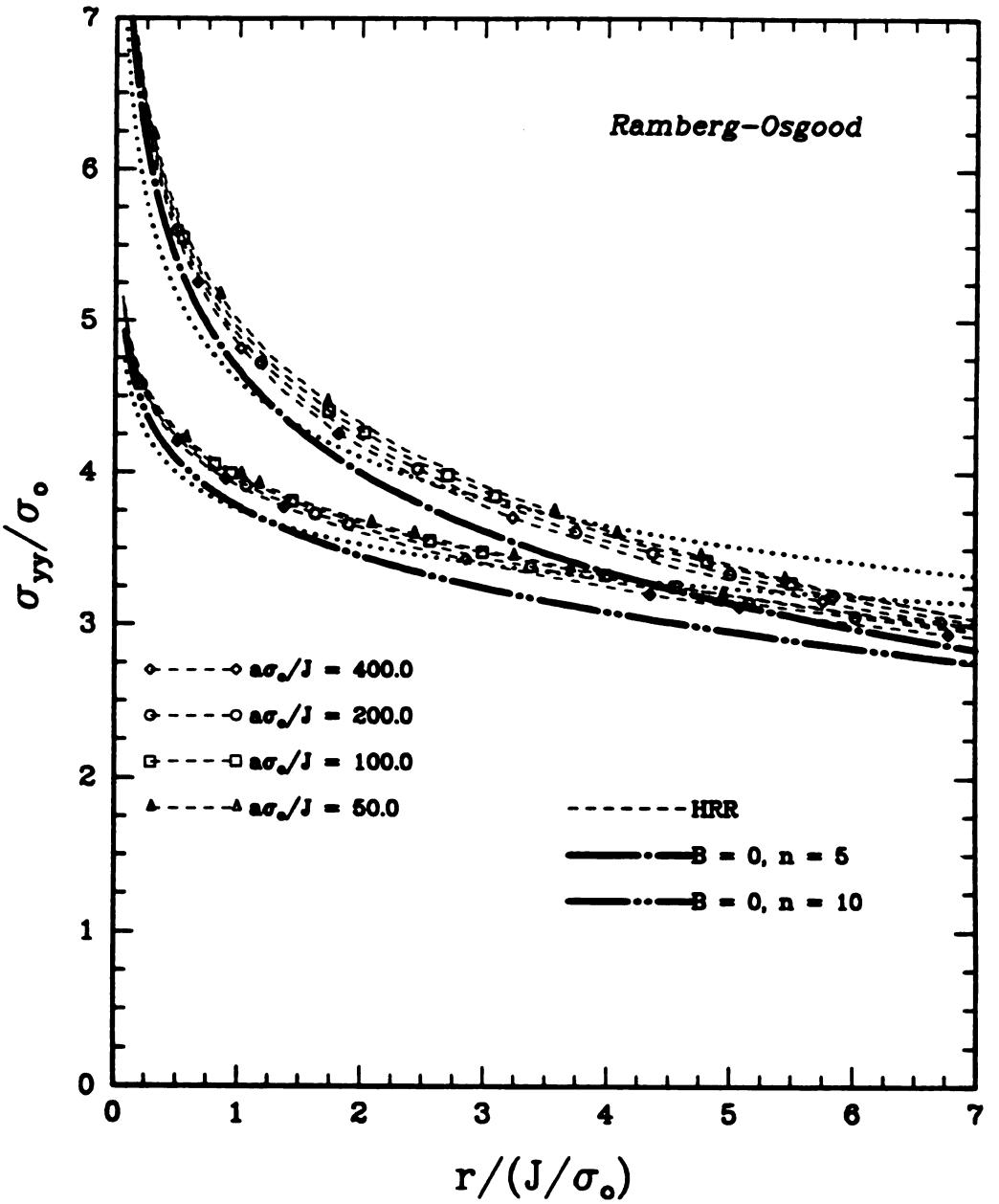

Figure 4.15: Normalized crack opening stress distribution in plane strain for biaxiality ratio B = 0.5338 and for $\theta = 0°$ for modified boundary layer problem.

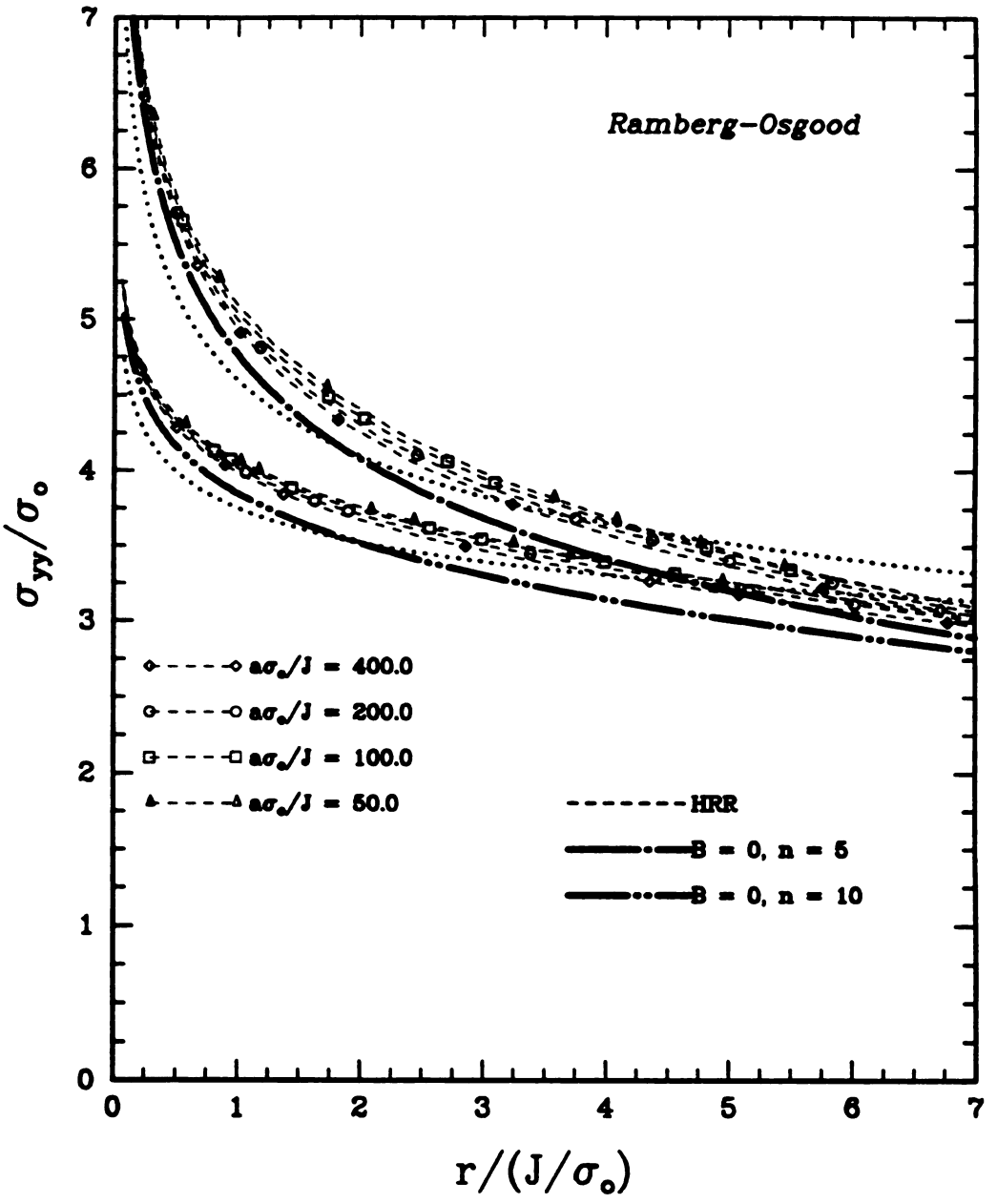

Figure 4.16: Normalized crack opening stress distribution in plane strain for biaxiality ratio B = 0.5564 and for $\theta = 0°$ for modified boundary layer problem.

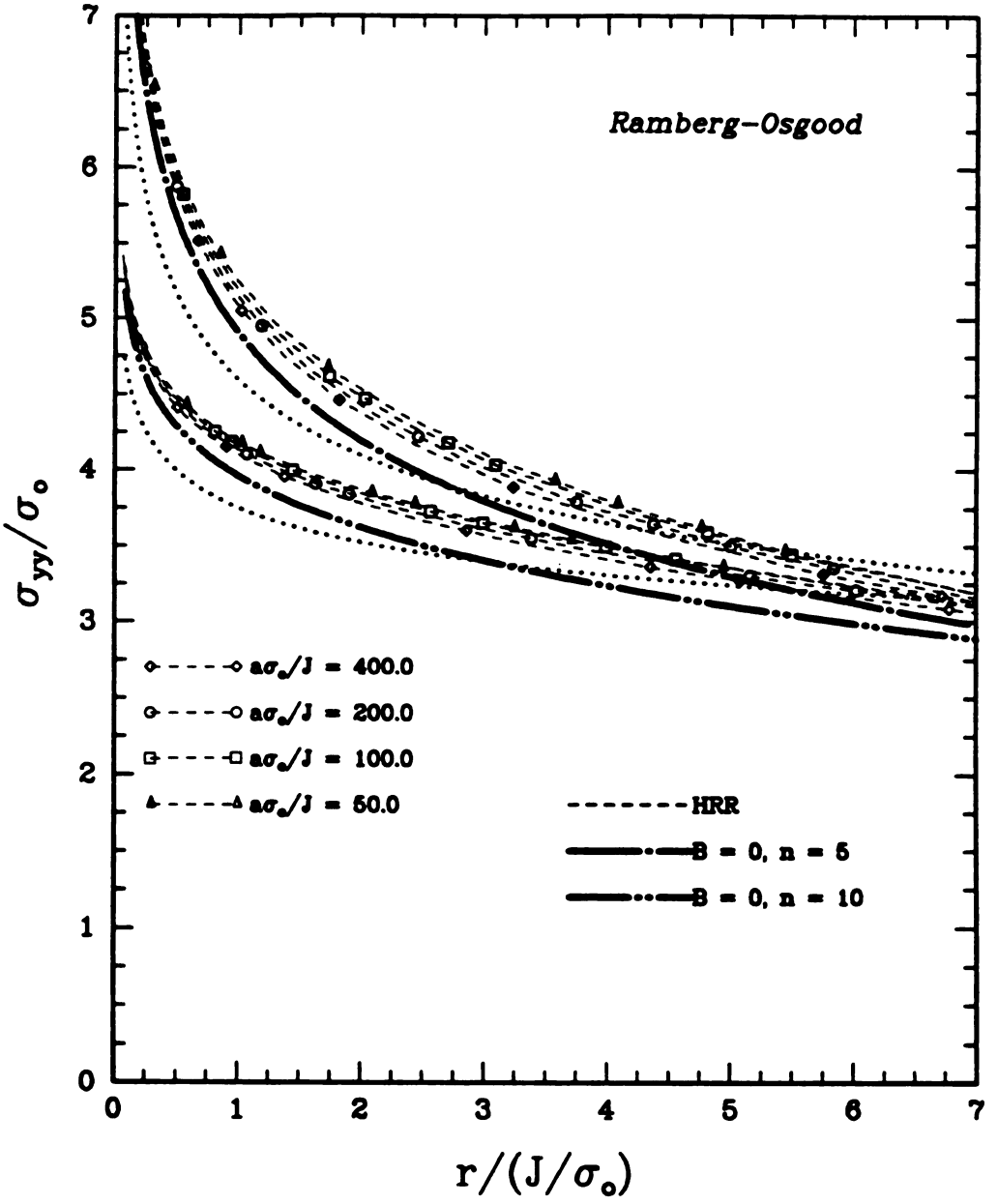

Figure 4.17: Normalized crack opening stress distribution in plane strain for biaxiality ratio B = 0.5703 and for $\theta = 0°$ for modified boundary layer problem.

But at $\frac{\sigma_{equivalent}}{\sigma_{yield}} = 1.2$, both the material responses showed the same magnitude and both had maximum at 71°. For n = 10 and B = 0, the material response behavior remains the same until $\frac{\sigma_{equivalent}}{\sigma_{yield}} = 1.2$, but when this value is exceeded the Ramberg-Osgood material response takes over from the Modified ones. The effect of T stress is very significant in the modified boundary layer and these are illustrated in Figures 4.20 to 4.23 for n = 5 and 10 for Ramberg-Osgood material only. The maximum extent of the plastic zone size varies from 71° to 130°. The effect of $\frac{\sigma_{equivalent}}{\sigma_{yield}}$ conceptually remains the same. There is less T-effect on the dominant singularity (J) and crack opening displacement, although there is an effect on over all shape of the plastic zone.

Particular attention is paid to the development of the stress ahead of the crack at a distance $r = \frac{2J}{\sigma_o}$ and $r = \frac{5J}{\sigma_o}$ as illustrated in Figure 4.24, for n = 5 and n = 10.

Figures 4.25 and 4.26 illustrates the comparison between full field (CT specimen) and the modified boundary layer solutions for $\frac{a}{w}$ 0.3958 and 0.5208. They seem to match even at $\frac{a}{\sigma_o} = 50$, which correponds to fully plastic case.

4.3.3 Polycarbonate Materials

A detailed analysis for Ramberg-Osgood material was done for various a/W ratios as was observed earlier. In this section elastic-plastic strain or stresses will be calculated using incremental plasticity theory for a/W = 0.4966 only. The procedure is the same as before. The semicircular domain consists of 256 elements and 833 nodes. In Figure 4.12 a comparison of normalized normal stress and in Figure 4.13 a comparison of crack opening stress between the boundary layer problem (B = 0) and the modified boundary layer problem (B = 0.5233) for $\frac{a\sigma_o}{J} = 44.38$ are made. The effect of biaxiality parameter is significant for normal stress, but it is less significant for crack opening stress.

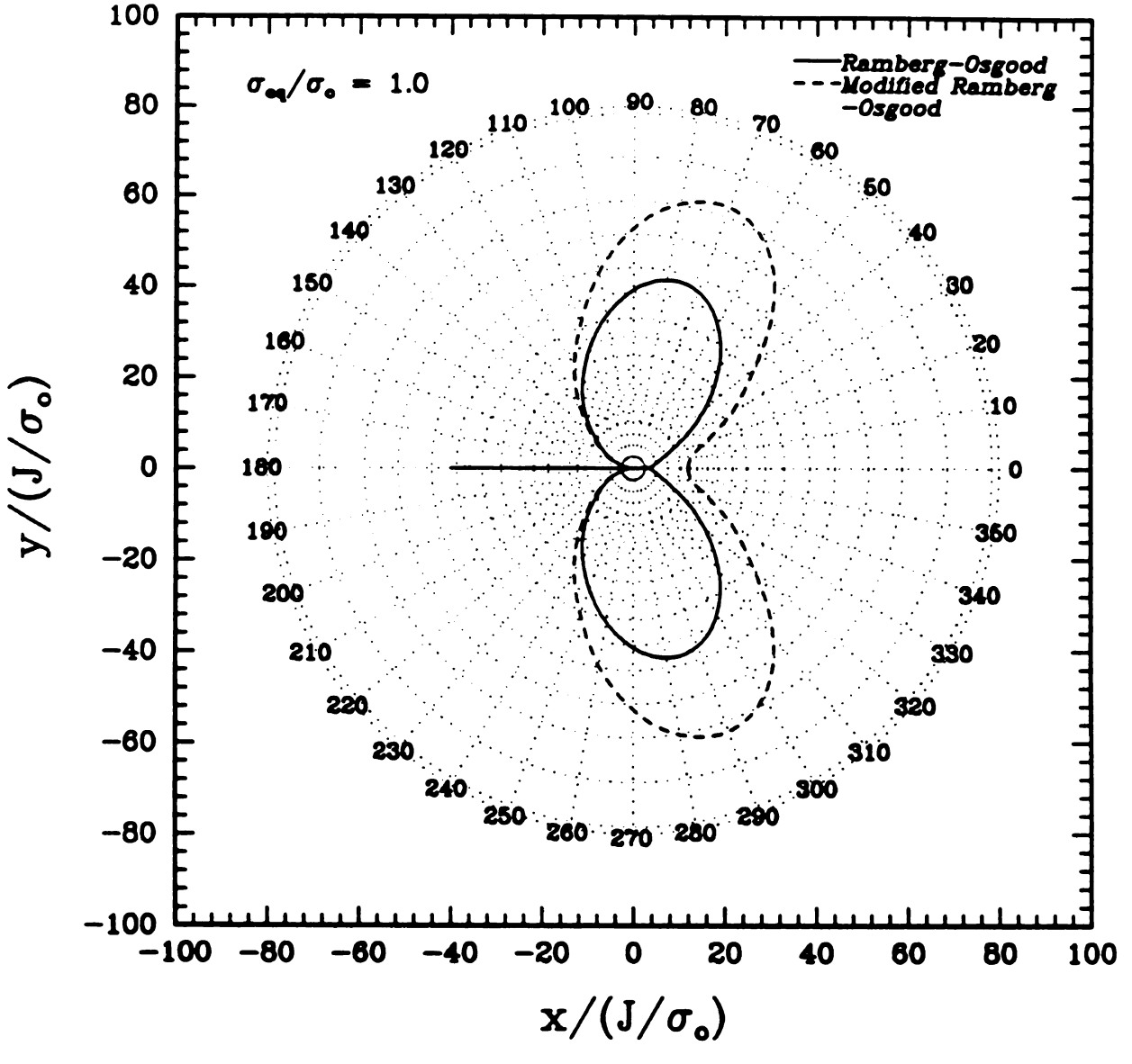

Figure 4.18: Comparision of plastic zones between Ramberg-Osgood and Modified Ramberg-Osgood in coordinate system, non dimensionalized with respect to the characteristic length parameter (J/σ_o), in plane strain for B = 0 and strain hardening value n = 5

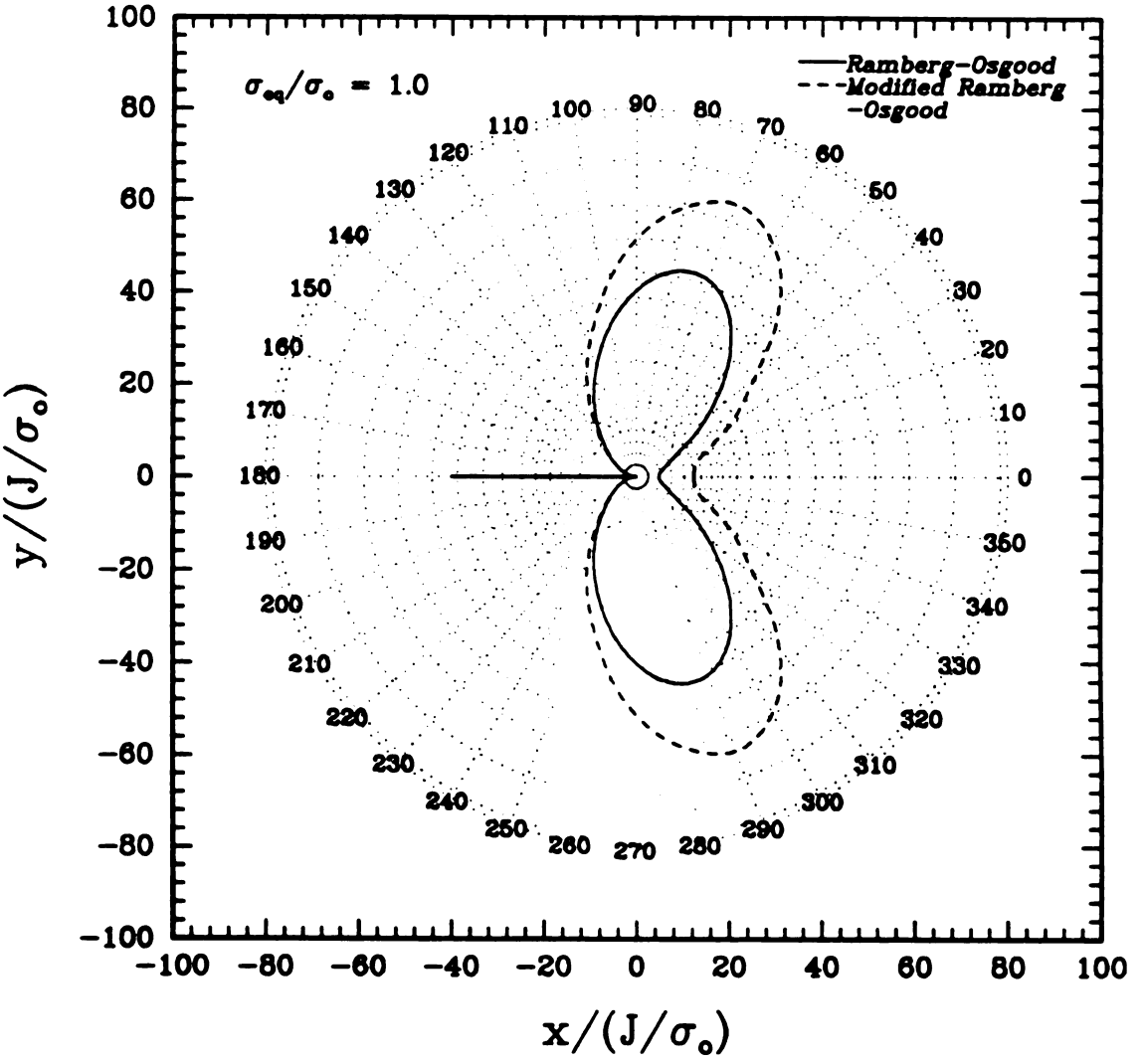

Figure 4.19: Comparision of plastic zones between Ramberg-Osgood and Modified Ramberg-Osgood in coordinate system, non dimensionalized with respect to the characteristic length parameter (J/σ_o), in plane strain for B = 0 and strain hardening value n = 10

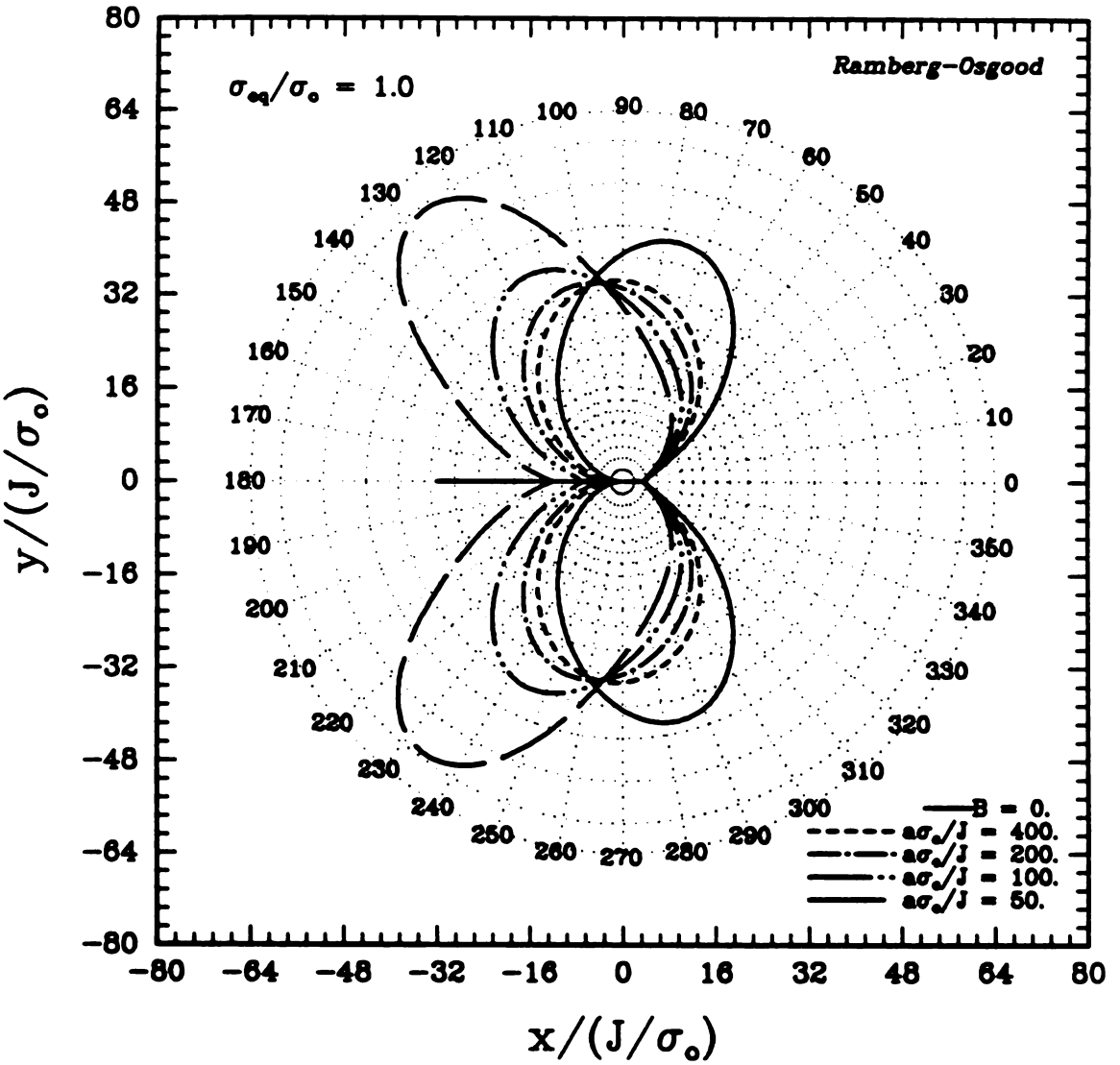

Figure 4.20: Effect of B = 0.4890 on plastic zones in coordinate system, non dimensionalized with respect to the characteristic length parameter (J/σ_o), in plane strain for σ_{eq}/σ_o = 1.0 and strain hardening value n = 5.

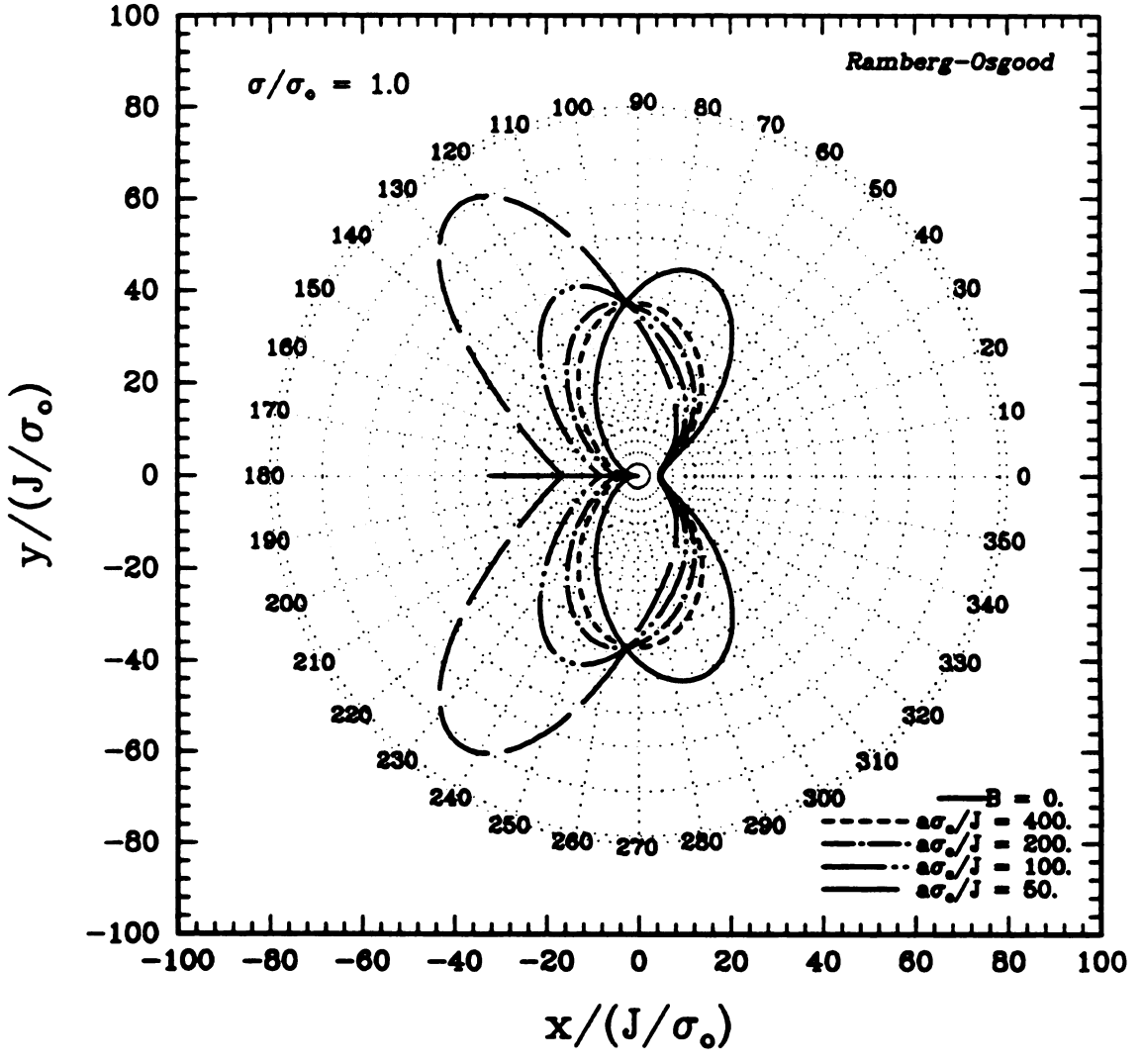

Figure 4.21: Effect of B = 0.4890 on plastic zones in coordinate system, non dimensionalized with respect to the characteristic length parameter (J/σ_o), in plane strain for σ_{eq}/σ_o = 1.0 and strain hardening value n = 10.

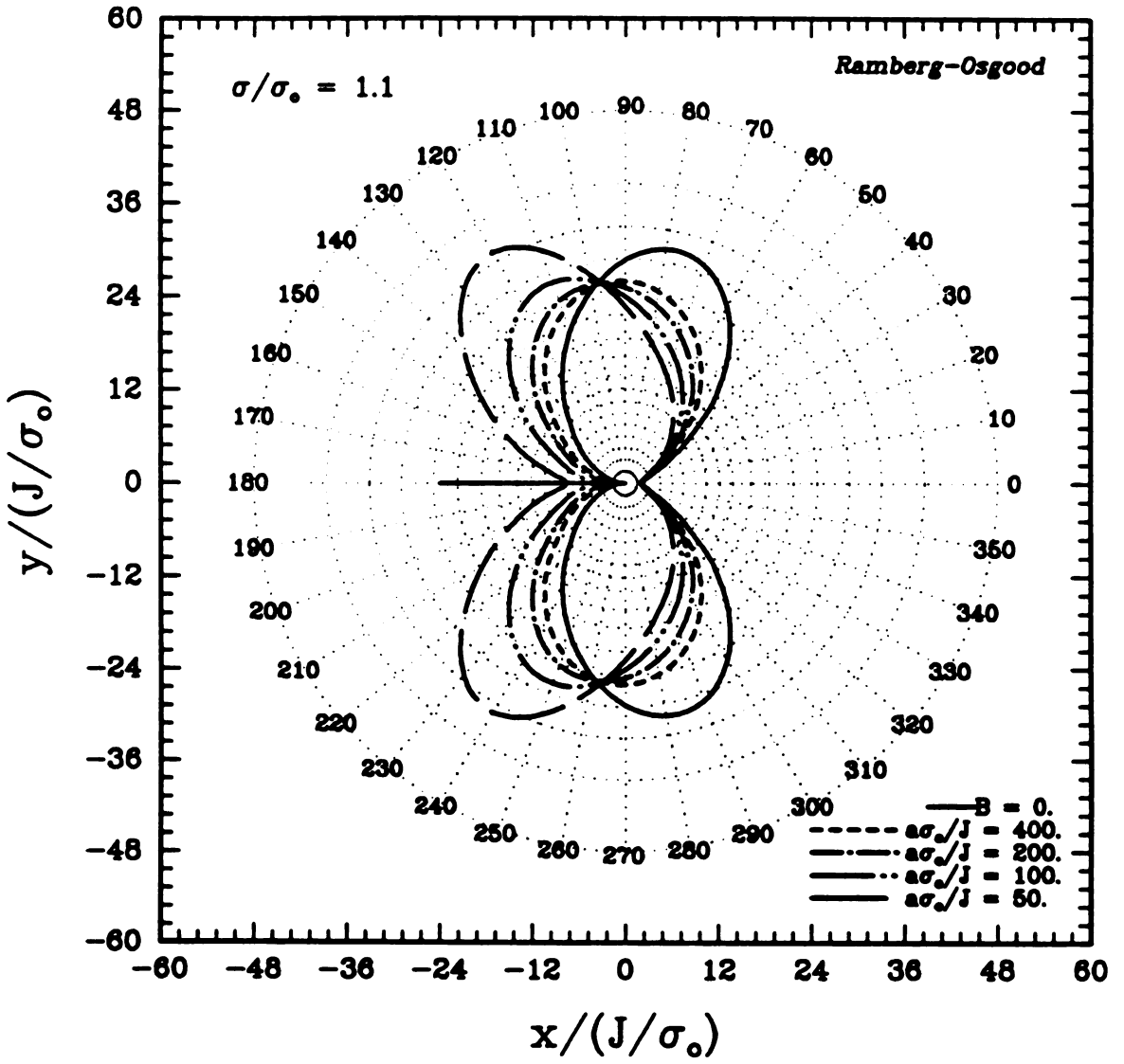

Figure 4.22: Effect of B = 0.4890 on plastic zones in coordinate system, non dimensionalized with respect to the characteristic length parameter (J/σ_o), in plane strain for $\sigma_{eq}/\sigma_o = 1.1$ and strain hardening value n = 5.

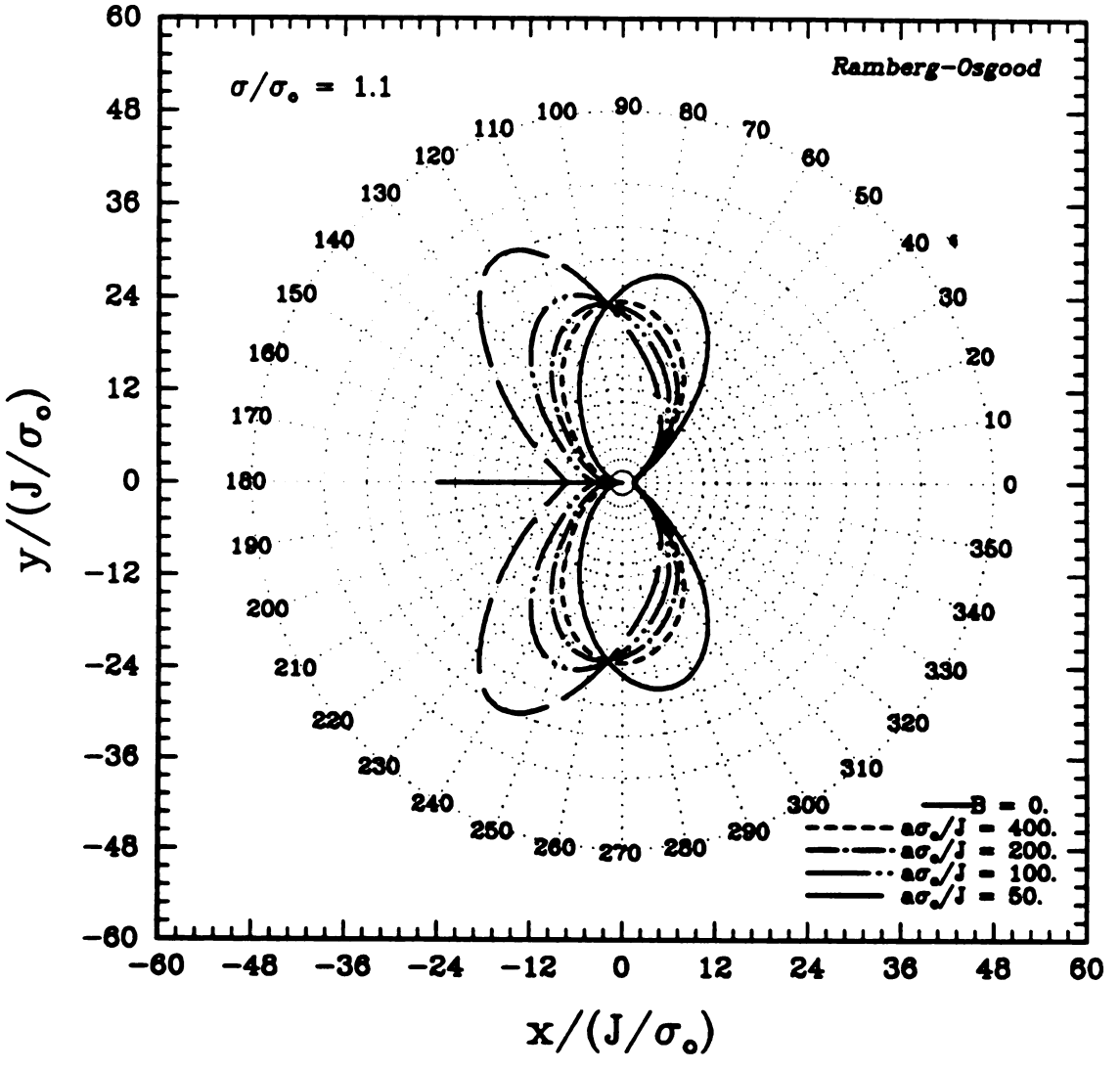

Figure 4.23. Effect of B = 0.4890 on plastic zones in coordinate system non dimensionalized with respect to the characteristic length parameter (J/σ_o), in plane strain for $\sigma_{eq}/\sigma_o = 1.1$ and strain hardening value n = 10.

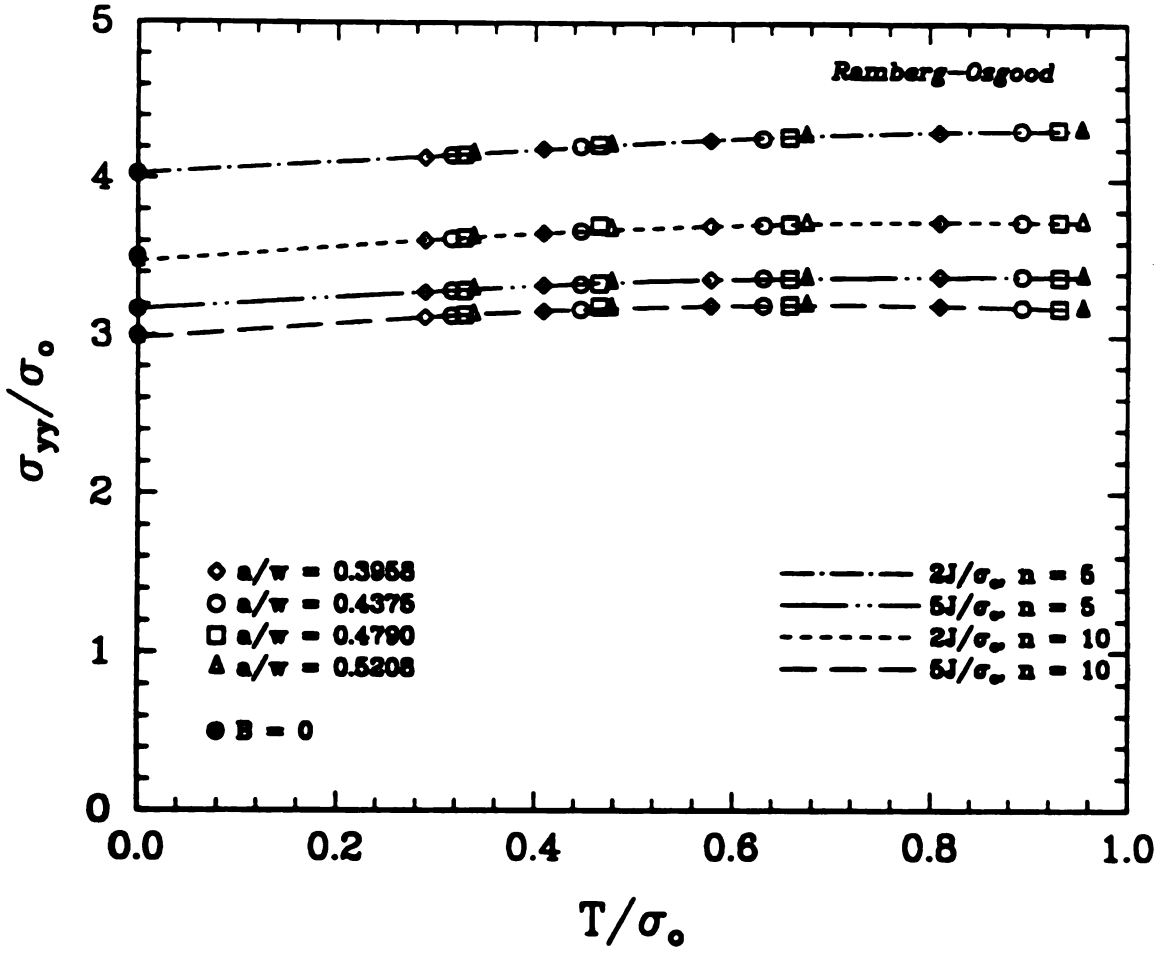

Figure 4.24: The crack opening stress directly ahead of the crack at a distance $2J/\sigma_o$ and $5J/\sigma_o$ for all a/W ratio considered in a CT specimen in modified boundary layer formulation.

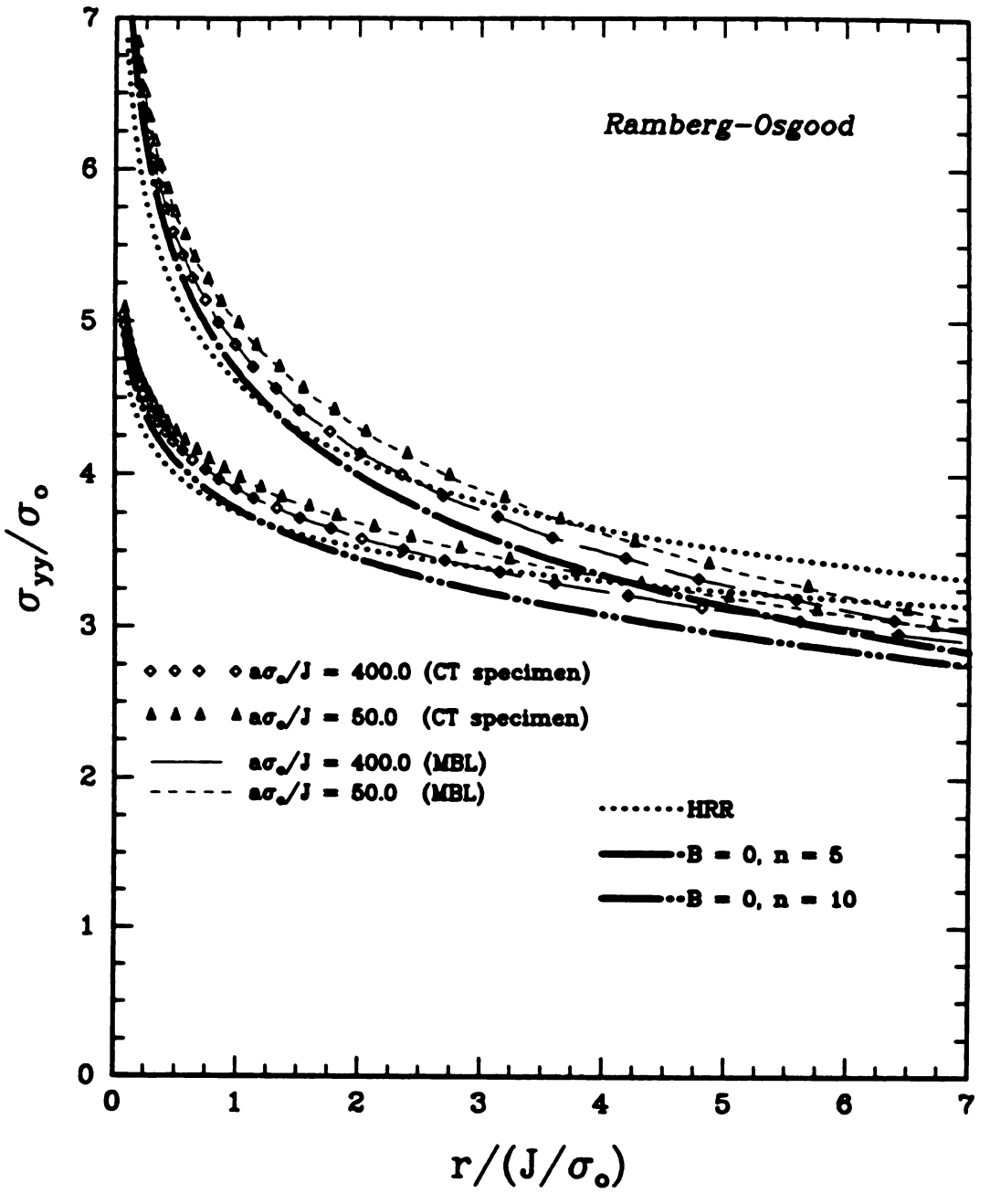

Figure 4.25: Corrected normalized crack opening stress distribution in plane strain for a/W = 0.3958 and $\theta = 0°$ for full scale CT specimen.

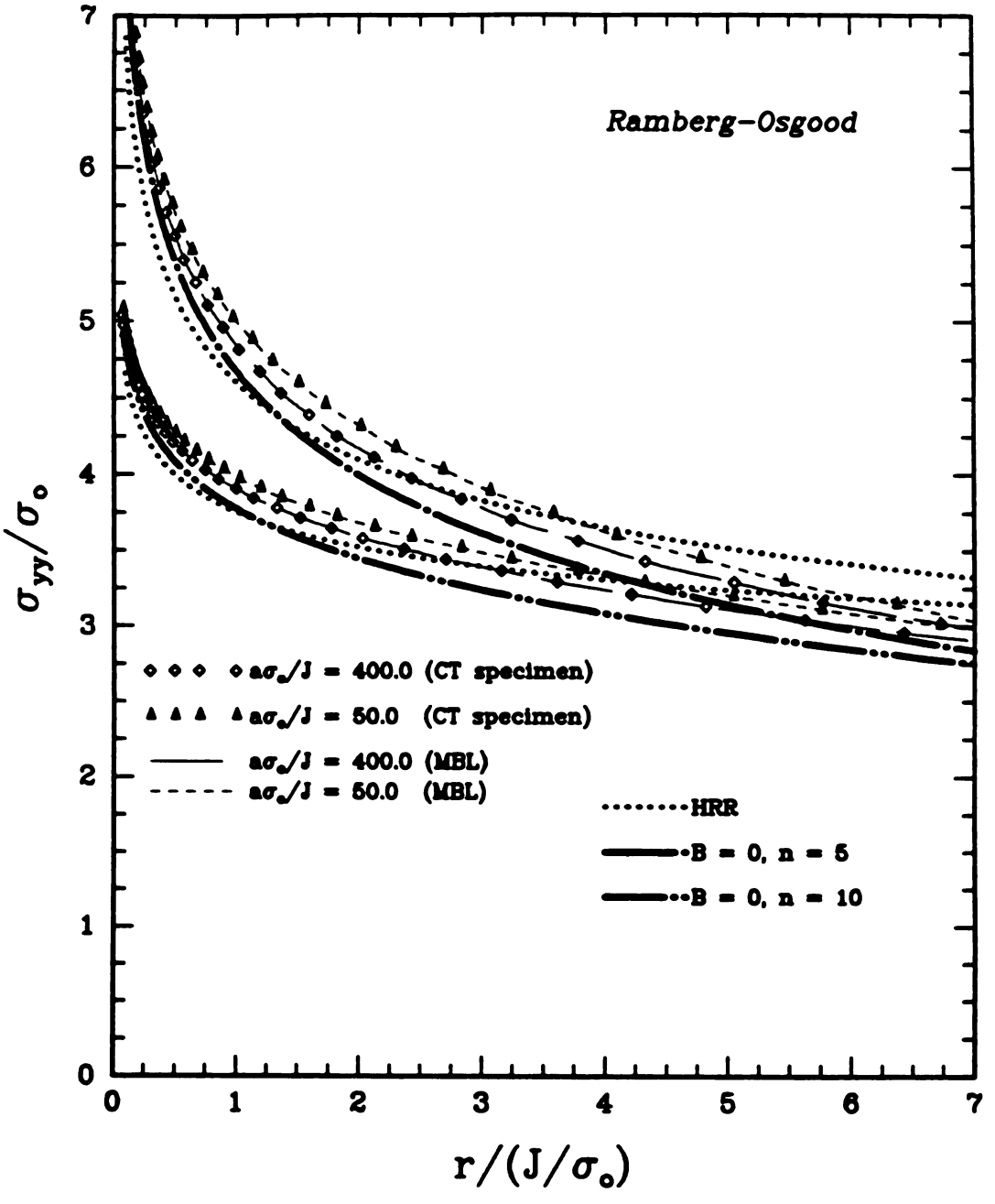

Figure 4.26: Corrected normalized crack opening stress distribution in plane strain for a/W = 0.5208 and $\theta = 0°$ for full scale CT specimen.

CHAPTER 5

EXPERIMENTAL TECHNIQUES

5.1 Introduction

In order to understand the deformation process near the crack tip in a thick specimen a crack opening displacement method, stress freezing, strain gages and a multiple embedded moire technique* were used. Although most of the present knowledge depends on two-dimensional crack tip stress field solutions, in which the values of SIFs remain constant along the crack fronts, there are cases where stress conditions are basically three-dimensional in character. Hartranft and Sih [49] and Sih [50] developed an approximate three-dimensional theory of plates, which was used to study the influence of the plate thickness on the stress variation in cracked plates. The results were expressed explicitly in terms of a set of cylindrical coordinates (r,θ,z), and the components of SIFs, k_j (j = 1,2,3) depend only on the z coordinate which coincides with the straight front of the crack. The singular variation in the polar radius r and the angular distribution in the polar angle θ of the components of stresses were given in planes normal to the crack edge. It was found that the local stress field was the

*Developed by Cloud and Paleebut [2]. The author has used their strain distribution results.

same as the stress field found for the two-dimensional crack problem, and only the values of the k_j -factors were varying along the crack front.

Three experimental technique have been used by others in solving this type of problem. Smith [51] used three-dimensional photoelasticity using frozen stress technique, Packman [52] used crack opening interferometry measuring the separation of the crack faces by observing the destructive interference of light reflected by the two crack faces, and Barker and Fourney [53] used scattered light speckle interferometry which measures the change in displacements on any plane in a transparent model through the use of coincident coherent sheets of light travelling in opposite directions. We evaluated k_j using COD, photoelasticity and embedded moire techniques.

Before going deeply into experimental procedures, the normalized stress distribution† for our specimen was calculated with the result shown in Figure 5.1. A comparison is made with 3D elastic finite element analysis. The results are not that bad, considering that the mesh is quite coarse. In plane strain the normalized stress distribution remains constant, but stress field falls off on the surface plane as we approach the crack tip. By knowing the variation of the components of the stress intensity factor k_j (j = 1,2,3) along three axes (i.e., longitudinal, transverse and thickness), one can completely evaluate the 3D stress field at the crack edge.

5.2 Crack Opening Displacement

A back face strain gage was fixed to the specimen to measure the amount of deformation needed either in terms of strain or crack opening displacement. Since the strain gage was adhesively bonded to the specimen, the same amount of deformation in the specimen would be transmitted to the gage. The crack opening displacement test is already relatively well developed and accepted. This method was standardized by British Standard [54] and there are nowadays various ways of predicting critical defect sizes using the COD approach.

---

† $$\sigma(r,\theta,z) = \frac{K_I}{\sqrt{2\pi r}}\frac{1}{4}\left\{\left[1 - \frac{3\nu}{1+\nu}\left(\frac{z}{r}\right)^2\right] sin\frac{\theta}{2} + sin\frac{3\theta}{2}\right\} \qquad (5.1)$$

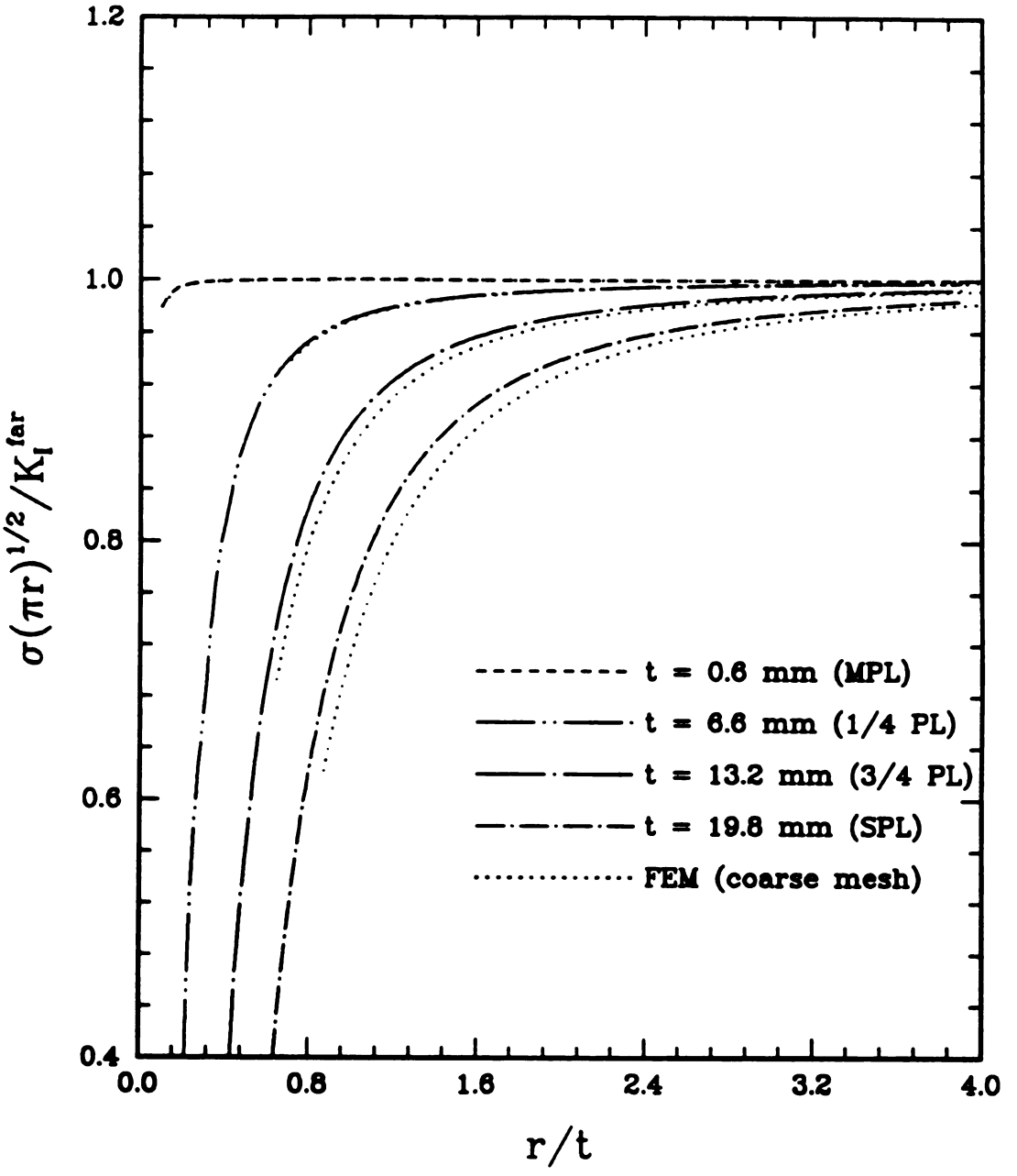

Figure 5.1: Normalized crack opening stress distribution through out the thickness of the specimen based on 3D elastic analytical solution and elastic FEM (NISA).

A device for measuring strain and /or displacement is important. Many such problems discussed earlier can be overcome by using a displacement transducer, especially because, in fracture mechanics testing, displacements within a given working range are more significant than the local strain measurements provided by conventional strain gages. Moreover, a transducer measuring total displacement between two application points is not affected by the surface microphenomena that exert no real influence on structural behavior. Commercially-available transducers, all instrumented with resistance strain gages, can be broken down into the following two main categories, both of which utilize cantilever sensors. These devices fall into two main catagories:

(a) front-affixed, with no transversal displacement measurements (design and calibration specifications in accordance with ASTM E 399 [42]. (b) Side-affixed, with transversal displacement measurements.

The above transducers are very expensive and may not meet the requirements because of the notch size of the CT specimens. A displacement gage was designed and constructed, and it is shown in Figure 5.2. All specifications, including measuring field size and the required degree of accuracy, were developed on the basis of experimental results and information obtained from ASTM standard [42], British standard [54] and Smith and Pascoe [55]. Minimum measuring base is 2.5 mm, resolution is 0.01 mm, working range is 10 mm, and linearity is 1% in the working range. Special care was excercised in making the transducer as light as possible and deformable in the direction of measurement so that the effects of stiffening on the test specimens would be minimized. Cantilever beams are made out of spring steel having 1200 microns thickness. The two cantilever beams are mounted on an aluminum base. Strain gages are bonded in both transverse and longitudinal directions in each of the cantilever beams, and they are configured in a full-bridge circuit. The calibration procedure recommended in ASTM E 399 [42] was repeated three times, removing and replacing the extensometer inside the calibrated device. The calibration setup is shown in Figure 5.3. A straight line was obtained when strain versus displacement was plotted as in Figure 5.4. The extensometer's measured linear response showed a maximum deviation in the least-square best-fit straight line of 0.2 %. While measuring local strain and stress response at the crack tip and/or notch tip in the CT specimen under monotonic loading, the extensometer and backface strain gages were fixed‡

‡refer also to Figure 3.3

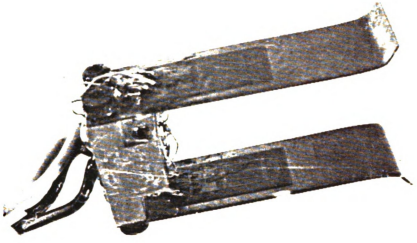

Figure 5.2: Home made clip gage.

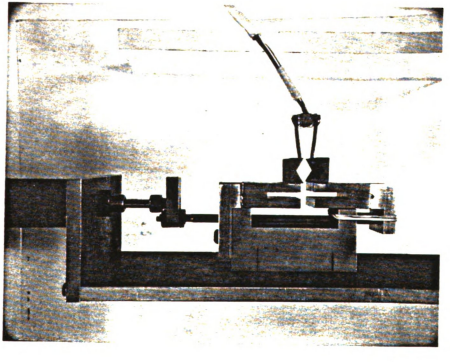

Figure 5.3: Calibration set up for clip gage.

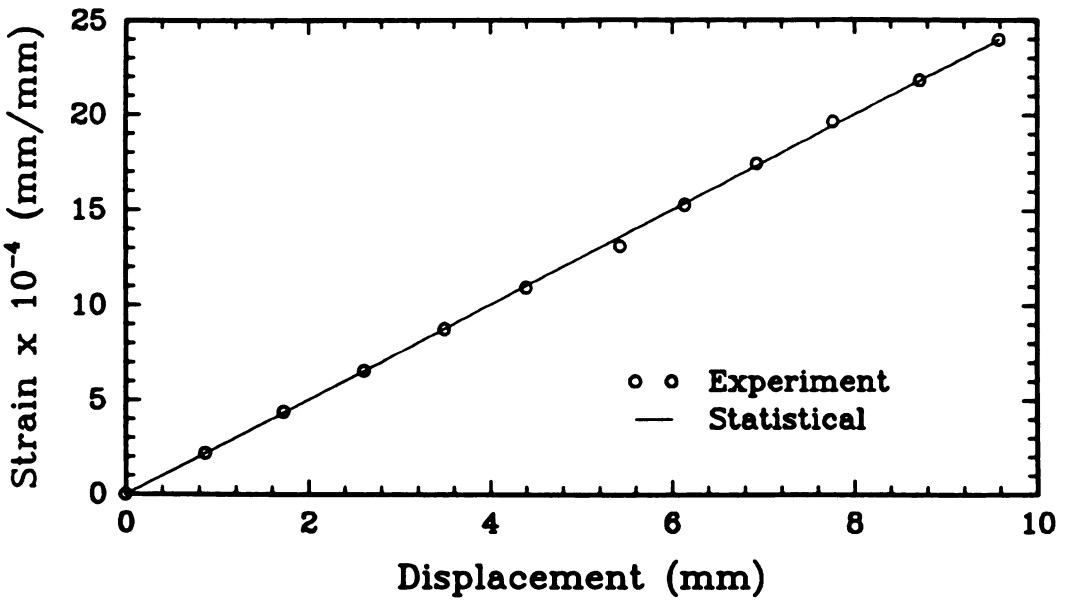

Figure 5.4: Calibration curve for the Clip gage.

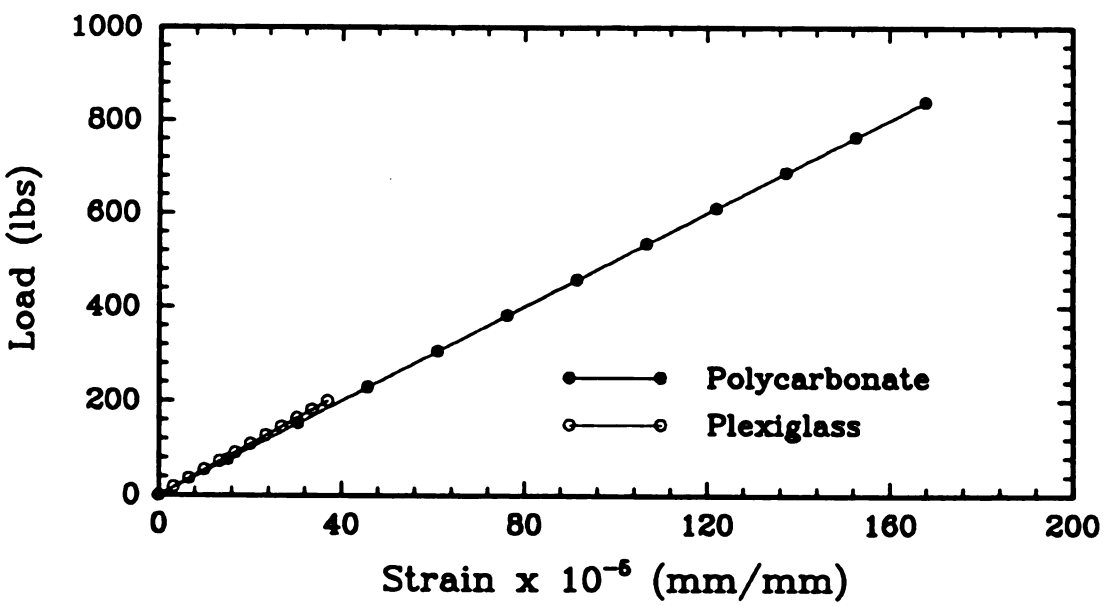

Figure 5.5: Measurement of clip gage strain after placing in the CT specimen with load varying monotonically.

Figure 5.5 and 5.6 show the relation between load versus strain obtained from the extensometer and load versus backface strain respectively for polycarbonate and plexiglass. The strain readings obtained from the extensometer and backface strain gage, as in Figure 5.7, are converted to displacement in mm using the calibration curve. Finally, load versus displacement curves corresponding to the extensometer and backface strain gage are obtained. The backface strain gage seems to be more accurate than the extensometer reading. Construction of a load-crack mouth opening displacement (CMOD) diagram with elastic-plastic components is shown in Figure 5.8.

The expression used for calculating the value of CTOD from a force-displacement (CMOD) curve is given in (5.2).

$$\delta = \delta_e + \delta_p \tag{5.2}$$

where

$$\delta_e = \left[\frac{Y^2(1-\nu^2)P^2}{2\sigma_y E B^2 W}\right] \tag{5.3}$$

and

$$\delta_p = \left[\frac{0.4(W-a)V_p}{0.4W + 0.6a + z}\right] \tag{5.4}$$

In the above expression, δ_p is the value of the plastic component of CTOD, Y the stress intensity coefficient[§], ν the ratio of Poisson, P the value of force to be taken from the test curve, σ_y the 0.2 % proof stress of the material, E the modulus of elasticity, B the thickness of the specimen, W its width, a the effective crack length, V_p the plastic component of the clip gage displacement (from the force-displacement record) and z the height of the knife-edges. There are several criteria in choosing the value of force to be taken from the force-displacement curve, depending upon the type of curve resulting from the test. These criteria can be summarized in the following: usually the maximum load just before its occurence is chosen; the force corresponding to the point of initiation of crack propagation is used when CTOD at initiation is needed.

[§]refer to BS 5762

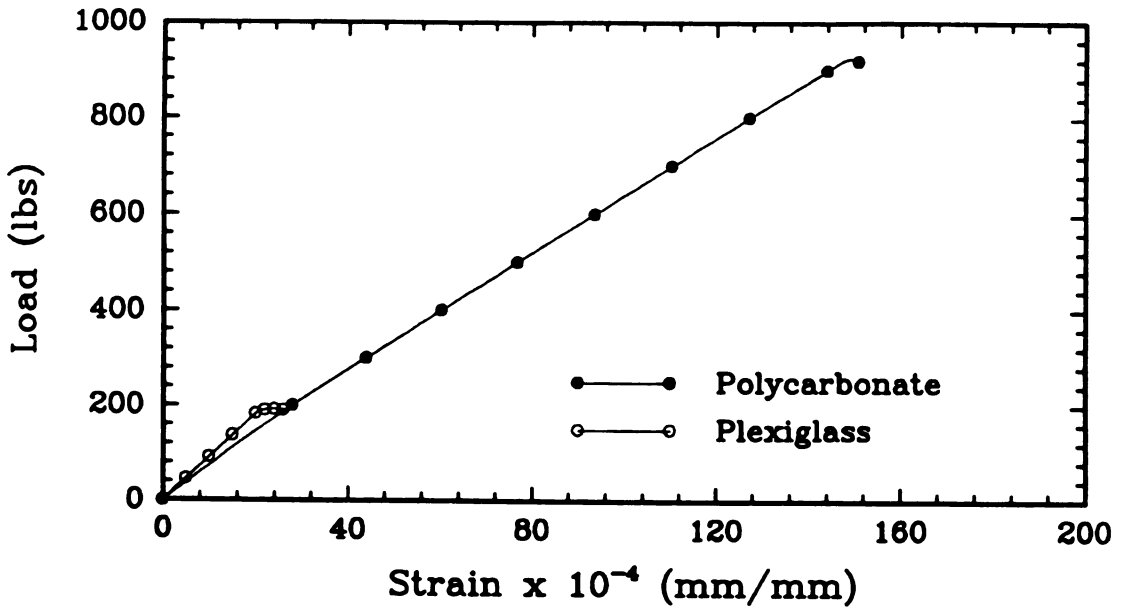

Figure 5.6: Measurement of back face strain after placing in the CT specimen with load varying monotonically.

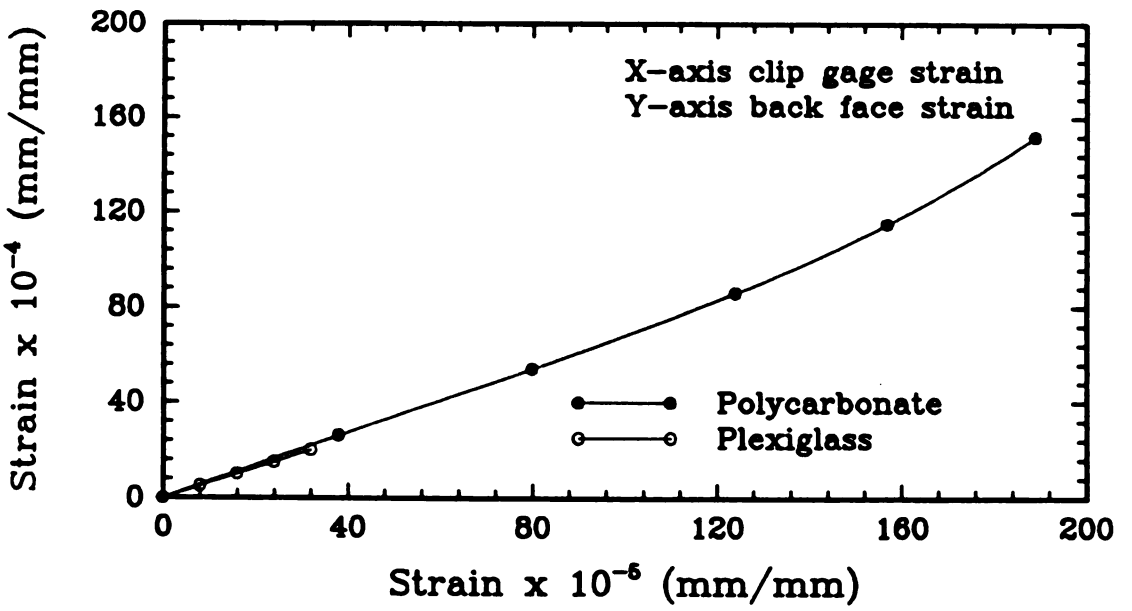

Figure 5.7: Relation between clip gage strain and back face strain under monotonic loading.

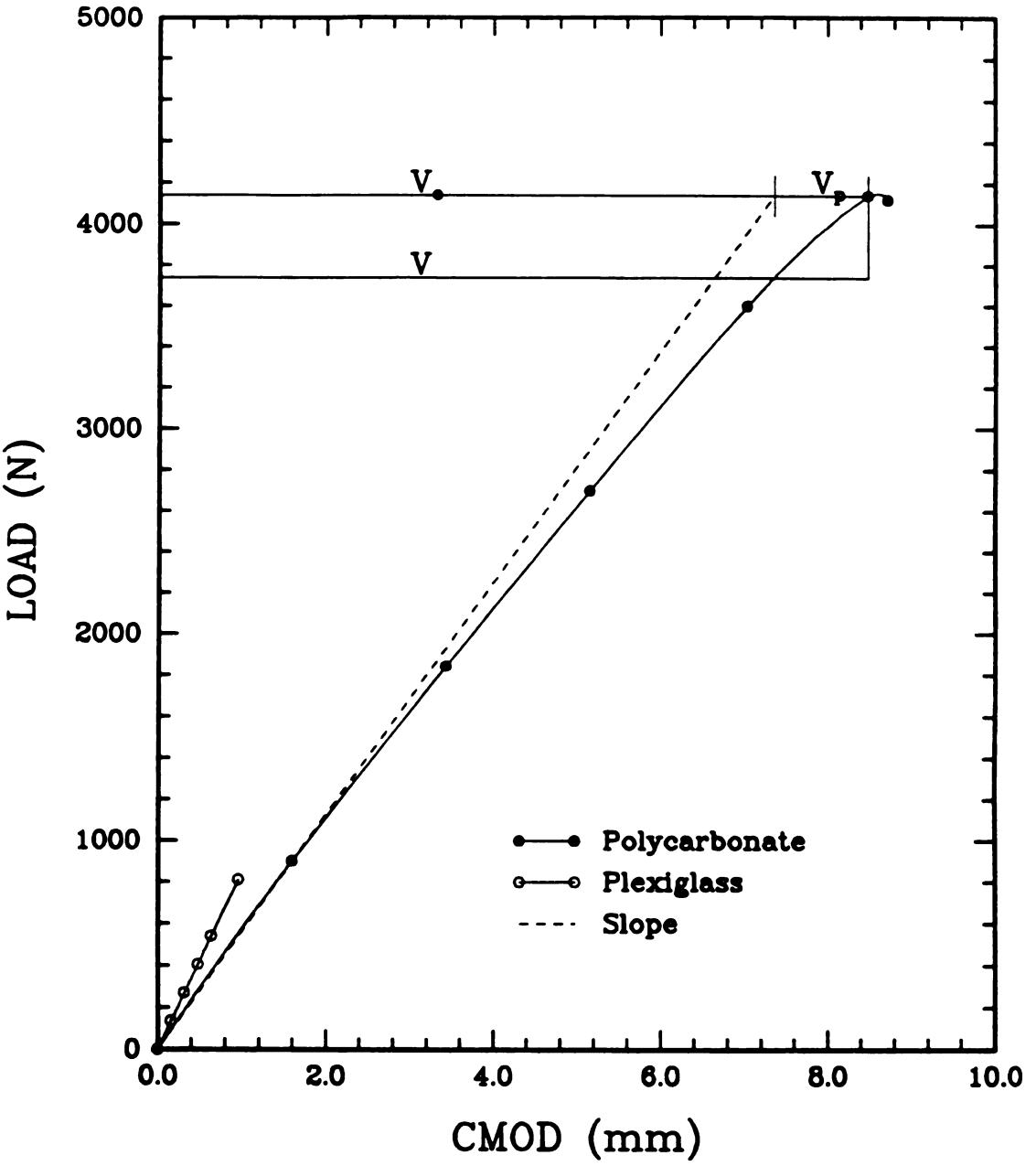

Figure 5.8: Construction of Load-crack mouth opening displacement (CMOD) diagram with elastic and plastic components.

Table 5.1. Estimated and measured crack tip opening displcement.

COD	Measured		Estimated	
	SPL	MPL	SPL	MPL
CMOD	0.978		---	0.885
SF*	0.463	0.75		
FEM	---	0.875		

*Stress freezing

Most materials which are analysed using the COD approach show considerable plasticity during the test, or even slow crack growth. Equation (5.3) was developed for a situation of pure elasticity (or very limited plasticity). Two different values of force were taken from the force-displacement record: P_{max} and P_e. P_{max} always corresponds to the maximum load reached in the test. P_e, the elastic force, is obtained by drawing a line parallel to the initial straight portion of the curve from the point of maximum force, thus giving the displacement V_e on the horizontal axis which is transported to the origin of the curve where a line perpendicular to the axis is drawn. The intercept of this line with the force-displacement curve gives P_e. Two values of δ_e are obtained, using P_{max} or P_{min} in (5.3), and compared for the two different material used.

A comparison of the CTOD values obtained from existing equation and measured are listed in Table 5.1. Using a clip gage or backface strain gage, one cannot find the effective crack-opening displacement in the case of plane stress, but for plane strain it is possible. CTOD is connected to the J integral in (5.5), (also refer to (4.7)). Once J is known, K_I can be calculated.

$$\delta = d(\alpha\epsilon_o, n)\frac{J}{\sigma_o} \tag{5.5}$$

With values of d = 0.3 for n = 3, with a very weak dependence of $\alpha\epsilon_o$, J can be obtained. The crack tip opening displacement provides a measure of the size of the plastic zone in which finite strains are important. One condition for J-dominance is R (the zone of dominance of the singularity field) greater than 3δ, and the second condition is that R be greater than the fracture process zone in which the microscopic separation processes occur. The second condition tells about small scale yielding. Both the criterion should be satisfied for small scale yielding to take place.

It was mentioned earlier that¶from stress freezing technique the deformation of the crack tip in mid-plane and in surface plane slices were measured. Figure 5.9 gives the exact profile of the deformed crack front following a parabola with 2p = 30 mm, from which also one can find the SIF in thickness direction. The distribution of CODs along sections parallel to the middle plane of the cracked plate, as measured, are shown in Figure 5.10, and they are also compared with the elastic equation and elastic-plastic FEM technique (only for plane strain). The stress intensity factor variation calculated in the surface plane and mid-plane are then normalized with far field stress. The estimated Mode-1 SIF in the midplane is almost 2.66 times greater than in the surface and is given in Figure 5.11.

¶refer to section 5.3

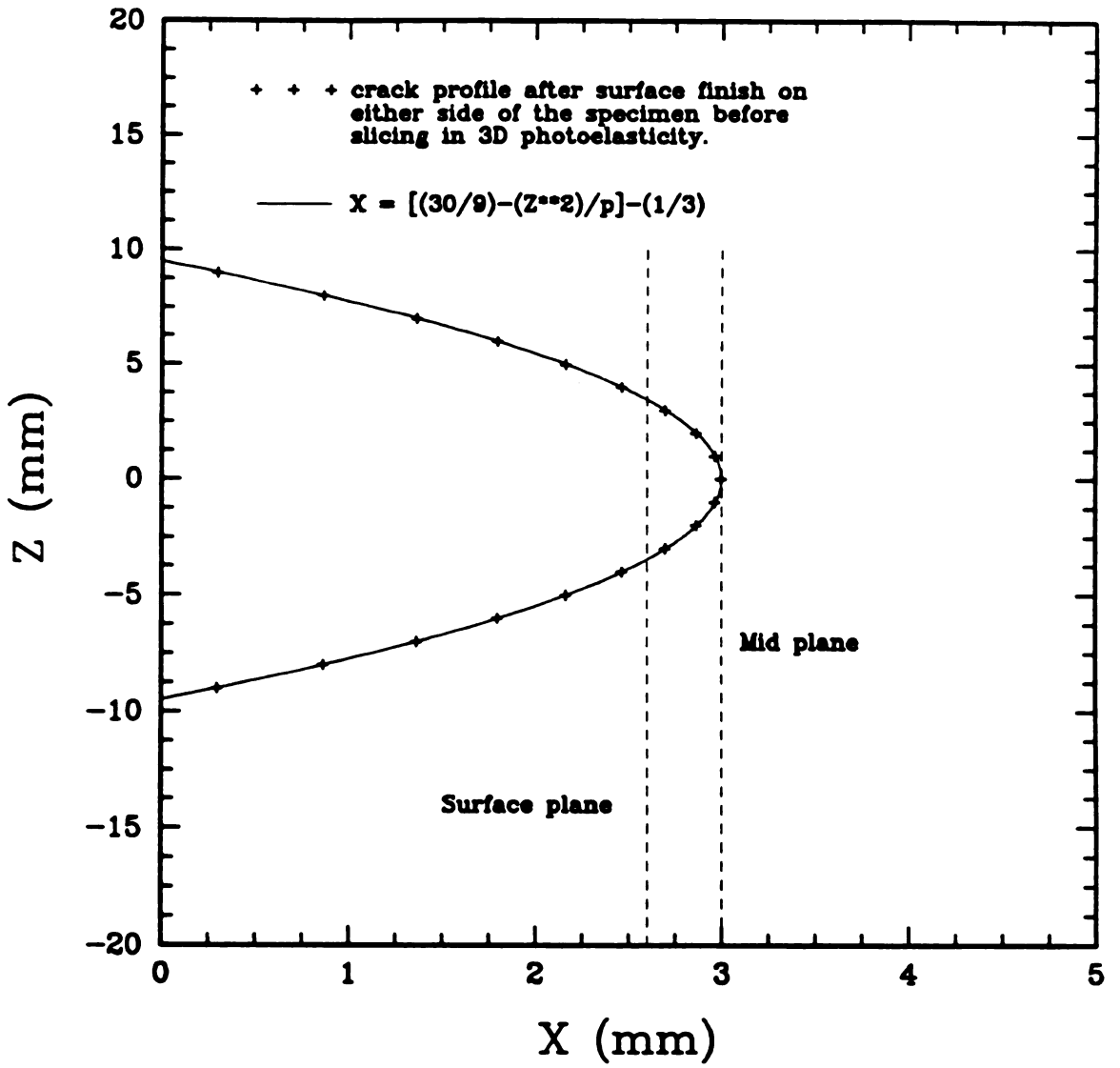

Figure 5.9: The exact profile of the deformed crack front following a parabolla with 2p = 30 mm; Z is the direction measuring the thickness of the specimen and X is the distance from the notch to pre-cracked end.

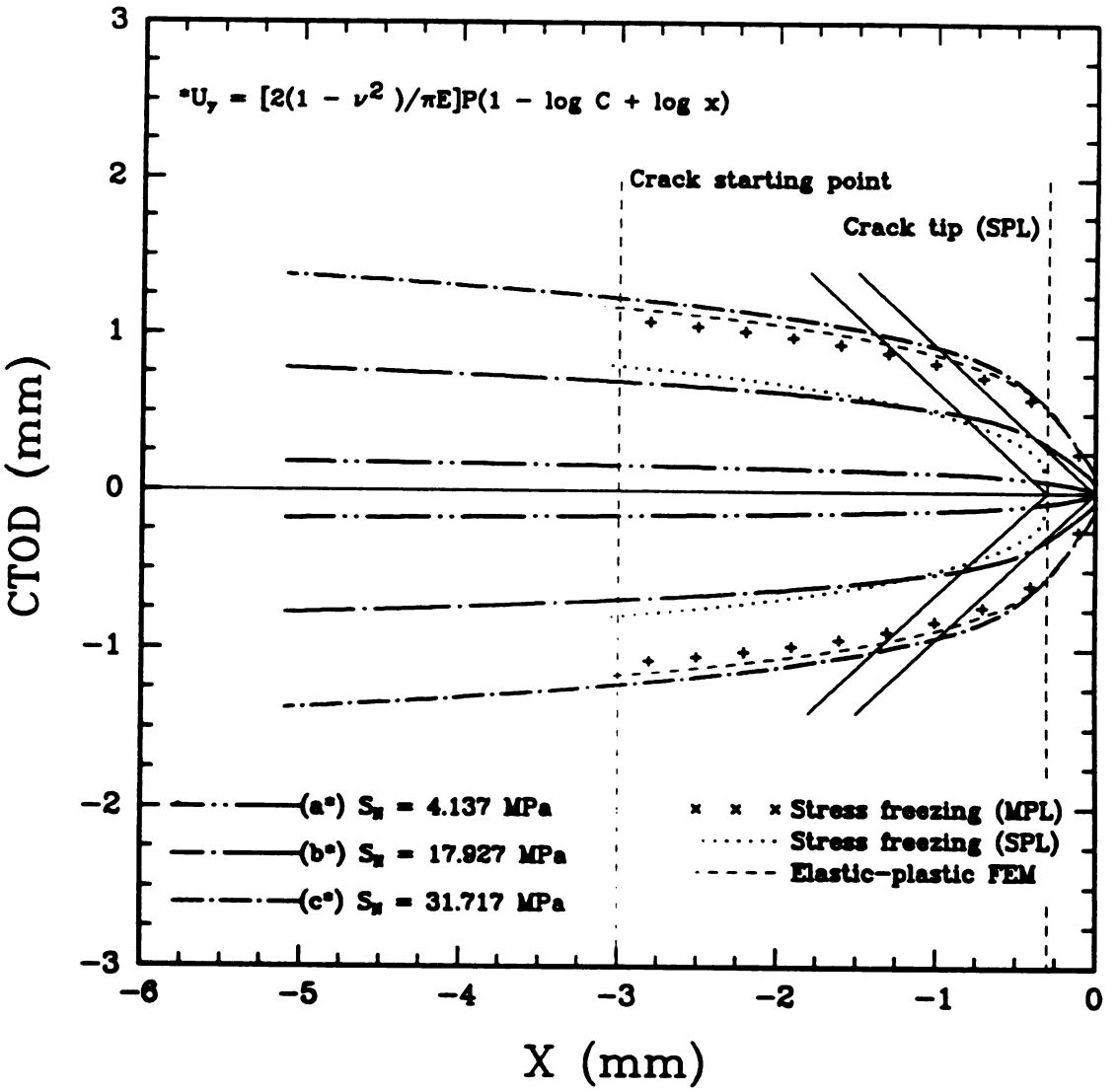

Figure 5.10: Crack opening displacement measured behind the crack tip.

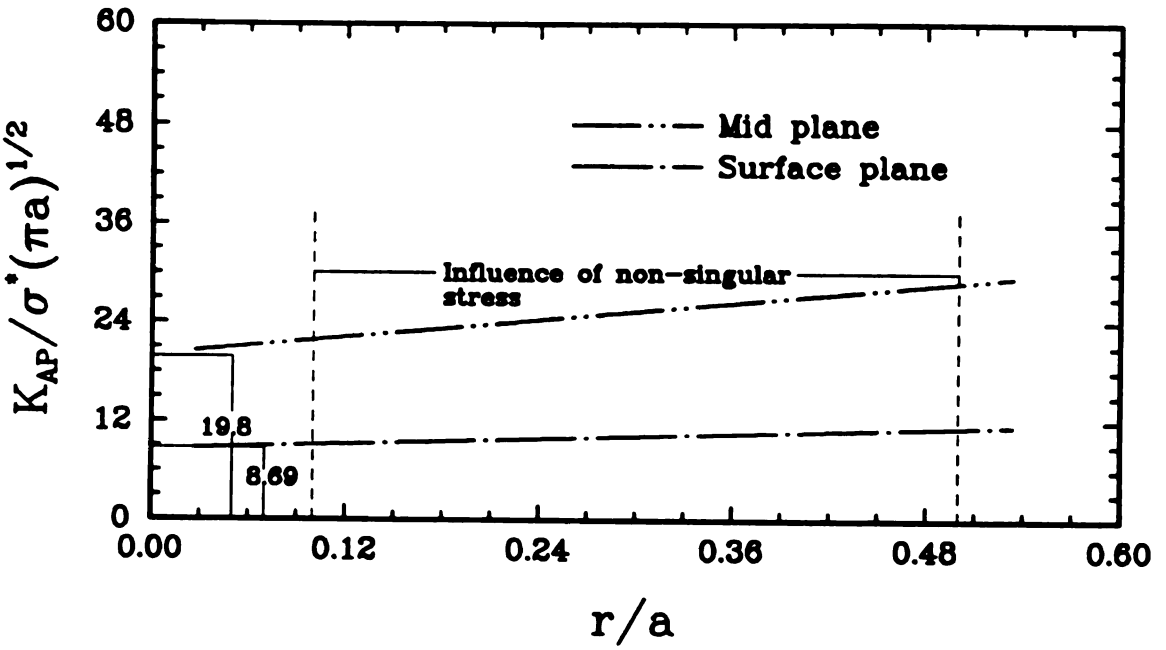

Figure 5.11. Estimation of Mode-1 stress intensity factor for mid plane and surface plane using CTOD technique, (*) indicates remote stress.

5.3 Three Dimensional Photoelasticity

5.3.1 Fundamentals of the stress freezing method

The basis of the frozen-stress method is the process by which deformations are permanently locked in the model. The four different techniques for locking deformation in the loaded model include stress-freezing, creep, curing and gamma-ray irradiation methods. In all these methods, the deformations are locked into the model on a molecular scale, thus permitting the models to be sliced without relieving the locked-in deformation. The stress freezing process is by far the most effective and most popular technique for locking the deformations in the model. This technique was used in the present investigation.

The stress-freezing method of locking in the model deformation due to an applied load is based on the diaphase behavior of many polymeric materials when they are heated. When the polymer is at room temperature, both sets of molecular bonds, the primary and secondary, act to resist deformation due to applied load. However, as the temperature of the polymer is increased, the secondary bonds break down and primary bonds in effect carry the entire applied load. The breaking of the secondary bond depends on the critical temperature and the time under load. Since the secondary bonds constitute a very large portion of the polymer, the deflections which the primary bonds undergo are quite large yet elastic in character. If the temperature of the polymer is lowered to room temperature while the load is maintained on the model, the secondary bonds will re-form between the highly elongated primary bonds and serve to lock them into their extended positions. When the load is removed, the primary bonds relax to a modest degree, but the main portion of their deformation is not recovered. The elastic deformation of the primary bonds is permanantly locked into the model by the re-formed secondary bonds. Moreover, these deformations are locked in on a molecular scale; thus the deformation and accompanying birefringence are maintained in any small section cut from the original model.

The procedure for the stress-freezing process is described below.

- Place the model in the stress-freezing oven.
- Heat the model relatively rapidly until the critical temperature is attained.

- Apply the required loads.
- Soak the model at least 2 to 4 hours until uniform temperature throughout the model is obtained.
- Cool the model slowly enough for temperature gradients to be minimized.
- Remove the load and slice the model.

5.3.2 Experimental set up

In order to carry out this experiment, an oven containing a loading device was built. The experimental set up is not shown here. The maximum temperature was 180°C. The load transducer was fabricated from a long cylindrical steel bar. A rectangular groove of about 0.5 X 0.5 inch was made, 5 inch below one end of the bar. The two ends of the rod are threaded. One end of the rod is connected to an hydraulic device and other to the specimen fixing device. Strain gages are mounted on the rectangular grooved region of the bar with two oppsite gages in the axial direction and two oppsite gages in the transverse direction. The four gages are positioned in the Wheatstone bridge of a strain indicator. The load cell was calibrated to read a maximum of 2000 lbs and this was tested in an Instron machine. This measuring unit was connected to a computer-controlled data acquisition system (System 4000, supplied by Measurements Group) which not only acquired the raw data but also uses the computer to provide data reduction appropriate to the input sensor, based on parameters entered by the user.

The compact tension specimens with $\frac{a}{W} = 0.4966$ (W = 102.29 mm and a = 50.8 mm) and 10 mm thick are made out of polycarbonate. Two such specimen are bonded with an epoxy resin and are cured at room temperature. A back face strain gage was fixed to the specimen to measure the amount of deformation needed either in terms of strain or crack opening displacement. Since the strain gage was adhesively bonded to the specimen, the same amount of deformation in the specimen would be transmitted to the gage. A dummy gage was also attached separately in the circuit making it a half bridge for temperature compensation. After mounting the specimen in the loading device, the home made clip gage was placed inside the grooved notch for measuring crack opening displacement. All the necessary wire connections are made

and connected to the data acquisition system. The stress freezing in polycarbonate was done at 120° ± 10° at a load level of 400 psi. The hydraulic based loading system showed a little drop in load, but it was corrected by adjusting the pressure. Strain-time and load-time data were digitized and stored on an IBM PC. Data were sampled and stored in the hard disc. Analog signals proportional to load and displacement were recorded using X-Y recorders.

5.3.3 Slicing the model and interpretation of the resulting fringe pattern

The specimen was annealed at approximately 80°C to remove as much as residual stress as possible. The three dimensional model wass sliced to remove planes of interest which can then be examined individually to determine the state of stress existing in that particular plane or slice. Three slices of thickness 3.5 mm were taken out from the model, each of which were polished to 2.54 mm‖ The slice is sufficiently thin in relation to the size of the model to ensure that the stresses do not change significantly in either magnitude or direction through the thickness of the slice. The three slices represents surface plane, quarter plane and midplane. The free surface of each of the three slices represents principal surfaces, since both the stress normal to the surface and the shearing stresses acting on the surface are zero. Each of these slices were examined in normal incidence; i.e., direction of light coincident with the transmission axes; in the polariscope.

In photoelastic analysis the stress distribution is sought as a function of the load. To determine this stress distribution accurately requires the careful calibration of the material fringe value C_σ. In any calibration technique one must select a body for which the theoretical stress distribution is accurately known. For this purpose a disc specimen of diameter 40.01 mm and 7.2 mm thick was chosen. The circular disc has axes of symmetry for both geometry and loading. The polarizer and analyzer are rotated, keeping their axes crossed, until the isoclinic line appears along the axes of symmetry. Then the transmission axes of the polarizer and analyzer are lined up parallel and perpendicular to the principal stress axes on the axes of symmetry. Since

‖A thickness variation is there due to localized plastic yielding near the crack tip.

the principal stress axes on the axes of symmetry are parallel and perpendicular to the symmetrical axis, this locates the directions of the transmission axes of the polarizer and analyzer. The directions of the transmission axes in the quarter-wave plates are located by placing them between crossed polarizer and analyzer, by rotating the quarter-wave plates untill extinction is seen. This position gives the principal axes of the quarter-wave plate. All the necessary markings are noted in terms of degrees. In this experiment, isoclinic lines are not important but isochromatic lines are necessary. In order to observe and record isochromatics without having them masked by isoclinics, the disc specimen is inserted into the polariscope and the quarter-wave plates are in place with their axes 45° from the axes of polarizer and analyzer, to create a circular polariscope.

The result is a dark field set up, which means that little light will be coming through the system. In this arrangement, the whole order isochromatic fringe is dark. A light field polariscope is obtained by rotating one of the polarizers in the dark field configuration by 90°. This procedure places the polarizers parallel, with the two $\frac{\lambda}{4}$ plates still being crossed. With the light field arrangement, it is the half order isochromatic fringes which appear dark, and they will fall between the fringes observed with dark field.

The isochromatic patterns are recorded for 38 lbs applied directly to the specimen in compression kept approximately for 10 minutes. Typical light and dark field photographs are shown in Figures 5.12 and 5.13. From elasticity the principal stresses σ_x and σ_y for a disc specimen are given.

The stress distribution along the horizontal central line of the disc:

$$\sigma_x = \frac{2R}{\pi dD}\left[\frac{D^2 - 4x^2}{D^2 + 4x^2}\right]^2 \tag{5.6}$$

$$\sigma_y = \frac{-2R}{\pi dD}\left[\frac{4D^4}{D^2 + 4x^2} - 1\right] \tag{5.7}$$

The stress distribution along the vertical central line of the disc:

$$\sigma_x = \frac{2P}{\pi dD} \tag{5.8}$$

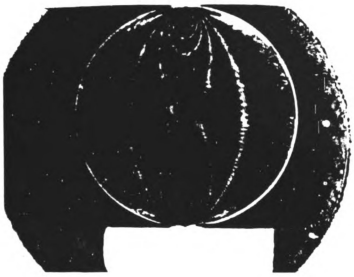

Figure 5.12. Light field isochromatic fringe pattern from disc specimen.

Figure 5.13. Dark field isochromatic fringe pattern from disc specimen.

$$\sigma_y = \frac{-2P}{\pi d}\left[\frac{2}{D-2y} + \frac{2}{D+2y} - \frac{1}{D}\right] \tag{5.9}$$

From photoelasticity theory, if σ_x and σ_y be the principal stress at a point in a two-dimensional plate of "momentarily linear elastic" material, it can be shown that absolute retardations present in terms of stress through absolute photoelastic coefficient C_1 and C_2 are;

$$R_1 = (C_1\sigma_x + C_2\sigma_y)\, d \tag{5.10}$$

$$R_2 = (C_1\sigma_x + C_2\sigma_y)\, d \tag{5.11}$$

where d is the thickness of the disc. The realtive retardation is;

$$R = R_1 - R_2 = (C_1 - C_2)\,(\sigma_x - \sigma_y)\, d \tag{5.12}$$

But $(C_1 - C_2)$ are difficult to measure, therefore they are replaced by C_σ, called the stress optic coefficient.

$$R = C_\sigma\,(\sigma_x - \sigma_y)\, d \tag{5.13}$$

$$\sigma_1 - \sigma_2 = \frac{m\lambda}{C_\sigma d} \tag{5.14}$$

where σ_1 is the principal stress in the x direction, σ_2 is the principal stress in the y direction, m is the fringe order, λ is the wave length of the light beam, and d is the thickness of the disc specimen.

A plot between fringe order and the stress difference resulted in the straight line shown in Figure 5.14. The slope of this line gives the stress optic coefficient. To obtain a calibration curve (5.13) has been used, which is also shown in Figure 5.14.

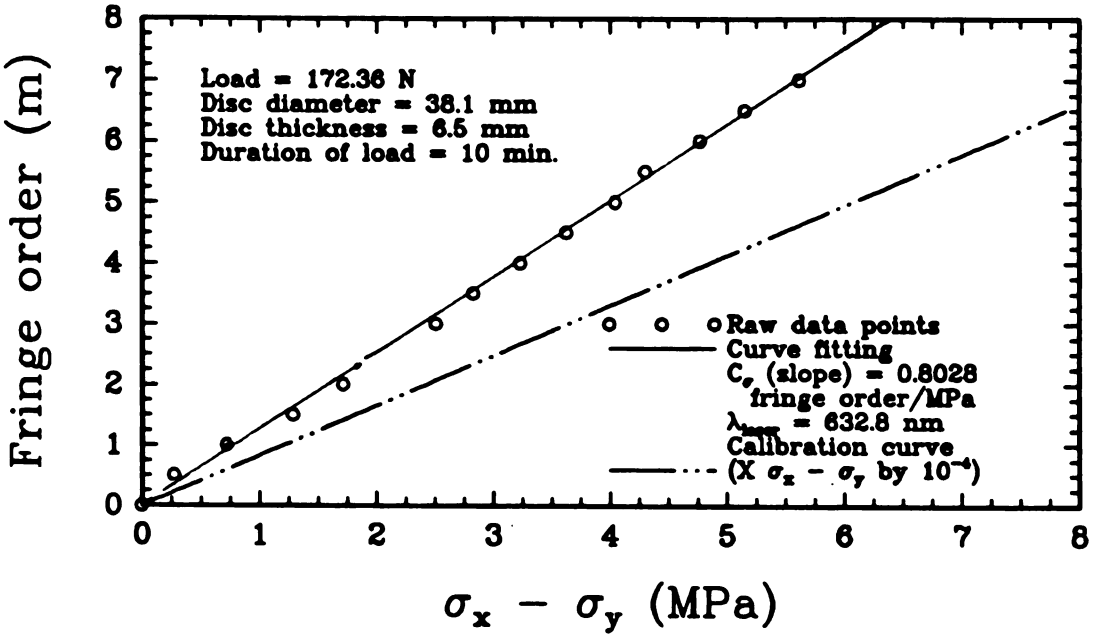

Figure 5.14. Fringe order versus stress difference obtained from the disc specimen and superimposed is the calibration curve.

Now the slices taken from the 3D model are observed in polariscope. The isochromatic fringe patterns were recorded in light field and dark field. Figure 5.15 represents light field isochromatic fringe patterns for the mid-plane and surface plane and Figure 5.16 represents dark field isochromatic fringe patterns corresponding to mid-plane and surface plane. The isochromatics are the locus of the points having equal maximum shear strain or stresses. In other words, if at any point on an isochromatic fringe the difference between the two principal stresses can be set corresponding to the yield point of the material, then the particular isochromatic may represent the boundary of the plastic zone based on the Tresca criterion of yielding, i.e., yielding by maximum shear stress theory. The isochromatic itself represents the plastic zone boundary. The isochromatic fringes from dark field for the mid-plane and surface plane are superimposed with the result shown in Figure 5.17.

It is well known that photoelastic measurements cannot easily be made in the immediate vicinity of a crack due to the plastic zone near the crack. Hence the photoelastic observations are usually made in zones slightly removed from the crack tip. In order to account for this and for the tilt of the isochromatic fringe loops, the solutions of William [13] can be used. Equation (1.12) can be used as a two parameter equation.** The two parameters are K_I and σ_{ox}. The Westgaard [56] equation is strictly valid in the near vicinity of the crack tip. Theoretically, the two parameter K_I and σ_{ox} can be evaluated from the photoelastic parameter m and ϕ (the fringe order and the isoclinic fringe parameter) experimentally determined at a point P (r, θ) in the region of validity of the above equation. For this one uses;

$$\sigma_x - \sigma_y = (\sigma_1 - \sigma_2)\, cos2\phi = \left[\frac{mC_\sigma}{h}\right] cos2\phi \tag{5.15}$$

$$2\sigma_{xy} = (\sigma_1 - \sigma_2)\, sin2\phi = \left[\frac{mC_\sigma}{h}\right] sin2\phi \tag{5.16}$$

where C_σ is the material fringe value and h the thickness of the specimen. From (1.12):

**refer to purpose of doing numerical analysis using FEM

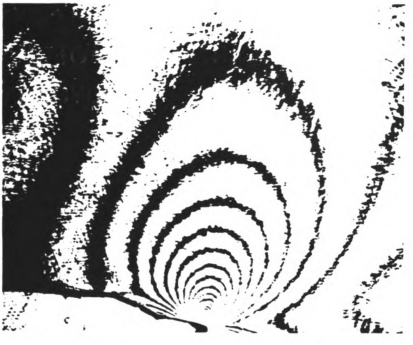

Figure 5.15: Dark field isochromatics fringe pattern in the mid-plane.

Figure 5.16: Dark field isochromatics fringe pattern in the surface plane.

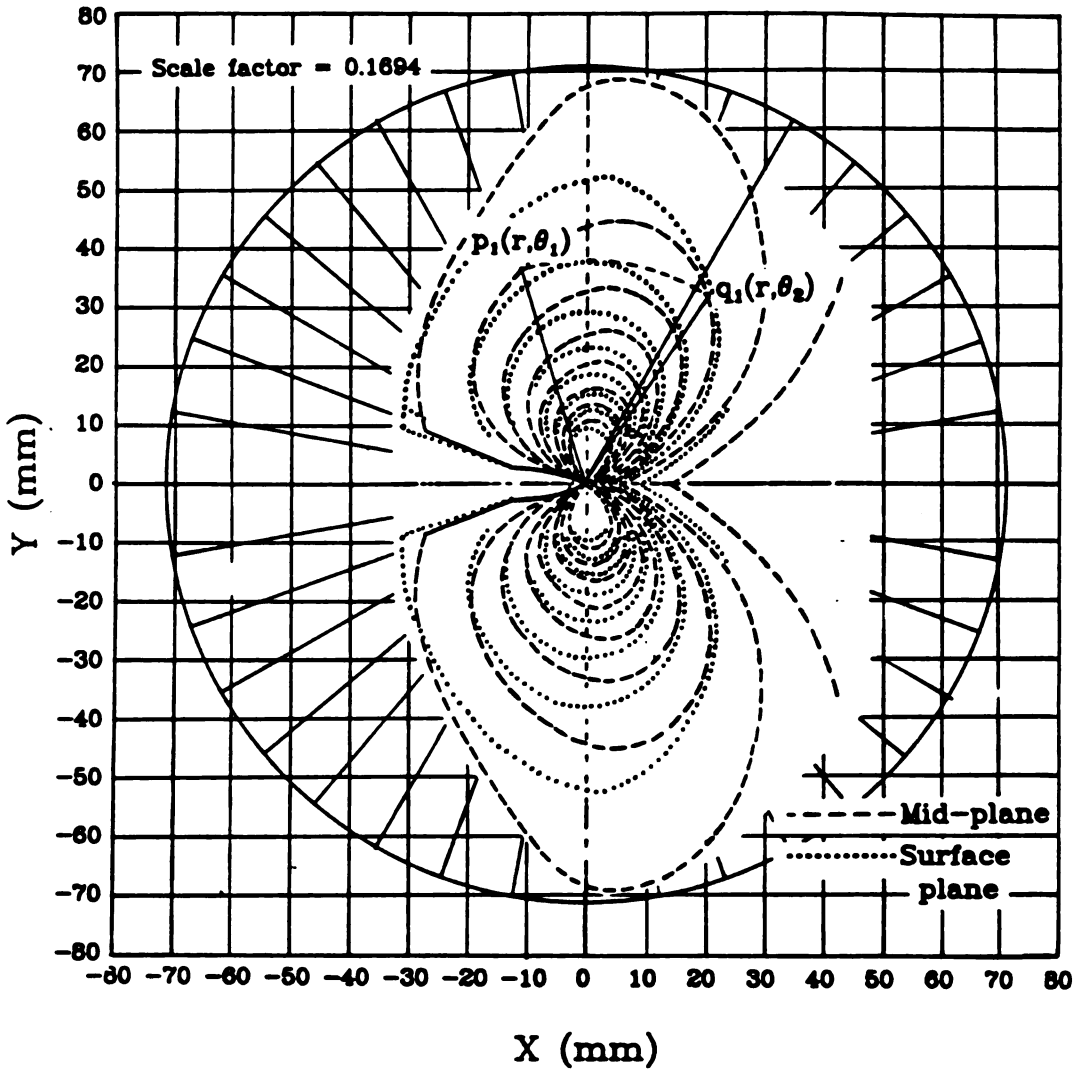

Figure 5.17: Isochromatic fringe pattern in the mid-plane and surface plane representing plastic zone.

$$4\sigma_{max}^2 = \left[\left(\frac{K_I}{\sqrt{2\pi r}}\right) sin\theta + \sigma_{ox} sin\frac{3\theta}{2}\right]^2 + \sigma_{ox} cos\frac{\theta}{2} \tag{5.17}$$

Selecting two points p_1 and q_1 lying on the same arc of radius r, in Figure 5.17 on a given isochromatic loop, (5.17) reduces to (5.18) given by Bradly and Kobayashi [57].

$$\sigma_{ox} = \frac{K_I}{\sqrt{2\pi r}} \frac{sin^2\theta_2 - sin^2\theta_1}{2sin\theta_1 sin(\frac{3\theta_1}{2}) - 2sin\theta_2 sin(\frac{3\theta_2}{2})} \tag{5.18}$$

From Redner [58] along $\theta = 60°$, $\sigma_{xy} = 0$ and σ_x and σ_y are the principal stresses. From (1.12) making measurement along $\theta = 60°$ line, parameter K_I can be measured. Finally we get;

$$\sigma_x - \sigma_y = \sigma_1 - \sigma_2 = \frac{K_I}{\sqrt{2\pi r}} . \frac{\sqrt{3}}{2} + \sigma_{ox} \tag{5.19}$$

Now by plotting the fringe order (m) of the CT specimen versus $\frac{1}{\sqrt{r}}$, the Mode-1 SIF†† was estimated. A comparison of biaxiality ratio calculated from FEM analysis in plane strain and stress freezing technique may be comparable (refer to Table 4.1b and Figure 5.18). However, in the surface plane, the biaxiality ratio couldn't be compared due to lack of data in the literature. In the analysis part there are two important areas to be considered: (i) The acceptable thickness of the slice in order to obtain a satisfactory or consistent value for the stress difference from photoelastic data and (ii) the domain (i.e. the radial distance from the notch tip) within which the observed photoelasticity data give reasonably consistent values for the stress difference. Errors in calculating SIF can be attributed to uncertainty in relative fringe values and locations.

††slope of Figure 5.18

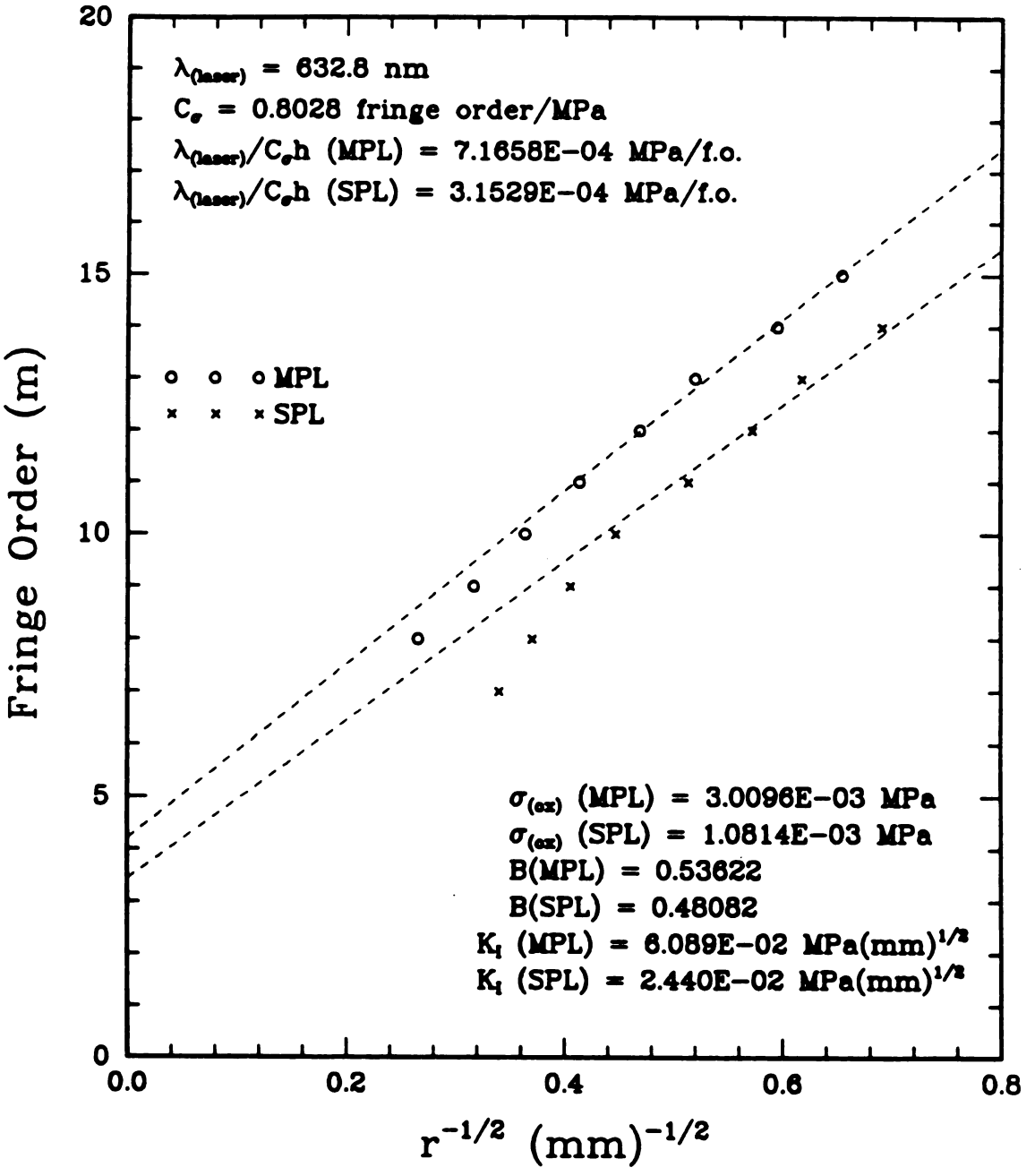

Figure 5.18: Estimation of Mode-1 stress intensity factor, non-singular stress and biaxiality parameter for CT specimen in mid-plane and surface plane.

5.4 Double Embedded Moire Technique

The literature survey and basic introduction to moire technique for this particular investigation were already given by Paleebut [1] and Cloud [2]. Only a summary of their experimental work is mentioned here. Two types of specimen were used. One type had two-way gratings, on the surface, quarter-and mid-planes. The other type incorporated electrical resistence strain gages on the surface, quarter, and midplanes. These two types of specimens had the same dimensions. Compact tension specimens of Merlon polycarbonate were used for this study.

Each grid was imaged separately by focusing the camera on the grid plane to get the maximum sharpness and contrast over the whole area near the crack tip. Separate data plates were recorded by focusing on the front surface, quarterplane, midplane, and back surface. For each specimen, four plates were recorded at each specimen load state, including zero load. Each photographic replica of a grid was treated by optical processing to obtain moire fringe patterns using a system shown schematically in Figures 5.19 and 5.20, which was developed by Cloud [59]. The light from a He-Ne laser was passed through a spatial filter which converted it to a moderately clean diverging beam. This beam was directed to a simple lens, whose output was parallel light. A moire submaster grating and one of the photoplates of a specimen grid were placed emulsion sides together in the optical path normal to the light beam. After passing through the photoplate, the beam, now containing diffraction components, was decollimated by a simple lens. At the focal plane, which is the transform plane of the field lens, there was placed a black paper screen containing a hole approximately 2.4 mm in diameter. This screen was retained in the filter mounting of a zoom lens mounted on a Nikon 35 mm camera. The hole in the filter mask was placed to coincide with the chosen diffraction ray group, a series of which appear as bright spots in the diffraction pattern. The image created in the camera by the light in the ray group contains interference fringes which are identical to moire fringes which would be formed by simple mechanical superposition of gratings having spatial frequencies equal to those causing the diffraction in the optical processor. After final adjustment, each moire fringe pattern was recorded on film. The moire fringe patterns were then enlarged and printed (refer to Figures 5.21a and 5.21b). Digitizing of the fringe patterns was performed on a Microdatatizer.

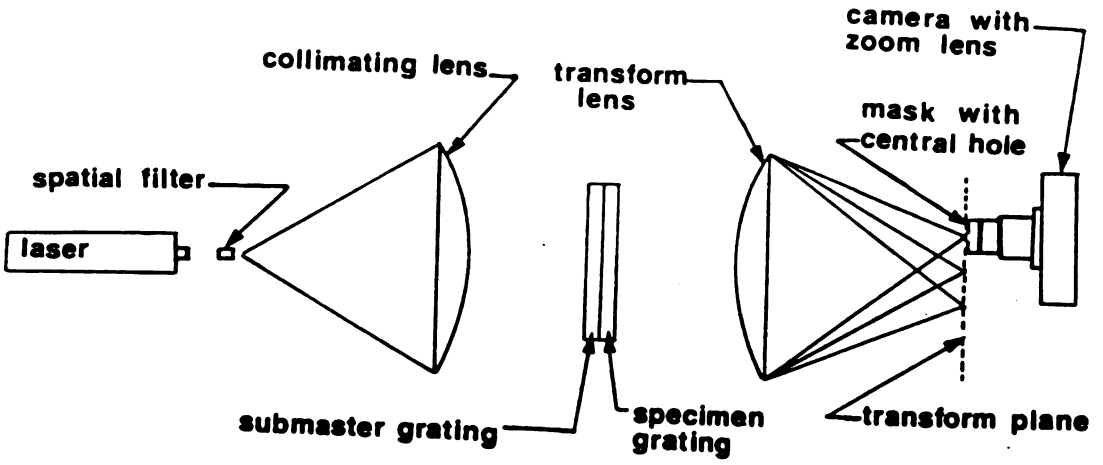

Figure 5.19: Schematic drawing of the optical processing system.

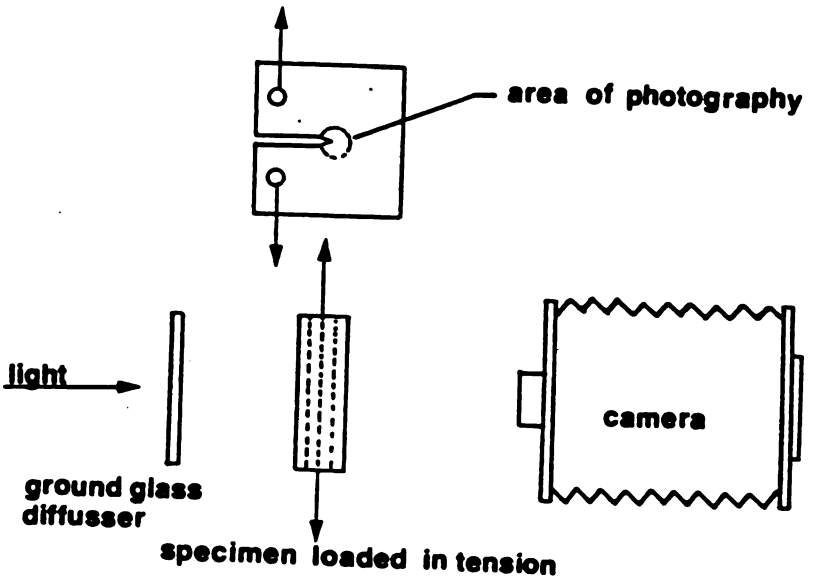

Figure 5.20: Schematic of the specimen set up.

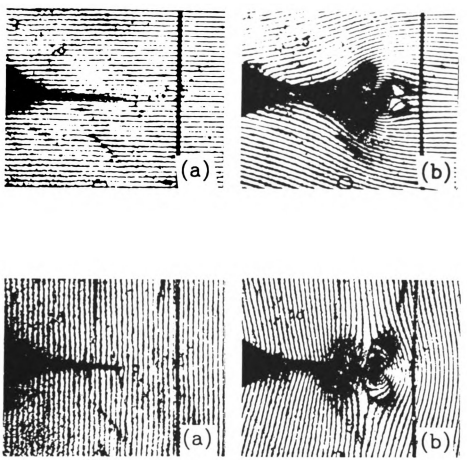

Figure 5.21: Moire fringe patterns in the quarter plane of a fatigue crack specimen obtained from a submaster having 19.96 l/mm; (top) patterns parallel to the crack line, (bottom) patterns perpendicular to the crack line; (a, left) not loaded, (b, right) loaded to 31.717 MPa.

The digitizing process was applied in turn to a moire data photograph (specimen loaded) and a zero strain (specimen not loaded) baseline photograph. These two sets of dizitized fringe data form a unit for computing and plotting of displacement and strain components. Since grids (2-way gratings) were used, both ϵ_{xx} and ϵ_{yy} could be determined in each plane studied. The horizontal grating yields displacement in the vertical direction, which is given by U_y = NP, where N is the fringe order and P is the pitch of the master grating. Strain in a direction perpendicular to the orientation of the specimen is simply the pitch of the analyzer grating multiplied by the slope of the fringe order plot at the point of question, which is given by;

$$\epsilon_{yy} = \frac{\partial u}{\partial y} = N\frac{\partial P}{\partial y} \tag{5.20}$$

A typical plot of fringe order versus distance is shown Figure 5.22. Two specimens with surface and embedded resistence strain gages were used by Paleebut and Cloud [2] to verify the results from the moire studies. A comparison of the strain component, ϵ_{yy} obtained from the double embedded moire method and the strain gage is shown in Figure 5.23 for mid-plane, quarter plane and surface plane‡‡and strain component, ϵ_{xx} is shown in Figure 5.24. Based on strain energy density criterion and elastic-plastic (modified BLP plane strain) finite element, the values of strain estimated are shown in Figure 5.23.

5.4.1 Measurement of Three Dimensional Mode-1 SIF

There are four factors that influence the Mode-1 stress intensity factor variations through the thickness of a compact tension specimen. The factors are the variation between plane-strain fracture toughness K_{IC} and the plane stress factor K_C; the residual stresses present in the specimen; the curvature of the crack front; and the thickness effect. The elastic stress field in the vicinity of a crack tip was given in (1). The displacement components are a function of material constants and do depend on whether the problem is plane strain or plane stress. The results can be compared with the three dimensional stress intensity factor determination using experimental techniques such as photoelasticity and moire technique of Smith, et. al. [60].

‡‡The author used the results of Paleebut [1] for verification and proper interpretation.

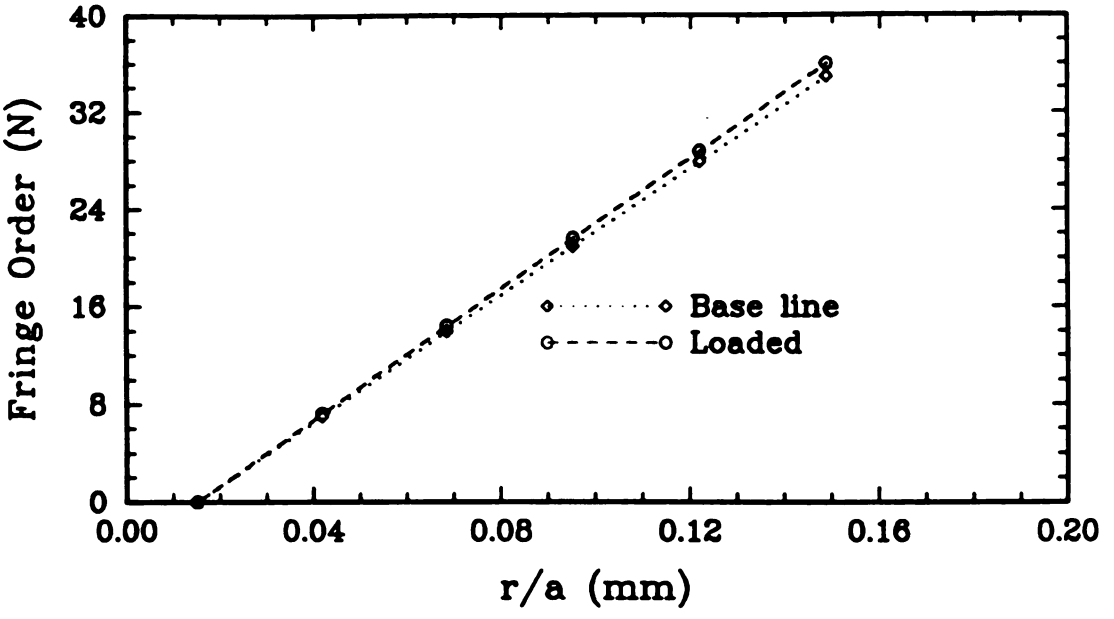

Figure 5.22: Plot of distance versus fringe order.

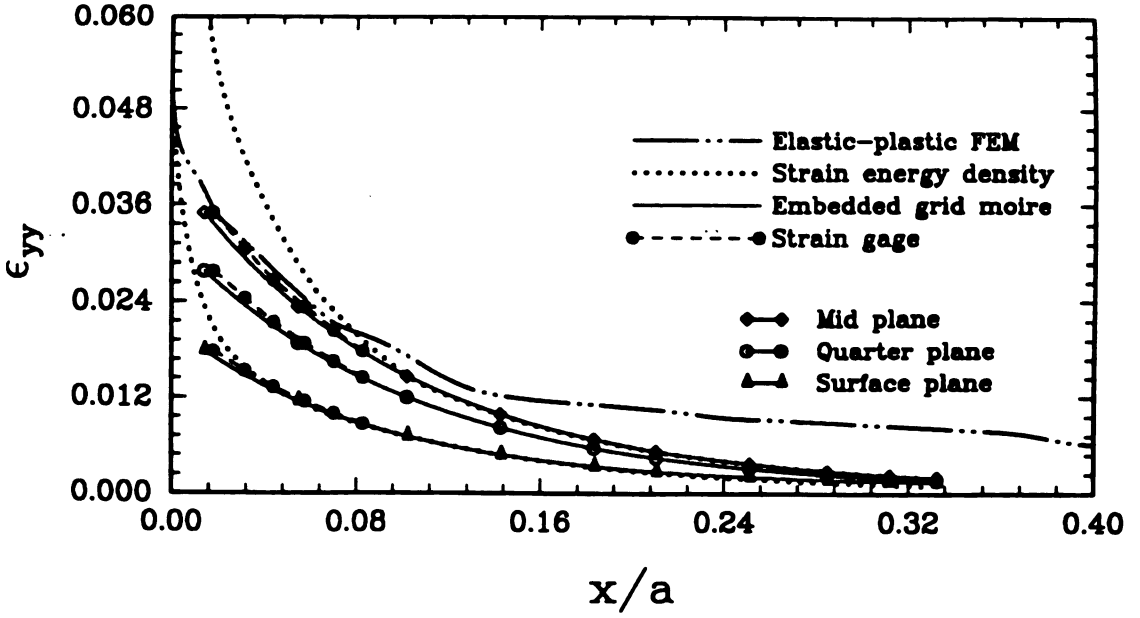

Figure 5.23: Crack opening strain distribution in a CT specimen for a/W = 0.4966 and $\theta = 0°$ based on embedded grid moire and strain gage technique.

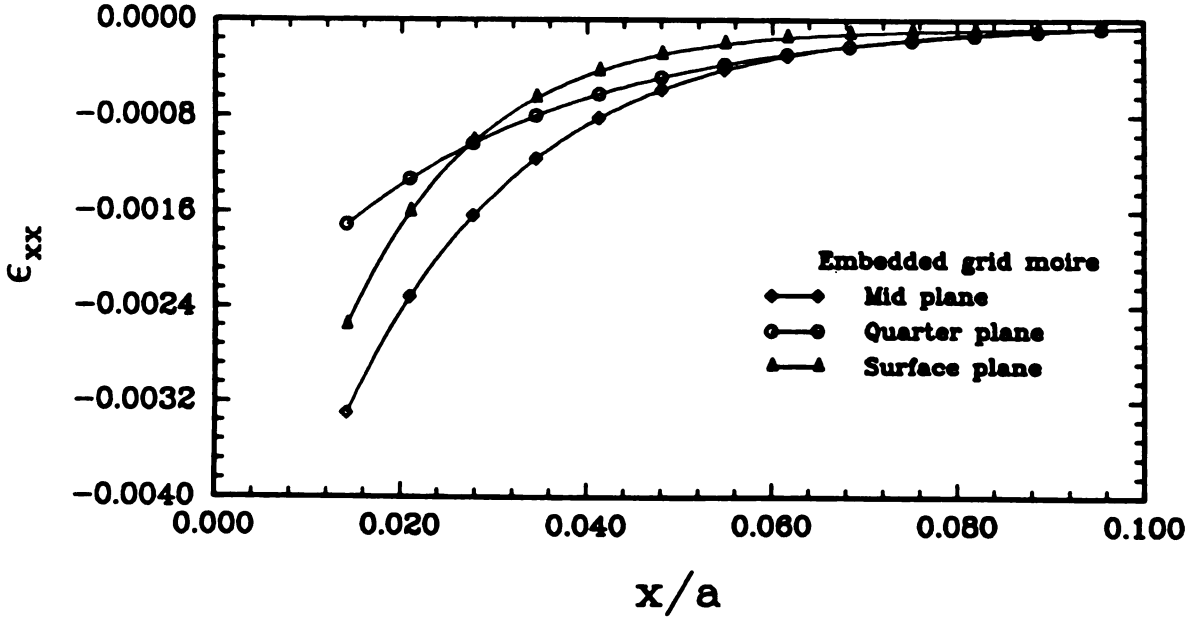

Figure 5.24: Transverse strain distribution in a CT specimen for a/W = 0.4966 and $\theta = 0°$ based on embedded grid moire and strain gage technique.

Near the crack tip, crack opening displacement along the crack is given by (1.9) in plane strain and (1.10) for plane stress. Here U_1 and U_2 are the displacements in the horizontal and vertical directions respectively, ν is the Poisson's ratio, and G is the shear modulus. The displacement and strain field surrounding the crack tip vary throughout the thickness of the specimen. Hence, the three dimensional stress-intensity factor is now a function of specimen thickness and material properties of the specimen. The stress intensity factor K_I is the sum of stress intensity factor $K_{(Py)}$, for the stress field surrounding the crack tip due to applied load P and the stress intensity factor K_{Ry} due to residual stresses in the specimen. The effect of residual stresses are cancelled because only the change in the displacement is measured. Hence $K_I = K_{Py}$. The change in the displacement is;

$$U_1 = \frac{K_I}{G}\sqrt{\frac{r}{2\pi}}cos\frac{\theta}{2}\left[1 - 2\nu + cos\frac{\theta}{2}\right] \tag{5.21}$$

$$U_2 = \frac{2K_I}{G}\sqrt{\frac{r}{2\pi}}sin\frac{\theta}{2}\left[2 - 2\nu - cos\frac{\theta}{2}\right] \tag{5.22}$$

The maximum shear stress in xy direction is given by:

$$\tau_{max} = \frac{NF}{2t} \tag{5.23}$$

where t is the layer thickness. The plastic zone size is given by (5.24) for plane strain and by (5.25) for plane stress.

$$r_y = \frac{1}{6}\left(\frac{K_{IC}}{\sigma_y}\right)^2 \tag{5.24}$$

$$r_y = \frac{1}{2}\left(\frac{K_{IC}}{\sigma_y}\right)^2 \tag{5.25}$$

For the full width of the plastic zone

$$r_p = 2r_y \tag{5.26}$$

Given r_y is the plastic zone size, K_{IC} is the fracture toughness of polycarbonate (9.3 ksi $\sqrt{in}$), and σ_y is the yield strength of the material, the effective stress intensity factor K_{eff} can be determined.

$$K_{eff} = \sigma\sqrt{\pi r_y} \tag{5.27}$$

After expressing the stress components in the xy plane in terms of singular terms proportional to the SIF plus terms representing the contribution of the nonsingular stress in the measurement zone which is near the crack tip along $\theta = \frac{\pi}{2}$, and thereafter computing the maximum shear stress in the xy plane; the resulting expression for apparent SIF (K_{AP}) as given by Smith and Epstein [61] is,

$$\frac{K_{AP}}{\sigma\sqrt{\pi a}} = \frac{K_I}{\sigma\sqrt{\pi a}} + f\left(\sigma_{ij}\left[\frac{r_y}{a}\right]\right) \tag{5.28}$$

and

$$\sigma_{ij} = \left(\frac{K_I}{\sqrt{r}}\right) f_{ij}(\theta) + \sigma_{ij}(r,\theta) \tag{5.29}$$

for i,j = x,y. Where $f_{ij}(\theta)$ is the stress eigenfunction. Turning, again to the moire results, the form of K_{AP}, using a grating parallel to the crack plane is,

$$K_{AP} = \frac{CU_x}{\sqrt{r_y}} \tag{5.30}$$

and perpendicular to the plane it is,

$$K_{AP} = \frac{CU_y}{\sqrt{r_y}} \tag{5.31}$$

where C contains the elastic constants of the material above the critical (room) temperature, σ is the load parameter, such as remote stress, K_I is Mode-1 SIF. σ_{ij} or σ_{ox} is given for stresses in a plane mutually orthogonal to the crack surface and crack border. σ_{ij} are normally taken to be constant for a given point to point. Equation (5.29) is applied in region $\theta = \frac{\pi}{2}$ observing that stress fringes tend to spread approxi-

mately normal to the crack surface. Figure 5.25 shows the variation of stress intensity factor throughout the thickness. The stress intensity factor is larger in the midplane than in the surface plane. A schematic of deformation process near the crack tip as observed is shown in Figure 5.26 and is left to the reader to consider. Equation (5.28) is modified by taking K_I as K_{Py}:

$$\frac{K_{AP}}{\sigma\sqrt{\pi a}} = \frac{K_{py}}{\sigma\sqrt{\pi a}} + f\left(\sigma_{ij}\left[\frac{r_y}{a}\right]\right) \tag{5.32}$$

After substituting (5.32) in (5.21) and (5.22), inplane displacements at the crack tip are obtained.

$$U_1 = \frac{2(1+\nu)}{E} K_{AP} \frac{\sqrt{r}}{2} cos\frac{\theta}{2}\left[1 - 2\nu - cos\frac{\theta}{2}\right] \tag{5.33}$$

$$U_2 = \frac{2(1+\nu)}{E} K_{AP} \frac{\sqrt{r}}{2} sin\frac{\theta}{2}\left[2 - 2\nu - cos\frac{\theta}{2}\right] \tag{5.34}$$

Equation (5.32) signifies that in the measurement zone, the normalized apparent SIF varies linearly with the square root of the normalized distance from the crack tip. The normalized apparent SIF versus $(\frac{r}{a})^{1/2}$ was plotted to locate the linear zone. A straight line is fitted to this data and extrapolated across the nonlinear region to the crack tip origin to give $K_I = \sigma\sqrt{\pi a}$, shown in Figure 5.27.

Analytical versus experimental results in the nonlinear zone are shown in Figure 5.28 . In this figure, the vertical axis denotes $G\frac{\gamma_{max}}{\sigma_o}$, where G is the shear modulus, γ_{max} is the maximum shear strain, and σ_o is the yield stress. The horizontal axis denotes $(\frac{Y\sigma_o^2}{K_I^2})$, where Y is the distance from the crack tip normal to crack plane and K_I is the Mode-1 stress intensity factor. The results are better because the displacements measured using the embedded grid technique are more accurate.

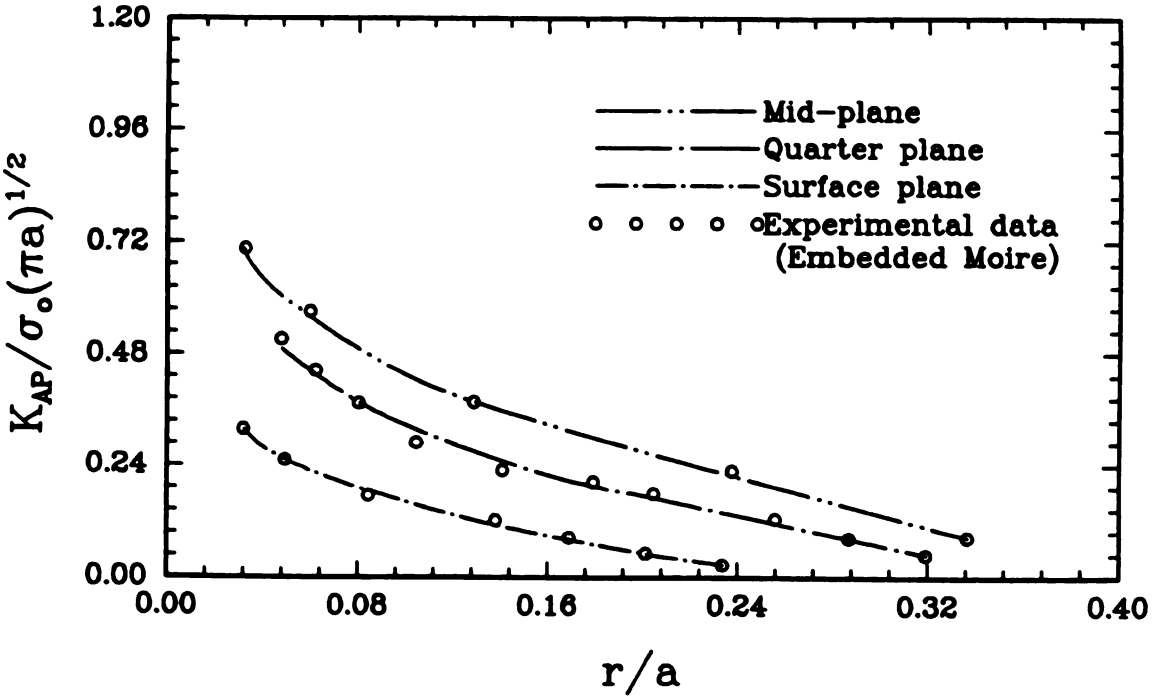

Figure 5.25: Variation of stress intensity factor throughout the thickness.

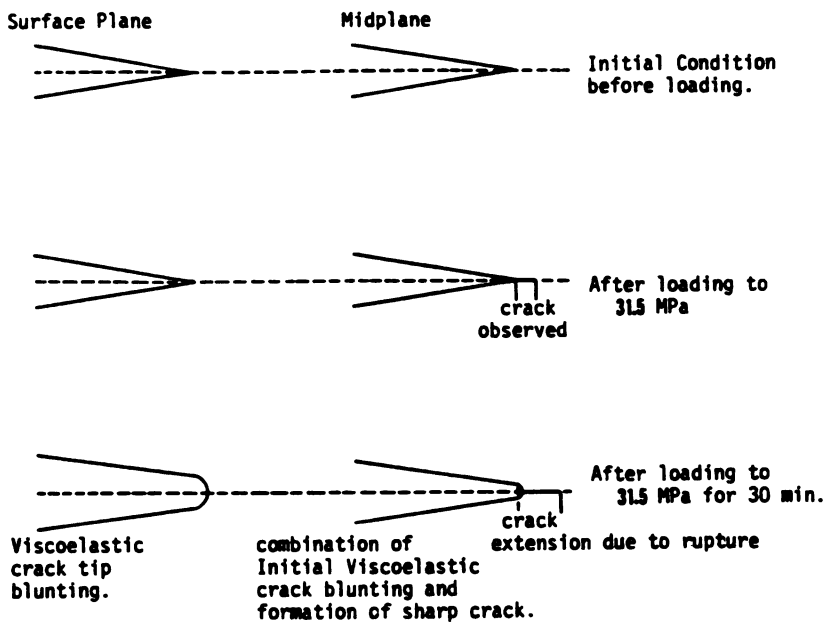

Figure 5.26: Schematic of deformation near the crack tip.

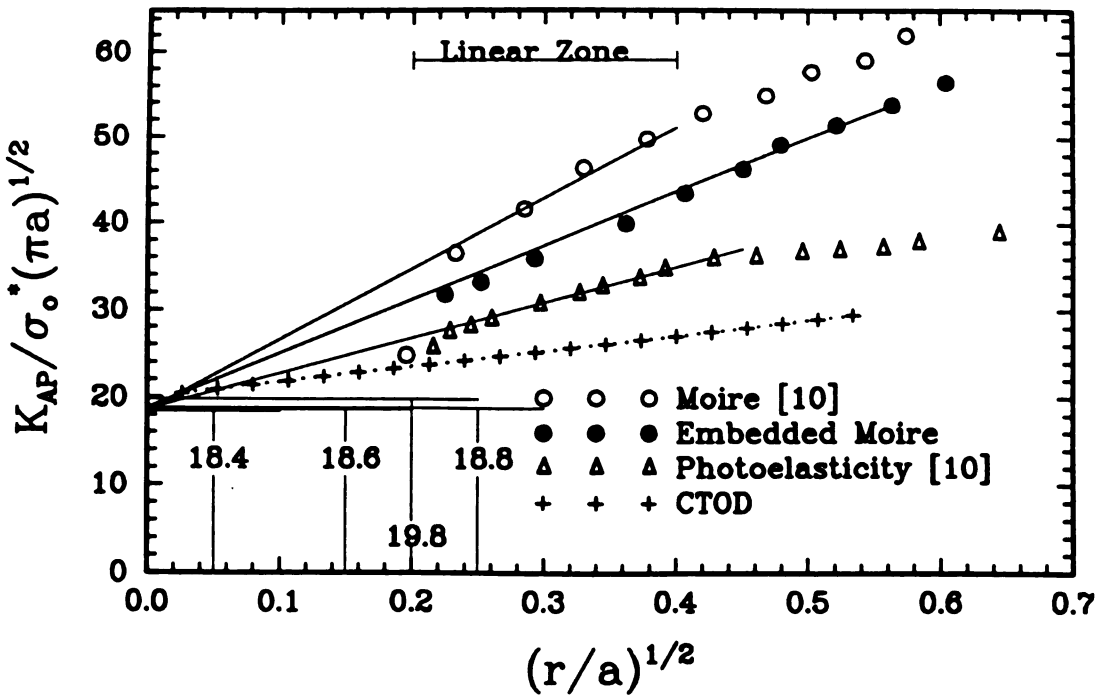

Figure 5.27: Estimation of Mode-1 SIF based on COD, 3D stress freezing, Moire and Double embedded moire techniques.

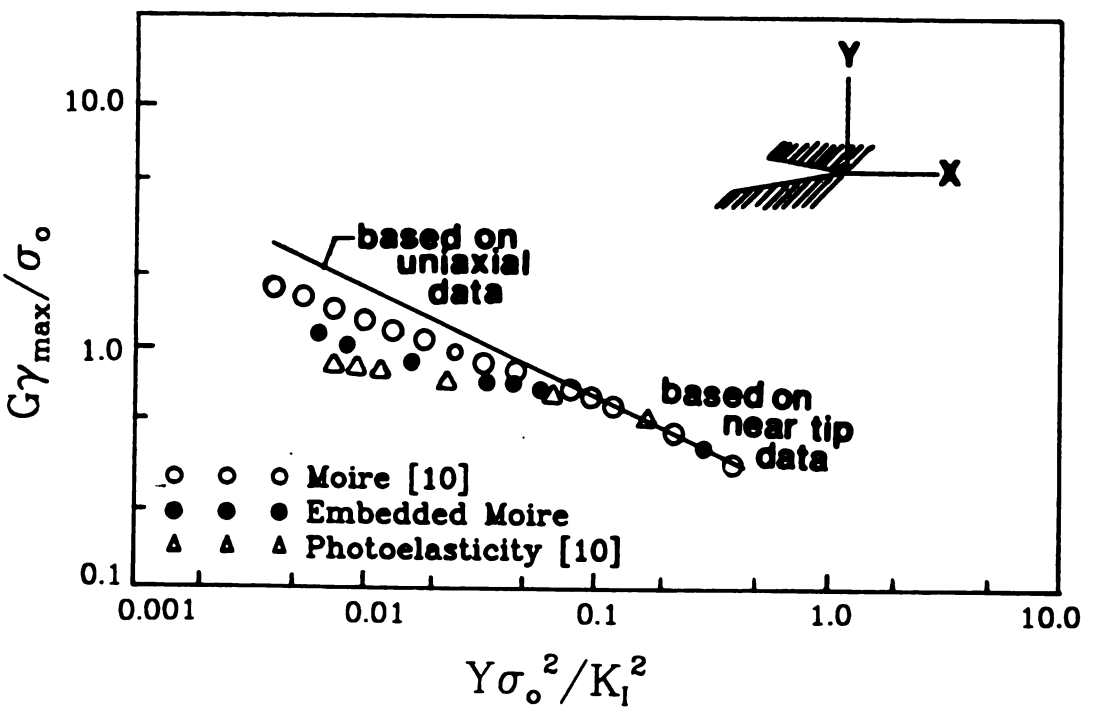

Figure 5.28: Analytical versus experimental results in the non linear zone.

5.5 Experimental Method to Find Size and Shape of the Plastic Zone

In photoelasticity the appropriate isochromatic lines themselves designate the plastic zones which may satisfy the yield criterion. Now, looking at the moire photograph in Figure 5.21b of the deformed crack tip, one suspects that there is really a plastic yielding. If there is not large scale yielding at the crack tip, then the measured strains should agree with the elastic prediction. The first approximation of plastic zone size r_p ahead of a notch tip was derived from the Von-Mises criterion on the basis of elastic stress distribution. The above equation doesn't describe the shape of the plastic zone. The following methods have been employed to find the shape and extent of the plastic zone.

(a) Experimental determination of constant strain or stress contour in the mid-plane, quarter-plane and surface-plane near the crack tip of the specimen using multiple embedded grid moire technique.

(b) Direct measurement of the plastic zone size on the surface plane only.

(c) Theoretical prediction of plastic zone size based on (b).

By simple geometry the size of the plastic zone indicated by moire photos can be found. The shape can be approximated by an ellipse. Suppose the ellipse's major half axis is a_1 and minor axis is b_1 ($= a_1\mu$, μ is the eccentricity ratio), then the equation for the upper half ellipse is;

$$\left(\frac{x_1 - a_1}{a_1}\right)^2 + \left(\frac{y_1}{\mu a_1}\right)^2 = 1 \tag{5.35}$$

The equation for the x axis in the x_1 y_1 coordinate system is;

$$y_1 = tg\,(-\varphi)\,x_1 = -x_1 tg\varphi \tag{5.36}$$

By writing (5.35) and (5.36) simultaneously, we have;

$$x_1 = \frac{2\mu^2 a_1}{\mu^2 + tg^2\varphi} \tag{5.37}$$

$$y_1 = \frac{2\mu^2 tg^2(\varphi) a_1}{\mu^2 + tg^2\varphi} \tag{5.38}$$

$$r_p = \sqrt{x_1^2 + y_1^2} = \frac{2\mu^2 a_1 sec(\varphi)}{\mu^2 + tg^2\varphi} \tag{5.39}$$

In terms of polar coordinates (5.39) is rewritten as

$$r_p = \frac{2\mu^2 a_1 sec(\varphi - \phi) a_1}{\mu^2 + tg^2(\varphi - \phi)} \tag{5.40}$$

Where φ is the angle varying from 0° to 90° for the upper half of the ellipse and ϕ is the angle of $r_{p(max)}$ with the axis. From the above equation r_p is found, and it describes the shape of the plastic zone with the given orientation. The ratio μ is an important factor in deciding the shape of the plastic zone. Substituting the value of r_p from (5.39) into (3.46) yields the stress contour. Figure 3.7 represents the methods to estimate the plastic zone size not only in the surface plane but also in the midplane. With an increase in the nominal stress S_n, the plastic zone size changes its orientation relative to the crack tip. This behavior is observed experimentally on the surface plane. Figures 3.11 to 3.13 show these results. By knowing the nature of the plastic zone size in the surface, the size and magnitude can be predicted in the quarter-plane and mid-plane. It is interesting to note that the plastic zone size increases with the increase in nominal stress S_N; at the same time the orientation of $r_{p(max)}$ with respect to the x-axis also changes. In general it indicates that a change in the plastic zone from a butterfly to a wedge shape occurs with an increase in intensity of strain.

5.5.1 Estimation of Increment in Plastic Zone

Another way to predict the plastic zone incremental (refer (3.52) and (3.66)) on the surface plane is as follows. Referring to Figure 3.7, the area of the upper part of the

plastic zone S_E is divided into three parts; S_1 is the area of three quarters of the ellipse; S_2 is the area of the triangle, and S_3 is the area of the curved side. S_1, S_2 and S_3 are not identical.

$$S_1 = \frac{3}{4}\pi\mu a_1^2 \tag{5.41}$$

$$S_2 = \frac{1}{2}ra_1 sin\varphi = \mu^2 a_1^2 \frac{tg^2\varphi}{\mu^2 + tg^2\varphi} \tag{5.42}$$

$$S_3 = \frac{1}{2}\mu a_1^2 cos\left[\frac{-2\mu^2}{\mu_1^2 + tg^2\varphi}\right] \tag{5.43}$$

$$S_E = S_1 + S_2 + S_3 = S_k a_1^2 \tag{5.44}$$

The total area of the ellipse, S, is given by (5.46), taking $a_1 = r_p$, where

$$S = 2S_E = S_k r_p^2 \tag{5.45}$$

$$S = 2S_k r_p . \triangle r_p \tag{5.46}$$

so,

$$\triangle r_p = \frac{S}{2S_k r_p} \tag{5.47}$$

The measured and estimated values of r_p from (5.40), $\triangle r_p$ from (5.47) and (3.52) are given in Table 5.2.

Table 5.2. Measured and estimated values r_p and Δr_p.

A- $S_N = 4.137 MPa$

Layer	r_p measured	r_p (5.40)	Δr_p (3.52)	Δr_p (5.47)
Surface-plane	0.0177	0.0193	0.0018	0.00174
Quarter-plane	0.0296	0.0304	0.0038	0.0036
Mid-plane	0.0532	0.0547	0.0049	0.0047

B- $S_N = 17.927 MPa$

Layer	r_p measured	r_p (5.40)	Δr_p (3.52)	Δr_p (5.47)
Surface-plane	0.0438	0.0047	0.0024	0.0033
Quarter-plane	0.0779	0.0806	0.0039	0.0047
Mid-plane	0.114	0.117	0.0054	0.0049

C- $S_N = 31.717 MPa$

Layer	r_p measured	r_p (5.40)	Δr_p (3.52)	Δr_p (5.47)
Surface-plane	0.0897	0.0901	0.0345	0.046
Quarter-plane	0.1494	0.0149	0.0497	0.0483
Mid-plane	0.1893	0.1904	0.0679	0.0653

CHAPTER 6

DISCUSSION AND CONCLUDING REMARKS

6.1 Discussion

It is well known that for most two-dimensional problems, the stress-intensity factor K_I can be obtained by analytic techniques (chapter 1) or by finite-element analysis (chapter 4). The stress intensity factor is a measure of amplitude of the stress field surrounding the crack and specimen geometry and how the load is applied. If the crack length is small in comparison with the thickness of the specimen, the deformation of a large portion of the body at some distance away from the surface is independent of the coordinate in the thickness direction (plane strain). On the other hand, if the crack length is large as compared to the specimen thickness, then the transverse shear and normal components of stress can be assumed to vanish throughout the thickness of the specimen and the other three in-plane stress components remain practically constant over the specimen (generalized plane stress). The stress field in the vicinity of the crack tip in a two dimensional problem is independent of material constants and do not differ between plane stress and plane strain. The displacement and strain components are a function of material constants and do depend on whether the problem is plane strain or plane stress. The crack opening strain in plane stress

is higher than in plane strain and differs only by a factor of 3.7931 for $\theta = 0°$. The stress intensity factor in plane stress differs from plane strain by $(1 - \nu^2)$. For any stress level, however small, a small plastic zone would be formed at the crack tip for a ductile material. The plastic zone size in plane stress is almost three times larger than in the plane strain. In polycarbonate the damage of the material ahead of a crack is by crazing. Crazing ahead of the crack may be modeled by yielding as the crack spreads. The von Mises yield condition cannot realistically describe material damage ahead of a crack where dilitation can play an important role. However we have assumed that the Mises yield criteria may describe the damaged zone near the crack tip. The increase in the crack tip radius causes the strain to increase in plane stress or in plane strain. The size and shape of the plastic zone depends on crack tip radius and the nominal stress. The local stress intensity factor for small scale yielding is related to the path independent J-integral. The latter applies to nonlinear elastic materials and cannot describe the irreversible physical damage process ahead of the crack. Since the analytical two-dimensional stress or strain fields are based on linear elasticity, the coordinates of the plastic zone size may be normalized with K_I or J and the yield strength of the material.

In many instances, the crack length may be of the same order of magnitude as the thickness of the specimen, and the in-plane stress can no longer be assumed to remain constant across the thickness direction since the free surface of the specimen can exert appreciable influence on the stress distribution. As a result, the crack driving force will vary along the crack front and the problem becomes three-dimensional. The generalized plane stress solution will not be a limit of the three-dimensional solution. Furthermore, it is incorrect to refer to the stress distribution on the surface layer of a plate with or without a crack as being in a state of generalized plane stress. The problem of plane strain does represent an exact special case of the more general three-dimensional problem. In fact, such a condition has been known to prevail in a region close to the crack border interior to the plate. The intensity of the local stress may be function of the thickness coordinate (refer to Sih [50]). The three-dimensional analytical tools that are available today may have difficulties, and they can, at best, give qualitative characteristic of the three-dimensional singular stresses. An elastic finite element analysis of a thick compact tension specimen was done, and the crack opening stress fields for various thicknesses are compared with the existing three-dimensional analytical tool. We observed that the difference in the variation of

the crack opening stress distribution between the two increases with increase in the thickness. This difference could be due to coarse mesh used or due to the limitation of the analytical solution. This question may be answered by experimental techniques.

The problem selected was the Mode-1 stress intensity factor variation along the crack front of a CT specimen. Three experimental techniques are capable of solving this type of problem. Three-dimensional photoelasticity using the frozen stress technique, moire using embedded grids*and finally the CTOD technique were used. Within the experimental limitation all the three techniques used gave a good estimate of Mode-1 SIF. The measured variation in the SIF (local) for this particular crack in the CT specimen is due to the curvature of the crack front and the thickness effect. The crack front of the tested CT specimen was not perfectly straight, but it was well within the ASTM tolerance for measuring plane-strain fracture toughness. The double embedded moire was demonstrated to be more successfully employed in connection with the frozen stress, moire interfermetry and CTOD techniques in order to measure displacement fields in the neighborhood of natural crack tips in a problem exhibiting strong three-dimensional effects. Displacement fields were converted to SIF values which compared favorably with photoelastic results by assuming a state of plane strain. In the double embedded moire technique for the plane strain case, the presence of an inverse-square root singularity in the stresses are assumed and boundary layer effects are ignored. It was shown in the analysis that the photoelastic and moire (embedded) results yield similar SIF values, but the apparent embedded moire SIF values are above the photoelastic results. This difference is due to the fact that the state of constraint away from the crack tip is less severe than the plane strain state assumed for the moire-displacement calculations. Two slices, one at the midplane and the other at the surface plane, were analyzed. Since experimental scatter of ± 2 to ± 10 percent is common in the photoelastic data, the results are considered to be reasonable. SIF predicted by CTOD technique are a little higher than embedded moire or photoelasticity results. The crack opening displacements along sections of the plate parallel to its mid-plane formed logarithmic curves, whereas along sections normal to the midplane of symmetry of the plate they gave almost a constant. This area indicated the zones of a crack flank under conditions of plane-strain. Along the outer strand the values of CODs diminished smoothly to limiting values corresponding to the lateral faces of the CT specimen. To study the localized elastic-plastic deformation within

*refer to Cloud and Paleebut [2]

the plastic zone of quasi-steady cracks and to asses the validity range of asymptotic formulation, the inclusion of non-singular elastic stresses are investigated. Ramerg-Osgood material was chosen initially and then polycarbonate material was studied. The elastic-plastic strain distribution ahead of the crack tip are affected significantly, while near-tip fields are relatively insensitive to the biaxiality ratio. The estimated values of the non-singular stress are comparable with the photoelastic investigations. The effect of this non-singular stress are explained for Ramberg-Osgood material in detail. Since the effects are known, only the strain distribution obtained from the modified boundary layer corresponding to polycarbonate material are compared to that of experimentally obtained strain from embedded moire. The results are comparable but the distance from the crack tip has been normalized with the initial crack length. The value of J-integral showed consistency only until 6 rings in the circular domain out of sixteen were chosen. The validity of the J-integral becomes questionable when applied to ductile fracture, a process that is load-time history dependent and involves cumulative damage regardless of whether the applied load is monotonic or cyclic. Having this in mind, the energy density approach for calculation of three dimensional strain and stress at the crack tip in CT specimens of polycarbonate was chosen.

The energy-based method is based on the assumption that the strain energy density distribution in the plastic zone ahead of a crack tip is the same as that determined on the basis of a pure elastic stress strain solution. The method is applied in the cases in which the plastic zone is small in comparison with the surrounding elastic field. The energy based method had been used for both plane stress and plane strain conditions. The stress redistribution caused by local yielding and the multiaxial stress state is taken into account. The elastic-plastic strains and stresses over the plastic zone ahead of the crack tip were determined using multiple embedded grid moire technique, and the data were compared with results obtained with strain gages. Because nominal stress S_N is high, approaching the yield strength σ_o, a correction for the plastic zone redistribution is applied. The plastic zone boundary was plotted with the help of coordinates noted down at all discrete points, considering the von-Mises criterion. We observed that plastic zone size in the surface plane is smaller than in the mid-plane. At the mid-plane, crack opening strain is higher since there is no free surface to impose a constraint on the hydrostatic stress and triaxiality builds up there. However, the hydrostatic stress along the mid-plane cannot be maintained on the surface of the

crack tip, and therefore a maximum in crack opening strain exists corresponding to the maximum for hydrostatic stress at some distance from the crack tip.

6.2 Conclusion

We have dealt with the interpretation of results obtained from embedded moire by Cloud and Paleebut [2] for the surface where plane stress exists (not the generalized plane stress) and for the internal layer where plane strain exists. The plane stress condition in the surface plane is reduced to uniaxial stress; and, in the plane strain condition, the stress state is reduced to a biaxial state. A total of four layers was employed in these experiments.

Strains are higher in the mid-plane than on the surface plane. Strain distribution measured by the multiple embedded grid technique is in good agreement with that of the strain gage technique. The theoretical estimation of strain is also comparable with the two experimental methods mentioned above.

The shape and magnitude of the plastic zone is predicted and measured. For different nominal stresses, changes in plastic zone shape, magnitude and orientation are observed. The contour of the plastic zone represents constant stress or strain values. Even much below the yield, a kidney-or-butterfly-shaped plastic zone is observed.

The calculated plastic zone size agrees with measurements. Because of the plastic yielding, stress redistribution occurs at the notch tip, increasing r_p by an increment $\triangle r_p$. The $\triangle r_p$ was calculated by two different methods, and the results are in good agreement. The above observations lead to the conclusion that a crack initiates at the mid-plane at any load for a given geometry at room temperature.

The apparent stress intensity factor values were computed from the embedded moire data along $\theta = \frac{\pi}{2}$. A common linear zone was established for layers along the crack border from which layers were taken. The Mode-1 SIF showed a good correlation with those obtained by moire and photoelasticity. The displacement values measured using embedded moire grid methods are more accurate than any other technique, and hence the results obtained show that Mode-1 SIF are comparable to the analytical result.

In our photoelastic investigations we computed the Mode-1 SIF in the mid-plane and in the surface plane. Mode-1 SIF in the mid-plane is almost 2.66 times larger than in the surface plane. Also the biaxiality parameters obtained from the experiments are reasonably good when compared to that obtained from a finite element solution in plane strain. In the surface plane the biaxiality parameter is 1.1 times smaller than in the mid-plane. The comparison of biaxiality parameter couldn't be made because of lack of reported results.

The effect of biaxiality parameter is more pronounced for a power hardening material than for a materials showing softening.

The CTOD technique also predicted similar variation of SIF from mid-plane to surface plane. However the predictions of SIF are higher than any other experimental results.

APPENDICES

APPENDIX A

Fortran code to solve energy density equations

```
      PROGRAM energy
C-----------------------------------------------------------------
C       THIS PROGRAM IS WRITTEN TO CALCULATE INELASTIC STRAIN AND
C       STRESSES BASED ON ENERGY DENSITY APPROACH. NUMERICAL
C       TECHNIQUE IS BASED ON PIECEWISE APPROXIMATION OF THE
C       MATERIAL STRESS-STRAIN CURVE.
C-----------------------------------------------------------------
C       THE FORTRAN CODE IS WRITTEN BY SUBRATO DHAR AT MICHIGAN
C       STATE UNIVERSITY (1989-90) AND MODIFIED AT MIT (1991-92).
C       REVISED ON 06-01-92.
C-----------------------------------------------------------------
C-----------------------------------------------------------------
C-----NLE  - NUMBER OF LINEAR ELEMENTS OF THE MATERIAL STRESS-
C            STRAIN CURVE.
C-----S    - NOMINAL STRESS FOR TENSION
C-----KT   - STRESS CONCENTRATION FACTOR
C-----SN   - NOMINAL STRESS IN TENSION
C-----EN   - NOMINAL STRAIN
C-----WN   - ENERGY DENSITY DUE TO THE NOMINAL STRESS AND STRAIN
C-----DSIG(I) - STRESS RANGE CORRESPONDING TO THE LINEAR ELEMENTS
C               OF THE MATERIAL STRESS-STRAIN CURVE
C-----DEPS(I) - STRAIN RANGE CORRESPONDING TO THE LINEAR ELEMENTS
C               OF THE MATERIAL STRESS-STRAIN CURVE
C-----------------------------------------------------------------
      REAL KT
      INTEGER I,J,K,M
      DOUBLE PRECISION SLYS,ELYS,WLYS,EELYS,PELYS,
```

```
     1 SLYN,ELYN,WLYN,EELYN,PELYN,EPSY
      DIMENSION DSIGS(100),DEPSS(100),X(100),Y(100),
     1 DSIGN(100),DEPSN(100),XP(100),XM(100),YM(100),
     1 XS(100),YS(100),RMIN(10),RMAX(10)
C-------------------------------------------------------------
      OPEN (UNIT=11, FILE='inp_dat1',STATUS='OLD')
      OPEN (UNIT=111, FILE='inp_dat2',STATUS='OLD')
      OPEN (UNIT=112, FILE='inp_dat3',STATUS='OLD')
      OPEN (UNIT=113, FILE='inp_dat4',STATUS='OLD')
C-------------------------------------------------------------
      OPEN (UNIT=12, FILE='out_fil1',STATUS='UNKNOWN')
      OPEN (UNIT=13, FILE='out_fil2',STATUS='UNKNOWN')
      OPEN (UNIT=14, FILE='out_fil3',STATUS='UNKNOWN')
      OPEN (UNIT=15, FILE='out_fil4',STATUS='UNKNOWN')
      OPEN (UNIT=16, FILE='out_inel',STATUS='UNKNOWN')
      OPEN (UNIT=17, FILE='out_elas',STATUS='UNKNOWN')
      OPEN (UNIT=18, FILE='out_dugd',STATUS='UNKNOWN')


C-----READ AND WRITE FILE------------------------------

      OPEN (UNIT=23, FILE='out_strss',STATUS='UNKNOWN')
c      OPEN (UNIT=25, FILE='eqstress',STATUS='UNKNOWN')
c      OPEN (UNIT=26, FILE='conteqs',STATUS='UNKNOWN')
C-------------------------------------------------------------
C----MATERIAL PROPERTIES AND GEOMETRIC DIMENSIONS-------------

      W  = 75.45
      A  = 37.49
      B  = 40.00
      PI = 3.141592654
      E  = 2206.4
      PNU = 0.45
      YST = 27.972

C----CRACK TIP RADIUS RO HAS TO BE CHANGED WHEN NECESSARY-----

      RHO = 0.

C-------------------------------------------------------------
C----STRESS AND STRAIN DISTRIBUTION ONLY--------------------


      WRITE(12,33)
33    FORMAT(/5X, 'Strain Energy Density Criterion (plane stress)'/,
     1 /2X, 'applied to notch'/,
     1 /1X,'-----------------------------------------'/,
     1 /5X, 'STRESS(ep)',5X, 'STRAIN(ep)',4X, 'STRAIN ENERGY'/,
     1 /1X,'-----------------------------------------'/)

      WRITE(13,44)
```

```
 44    FORMAT(/5X, 'Neubers criterion (plane stress)'/,
     1 /5X, 'applied to notch'/,
     1 /1X,'-----------------------------------------------'/,
     1 /5X, 'STRESS(ep)',5X, 'STRAIN(ep)',4X, 'STRAIN ENERGY'/,
     1 /1X,'-----------------------------------------------')


 C-----ELASTIC,ELASTIC-PLASTIC AND PLASTIC STRAIN ONLY--------

       WRITE(14,55)
 55    FORMAT(/5X, 'Strain Energy Density Criterion (plane stress)'/,
     1 /5X, 'applied to notch'/,
     1 /1X,'-----------------------------------------------'/,
     1 /5X, 'STRAIN(ep)',5X, 'STRAIN(e)',5X, 'STRAIN(p)'/,
     1 /1X,'-----------------------------------------------')

       WRITE(15,66)
 66    FORMAT(/5X, 'Neubers criterion (plane stress)'/,
     1 /1X, 'applied to notch'/,
     1 /1X,'-----------------------------------------------'/,
     1 /5X, 'STRAIN(ep)',5X, 'STRAIN(e)',5X, 'STRAIN(p)'/,
     1 /1X,'-----------------------------------------------')

 C----PLANE STRESS-----------------------------------------

       I = 0
       DO 97 M=1,1000
       I = I+1
 97    READ(11,*,ERR=98) X(M),Y(M)
 98    CONTINUE
       DO 99 J = 1, I-2
       DEPSS(J) = X(J+1) - X(J)
       DSIGS(J) = Y(J+1) - Y(J)
       NLES=J
 99    CONTINUE
       REWIND (11)

 C-----SPECIMEN CONFIGURATION USED TO CALCUALTE NOMINAL STRESS----
 C-----IN CASE OF BLUNT NOTCH OR CRACK---------------------------

       DO 997 LOAD = 0,7000,200
       KT=1.75
       S = (2.0*LOAD*((2.0*W)+A))/(((W-A)**2)*B)
 c      WRITE(*,*)S
       CALL NOTCH (NLES,DEPSS,DSIGS,SLYS,ELYS,WLYS,KT,S,E,EELYS,PELYS)
 997   CONTINUE

 C-----STRESS AND STRAIN DISTRIBUTION ONLY-----------------------

       WRITE(12,333)
 333   FORMAT(/2X, 'Strain Energy Density Criterion (plane strain)'/,
```

```
     1 /5X, 'applied to notch'/,
     1 /1X,'-----------------------------------------------'/,
     1 /5X, 'STRESS(ep)',5X, 'STRAIN(ep)',4X, 'STRAIN ENERGY'/,
     1 /1X,'-----------------------------------------------')

      WRITE(13,444)
444    FORMAT(/5X, 'Neubers criterion (plane strain)'/,
     1 /5X, 'applied to notch'/,
     1 /1X,'-----------------------------------------------'/,
     1 /5X, 'STRESS(ep)',5X, 'STRAIN(ep)',4X, 'STRAIN ENERGY'/,
     1 /1X,'-----------------------------------------------')

C-----ELASTIC,ELASTIC-PLASTIC AND PLASTIC STRAIN ONLY----------

      WRITE(14,555)
555   FORMAT(/5X, 'Strain Energy Density Criterion (plane strain)'/,
     1 /5X, 'applied to notch'/,
     1 /1X,'-----------------------------------------------'/,
     1 /5X, 'STRAIN(ep)',5X, 'STRAIN(e)',5X, 'STRAIN(p)'/,
     1 /1X,'-----------------------------------------------')

      WRITE(15,666)
666   FORMAT(/5X, 'Neubers criterion (plane strain)'/,
     1 /5X, 'applied to notch'/,
     1 /1X,'-----------------------------------------------'/,
     1 /5X, 'STRAIN(ep)',5X, 'STRAIN(e)',5X, 'STRAIN(p)'/,
     1 /1X,'-----------------------------------------------')

C-------------------------------------------------------------
C-----PLANE STRAIN---------------------------------------------

      I = 0
      DO 87 M=1,1000
      I = I+1
87    READ(11,*,ERR=88) X(M),Y(M)
      XP(M) = (Y(M)/E)-X(M)
      MU = (PNU+(E*XP(M)/2.0*Y(M)))/(1.0+(E*XP(M)/Y(M)))
      X(M) = (X(M)*(1.0-MU**2))/(SQRT(1.0-MU+MU**2))
      Y(M) = Y(M)/(SQRT(1.0-MU+MU**2))
88    CONTINUE
      DO 89 J = 1, I-2
      DEPSN(J) = X(J+1) - X(J)
      DSIGN(J) = Y(J+1) - Y(J)
      NLEN=J
89    CONTINUE
      REWIND (11)

C-----SPECIMEN CONFIGURATION USED TO CALCUALTE NOMINAL STRESS----
C-----IN CASE OF BLUNT NOTCH OR CRACK----------------------------

      DO 887 LOAD = 0,7000,200
```

```
      KT=3.45
      S = (2.0*LOAD*((2.0*W)+A))/(((W-A)**2)*B)
c      WRITE(*,*)S
      CALL NOTCH (NLEN,DEPSN,DSIGN,SLYN,ELYN,WLYN,KT,S,E,EELYN,PELYN)

887   CONTINUE
c      CALL FLOW (EPSI,SIG,EPSIhrr1,EPSIhrr2)

C-----SPECIMEN CONFIGURATION USED TO CALCUALTE STRESS INTENSITY
C-----FACOR  AND ELASTIC-PLASTIC STRESS AND STRAIN IN CASE OF
C-----SHARP CRACK-----------------------------------------------

      LOAD = 632.95
      S = (2.0*LOAD*((2.0*W)+A))/(((W-A)**2)*B)
      write(*,*)SSS
C-----DATA FOR KT VARIATION WITH NORMALIZED DISTANCE-------------
C-----M FOR MIDPLANE AND S FOR SURFACE PLANE---------------------

      WRITE(12,707)
707    FORMAT(/2X, 'Strain Energy Density Criterion (plane stress)'/,
     1 /2x, 'applied to sharp crack for KI varying with distance'/,
     1 /1X,'-----------------------------------------------'/,
     1 /5X, 'STRESS(ep)',5X, 'STRAIN(ep)',4X, 'STRAIN ENERGY'/,
     1 /1X,'-----------------------------------------------'/)

      WRITE(16,717)
717    FORMAT(/2X, 'Inelastic strain (SURFACE PLANE) ahead of'/,
     1 /2x, 'a sharp crack tip for KI varying with distance'/,
     1 /1X,'-----------------------------------------------'/,
     1 /5X, 'Distance (X)',5X, 'STRAIN',5X, 'STRESS'/,
     1 /1X,'-----------------------------------------------'/)

      WRITE(14,808)
808    FORMAT(/2X, 'Strain Energy Density Criterion (SURFACE PLANE)'/,
     1 /2x, 'applied to sharp crack for KI varying with distance'/,
     1 /1X,'-----------------------------------------------'/,
     1 /5X, 'STRESS(ep)',5X, 'STRAIN(ep)',4X, 'STRAIN ENERGY'/,
     1 /1X,'-----------------------------------------------'/)

C-------------------------------------
      IJJ = 0
      DO 9007 M=1,2000
      READ(113,*,ERR=9008) XS(M),YS(M)
      KT = YS(M)
      CALL NOTCH (NLES,DEPSS,DSIGS,SLYS,ELYS,WLYS,KT,S,E,EELYS,PELYS)
      WRITE(16,901)XS(M),ELYS
901   FORMAT(1X,2(1PE15.7))
      IJJ = IJJ+1
9007    CONTINUE
9008    CONTINUE
C-------------------------------------
```

```
      WRITE(12,747)
747    FORMAT(/2X, 'Strain Energy Density Criterion (plane strain)'/,
     1 /2x, 'applied to sharp crack for KI varying with distance'/,
     1 /1X,'-----------------------------------------------'/,
     1 /5X, 'STRESS(ep)',5X, 'STRAIN(ep)',4X, 'STRAIN ENERGY'/,
     1 /1X,'-----------------------------------------------')

      WRITE(16,757)
757    FORMAT(/2X, 'Inelastic strain (MID PLANE) ahead of'/,
     1 /2x, 'a sharp crack tip for KI varying with distance'/,
     1 /1X,'-----------------------------------------------'/,
     1 /5X, 'Distance (X)',5X, 'STRAIN',5X, 'STRESS'/,
     1 /1X,'-----------------------------------------------')

      WRITE(14,667)
667    FORMAT(/2X, 'Strain Energy Density Criterion (plane stress)'/,
     1 /2x, 'applied to sharp crack for KI varying with distance'/,
     1 /1X,'-----------------------------------------------'/,
     1 /5X, 'STRESS(ep)',5X, 'STRAIN(ep)',4X, 'STRAIN ENERGY'/,
     1 /1X,'-----------------------------------------------')

C---------------------------------------
      IJJJ = 0
      DO 9097 M=1,2000
      READ(111,*,ERR=9098) XM(M),YM(M)
      KT = YM(M)
      CALL NOTCH (NLEN,DEPSN,DSIGN,SLYN,ELYN,WLYN,KT,S,E,EELYN,PELYN)
      WRITE(16,9042)XM(M),ELYN
9042   FORMAT(1X,2(1PE15.7))
      IJJJ = IJJJ+1
9097    CONTINUE
9098    CONTINUE
C-------------------------------------------------------------
C-----ESTIMATION OF PLASTIC ZONE SIZE AND SHAPE--------------

      FACTOR = (((2.0+(A/W))*(0.886+4.64*(A/W)-13.32*((A/W)**2)+
     1 14.72*((A/W)**3)-5.6*((A/W)**4))))/(((SQRT(1.0-(A/W)))**3)*
     1 SQRT(A/W)*SQRT(PI))

      KIN = S*(SQRT(PI*A))*FACTOR

C-----THE VALUE OF J INTEGRAL TO BE CHANGED FOR PLANE STRAIN (PJ)
C-----AND PLANE STRESS (PJS)

      PJ = (1.0 - PNU*PNU)*(KIN*KIN)/E
      PJS = (KIN*KIN)/E

      write(*,*)KIN,PJ,FACTOR

C-----BLUNT AND SHARP CRACK OR NOTCH BASED ON RHO------------
C-----ELASTIC STRESS DISTRIBUTION----------------------------
```

```
C     START THE OUTER THETA LOOP (I LOOP)
C     THETA VARIES FROM 0 to 180.
      JJ = 0
      DO 999 M=1
      NTHETA=0
      DO 191 I=1,37
c      WRITE(23,*)NTHETA
      THERAD = NTHETA*(PI/180.D0)

C     FOR GIVEN VALUE OF THETA LOOP ALL VALUES OF R (J LOOP)

      DO 511 K =0,5
      RMIN(K) = 0.001*(10**(K))
      RMAX(K+1) = 10.*RMIN(K)
      PINC = (RMAX(K+1)-RMIN(K))/40.d0
      R = RMIN(K)

      DO 192 J=1,40
      R = RMIN(K)+PINC*FLOAT(J-1)

      SIGX = (KIN/(SQRT(2.0*PI*R)))*(COS(THERAD/2.0)*
     1 (1.0 - SIN(THERAD/2.0)*SIN(3.0*THERAD/2.0))-
     1 COS(3.0*THERAD/2.0)*(RHO/(R)))

      SIGY = (KIN/(SQRT(2.0*PI*R)))*(COS(THERAD/2.0)*
     1 (1.0 + SIN(THERAD/2.0)*SIN(3.0*THERAD/2.0))+
     1 COS(3.0*THERAD/2.0)*(RHO/(R)))

      SIGXY = (KIN/(SQRT(2.0*PI*R)))*(COS(THERAD/2.0)*
     1 SIN(THERAD/2.0)*COS(3.0*THERAD/2.0)-
     1 SIN(3.0*THERAD/2.0)*(RHO/(R)))

C-----PLANE STRAIN (SIZPN = ####) AND PLANE STRESS (SIZPN = 0)

      SIGZPN = PNU*(SIGX+SIGY)
c      SIGZPN =0.
C-----------------------------
      XX1=(R*YST)/PJ
      RR1=(SIGX/YST)
      RR2=(SIGY/YST)
      RR3=(SIGZPN/YST)
      RR4=(SIGXY/YST)
      EPSX=(SIGX/E)-PNU*((SIGY+SIGZPN)/E)
      EPSY=(SIGY/E)-PNU*((SIGX+SIGZPN)/E)
      HYDRO=(SIGX+SIGY+SIGZPN)/3.0

      TERM1=(SIGX-SIGY)**2 + (SIGY-SIGZPN)**2 +(SIGZPN-SIGX)**2 +
     1 (6.0*(SIGXY**2))
      TERM2=SQRT(TERM1)
      TERM3=0.707106*(TERM2)
```

```
      VON=(TERM3/YST)
      XCORD = XX1*COS(THERAD)
      YCORD = XX1*SIN(THERAD)
      XR = R/(A)

      IF(THERAD .EQ. 0) THEN
      WRITE(17,1000)XR,EPSY
1000   FORMAT(2X,1(1PE15.7),2X,1(1PE15.7))
      ENDIF
      JJ=JJ+1
      WRITE(23,101) JJ,J,R,XCORD,YCORD,XX1,VON
101   FORMAT(2X,1(I10),2X,1(I10),2X,1(1PE15.7),2X,1(1PE15.7),
     1 2X,1(1PE15.7),2X,1(1PE15.7),2X,1(1PE15.7))

192   CONTINUE
511   CONTINUE

C     NOW GO BACK AND USE NEXT VALUE OF THETA
      NTHETA = NTHETA + 5.0

191   CONTINUE
999   CONTINUE

      CALL DUGDALE (TY,SA,PI,COD)

      STOP
      END
C-------------------------------------------------------
C-----COMPARISION OF PLASTIC ZONE SIZE WITH DUGDALE THEORY-------
C-----SA IS RATIO OF MAXIMUM PLASTIC ZONE RADIUS AND CRACK LENGTH
C-----TY IS RATIO OF NORMAL STRESS APPLIED AND YIELD STRESS.

      SUBROUTINE DUGDALE (TY,SA,PI,COD)
      DOUBLE PRECISION TY,SA

C-----PLASTIC ZONE

      DO 21 TY=0.0,1.0,0.1
      SA = 2.0*SIN((PI/4.0)*TY)*SIN((PI/4.0)*TY)
      WRITE(18,100)TY,SA
100   FORMAT(2X,1(1PE15.7),2X,1(1PE15.7))
21    CONTINUE

C-----CRACK OPENING DISPLACEMENT

      DO 22 TY=0.0,1.0,0.1
      COD = (2.0/PI)*log((1+SIN((PI/2.0)*(TY)))/
     1 (1-SIN((PI/2.0)*(TY))))
      WRITE(18,100)COD,TY
101   FORMAT(2X,1(1PE15.7),2X,1(1PE15.7))
22    CONTINUE
```

```
C-----STRAIN ENERGY RELEASE RATE

      END
C-----------------------------------------------------------------
C-----------------------------------------------------------------
      SUBROUTINE NOTCH (NLE,DEPS,DSIG,SLY,ELY,WLY,KT,S,E,EELY,PELY)
C-----------------------------------------------
      REAL KT
      INTEGER I,J,L,N
      DOUBLE PRECISION SLY,ELY,WLY
      DIMENSION DSIG(100),DEPS(100),H(100),P(100)
C-----------------------------------------------
      YST=27.972
      YSN=0.0126
      WSTN=YST*YSN

      DO 100 J=1,NLE
100   SNG = 1.
      IF(S .LT. 0.) SNG = -1.
      TR=0
      I = 0
      WN = 0
      H(1) = 0
      SN = 0
      EN = 0
C-----------------------------
      DO 110 N = 1, NLE
110   P(N) = 0
120   I = I + 1
c      IF(I .GT. NLE) GO TO 420
      IF(SNG .GT. 0) GO TO 130
      DP = -5
      GO TO 140
130   DP = 5
140   DP = DP/10
150   P(I) = P(I) + DP
      SN = SN + DSIG(I)*DP
      EN = EN + DEPS(I)*DP
      H(1) = 0.
      DO 160 J = 2, I+1
160   H(J) = H(J-1) + DSIG(J-1)*P(J-1)
      WN = 0.
      DO 170 L = 1, I
170   WN = WN + (H(L) + H(L+1))*0.5*DEPS(L)*P(L)
      SS = SN
      IF(ABS(SS) .GT. ABS(S)) GO TO 180
      IF(ABS(P(I)) .GT. 1) GO TO 190
      GO TO 220
180   P(I) = P(I) - DP
      SN = SN - DSIG(I)*DP
```

```
      EN = EN - DEPS(I)*DP
      GO TO 140
190   IF(SNG .LT. 0) GO TO 200
      DQ = ABS(P(I)) - 1.0
      GO TO 210
200   DQ = - (ABS(P(I)) -1.0)
210   P(I) = P(I) - DQ
      SN = SN - DSIG(I)*DQ
      EN = EN - DEPS(I)*DQ
      GO TO 120
220   IF(ABS(((SS - S)/S)) .GT. 1.0E-05) GO TO 150
C-----------------------------------------------------
230   C = WN*(KT**2)
240   IF(TR .EQ. 1.) C = SN*EN*(KT**2)
250   I = 0
      H(1) = 0
      SLY =0
      ELY = 0
      WLY = 0
      DO 260 N = 1, NLE
260   P(N) = 0
270   I = I + 1
c      IF(I .GT. NLE) GO TO 420
      IF(SNG .GT. 0) GO TO 290
      DP = -5
      GO TO 300
290   DP = 5
300   DP = DP/10
310   P(I) = P(I) + DP
      SLY = SLY + DSIG(I)*DP
      ELY = ELY + DEPS(I)*DP
      EELY=SLY/E
      PELY=ELY-EELY
      IF(TR .EQ. 1.) GO TO 340
      DO 320 J = 2, I + 1
320   H(J) = H(J-1) + DSIG(J-1)*P(J-1)
      WLY = 0.
      DO 330 L = 1, I
330   WLY = WLY + (H(L) + H(L + 1))*0.5*DEPS(L)*P(L)
      GO TO 350
340   WLY = SLY*ELY
350   IF(ABS(WLY) .GT. ABS(C)) GO TO 360
      IF(ABS(P(I)) .GT. 1) GO TO 370
      GO TO 390
360   P(I) = P(I) - DP
      SLY = SLY - DSIG(I)*DP
      ELY = ELY - DEPS(I)*DP
      EELY=SLY/E
      PELY=ELY-EELY
      GO TO 300
370   IF(SNG .LT. 0) GO TO 375
```

```
      DQ = ABS(P(I)) - 1.0
      GO TO 380
375   DQ = -(ABS(P(I)) - 1.0)
380   P(I) = P(I) - DQ
      SLY = SLY - DSIG(I)*DQ
      ELY = ELY - DEPS(I)*DQ
      EELY=SLY/E
      PELY=ELY-EELY
      GO TO 270
390   IF(ABS(((C-WLY)/C)) .GT. 1.0E-05) GO TO 310
c      SLY=SLY/YST
c      WLY=WLY/WSTN
      SNM=KT*SN

      IF(TR .EQ. 1.) GO TO 405

c      WRITE(12,400) SLY,ELY,WLY
c400   FORMAT(1X,3(1PE15.7))

       WRITE(12,400) ELY,SNM
400    FORMAT(1X,2(1PE15.7))

      WRITE(14,401) ELY,EELY,PELY
401   FORMAT(1X,3(1PE15.7))

      TR = 1.
      GO TO 240

c405   WRITE(13,410) SLY,ELY,WLY
c410   FORMAT(1X,3(1PE15.7))

405   WRITE(13,410) ELY,SNM
410   FORMAT(1X,2(1PE15.7))

      WRITE(15,411) ELY,EELY,PELY
411   FORMAT(1X,3(1PE15.7))

c420   WRITE(*,430)
c430   FORMAT(/9X, 'REQUIRED EXTENSION OF THE STRESS-STRAIN CURVE!'/)
      END
C-------------------------------------------------------------
C-------------------------------------------------------------
C-----RAMBERG OSGOOD MATERIAL FLOW CURVE---------------------

      SUBROUTINE FLOW (EPSI,SIG,EPSIhrr1,EPSIhrr2)
      INTEGER N
      DOUBLE PRECISION EPSI,SIG,EPSIhrr1,EPSIhrr2

      DO 200 N=3,5,2
      DO 100 SIG=0.,130.0,5.
      E    = 2206.4
```

```
      SIGY = 55.944
      EPSIY= SIGY/E
      alpha = 0.5
      EPSI = ((SIG/SIGY)+alpha*(SIG/SIGY)**N)*EPSIY

c      EPSI = EPSI/EPSIY
c      SIG = SIG/SIGY

C-----HRR FLOW CURVE---------------------------------------

      EPSIhrr1 = (SIG/SIGY)*EPSIY
      EPSIhrr2 = ((SIG/SIGY)**N)*EPSIY

c      EPSI1 = EPSIhrr1/EPSIY
c      EPSI2 = EPSIhrr2/EPSIY
c      SIG = SIG/SIGY

      WRITE(16,101) EPSI,SIG
      WRITE(17,101) EPSIhrr1,SIG
      WRITE(18,101) EPSIhrr2,SIG
101   FORMAT(1(1PE15.7),2X,1(1PE15.7))

100   CONTINUE
200   CONTINUE

      END
C-------------------------------------------------------------
c=============================================================
      SUBROUTINE DATA1 (y0,XXXX,YYYY,XX,YY,RP,C,DNNTHETA)
      IMPLICIT REAL*8(A-H,O-Z)
      DIMENSION XX(200),YY(200),C(10)
c     DIMENSION y0(10)
C
      OPEN (UNIT=25, FILE='eqstress',STATUS='OLD')
c=============================================================
      DO 999 L=1,4,1
      XMIN=0.001*(10**L)
      XMAX=XMIN*10.0
      I = 0
c-------------------------------------------------------
      DO 9999 M=1,1000
      READ(25,*,ERR=998)NODE,XXXX,YYYY
C      WRITE(*,*) 'CHECK NUMBER OF DATA POINTS'
      IF((XXXX.GT.XMIN).AND.(XXXX.LE.XMAX)) THEN
      I=I+1
      XX(I)=XXXX
      YY(I)=YYYY
      ENDIF
9999  CONTINUE
c-------------------------------------------------------
998   CONTINUE
```

```
      write(*,*)' I=',i,' XMIN=',xmin,' XMAX=',xmax
      IF(i.gt.0 .and. y0.lt.yy(1) .and. y0.ge.yy(i)) then
      do 234 j=1,i
      write(*,*)XX(j),YY(j),'    %%%%'
234   continue
      CALL FITTING (y0,XX,YY,RP,C,I,DNNTHETA,1,XMIN,XMAX)
c      DNNTHET=DNNTHETA*(180.d0/3.14159)
c      write (*,*)DNNTHET,RP
      endif
      REWIND (25)
999   CONTINUE
      END
C=======================================================================
      SUBROUTINE FITTING (y0,XX,YY,RP,C,N,DNNTHETA,INDEX,XMIN,XMAX)
      IMPLICIT REAL*8(A-H,O-Z)
      DIMENSION C(10),A(10,10),XN(200),XX(200),YY(200)
      MS=4
      MF=4
      IF(MF .LE.(N-1)) GO TO 5
      MF=N-1
C      WRITE(6,200) MF
C200   FORMAT(1H0, 42HDEGREE OF POLYNOMIAL CANNOT EXCEED N - 1. /
C     +   1H , 47HREQUESTED MAXIMUM DEGREE TOO LARGE - REDUCED TO , I3)
5     MFP1=MF+1
      MFP2=MF+2
      DO 10 I=1,N
10    XN(I)=1.
      DO 30 I=1,MFP1
      A(I,1)=0.
      A(I,MFP2)=0.
      DO 20 J=1,N
      A(I,1)=A(I,1)+XN(J)
      A(I,MFP2)=A(I,MFP2)+YY(J)*XN(J)
20    XN(J)=XN(J)*XX(J)
30    CONTINUE
      DO 50 I=2,MFP1
      A(MFP1,I)=0.
      DO 40 J=1,N
      A(MFP1,I)=A(MFP1,I)+XN(J)
40    XN(J)=XN(J)*XX(J)
50    CONTINUE
      DO 70 J=2,MFP1
      DO 60 I=1,MF
60    A(I,J)=A(I+1,J-1)
70    CONTINUE
C      WRITE(6,201) ((A(I,J),J=1,MFP2),I=1,MFP1)
C201   FORMAT(1H0,9F13.5)
      CALL LUDCMQ (A,MFP1,10)
      MSP1=MS+1
      DO 95 I=MSP1,MFP1
      DO 90 J=1,I
```

```
90    C(J)=A(J,MFP2)
      CALL SOLNQ (A,C,I,10)
      IM1=I-1
C      WRITE(6,202) IM1,(C(J),J=1,I)
C202   FORMAT (1H0, 14HFOR DEGREE OF , I2, 17H COEFFICIENTS ARE,/
C     +   1H , 10X, 11F11.3)
c-----------------------------------------------------------------------
      IF (INDEX .EQ. 1) THEN
          CALL XROOT(C,Y0,XMIN,XMAX,RP)
          X1=RP*COS(DNNTHETA)
          Y1=RP*SIN(DNNTHETA)
          WRITE (26,102) X1,Y1
          END IF
102   FORMAT(1(1PE15.7),2X,1(1PE15.7))
c-----------------------------------------------------------------------
      BETA=0.0
      DO 94 IPT=1,N
      SUM=0.0
      DO 93 ICOEF=2,I
      JCOEF=I-ICOEF+2
      SUM=(SUM+C(JCOEF))*XX(IPT)
93    CONTINUE
      SUM=SUM+C(1)
      BETA=BETA+(YY(IPT)-SUM)**2
94    CONTINUE
      BETA=BETA/(N-I)
C      WRITE (6,203)BETA
C203   FORMAT(1H , 10X, 9H BETA IS , F10.5)
95    CONTINUE
      RETURN
      END
c++++++++++++++++++++++++++++++++++++++++++++++++++++++++++++++++++++++++
      FUNCTION F(C,X)
      IMPLICIT REAL*8(A-H,O-Z)
      DIMENSION C(1)
      F= C(5)*X**4 + C(4)*X**3 + C(3)*X**2 + C(2)*X + C(1)
      RETURN
      END
ccccccccccccccccccccccccccccccccccccccccccccccccccccccccccccccccccccccc
      SUBROUTINE XROOT (C,Y0,XMIN,XMAX,RP)
      IMPLICIT REAL*8(A-H,O-Z)
       fmin=f(c,xmin)
       fmax=f(c,xmax)
       write(*,*)'y0= ',y0, ' XMIN=',xmin,' XMAX=',xmax,' fmin=',fmin,
     + ' fmax=',fmax
      IF((Y0-F(C,XMIN))*(Y0-F(C,XMAX)) .GT. 0 )  GO TO 99
1     X=(XMIN+XMAX)/2.0
C     WRITE (*,*) 'X=',X
      IF (ABS(Y0-F(C,X)) .LT. .00001) GO TO 100
      IF (Y0-F(C,X) .LT. 0.) THEN
      XMIN=X
```

```
      GO TO 1
      ELSE
      XMAX=X
      GO TO 1
      ENDIF
100   RP=X
      RETURN
99    WRITE(*,*) 'xmin and xmax are wrong'
      RP = 99999999.0
      RETURN
      END
CCCCCCCCCCCCCCCCCCCCCCCCCCCCCCCCCCCCCCCCCCCCCCCCCCCCCCCCCCCCCCCCCCCCCCCCCCCCCCC
      SUBROUTINE LUDCMQ (A,N,NDIM)
      IMPLICIT REAL*8(A-H,O-Z)
      DIMENSION A(NDIM,NDIM)
      DO 30 I=1,N
      DO 30 J=2,N
      SUM=0.
      IF (J .GT. I) GO TO 15
      JM1=J-1
      DO 10 K=1,JM1
10    SUM=SUM+A(I,K)*A(K,J)
      A(I,J)=A(I,J)-SUM
      GO TO 30
15    IM1=I-1
      IF(IM1 .EQ. 0.) GO TO 25
      DO 20 K=1,IM1
20    SUM=SUM+A(I,K)*A(K,J)
25    IF (ABS(A(I,I)) .LT. 1.0E-10) GO TO 99
      A(I,J)=(A(I,J)-SUM)/A(I,I)
30    CONTINUE
      RETURN
99    WRITE (6,100) I
100   FORMAT(1HO, 32H REDUCTION NOT COMPLETED BEACAUSE ,
     +   38H SMALL VALUE FOUND FOR DIVISOR IN ROW , I3)
      RETURN
      END
CCCCCCCCCCCCCCCCCCCCCCCCCCCCCCCCCCCCCCCCCCCCCCCCCCCCCCCCCCCCCCCCCCCCCCCCCCCCCCC
      SUBROUTINE SOLNQ (A,B,N,NDIM)
      IMPLICIT REAL*8(A-H,O-Z)
      DIMENSION A(NDIM,NDIM),B(NDIM)
      B(1)=B(1)/A(1,1)
      DO 20 I=2,N
      IM1=I-1
      SUM=0.
      DO 10 K=1,IM1
10    SUM=SUM+A(I,K)*B(K)
20    B(I)=(B(I)-SUM)/A(I,I)
      DO 40 J =2,N
      NMJP2=N-J+2
      NMJP1=N-J+1
```

```
      SUM=0.
      DO 30 K=NMJP2,N
30    SUM=SUM+A(NMJP1,K)*B(K)
40    B(NMJP1)=B(NMJP1)-SUM
      RETURN
      END
```

APPENDICES

APPENDIX B

Fortran code for contour mapping

```
      PROGRAM CRACK
C-----------------------------------------------------------------
C     THIS PROGRAM IS DEVELOPED TO CALCULATE THE PLASTIC
C     ZONE SIZE AND SHAPE FROM NODAL DATA OBTAINED FROM
C     ABAQUS.
C-----------------------------------------------------------------
C     THE FORTRAN CODE IS WRITTEN BY SUBRATO DHAR AT MIT
C     (1990-91) AND REVISED ON 06-04-92.
C-----------------------------------------------------------------
      IMPLICIT REAL*8(A-H,O-Z)
      DIMENSION XX(200),YY(200),C(10)
C=================================================================
4     FORMAT(A20)
C=================================================================
      OPEN (UNIT=11, FILE='coord',STATUS='OLD')
      OPEN (UNIT=12, FILE='stress',STATUS='OLD')
c      OPEN (UNIT=13, FILE='strain',STATUS='OLD')
c      OPEN (UNIT=14, FILE='disp',STATUS='OLD')
C=================================================================
c      OPEN (UNIT=15, FILE='sxx',STATUS='UNKNOWN')
c      OPEN (UNIT=16, FILE='syy',STATUS='UNKNOWN')
c      OPEN (UNIT=17, FILE='szz',STATUS='UNKNOWN')
c      OPEN (UNIT=18, FILE='sxy',STATUS='UNKNOWN')
c      OPEN (UNIT=19, FILE='exx',STATUS='UNKNOWN')
c      OPEN (UNIT=20, FILE='eyy',STATUS='UNKNOWN')
c      OPEN (UNIT=21, FILE='ezz',STATUS='UNKNOWN')
c      OPEN (UNIT=22, FILE='exy',STATUS='UNKNOWN')
c      OPEN (UNIT=23, FILE='uxx',STATUS='UNKNOWN')
c      OPEN (UNIT=24, FILE='uyy',STATUS='UNKNOWN')
C=================================================================
      OPEN (UNIT=25, FILE='eqstress',STATUS='UNKNOWN')
```

```
      OPEN (UNIT=26, FILE='conteqs',STATUS='UNKNOWN')
c      OPEN (UNIT=30, FILE='meanstrs',STATUS='UNKNOWN')
C=====================================================================
      E=400.0
      PNU=0.3
      PJ=115.8
      SIGY=1.0
      EPSY=0.0025
      PI=3.141569
      M=400
C=====================================================================
      DO 60 y0=1.0,1.5,0.1
      DO 20 K=1,129,4
      I=0
10    READ(11,*)NODE,X,Y
      READ(12,*)NODE,INT,S11,S22,S33,S44
c      READ(13,*)NODE,INT,E11,E22,E33,E44
c      READ(14,*)NODE,UX,UY
c---------------------------------------------------------------------
      NODEL=51200+K
      NODEA=(((NODE-K)/M)*M)
      NODEB=(NODE-K)
c---------------------------------------------------------------------
      IF((NODE.EQ.(400+K))) THEN
      DNNTHETA=(atan2(Y,X))
      ANGLE=DNNTHETA*(180.d0/3.14159)
c      WRITE(15,102)ANGLE
c      WRITE(16,102)ANGLE
c      WRITE(17,102)ANGLE
c      WRITE(18,102)ANGLE
c      WRITE(19,102)ANGLE
c      WRITE(20,102)ANGLE
c      WRITE(21,102)ANGLE
c      WRITE(22,102)ANGLE
c      WRITE(23,102)ANGLE
c      WRITE(24,102)ANGLE
c       WRITE(30,102)ANGLE
      ENDIF
c---------------------------------------------------------------------
      IF((NODE.GE.(400+K)) .AND. (NODEA.EQ.NODEB))THEN
      RXY=SQRT((X*X)+(Y*Y))
c---------------------------------------------------------------------
      XX1=(RXY*SIGY)/PJ
      RR1=(S11/SIGY)
      RR2=(S22/SIGY)
      RR3=(S33/SIGY)
      RR4=(S44/SIGY)
      SIGM=(S11+S22+S33)/3.0
c-----------------------------------------
c      XX2=(RXY*EPSY*E)/PJ
c      EE1=(E11/EPSY)
```

```
c       EE2=(E22/EPSY)
c       EE3=(E33/EPSY)
c       EE4=(E44/EPSY)
c-------------------------------------------
      TERM1=(S11-S22)*(S11-S22)
      TERM2=(S22-S33)*(S22-S33)
      TERM3=(S33-S11)*(S33-S11)
      TERM4=(6.0*S44*S44)
      TERM5=(TERM1+TERM2+TERM3+TERM4)
      TERM6=SQRT(TERM5)
      TERM7=0.707106*(TERM6)
      AMISES=TERM7
      VON=(AMISES/SIGY)
c-------------------------------------------
c       WRITE(15,101)XX1,RR1
c       WRITE(16,101)XX1,RR2
c       WRITE(17,101)XX1,RR3
c       WRITE(18,101)XX1,RR4
c       WRITE(19,101)XX2,EE1
c       WRITE(20,101)XX2,EE2
c       WRITE(21,101)XX2,EE3
c       WRITE(22,101)XX3,EE4
c       WRITE(23,101)X,UX
c       WRITE(24,101)X,UY
      WRITE(25,101)XX1,VON
c       WRITE(30,101)XX1,SIGM
C-------------------------------------------
      ENDIF
101   FORMAT(1(1PE15.7),2X,1(1PE15.7))
c-------------------------------------------
      I=I+1
      IF(NODE .LT. NODEL) GO TO 10
102   FORMAT(1(1PE15.7))
c-----------------------------------------------------------------
      CLOSE (25)
      CALL DATA1 (y0,XXXX,YYYY,XX,YY,RP,C,DNNTHETA)
c-----------------------------------------------------------------
      REWIND (11)
      REWIND (12)
c       REWIND (13)
c       REWIND (14)
c-----------------------------------------------------------------
20    CONTINUE
c       REWIND (15)
c       REWIND (16)
c       REWIND (17)
c       REWIND (18)
c       REWIND (19)
c       REWIND (20)
c       REWIND (21)
c       REWIND (22)
```

```
c      REWIND (23)
c      REWIND (24)
c       REWIND (30)
60    CONTINUE
c-----------------------------------------------------------------
      STOP
      END
c=================================================================
      SUBROUTINE DATA1 (y0,XXXX,YYYY,XX,YY,RP,C,DNNTHETA)
      IMPLICIT REAL*8(A-H,O-Z)
      DIMENSION XX(200),YY(200),C(10)
c     DIMENSION y0(10)
C
      OPEN (UNIT=25, FILE='eqstress',STATUS='OLD')
c=================================================================
      DO 999 L=0,6,1
      XMIN=0.0001*(10**L)
      XMAX=XMIN*10.0
      I = 0
c-----------------------------------------------------
      DO 9999 M=1,1000
      READ(25,*,ERR=998)XXXX,YYYY
C      WRITE(*,*) 'CHECK NUMBER OF DATA POINTS'
      IF((XXXX.GT.XMIN).AND.(XXXX.LE.XMAX)) THEN
      I=I+1
      XX(I)=XXXX
      YY(I)=YYYY
      ENDIF
9999  CONTINUE
c-----------------------------------------------------
998   CONTINUE
      write(*,*)' I=',i,' XMIN=',xmin,' XMAX=',xmax
      IF(i.gt.0 .and. y0.lt.yy(1) .and. y0.ge.yy(i)) then
      do 234 j=1,i
      write(*,*)XX(j),YY(j),'    %%%%'
234   continue
      CALL FITTING (y0,XX,YY,RP,C,I,DNNTHETA,1,XMIN,XMAX)
      DNNTHET=DNNTHETA*(180.d0/3.14159)
      write (*,*)DNNTHET,RP
      endif
      REWIND (25)
999   CONTINUE
      END
C=================================================================
      SUBROUTINE FITTING (y0,XX,YY,RP,C,N,DNNTHETA,INDEX,XMIN,XMAX)
      IMPLICIT REAL*8(A-H,O-Z)
      DIMENSION C(10),A(10,10),XN(200),XX(200),YY(200)
      MS=4
      MF=4
      IF(MF .LE.(N-1)) GO TO 5
      MF=N-1
```

```
C      WRITE(6,200) MF
C200   FORMAT(1H0, 42HDEGREE OF POLYNOMIAL CANNOT EXCEED N - 1. /
C     +   1H , 47HREQUESTED MAXIMUM DEGREE TOO LARGE - REDUCED TO , I3)
5     MFP1=MF+1
      MFP2=MF+2
      DO 10 I=1,N
10    XN(I)=1.
      DO 30 I=1,MFP1
      A(I,1)=0.
      A(I,MFP2)=0.
      DO 20 J=1,N
      A(I,1)=A(I,1)+XN(J)
      A(I,MFP2)=A(I,MFP2)+YY(J)*XN(J)
20    XN(J)=XN(J)*XX(J)
30    CONTINUE
      DO 50 I=2,MFP1
      A(MFP1,I)=0.
      DO 40 J=1,N
      A(MFP1,I)=A(MFP1,I)+XN(J)
40    XN(J)=XN(J)*XX(J)
50    CONTINUE
      DO 70 J=2,MFP1
      DO 60 I=1,MF
60    A(I,J)=A(I+1,J-1)
70    CONTINUE
C      WRITE(6,201) ((A(I,J),J=1,MFP2),I=1,MFP1)
C201   FORMAT(1H0,9F13.5)
      CALL LUDCMQ (A,MFP1,10)
      MSP1=MS+1
      DO 95 I=MSP1,MFP1
      DO 90 J=1,I
90    C(J)=A(J,MFP2)
      CALL SOLNQ (A,C,I,10)
      IM1=I-1
C      WRITE(6,202) IM1,(C(J),J=1,I)
C202   FORMAT (1H0, 14HFOR DEGREE OF , I2, 17H COEFFICIENTS ARE,/
C     +   1H , 10X, 11F11.3)
C-----------------------------------------------------------------------
      IF (INDEX .EQ. 1) THEN
          CALL XROOT(C,Y0,XMIN,XMAX,RP)
          X1=RP*COS(DNNTHETA)
          Y1=RP*SIN(DNNTHETA)
          WRITE (26,102) X1,Y1
          END IF
102   FORMAT(1(1PE15.7),2X,1(1PE15.7))
C-----------------------------------------------------------------------
      BETA=0.0
      DO 94 IPT=1,N
      SUM=0.0
      DO 93 ICOEF=2,I
      JCOEF=I-ICOEF+2
```

```
      SUM=(SUM+C(JCOEF))*XX(IPT)
93    CONTINUE
      SUM=SUM+C(1)
      BETA=BETA+(YY(IPT)-SUM)**2
94    CONTINUE
      BETA=BETA/(N-I)
C      WRITE (6,203)BETA
C203   FORMAT(1H , 10X, 9H BETA IS , F10.5)
95    CONTINUE
      RETURN
      END
C-----------------------------------------------------------------
      FUNCTION F(C,X)
      IMPLICIT REAL*8(A-H,O-Z)
      DIMENSION C(1)
      F= C(5)*X**4 + C(4)*X**3 + C(3)*X**2 + C(2)*X + C(1)
      RETURN
      END
C-----------------------------------------------------------------
      SUBROUTINE XROOT (C,Y0,XMIN,XMAX,RP)
      IMPLICIT REAL*8(A-H,O-Z)
       fmin=f(c,xmin)
       fmax=f(c,xmax)
       write(*,*)'y0= ',y0, ' XMIN=',xmin,' XMAX=',xmax,' fmin=',fmin,
     + ' fmax=',fmax
      IF((Y0-F(C,XMIN))*(Y0-F(C,XMAX)) .GT. 0 )  GO TO 99
1     X=(XMIN+XMAX)/2.0
C     WRITE (*,*) 'X=',X
      IF (ABS(Y0-F(C,X)) .LT. .00001) GO TO 100
      IF (Y0-F(C,X) .LT. 0.) THEN
      XMIN=X
      GO TO 1
      ELSE
      XMAX=X
      GO TO 1
      ENDIF
100   RP=X
      RETURN
99    WRITE(*,*) 'xmin and xmax are wrong'
      RP = 99999999.0
      RETURN
      END
C-----------------------------------------------
      SUBROUTINE LUDCMQ (A,N,NDIM)
      IMPLICIT REAL*8(A-H,O-Z)
      DIMENSION A(NDIM,NDIM)
      DO 30 I=1,N
      DO 30 J=2,N
      SUM=0.
      IF (J .GT. I) GO TO 15
      JM1=J-1
```

```
      DO 10 K=1,JM1
10    SUM=SUM+A(I,K)*A(K,J)
      A(I,J)=A(I,J)-SUM
      GO TO 30
15    IM1=I-1
      IF(IM1 .EQ. 0.) GO TO 25
      DO 20 K=1,IM1
20    SUM=SUM+A(I,K)*A(K,J)
25    IF (ABS(A(I,I)) .LT. 1.0E-10) GO TO 99
      A(I,J)=(A(I,J)-SUM)/A(I,I)
30    CONTINUE
      RETURN
99    WRITE (6,100) I
100   FORMAT(1H0, 32H REDUCTION NOT COMPLETED BEACAUSE ,
     +   38H SMALL VALUE FOUND FOR DIVISOR IN ROW , I3)
      RETURN
      END
C-------------------------------------------------------
      SUBROUTINE SOLNQ (A,B,N,NDIM)
      IMPLICIT REAL*8(A-H,O-Z)
      DIMENSION A(NDIM,NDIM),B(NDIM)
      B(1)=B(1)/A(1,1)
      DO 20 I=2,N
      IM1=I-1
      SUM=0.
      DO 10 K=1,IM1
10    SUM=SUM+A(I,K)*B(K)
20    B(I)=(B(I)-SUM)/A(I,I)
      DO 40 J =2,N
      NMJP2=N-J+2
      NMJP1=N-J+1
      SUM=0.
      DO 30 K=NMJP2,N
30    SUM=SUM+A(NMJP1,K)*B(K)
40    B(NMJP1)=B(NMJP1)-SUM
      RETURN
      END
C-------------------------------------------------------
```

APPENDICES

APPENDIX C

Fortran code containing COD data

```
      PROGRAM cod
C-----------------------------------------------------------------
C     MEASUREMENT OF CRACK OPENING DISPLACEMENT IN COMPACT
C     TENSION SPECIMEN MADE OUT OF POLYCARBONATE AND PLEXIGLASS.
C     THE PROGRAM CONTAINS EXPERIMENTAL DATA AND ANALYTICAL
C     RESULTS CORRESPONDING TO ELASTIC AND PLASTIC PARTS OF
C     CRACK OPENING DISPLACEMENT.
C-----------------------------------------------------------------
      INTEGER I,J,K,L,M,N
      DOUBLE PRECISION SLOPE1,X1,SLOPE2,X2,X(10),X(10),Y(10),
     1 LOAD1,LOAD2,LOAD(10),LOAD(10)
c-----------------------------------------------------------------
      OPEN (UNIT=11, FILE='cod_cal', STATUS='UNKNOWN')
      OPEN (UNIT=12, FILE='lod1_cod', STATUS='UNKNOWN')
      OPEN (UNIT=13, FILE='lod2_cod', STATUS='UNKNOWN')
      OPEN (UNIT=14, FILE='lod1_bfs', STATUS='UNKNOWN')
      OPEN (UNIT=15, FILE='lod2_bfs', STATUS='UNKNOWN')
      OPEN (UNIT=16, FILE='bfs1_cod', STATUS='UNKNOWN')
      OPEN (UNIT=17, FILE='bfs2_cod', STATUS='UNKNOWN')
      OPEN (UNIT=18, FILE='lod1_dis', STATUS='UNKNOWN')
      OPEN (UNIT=19, FILE='lod2_dis', STATUS='UNKNOWN')
      OPEN (UNIT=20, FILE='poly', STATUS='UNKNOWN')
C----CALIBRATION OF CLIP GAGE-----------------------------------
C----X AXIS IS THE DISPLACEMENT OF THE CLIP GAGE, AND Y AXIS IS
C----THE CLIP GAGE STRAIN (x 10E-04 mm/mm).

      SLOPE1=10.0
      DO 100 X1 = 0., 2.4, 0.218
      COD=SLOPE1*X1
      WRITE(11,1001) X1, COD
1001  FORMAT(1X,4(2X,1PE15.7))
```

```
100   CONTINUE

C----CLIP GAGE FIXED TO THE CT SPECIMEN MADE OUT OF-------------
C----POLYCARBONATE AND PLEXIGLASS-------------------------------
C----X AXIS IS THE CLIP GAGE STRAIN (x 10E-05 mm/mm), AND Y AXIS
C----IS THE LOAD (LBS) APPLIED TO THE SPECIMEN.

C----PLEXIGLASS--------------
      SLOPE2=10.81
      DO 200 X2 = 0., 18.5, 1.6818
      LOAD1=SLOPE2*X2
      WRITE(12,1002) X2, LOAD1
1002  FORMAT(1X,4(2X,1PE15.7))
200   CONTINUE

C----POLYCARBONATE-------------
      SLOPE3=10.0
      DO 300 X3 = 0., 84., 7.63636
      LOAD2=SLOPE3*X3
      WRITE(13,1003) X3, LOAD2
1003  FORMAT(1X,4(2X,1PE15.7))
300   CONTINUE

C-----DATA FOR LOAD VERSUS BACKFACE STRAIN GAGE IN---------------
C-----POLYCARBONATE AND PLEXIGLASS-------------------------------
C-----X AXIS IS BACKFACE STRAIN READINGS (x 10-E04 mm/mm) AND Y
C-----AXIS IS THE LOAD (LBS).

C-----POLYCARBONATE----------
      DO 400 I = 1,10,1
      X(1) = 0.0
      X(2) = 14.0
      X(3) = 22.0
      X(4) = 30.2
      X(5) = 38.4
      X(6) = 46.8
      X(7) = 55.2
      X(8) = 63.6
      X(9) = 72.0
      X(10) = 75.4
C----------------------
      Y(1) = 0.0
      Y(2) = 200.0
      Y(3) = 300.0
      Y(4) = 400.0
      Y(5) = 500.0
      Y(6) = 600.0
      Y(7) = 700.0
      Y(8) = 800.0
      Y(9) = 900.0
      Y(10) = 920.0
```

```
      WRITE(14,1004) X(I), Y(I)
1004  FORMAT(1X,4(2X,1PE15.7))
400   CONTINUE

C-----PLEXIGLASS----------
      DO 500 J = 1,8,1
      X(1) = 0.0
      X(2) = 2.5
      X(3) = 5.0
      X(4) = 7.5
      X(5) = 10.0
      X(6) = 11.0
      X(7) = 12.0
      X(8) = 13.0
C----------------------
      Y(1) = 0.0
      Y(2) = 45.625
      Y(3) = 91.25
      Y(4) = 136.875
      Y(5) = 182.5
      Y(6) = 190.0
      Y(7) = 192.0
      Y(8) = 190.0
      WRITE(15,1005) X(J), Y(J)
1005  FORMAT(1X,4(2X,1PE15.7))
500   CONTINUE

C-----DATA FOR BACK FACE STRAIN GAGE VERSUS CLIP GAGE IN---------
C-----POLYCARBONATE AND PLEXIGLASS------------------------------
C-----X AXIS IS THE CLIP GAGE READINGS (x 10E-05) AND Y AXIS IS
C-----THE BACK FACE STRAIN READINGS (x 10E-05).

C-----POLYCARBONATE----------
      DO 600 K = 1,6,1
      X(1) = 0.0
      X(2) = 19.0
      X(3) = 40.0
      X(4) = 62.0
      X(5) = 78.5
      X(6) = 94.5
C----------------------
      Y(1) = 0.0
      Y(2) = 13.0
      Y(3) = 27.0
      Y(4) = 43.0
      Y(5) = 57.5
      Y(6) = 76.0
      WRITE(16,1006) X(K), Y(K)
1006  FORMAT(1X,4(2X,1PE15.7))
600   CONTINUE
```

```
C-----PLEXIGLASS----------
      DO 700 L = 1,5,1
      X(1) = 0.0
      X(2) = 4.0
      X(3) = 8.0
      X(4) = 12.0
      X(5) = 16.0
C----------------------
      Y(1) = 0.0
      Y(2) = 2.5
      Y(3) = 5.0
      Y(4) = 7.5
      Y(5) = 10.0
      WRITE(17,1007) X(L), Y(L)
1007  FORMAT(1X,4(2X,1PE15.7))
700   CONTINUE

C-----DATA FOR LOAD VERSUS DISPLACEMENT FOR----------------------
C-----POLYCARBONATE AND PLEXIGLASS-------------------------------
C-----X AXIS IS THE CRACK OPENING DISPLACEMENT IN mm, AND Y AXIS
C-----IS THE LOAD (LBS).
      CONV=4.5
C-----POLYCARBONATE----------
      DO 800 M = 1,7,1
      X(1) = 0.0
      X(2) = 0.2
      X(3) = 0.43
      X(4) = 0.65
      X(5) = 0.88
      X(6) = 1.06
      X(7) = 0.98
C----------------------
      Y(1) = 0.0
      Y(2) = 200.0
      Y(3) = 410.0
      Y(4) = 600.0
      Y(5) = 800.0
      Y(6) = 920.0
      Y(7) = 940.0
      LOAD(M) = Y(M)*CONV
      WRITE(18,1008) X(M), LOAD(M)
1008  FORMAT(1X,4(2X,1PE15.7))
800   CONTINUE

C-----PLEXIGLASS----------
      DO 900 N = 1,6,1
      X(1) = 0.0
      X(2) = 0.02
      X(3) = 0.04
      X(4) = 0.06
      X(5) = 0.08
```

```
      X(6) = 0.12
C----------------------
      Y(1) = 0.0
      Y(2) = 30.0
      Y(3) = 60.0
      Y(4) = 90.0
      Y(5) = 120.0
      Y(6) = 180.0
      LOAD(N) = Y(N)*CONV
      WRITE(19,1009) X(N), LOAD(N)
1009  FORMAT(1X,4(2X,1PE15.7))
900   CONTINUE
C-------------------------------------------------------C

C-------------------------------------------------------C
C-------------------------------------------------------C
C-----CALCULATION OF PLASTIC ZONE SIZE-----------------C
C-----VR IS V(A/W), A IS CRACK LENGTH, W IS THE WIDTH,
C-----V IS TOTAL CRACK MOUTH OPENING DISPLACEMENT, VE IS
C-----ELASTIC PART AND VP IS PLASTIC PART, VEFF IS V(AEFF/W),
C-----AEFF=A+R, R IS THE PLASTIC ZONE RADIUS.

      V=1.06
      VE=0.92
      VP=0.14
      A=37.49
      W=75.45

      CONST = (2.163+12.219*(A/W)-20.065*(A/W)**2-0.993*(A/W)**3
     + 20.609*(A/W)**4-9.931*(A/W)**5)
      VR = ((1.0+(A/W)**2)/(4.0*(1.0-(A/W)**2)*(A/W)))*CONST

      VEF= ((A/W)*VR*(VP/VE)) + (A/W)*VR
      DO 99 R=0.,10.,1.
      VEFF= (W/(A+R))*VEF
      WRITE(20,1010) R,VEFF
1010  FORMAT(1X,4(2X,1PE15.7))
99    CONTINUE

C-----THE VALUES OF THE VEFF AND R IS KNOWN AND IS EXPRESSED
C-----IN TERMS OF POLYNOMIAL EQUATION USING SUBROUTINE POLDHAR
      DO 999 Q=0.,10.,1.
      VEFF1=1.597+0.808*Q-0.166*(Q**2)
      WRITE(*,*)Q,VEFF1
999   CONTINUE
      END
```

APPENDICES

APPENDIX D

For (a/W) = 0.3958 and $\theta = 151.88°$

r°	Sx(ct)	Sx(blp)	T	B	NODE
2.7755722E-07	1.4801920E+02	1.4784985E+02	1.6935000E-01	1.9999106E+00	309
5.5511449E-07	7.1953383E+01	7.1849969E+01	1.0341375E-01	1.2212475E+00	509
9.8212564E-07	5.8455282E+01	5.8363618E+01	9.1663750E-02	1.0824878E+00	709
1.4091371E-06	4.5125610E+01	4.5045465E+01	8.0145000E-02	9.4645904E-01	909
2.0660768E-06	3.9349854E+01	3.9274758E+01	7.5096250E-02	8.8683667E-01	1109
2.7230172E-06	3.2861001E+01	3.2791508E+01	6.9492500E-02	8.2066012E-01	1309
3.7336938E-06	2.8906687E+01	2.8840645E+01	6.6042500E-02	7.7991792E-01	1509
4.7443713E-06	2.4924474E+01	2.4861875E+01	6.2598750E-02	7.3924952E-01	1709
6.2992594E-06	2.2140697E+01	2.2080521E+01	6.0176250E-02	7.1064141E-01	1909
7.8541480E-06	1.9363467E+01	1.9305696E+01	5.7771250E-02	6.8223997E-01	2109
1.0246283E-05	1.7314502E+01	1.7258512E+01	5.5990000E-02	6.6120459E-01	2309
1.2638418E-05	1.5266258E+01	1.5212043E+01	5.4215000E-02	6.4024302E-01	2509
1.6318624E-05	1.3702480E+01	1.3649622E+01	5.2857500E-02	6.2421185E-01	2709
1.9998837E-05	1.2140675E+01	1.2089171E+01	5.1503750E-02	6.0822497E-01	2909
2.5660694E-05	1.0922675E+01	1.0872229E+01	5.0446250E-02	5.9573660E-01	3109
3.1322557E-05	9.7070837E+00	9.6576916E+00	4.9392125E-02	5.8328808E-01	3309
4.0033110E-05	8.7465852E+00	8.6980270E+00	4.8558250E-02	5.7344057E-01	3509
4.8743659E-05	7.7882857E+00	7.7405586E+00	4.7727125E-02	5.6362554E-01	3709
6.2144506E-05	7.0248955E+00	6.9778318E+00	4.7063750E-02	5.5579153E-01	3909
7.5545362E-05	6.2633373E+00	6.2169339E+00	4.6403375E-02	5.4799294E-01	4109
9.6162055E-05	5.6535409E+00	5.6076684E+00	4.5872500E-02	5.4172366E-01	4309
1.1677878E-04	5.0452336E+00	4.9998885E+00	4.5345125E-02	5.3549571E-01	4509
1.4849671E-04	4.5565415E+00	4.5116228E+00	4.4918750E-02	5.3046050E-01	4709
1.8021473E-04	4.0690529E+00	4.0245568E+00	4.4496125E-02	5.2546959E-01	4909
2.2901159E-04	3.6765893E+00	3.6324368E+00	4.4152500E-02	5.2141160E-01	5109
2.7780847E-04	3.2850978E+00	3.2412849E+00	4.3812875E-02	5.1740086E-01	5309
3.5288070E-04	2.9694846E+00	2.9259495E+00	4.3535125E-02	5.1412082E-01	5509
4.2795284E-04	2.6546569E+00	2.6113954E+00	4.3261500E-02	5.1088949E-01	5709
5.4344849E-04	2.4006216E+00	2.3575851E+00	4.3036500E-02	5.0823239E-01	5909
6.5894409E-04	2.1472204E+00	2.1044052E+00	4.2815250E-02	5.0561957E-01	6109
8.3662967E-04	1.9426310E+00	1.8999990E+00	4.2632000E-02	5.0345551E-01	6309
1.0143153E-03	1.7385541E+00	1.6961015E+00	4.2452625E-02	5.0133721E-01	6509
1.2876774E-03	1.5737239E+00	1.5314218E+00	4.2302125E-02	4.9955991E-01	6709
1.5610362E-03	1.4093081E+00	1.3671525E+00	4.2155625E-02	4.9782984E-01	6909
1.9815949E-03	1.2764773E+00	1.2344465E+00	4.2030750E-02	4.9635515E-01	7109
2.4021545E-03	1.1439813E+00	1.1020715E+00	4.1909750E-02	4.9492622E-01	7309
3.0491725E-03	1.0369190E+00	9.9511459E-01	4.1804425E-02	4.9368240E-01	7509
3.6961816E-03	9.3012753E-01	8.8842465E-01	4.1702875E-02	4.9248316E-01	7709
4.6915873E-03	8.4382347E-01	8.0221191E-01	4.1611563E-02	4.9140482E-01	7909
5.6869842E-03	7.5773839E-01	7.1621440E-01	4.1523912E-02	4.9036974E-01	8109
7.2183772E-03	6.8816014E-01	6.4671804E-01	4.1442100E-02	4.8940359E-01	8309
8.7497613E-03	6.1875874E-01	5.7739520E-01	4.1363537E-02	4.8847581E-01	8509
1.1105742E-02	5.6265839E-01	5.2137143E-01	4.1286962E-02	4.8757151E-01	8709
1.3461740E-02	5.0670080E-01	4.6548763E-01	4.1213175E-02	4.8670013E-01	8909
1.7086327E-02	4.6146281E-01	4.2032344E-01	4.1139375E-02	4.8582860E-01	9109
2.0710915E-02	4.1633926E-01	3.7527210E-01	4.1067162E-02	4.8497582E-01	9309
2.6287164E-02	3.7985618E-01	3.3886182E-01	4.0994362E-02	4.8411610E-01	9509
3.1863478E-02	3.4346463E-01	3.0254252E-01	4.0922112E-02	4.8326288E-01	9709
4.0442382E-02	3.1404690E-01	2.7318909E-01	4.0857813E-02	4.8250354E-01	9909
4.9021285E-02	2.8469887E-01	2.4390900E-01	4.0789875E-02	4.8170124E-01	10109
6.2219603E-02	2.6098931E-01	2.2024450E-01	4.0744813E-02	4.8116908E-01	10309
7.5417967E-02	2.3733370E-01	1.9663912E-01	4.0694575E-02	4.8057581E-01	10509
9.5723040E-02	2.1828816E-01	1.7756091E-01	4.0727250E-02	4.8096168E-01	10709
1.1602843E-01	1.9926897E-01	1.5853035E-01	4.0738625E-02	4.8109601E-01	10909
1.4726705E-01	1.8406570E-01	1.4314944E-01	4.0916262E-02	4.8319379E-01	11109
1.7850567E-01	1.6888391E-01	1.2780694E-01	4.1076970E-02	4.8509164E-01	11309
2.2656457E-01	1.5710220E-01	1.1540691E-01	4.1695291E-02	4.9239360E-01	11509
2.7462429E-01	1.4527259E-01	1.0303782E-01	4.2234768E-02	4.9876446E-01	11709
3.4856179E-01	1.3658847E-01	9.3040371E-02	4.3548101E-02	5.1427406E-01	11909
4.2249930E-01	1.2796289E-01	8.3068022E-02	4.4894865E-02	5.3017844E-01	12109
5.3624952E-01	1.2309459E-01	7.5008440E-02	4.8086147E-02	5.6786535E-01	12309
6.5000021E-01	1.1837273E-01	6.6968626E-02	5.1404103E-02	6.0704820E-01	12509
8.2499982E-01	1.1647022E-01	6.0469842E-02	5.6000379E-02	6.6132716E-01	12709
9.9999989E-01	1.1501807E-01	5.4055119E-02	6.1762954E-02	7.2937934E-01	12909

BIBLIOGRAPHY

BIBLIOGRAPHY

[1] Paleebut, S., *An Experimental Study of Three Dimensional Strain Around Cold Worked Holes and in Thick Compact Tension Specimen*, Ph.D thesis, Michigan State University, East Lansing, MI 48824, 1982.

[2] Cloud, G. L. and Paleebut, S., *Surface and Interior Strain in Thick Crack Specimen by Multiple Embedded Grid Moire and Strain Gages*, Proc V International Congress on Experimental Mechanics, Montreal, Canada, pp 111-116, Soc. Exp. Mech., June 1984.

[3] NISA, Engineering Mechanics Research Corporation, Center for Engineering and Computer Technology, Troy, MI 48099.

[4] Hibbit, Karlsson and Sorenson, ABAQUS User Manual, Providence, R. I., 1987.

[5] Howland, R. C. J., *On the Stresses in the Neighbourhood of Circular Hole in a Strip Under Tension*, Philosophical Trans. Royal Soc. London, series A229, pp. 49-86, 1930.

[6] Peterson, R. E., *Stress Concentration Design Factors*, John Wiley, NY, 1953.

[7] Neuber, H., *Theory of Stress Concentration for Shear Strained Prismatic Bodies with Arbitrary Non-linear Stress-strain Law*, J. Appl. Mech., **28**, pp 544-550, 1961.

[8] Irwin, G. R., *Analysis of Stresses and Strains Near the End of Crack Traversing a Plate*, J. Appl. Mech., **24**, pp 361-364, 1957.

[9] Irwin, G. R., *Plastic Zone Near a Crack and Fracture Toughness*, Proc. 7^{th} Sagamore Ordinance Material Conference IV, pp 63-79, 1957.

[10] Creger, M. and Paris, P. C., *Elastic Field Equations for Blunt Cracks with Reference to Stress Corrosion Cracking*, Int. J. Fracture Mech., **3**, pp 247-252, 1967.

[11] Zhang, J. P. and Venugopal, D., *Effect of Notch Radius and Anisotropy on the Crack Tip Plastic Zone*, Engng. Fract. Mech., **26**, pp 913-925, 1987.

[12] Paris, P. C. and Sih, G. C., *Fracture Toughness and Its Applications*, ASTM STP 381, pp 30-85, 1965.

[13] William, M. L., *On the Stress Distribution at the Base of a Stationary Crack*, ASME J. Appl. Mech., **24**, pp 111-114, 1957.

[14] Annual Book of A. S. T. M. Standards, A. S. T. M. Society for Testing and Materials, Philadelphia, Pa., **31**, pp 911, 1970.

[15] Rice, J. R., *Limitation to the Small Scale Yielding Approximation for Crack Tip Plasticity*, J. Mech. Phys. Solids, **22**, pp 17-26, 1974.

[16] Rice, J. R., *A Path Independent Integral and Approximation Analysis of Strain Concentration by Notches and Cracks*, J. Appl. Mech., **35**, pp 379-386, 1968.

[17] Hutchinson, J. W., *Singular Behavior at the End of a Tensile Crack in a Hardening Material*, J. Mech. phys. Solids, **16**, pp 13-31, 1968.

[18] Rice, J. R. and Rosengreen, G. R., *Plane Strain Deformation Near a Crack Tip in a Power-law Hardening Material*, J. Mech. Phys. Solids, **16**, pp 1-12, 1968.

[19] Shih, C. F., *Table of Hutchinson-Rice and Rosengreen Singular Field Quantities*, Divison of Engineering, Brown University, Providence, RI 02912, June 1983.

[20] Walker, T. J., *A Quantitative Strain-and-Stress Criterion for Failure in the Vicinity of Sharp Cracks*, Nuclear Technol., **23**, pp 189-203, 1982.

[21] Schijve, J., *Stress Gradient Around Notches*, Fatigue Engng Mat. Struct., **5**, pp 325-332, 1982.

[22] Molski, K. and Glinka, G., *A method of Elastic-Plastic Stress and Strain Calculations of a Notch Root*, Mater. Sci. Engng., **50**, pp 93-100, 1981.

[23] Glinka, G., *Calculation of Inelastic Notch-Tip Strain-Stresses Histories Under Cyclic Loading*, Engng. Fracture Mech., **22**, pp 834-854, 1985.

[24] Hardrath, H. F. and Ohman, L., *A Study of Elastic Stress Concentration Factors due to Notches and Fillets in Flat Plates*, NASA report, **117**, 1953.

[25] Stowell, E. Z., *Stress and Strain Concentration at a Circular Hole in an Infinite Plate*, NASA Technical note, **2073**, 1950.

[26] Hult, J. A. H. and McClintock, F. A., *Elastic-plastic Stress and Strain Distribution Around Sharp Notches Under Repeated Shear*, Proc. 9^{th} Int. Cong. of Applied Mechanics, **8**, Brussels, pp 51-58, 1956.

[27] Barispolsky, B. M., *Development of a Combined Experimental and Numerical Method for the Thermoelastic Analysis*, Proc. SESA spring meeting, 1981.

[28] Balas, J., Sladek., J. and Drzik, M., *Stress Analysis by Combination of Holographic Interferometry and Boundary Integral Method*, Exp. Mech., **23**, pp 196-202, 1983.

[29] Weathers, J. M., Foster, W. A., Swinson, W. E. and Turner, J. L., *Integration of Laser Speckle and Finite Element Technique of Stress Analysis*, Exp. Mech., pp 60-85, 1985.

[30] Kannien, M. F., Rybcki, E. F., Stonesifer, R. B., Broek, D., Rosenfield, C. W., Marchall and Hahn, G. T., Elastic-plastic Fracture Mechanics for Two Dimensional Stable Crack Growth and Instability Problems, Elastic-plastic Fracture (Edited by Landes, J. D., Begley, J. A. and Clarke, G. A.), ASTM STP 668, pp 65-120, 1979.

[31] Shih, C. F., deLorenzi, H. G. and Andrews, W. R., *Studies on Crack Initiation and Stable crack Growth*, Elastic-plastic Fracture (Edited by Landes, J. D., Begley, J. A. and Clarke, G. A.), ASTM STP 668, pp65-120, 1979.

[32] Segalman, D. J., Woyak, D. B. and Rowlands, R. E., *Smooth Spline like Finite Element Differentiation of Full Field Experimental Data Over Arbitrary Geometry*, Exp. Mech., **19**, pp 429-437, 1979.

[33] Kobayashi, A. S., *Hybrid Experimental-Numerical Stress Analysis*, Exp. Mech., **23**, pp 338-347, 1983.

[34] Hareesh, T. V. and Chiang, T. V. *Integrated Experimental-Finite elment Approach for Studying Elasto- plastic crack-tip fields*, Engng. Fract. Mech., **31**, pp 451-461, 1988.

[35] Brinson, H. F., *The Viscoelastic Behavior of a Ductile Polymer*, Deformation and Fracture of High Polymers, (Edited by Kauch et al.), Plenum Press, NY, 397-416, 1974.

[36] Brinson, H. F., *The Ductile Fracture of Polycarbonate*, Exp. Mech., **10**, pp 72-77, 1970.

[37] A Engineering Handbook on Merlon Polycarbonate, Mobay Chemical Company, Pittsburg, Pa, 15205.

[38] Nisitani, H. and Hyakutake, H., *Condition for Determining the Static Yield and Fracture of a Polycarbonate Plate Specimen with Notches*, Engng. Fract. Mech., **22**, pp 359-368, 1985.

[39] Raske, D. T. and Morrow Dean Jo, *Manual on Low Cycle Fatigue Testing*, ASTM STP 465, pp 1-26, 1969.

[40] ASTM Standard E-606-77, Annual Book of ASTM Standards part 10, American Society for Testing and Materials, pp 614-631, 1977.

[41] Dowling, N. E., Brose, W. R. and Wilson, W. K., *Notched Member Fatigue Life Prediction by the Local Strain Approach*, Advances in Engineering, vol-6 (edited by Wetzel, R. M.), pp 55-84, 1979.

[42] A. S. T. M. E 399, *Standard Test Method for Plane-Strain Fracture Toughness*, Vol. 03.01, 1986.

[43] Knott, J. F., *Fundamentals of Fracture Mechanics*, Butterworths, London-Boston, pp 67-68, 1973.

[44] Leevers, P. S. and Radon, J. C., *In Stress Biaxiality in Various Fracture Specimens Geometry*, Int. J. Fract., **19** pp 311-325, 1983.

[45] Cotterell, B., Int. J. Fract. Mech., **2**, pp 526-533, 1966.

[46] Kfouri, A. P., *Some Evaluation of the Elastic T-term using Eshelby's Method*, Int. J. Fract., **30**, pp 301-315, 1986.

[47] Larsson, S. G. and Carlsson, A. J., *Influence of non-singular Stress Terms and Specimen Geometry on Small-Scale Yielding at Crack Tips in Elastic-plastic Material*, J. Mech. Phys. Solids, **21**, pp 263-278, 1973.

[48] Wang, Y., *A Two-Parameter Characterization of Elastic-Plastic Crack Tip Fields and Application to Cleavage Fracture*, Ph.D thesis, Massachusettes Institute of Technology, Cambridge, May 1991.

[49] Hartranft, R. J. and Sih, G. C., *An Approximate Three Dimensional Theory of Plates with Application to Crack Problem*, Int. J. Engng. Sci., **8**, pp 711-729, 1970.

[50] Sih, G. C., *Bending of Cracked Plate with Arbitrary Stress Distribution Across the Thickness*, J. of Engng. for Industry, **92**, pp 350-356, 1970.

[51] Smith, C. W., *Use of Three Dimensional Photoelasticity and Progress, in related areas*: Experimental techniques in Fracture Mechanics, A. S. Kobayashi, ed., Iowa State University Press, Ames, IA, **2**, pp 3-58, 1975.

[52] Packman, P. F., *The Role of Interferometry in Fracture Studies in realted areas*: Experimental techniques in Fracture Mechanics, A. S. Kobayashi, ed., Iowa State University Press, Ames, IA, **2**, pp 59-87, 1975.

[53] Barker, D. B. and Fourney, M. E., *Displacement Measurement in the Interior of 3-D Bodies Using Scattered- light Speckle Patterns*, Exp. Mech., **16**, pp 209-214, 1976.

[54] Methods for Crack Opening Displacement (COD) Testing, British Standard BS 5762, 1979.

[55] Smith, E. W. and Pascoe, K. J., *Practical Strain Extensometer for Biaxial Cruciform Specimens*, J. Strain, 103-106; 175-181, 1984.

[56] Westgaard, H. M., *Bearing Pressure and Cracks*, Trans. Am. Soc. Mech. Engrs, J. App. Mech, **6**, pp A49-A52, 1939.

[57] Bradly, W. B. and Kobayashi, A. S., *An Investigation of Propagating cracks by Dynamic Photoelasticity*, Exp. Mech., **10(3)**, pp 106-113, 1970.

[58] Redner, A. S., *Experimental Determination of Stress Intensity Factors -A review of Photoelastic Approach*, In Proc. of an International Conference on Fracture Mechanics and Technology, Vol. 1, pp 607-622, Sijthoff and Noordhof, 1977.

[59] Cloud, G. L., *Simple Optical Processing of Moire Grating Photographs*, Exp. Mech., **20(8)**, pp 265-272, 1980.

[60] Smith, C. W., Post, D., Hiatt, G. and Nicoletto, G., *Displacement Measurement Around Cracks in Three-dimensional Problems by a Hybrid Experimental Technique*, Exp. Mech., **20(4)**, pp 15-20, 1983.

[61] Smith, C. W. and Epstein, J. S., *Measurement of Three Dimensional Effects in Cracked Bodies*, Proc. 5^{th} International Congress on Experimental Mechanics, Montreal, Canada, pp 102-110, Soc. Exp. Mech., June 1984.